Noninvasive Quantification of Drug Delivery From an Implantable MEMS Device

by

Audrey M. Johnson

B.S., Chemical Engineering
University of Califomia at Berkeley, 1998

M.S., Chemical Engineering Practice
Massachusetts Institute of Technology, 2001

Submitted to the Department of Chemical Engineering in
Partial Fulfillment of the Requirements for the Degree of

DOCTOR OF PHILOSOPHY IN CHEMICAL ENGINEERING

at the

MASSACUSETTS INSTITUTE OF TECHNOLOGY
[February 2005
September 2004

Signature of Author..
Audrey M. Johnson
Department of Chemical Engineering
September 15, 2004

Certified by..
Robert S. Langer
Professor of Chemical and Biomedical Engineering
Thesis Supervisor

Accepted by..
Daniel Blankschtein
Professor of Chemical Engineering
Chairman, Committee for Graduate Studies

NONINVASIVE QUANTIFICATION OF DRUG DELIVERY FROM AN IMPLANTABLE MEMS DEVICE

by

Audrey M. Johnson

To be submitted to the Department of Chemical Engineering in
September 2004 in partial fulfillment of the requirements for the
Degree of Doctor of Philosophy in Chemical Engineering

Abstract

The goal of this thesis was to develop a method for quantifying the rate of release of drugs from an implanted MEMS (micro electro mechanical systems) drug delivery device without disrupting the surrounding tissue. Most current methods for evaluating tissue response to implants and drug release are invasive and destructive. A method for measuring drug transport from implants *in vivo*, non-invasively and in real time, would have the potential to yield new information about the body's response to implants and the impact of the tissue response on drug and analyte transport.

An impedance based sensor was designed to monitor the release of drug from the drug delivery MEMS device reservoirs. The sensor measures the change in conductivity of the contents of the reservoir as the drug dissolves, which is related to the drug release rate. A four element equivalent circuit was developed to describe the impedance spectrum of the reservoirs based on the physical components of the system. The solution resistance and double layer capacitance elements are functions of the amount of drug that has dissolved and were used to measure the drug release rate in real time.

The sensors were tested by monitoring drug release *in vitro* in saline. Independent measurements of the radioactive tracer released from the well were in complete quantitative agreement with the release rates measured by the electrochemical sensors. A finite element transport model of the system also gave predicted release times in agreement with the sensor and radioactivity measurements of release times in stirred saline.

MEMS devices with impedance sensors were implanted subcutaneously in rats and activated after 3-11 days post-implantation. Release of radiolabeled mannitol was monitored by the sensors *in vivo* in real time and corroborated by scintillation of urine samples. The goal of monitoring drug delivery from an implant *in vivo*, in real time and without disturbing the tissue environment, was accomplished. The results described in this thesis suggest a number of future studies including feedback-controlled delivery of drugs and real-time monitoring and analysis of the effect of the immune response to foreign bodies on drug and analyte transport.

Thesis supervisor: Robert S. Langer

Kenneth J. Germeshausen Professor of
Chemical and Biomedical Engineering

Acknowledgements

I would like to thank everyone who helped make this thesis a reality.

Bob Langer gave me the freedom to come up with a project I liked and encouraged me to think big and take risks. My committee provided guidance and encouragement as well as key technical advice. With Bill Deen for transport, Don Sadoway for electrochemistry, and Michael Cima for materials issues, who could go wrong? I would also like to thank Ken Beers for numerical methods advice and Mark Zahn for explaining just enough solid state electronics for me to figure out my equivalent circuit.

MTL researchers and technicians provided invaluable practical advice on how to make MEMS devices that actually work. Dave Terry, Vicky Diadiuk, Dan Adams, Gwen Donahue, Paul Tierney, Kurt Broderick, Dennis Ward, Bob Bicchieri, and Joe Walsh all helped me find my way around in the microfabrication lab, an alien world of bunny suits, wafers and fabwipes.

I could not have succeeded without the advice and support of the other microchip researchers Rebecca Shawgo, Amy Richards-Grayson, Nolan Flynn, John Santini, Yawen Li, Grace Kim, and Karen Daniel. Thanks are also due to the myriad Langer lab researchers that helped me keep it together, especially David Lavan, Joe Seidel, Mariah Hahn, and Milica Radisic.

Friends in several other chemical engineering labs also gave the benefit of their expertise. Dean Delongchamp in Paula Hammond's lab helped with electrochemistry, Carlos Rinaldi in Howard Brenner's lab helped use Maxwell's equations in spherical coordinates (phew!), Kim Bryant and Ian Zacharia in Bill Deen's lab gave me advice on agarose gels and FEMLAB modeling, and Leonel Arana, Nuria deMas, and Jason Kralj in Klavs Jensen's lab helped me with shadow masks and other fabrication issues. Jeff Tester's lab in the basement (Josh Taylor, Matt Reagan, Anish Goel, Murray Height, Patty Sullivan, Jason Ploeger, Heather Stern, Russ Lachance, Chad Augustine, and of course, my husband Mike Timko) took me on bike and ski trips, let me scrounge around for random parts and borrow tools, and listened to my complaints when my experiments refused to cooperate.

Then, of course, there are the people who actually did the work (well, not quite all of it, but to hear them talk...): my talented UROPs. It was a pleasure to work with Andrea Noronha, Roxanne Lau, Ines Sherifi, and Priya Shah, even if most of them had the temerity to graduate before me.

resistance, double layer capacitance, silicon resistance and capacitance terms, was developed to describe the impedance spectrum of the reservoirs based on the physical components of the system. The solution resistance and double layer capacitance elements are functions of the amount of drug that has dissolved and were used to measure the drug release rate in real time.

The sensors were tested by monitoring drug release *in vitro* in stirred saline and in a laminar flow cell. The experiments in stirred saline gave consistent release times, while the flow cell experiments showed significant variability, likely due to incomplete opening of the reservoir membranes. Most importantly, independent measurements of the radioactive tracer released from the well were in complete quantitative agreement with the release rates measured by the electrochemical sensors. A finite element model of the system, represented by a conical approximation in cylindrical coordinates, also gave predicted release times in agreement with the sensor and radioactivity measurements of release times in stirred saline. The success of the mathematical model strongly suggests that drug release from the drug reservoirs is a process of dissolution and diffusion.

MEMS devices with impedance sensors were implanted subcutaneously in rats and activated after 3-11 days post-implantation. Release of radiolabeled mannitol was monitored by the sensors *in vivo* in real time and corroborated by scintillation of urine samples. Significant variability in the measured release time was observed between animals, demonstrating the utility of sensors for noninvasive monitoring of drug release rate *in vivo*. The goal of monitoring drug delivery from an implant *in vivo*, in real time and without disturbing the tissue environment, was accomplished. The results described in this thesis suggest a number of future studies including feedback-controlled delivery of drugs and real-time monitoring and analysis of the effect of the immune response to foreign bodies on drug and analyte transport.

Thesis supervisor: Robert S. Langer

Kenneth J. Germeshausen Professor of
Chemical and Biomedical Engineering

The support of family and friends kept me happy and healthy during my tenure here at MIT. Friends from first year classes, roommates, and friends at church have made my time at MIT fun despite the work. My family can take credit for getting me here in the first place and for keeping me happy to be here by sending enough care packages to keep me stocked with chocolate in perpetuity.

Saving the best for last, I would like to thank my husband, Michael, for everything. Meeting you was the best thing that happened to me at MIT, even including getting my doctorate after six long years!

Table of Contents

List of Figures

List of Tables

1. Introduction

The research presented in this thesis developed from one particularly challenging problem – how can one evaluate what's going on around a device implanted within the body without perturbing the very system one is trying to study? The cumulative results of many biocompatibility studies on explanted tissue and implants have given us a general idea of the usual process of wound healing and resolution around implants of a variety of types. However, the results make it clear that every implant, every tissue, and every organism differs from the 'typical' response, often markedly. We do not have a complete picture of the mechanisms and inputs to the system that would allow us to predict *a priori* the tissue response to a particular implant in a particular host. For every new implant, many new studies must be done to evaluate its functioning *in vivo*, and there is always the risk of an adverse response.

Certain types of implants are particularly affected by the tissue response, according to the degree with which they must interact with their environment. Tissue engineered implants, designed to integrate into the host, are critically dependent on the tissue environment surrounding them. The very purpose of *in vivo* sensors is to interact with the body, and as of yet no one has been able to make a truly long term implantable sensor that can function without frequent recalibration. Drug delivery devices are also impacted, particularly those like the MEMS device that are designed to deliver quick pulses of therapeutics. In all three of these cases, a key aspect of the tissue response is how it affects *transport* to and from the implant: of oxygen and nutrients, analytes, or drugs.

The study of transport of solutes naturally appeals to chemical engineers, and *in vivo* transport is a field offering many challenges. Most methods for measuring drug transport *in vivo* involve explantation of the tissue or are limited in resolution or application. The MEMS drug delivery device offers a unique platform for studying transport *in vivo*, because it is an active device in which the timing of delivery can be precisely controlled, and because it is already 'wired', or electrically connected. Still, measuring drug transport from the device without disturbing the surrounding tissue is not a simple problem.

An impedance-based sensor was developed that applies a small voltage across the reservoir of a MEMS drug delivery device in order to measure the conductivity of the reservoir contents (drug). After the reservoir is opened, body fluid enters the reservoir as the drug slowly dissolves and diffuses out into the environment. As the reservoir fills with fluid, the conductivity increases and the impedance signal changes. By monitoring the impedance over time, one can determine the rate of drug release and transport without affecting the tissue surrounding the device. This thesis describes the fabrication, characterization, modeling, and *in vitro* and *in vivo* testing of MEMS drug delivery devices with integrated impedance sensors for non-invasive monitoring of drug transport in real time.

1.1. Biocompatibility of implants

The response of an organism to a foreign body is naturally hostile, as immune cells release toxic chemical agents to destroy the invader.[1,2] If the foreign body is not destroyed, it is often walled off from the rest of the organism by an avascular fibrous capsule of tissue that inhibits transport of substances such as oxygen or nutrients between the body and the implant.[3] The precise nature of the response varies according to the foreign material, the implant site, the species receiving the implant, and from individual to individual.[4] Materials generally considered 'biocompatible' are not exempt from this response; biocompatibility is commonly defined as simply "the ability of a material to perform with an appropriate host response in a specific application."[5] A biocompatible material is therefore one which avoids a high degree of immune response that could cause intolerable side effects and that continues to function despite the foreign body response that does occur.

The formation of a fibrous capsule around implanted devices has particularly important implications for drug delivery and sensing applications. Current drug delivery implants are usually designed for a slow, steady release of drug over time. In such a case, the transport profile of drug is pseudo-steady state and evolves only slowly, so that while the fibrous capsule affects drug release, the device is still able to function.[6,7] However, in the case of active devices, where quick pulsatile or more complex release profiles are desired, the isolation of the implant causes a measurement offset and a time lag due to the finite amount of time required for diffusion of the drug through the capsule.[8,9] The time delay is also a key factor in the performance of *in vivo* sensors.[10,11] Even if sensor components are made resistant to the immune response, the sensor must be continually recalibrated to account for the changing conditions in the tissue surrounding it.[12] Recalibration generally involves sampling of blood or interstitial fluid and defeats the purpose of an implanted sensor, which is usually to avoid frequent invasive testing.

1.2. Existing methods to measure drug transport *in vivo*

Most methods for determining the extent of implant encapsulation and the drug dissolution profile in the vicinity of an implant involve invasive methods such as release of a radiolabeled compound or fluorophore followed by explantation of the implant and the surrounding tissue for sectioning and histology.[13,14] Alternatively, the capsular tissue from around the implant may be removed from the implant and placed in a diffusion chamber for *ex vivo* permeability studies.[15,16] In all of these methods, the measurement results in the destruction of the sample. Each data point requires a different implant and animal, contributing to a high variability in measurements. For *ex vivo* studies, it is unclear whether the transport characteristics of explanted tissue are truly representative of the *in vivo* properties.

Other, non-destructive methods have significant limitations. Fluorescent methods involving direct observation of drug are restricted to unique systems such as the translucent rabbit ear[17] or rat dorsal skin clamped in a glass window for viewing.[18] Pharmacokinetic studies also involve monitoring of drug distributions *in vivo*, and significant work has been done to find non-invasive methods for this purpose. Microdialysis is a minimally invasive way of sampling species in interstitial fluid by a needle probe, but still requires some perturbation of the system and is limited in resolution and accuracy.[19,20] Nuclear imaging methods such as PET (positron emission tomography), MRI (magnetic resonance imaging), and CT (computerized tomography) scanning are also used in pharmacokinetics, and CT scanning has been used to observe release of drug from implanted polymer millirods *in vivo*.[21,22] However, these methods are limited to detection of certain compounds (short half-life radioisotopes for PET, certain nuclei especially ^{19}F or ^{195}Pt for MRI, heavy elements such as platinum or iodine for CT), have spatial resolution of 1mm or larger, and/or often have sensitivities above the therapeutic concentration of drug.[23,24,25]

Measurements of blood and urine drug levels also give some feedback on the operation of a drug delivery device. However, blood and urine drug concentrations and the release rate of a drug from an implant are often only distantly related. Many transport barriers exist between the implant region and the point of measurement. In addition, the pharmacokinetics of many drugs are quite complex, and often the compound is metabolized so rapidly that its degradation products are detected in the blood or urine, rather than the drug itself.[26;27,28]

1.3. MEMS drug delivery device

A drug delivery MEMS device was developed previously in our laboratory by John Santini[29,30] and the miniaturization, packaging, biocompatibility testing[31,32,33] and development of a more reliable *in vivo* activation electrochemistry protocol[34,35] were performed by Rebecca Shawgo in conjunction with Aron Rosenberg, Yawen Li, Betty Tyler and Gabriela Voskerician.[36] The device enables the release of multiple drugs independently in a pulsatile fashion, which allows the design of previously unachievable complex release profiles. It consists of an array of microreservoirs etched into a silicon substrate, each capped by a thin gold membrane. Upon application of a 1 V potential vs. platinum in the presence of chloride ion, the gold membrane oxidizes to form soluble gold chloride, thinning the membrane until it fails. The drug within the reservoir then dissolves into the surroundings as aqueous solution or interstitial fluid penetrates into the reservoir, as depicted pictorially in Figure 1.1.

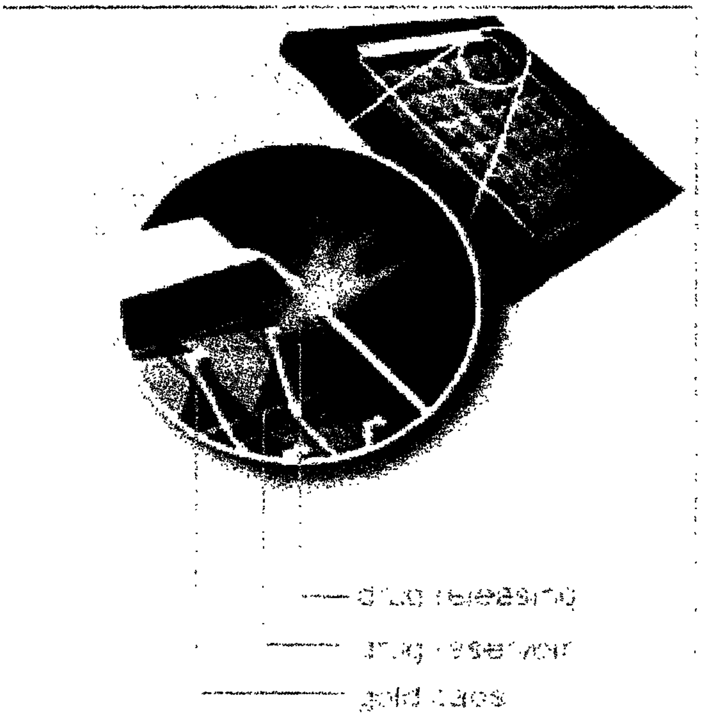

Figure 1.1. Schematic rendering of a MEMS drug delivery device showing drug releasing from a reservoir. Courtesy of MicroCHIPS, Inc.

1.4. Drug release sensor

This thesis presents a modification of the drug delivery MEMS device in which two electrodes within each drug reservoir serve as a novel drug release sensor, as depicted in Figure 1.2. Each reservoir has the shape of a square pyramid due to the anisotropic etch used to create them, and the electrodes cover two opposing sides of this pyramid. Two-electrode impedance spectroscopy is used to measure the electrical characteristics of the reservoir. As the drug dissolves, the change in the electrical signature of the system allows real time monitoring of the rate of transport of drug away from the device.

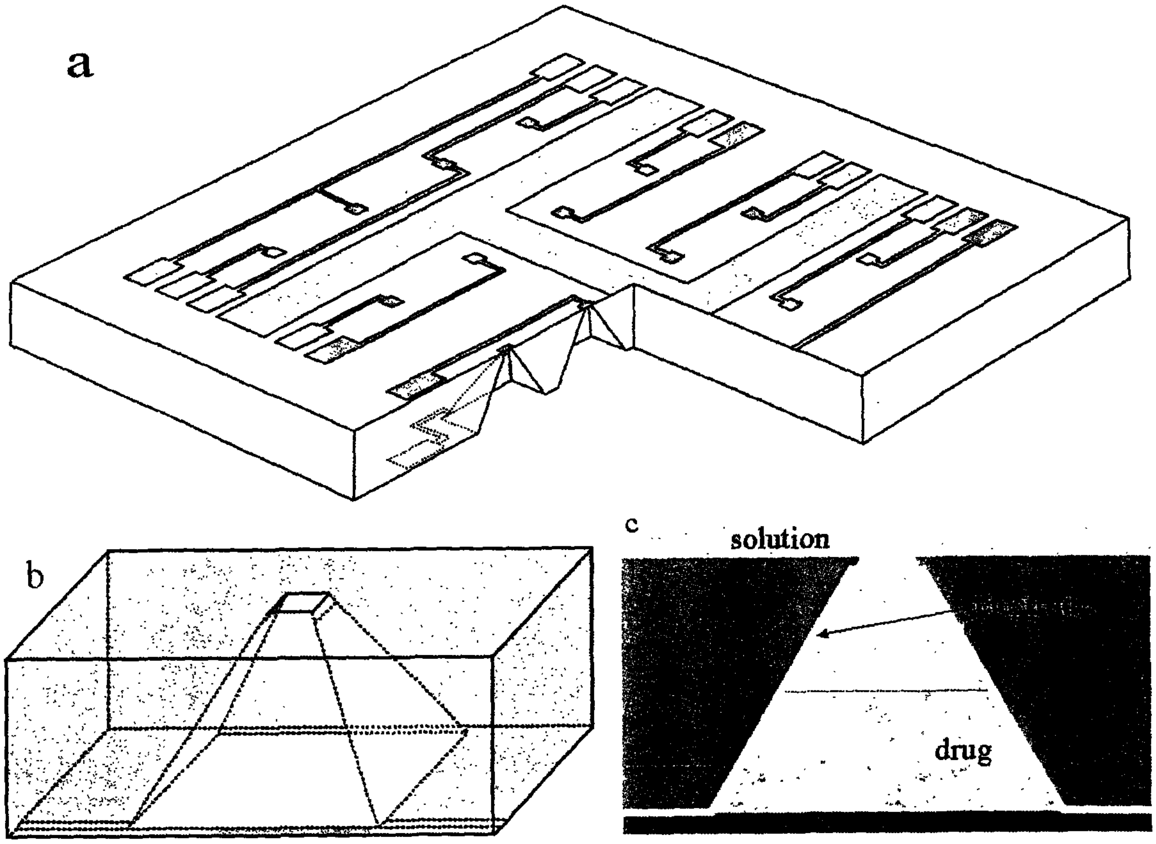

Figure 1.2. The MEMS drug delivery device with drug release sensors; **a)** cutaway perspective view of the prototype, with electrodes on the top surface for drug release and electrodes on the bottom surface and in the reservoirs for drug release monitoring, dimensions 5 x 5 x 0.3 mm, **b)** view of one device reservoir showing electrode configuration, to scale, **c)** idealized representation of drug release from a reservoir.

The sensor signal is related to the physical system by means of an equivalent circuit,[37] and the resistance and capacitance so obtained are related to the rate of drug dissolution and transport by a finite element transport model. Radiolabeled mannitol, a model drug, was released into stirred saline and into a laminar flow cell, demonstrating that the sensor signal is directly related to the rate of drug release measured by scintillation counting. Finally, MEMS drug delivery devices with impedance sensors were implanted in rats and the rate of drug release *in vivo* was measured in real time, non-invasively.

1.8. References

1. J. M. Anderson, Biological responses to materials, *Annual Review of Materials Research*, **31**, 81-110 (2001).
2. S. Werner and R. Grose, Regulation of wound healing by growth factors and cytokines, *Physiological Reviews*, **83**, 835-870 (2002).
3. J. Bodziony, Bioartificial endocrine pancreas: foreign-body reaction and effectiveness of diffusional transport of insulin and oxygen after long-term implantation of hollow fibers into rats, *Research in Experimental Medicine*, **192**, 305-316 (1992).
4. D. F. Williams, Fundamental Aspects of Biocompatibility, CRC Press, Boca Raton, FL (1981).
5. D. F. Williams, Definitions in biomaterials, in Progress in Biomedical Engineering, D. F. Williams, Editor, Elsevier, Amsterdam (1987).
6. B. D. Ratner, Reducing capsular thickness and enhancing angiogenesis around implant drug release systems, *Journal of Controlled Release*, **78**, 211-218 (2002).
7. J. M. Anderson, H. Niven, J. Pelagalli, L. S. Olanoff, and R. D. Jones, The role of the fibrous capsule in the function of implanted drug-polymer sustained release systems, *Journal of Biomedical Materials Research*, **15**, 889-902 (1981).
8. P. S. Leppert, L. Cammack, R. Cargill, L. Coffman, M. Cortese, K. Engle, C. Krupco, and J. A. Fix, Interspecies differences in systemic drug availability following subcutaneous pulsatile administration in cattle, sheep, dogs, and rats, *Journal of Biomedical Materials Research*, **28**, 713-722 (1994)..
9. E. Fournier, C. Passirani, C. N. Montero-Menei, and J. P. Benoit, Biocompatibility of implantable synthetic polymeric drug carriers: focus on brain biocompatibility, *Biomaterials*, **24**, 3311-3331 (2003).
10. M. C. Frost and M. E. Meyerhoff, Implantable chemical sensors for real-time clinical monitoring: progress and challenges, *Current Opinions in Chemical Biology*, **6**, 633-641 (2002).
11. M. Gerritsen, J. A. Jansen, A. Kros, R. J. M. Nolte, and J. A. Lutterman, Performance of subcutaneously implanted glucose sensors: a review, *Journal of Investigational Surgery*, **11**, 163-174 (1998).
12. C. Choleau, J. C. Klein, G. Reach, B. Aussedat, V. Demaria-Pesce, G. S. Wilson, R. Gifford, and W. K. Ward, Calibration of a subcutaneous amperometric glucose sensor implanted for 7 days in diabetic patients Part 2. Superiority of the one-point calibration method, *Biosensors and Bioelectronics*, **17**, 647-654 (2002).
13. J. F. Strasser, L. K. Fun, S. Eller, S. A. Grossman, and W. M. Saltzman, Distribution of 1,3-bis(2-chloroethyl)-1-nitrosourea and tracers in the rabbit brain

after interstitial delivery by biodegradable polymer implants, *Journal of Pharmacology and Experimental Therapeutics*, **275**, 1647-1655, (1995).

14. P. Kortesuo, M. Ahola, S. Karlsson, I. Kangasniemi, A. Yli-Urpo, and J. Kiesvaara, Silica xerogel as an implantable carrier for controlled drug delivery – evaluation of drug distribution and tissue effects after implantation, *Biomaterials*, **21**, 193-198 (2000).
15. A. A. Sharkawy, B. Klitzman, G. A. Truskey, and W. M. Reichert, Engineering the tissue which encapsulates subcutaneous implants. I. Diffusion properties, *Journal of Biomedical Materials Research*, **37**, 401-412 (1997).
16. R. C. Wood, E. L. LeCluyse, and J. A. Fix, Assessment of a model for measuring drug diffusion through implant-generated fibrous capsule membranes, *Biomaterials*, **16**, 957-959 (1995).
17. G. R. Martin and R. K. Jain, Noninvasive measurement of interstitial pH profiles in normal and neoplastic tissue using fluorescence ratio imaging microscopy, *Cancer Research*, **54**, 5670-5674 (1994).
18. K. Erickson, R. D. Braun, D. Yu, J. Lanzen, D. Wilson, D. M. Brizel, T. W. Secomb, J. E. Biaglow, and M. W. Dewhirst, Effect of longitudinal oxygen gradients on effectiveness of manipulation of tumor oxygenation, *Cancer Research*, **63**, 4705-4712 (2003).
19. K. E. Garrison, S. A. Pasas, J. D. Cooper, and M. I. Davies, A review of membrane sampling from biological tissues with applications in pharmacokinetics, metabolism and pharmacodynamics, *European Journal of Pharmaceutical Science*, **17**, 1-12 (2002).
20. M. Muller, Microdialysis in clinical drug delivery studies, *Advanced Drug Delivery Reviews*, **45**, 255-269 (2000).
21. K. A. Salem, A. Szymanski-Exner, R. S. Lazebnik, M. S. Breen, J. Gao, and D. L. Wilson, X-ray computed tomography methods for *in vivo* evaluation of local drug release systems, *IEEE Transactions in Medical Imaging*, **21**, 1310-1316 (2002).
22. A. Szymanski-Exner, N. T. Stowe, K. Salem, R. Lazebnik, J. R. Haaga, D. L. Wilson, and J. Gao, Noninvasive monitoring of local drug release using X-ray computed tomography: optimization and *in vitro/in vivo* validation, *Journal of Pharmaceutical Science*, **92**, 289-296 (2003).
23. W. Wolf, Introduction and overview of noninvasive drug monitoring, *Advanced Drug Delivery Reviews*, **41**, 1-5 (2000).
24. R. E. Port and W. Wolf, Noninvasive methods to study drug distribution, *Investigational New Drugs*, **21**, 157-168 (2003).
25. A. J. Fischman, N. M. Alpert, and R. H. Rubin, Pharmacokinetic imaging: a noninvasive method for determining drug distribution and action, *Clinical Pharmacokinetics*, **41**, 581-602 (2002).
26. B. J. Gudzinowicz, B. T. Younkin, Jr., and M. J. Gudzinowicz, Drug Dynamics for Analytical, Clinical, and Biological Chemists, Marcel Dekker, New York (1984).
27. X. Li and W. K. Chan, Transport, metabolism and elimination mechanisms of anti-HIV agents, *Advanced Drug Delivery Reviews*, **39**, 81-103 (1999).

28. V. T. DeVita, C. Denham, J. D. Davidson, and V. T. Oliverio, The physiological disposition of the carcinostatic 1,3-bis(2-chloroethyl)-1-nitrosourea (BCNU) in man and animals, *Clinical and Pharmacological Therapeutics,* **8**, 566 (1967).

29. J. T. Santini Jr., A controlled release microchip, *Massachusetts Institute of Technology, Doctoral Thesis* (1999).

30. J. T. Santini Jr., M. J. Cima, and R. Langer, A controlled-release microchip, *Nature*, **397**, 335 (1999).

31. G. Voskerician, M. S. Shive, R. S. Shawgo, H. von Recum, J. M. Anderson, M. J. Cima, R. Langer, Biocompatibility and biofouling of MEMS drug delivery devices, *Biomaterials*, **24**, 1959-1967 (2003).

32. G. Voskerician, R. S. Shawgo, P. A. Hiltner, J. M. Anderson, M. J. Cima, and R. Langer, In vivo inflammatory and wound healing effects of gold electrode voltammetry for MEMS micro-reservoir drug delivery device, *IEEE Transactions in Biomedical Engineering*, **51**, 627-635 (2004).

33. R. S. Shawgo, In vivo activation and biocompatibility of a MEMS microreservoir drug delivery device, *Massachusetts Institute of Technology, Doctoral Thesis* (2004).

34. A. Rosenberg, In vitro electrochemical testing of a microchip based controlled release drug delivery device, *Massachusetts Institute of Technology, Masters Thesis* (2001).

35. Y. Li, R. S. Shawgo, B. Tyler, P. T. Henderson, J. S. Vogel, A. Rosenberg, P. B. Storm, R. Langer, H. Brem, M. J. Cima, In vivo release from a drug delivery MEMS device, (accepted to *J. Controlled Release*, in press).

36. R. S. Shawgo, G. Voskerician, H. L. Ho Duc, Y. Li, A. Lynn, M. McEwan, R. Langer, J. M. Anderson, and M. J. Cima, Repeated in vivo electrochemical activation of MEMS drug delivery device and the biological effects, (accepted to *Journal of Biomedical Materials Research*).

37. A. M. Johnson, D. R. Sadoway, M. J. Cima, and R. Langer, Design and testing of an impedance-based sensor for monitoring drug delivery, (accepted to *Journal of the Electrochemical Society*).

2. Overview of Methods

Once the goal of monitoring drug release and transport from the MEMS drug delivery device had been set, the problem was broken down into key tasks. After setting the goal, the problem was broken down into key tasks. First, a sensing method for drug release monitoring was chosen. Two methods were proposed: the sensing of impedance within the drug reservoir to monitor drug dissolution and diffusion, and the integration of pixilated radioactivity detectors onto the device for sensing diffusion of radiolabeled drug away from the device. The impedance method was chosen as the more easily accomplished, although it is less direct because the rate of transport of drug away from the device is inferred from conductivity measurements of dissolution rate inside the reservoir.

The first task was the microfabrication of a modified MEMS drug delivery device that would include impedance electrodes within the reservoirs (chapter 3). An equivalent circuit was developed that relates the impedance spectrum to the actual physical characteristics of the sensors (chapter 4). The rate of drug dissolution can be calculated from the impedance spectra using the equivalent circuit model to calculate the reservoir conductivity. The reservoir conductivity and drug dissolution rate are determined by the rate of drug transport away from the device, which was modeled using finite element analysis in the FEMLAB programming environment (chapter 7). The impedance measurement method was validated *in vitro* by release of radiolabeled mannitol from the device into saline (chapter 5). The measurements of drug release rate from scintillation of the release medium and from the impedance measurement paralleled each other closely. Finally, the devices were implanted subcutaneously in rats and the drug release rate was measured non-invasively, in real time, after 3, 4, 10, and 11 days post-implantation (chapter 6). The following sections describe the main challenges involved in accomplishing each of these tasks as part of accomplishing the goal of monitoring drug transport *in vivo.*

2.1. Device microfabrication and packaging

The MEMS devices had to be fabricated before they could be tested. The microfabrication facility at MIT is a valuable shared resource, and significant training and preparation are required before a user is allowed to perform processing there. The fabrication of MEMS rather than traditional integrated circuits is still more of an art than a science and requires a certain amount of hands-on experience before the processing goes relatively smoothly. Once the process of making a MEMS drug delivery device was mastered, the process had to be modified to include fabrication of impedance electrodes within the device reservoirs. This involves the patterning of a three dimensional surface, which requires non-standard processing techniques. A shadow masking technique was adopted with success. However, the new process involves many more steps than the original fabrication of drug delivery MEMS, and each additional processing step increases the time required for fabrication and reduces the overall yield.

The packaging of the devices is also difficult simply because the devices are so small (5 x 5 x 0.3 mm). Tiny, precise amounts of drug must be loaded in each reservoir and sealed to withstand the harsh environment of saline or living tissue. Electrical connections must be made to both the top and bottom surface of the device, for the activation electrodes and for the impedance electrodes. The packaging process was modified to allow the embedding of the backside connections in epoxy to protect them prior to making the frontside connections. The electrical connections must also be insulated from the harsh environment. The packaging method developed was sufficient to allow reliable operation of the devices up to 2 weeks *in vivo*. The reliability of device functioning (and therefore the amount of data collected) was inhibited by the inconsistency of the corrosion method used to open the reservoirs. A new reservoir opening method, the 'fuse chip', has since been developed by MicroCHIPS researchers, that should make the MEMS devices much more reliable and easier to use.

2.2. Equivalent circuit analysis

Impedance spectroscopy is a commonly used technique that is complicated by the fact that it almost always yields what seems to be good data, even when it is not really measuring the quantity of interest. Control experiments and a good physical understanding of the system are critical to ensure that the data are meaningful. The data are analyzed by means of an equivalent circuit, which represents the physical system in terms of a network of resistors and capacitors. An equivalent circuit was developed and validated that describes the MEMS sensors in terms of four circuit elements. First, the conductivity of PBS solutions was measured in a standard conductivity cell. The measured conductivities compared well with the theoretical conductivities calculated from Kohlrausch's law. Then a 100x scale model of the device reservoirs was constructed to evaluate the effects of the pyramidal geometry on the impedance. The linear dependence of the solution resistance on the inverse depth of liquid in the reservoir model matched the expected dependence calculated from the geometry of the system. Finally, impedance measurements were performed on the MEMS sensors to determine the appropriate equivalent circuit. The equivalent circuit was then used to relate the sensor signal to the conductivity of the drug reservoir, and then to the rate of drug dissolution and transport.

2.3. *In vitro* release monitoring

In vitro releases serve two purposes: first, the simple purpose of making sure the device works (activates, releases, monitors), and second, the evaluation of how drug transport from the device affects the dissolution rate and sensor signal. A laminar flow cell was designed to provide a controlled transport environment, but was difficult to align and seal consistently. The release times in the flow cell were highly variable, likely due to incomplete removal of the gold membrane from the device opening. Further releases were performed in a stirred saline solution, with more consistent release times of approximately 2 hours. Radiolabeled mannitol was used as a model drug because of its simple pharmacokinetics. The release rate measured by scintillation counting of the release medium was compared to the release rate measured using the impedance sensors and found to be 5-10 minutes longer. The lag time between the sensors and the scintillation counting is thought to be due to the dilution of the concentrated mannitol solution in the reservoir after dissolution is complete. The experimentally measured rates were also compared to the release rates predicted by the mathematical simulation.

2.4. *In vivo* release monitoring

It is often said that adding the words *"in vivo"* to a thesis proposal automatically extends the tenure of the graduate student by at least one year. Animal experiments must be designed carefully to prevent undue suffering and keep the animals healthy throughout the experiment. The type of animal limits what can be measured, by limiting the length of time they can be safely anesthetized, how many and what types of samples can be taken (i.e. blood or urine), and how the samples can safely be taken (for example, urine can be collected continuously through a catheter or at naturally irregular intervals). Beyond these basic limitations, working *in vivo* is difficult for many additional reasons, including the need to design the implant to survive surgical implantation and the 'messy' tissue environment as well as the inability to observe or adjust the implant after implantation. The *in vivo* rat implantation studies were greatly facilitated by the laboratory of Dr. Henry Brem at Johns Hopkins University, especially by lab administrator Betty Tyler. Their surgical and animal care expertise enabled these experiments to be performed successfully in a short time frame and with a minimum of complications.

Two sets of devices were prepared with radioactive mannitol and implanted subcutaneously in rats. The first set demonstrated that the impedance sensors were able to monitor drug release *in vivo*, but the data were limited by breakage of many reservoir membranes and degradation in the quality of the electrical insulation over time. The second set of devices was prepared in accordance with the lessons learned from the first experiment, and several drug releases were successfully monitored at release times 3, 4, 10, and 11 days post-implantation. Data were limited to short implantation times by the gradual infiltration of water into the epoxy used to insulate the wires. Release monitoring was limited to 5-6 hours by the risks associated with long anesthesia. In addition, the corrosion method used to open the reservoirs was relatively unreliable *in vivo*, leading to fewer successful opened reservoirs for release monitoring. Despite these limitations, the sensors successfully monitored several drug releases from the implants without disturbing the tissue environment. The tissue reaction and the release rates varied significantly between animals, showing the potential utility of implanted sensors to monitor drug release.

2.5. Mathematical simulation of release

The transport model is considerably simplified by the exclusion of convection due to the avascular nature of the tissue that normally encapsulates subcutaneous implants. The complexity arises from the geometry of the system – the square pyramidal reservoir has a significant base angle of 54.4° that cannot be neglected, and the x, y, and z length scales involved (width, height of reservoir, thickness of tissue) are of similar order of magnitude. The dissolution interface moves as the drug dissolves, giving rise to the sensor signal, making it a moving boundary problem. The problem is therefore time-varying and three-dimensional with a moving interface. The system was simplified to two dimensions in cylindrical coordinates and modeled as a cylinder in MATLAB with assistance from Dr. Ken Beers. The MATLAB model used a mass balance at the interface in conjunction with an axial stretch factor to cope with the moving boundary. The problem was later simulated in FEMLAB with a concentration-dependent diffusivity to mimic the moving interface. The step change in diffusivity was tuned to obtain agreement between the MATLAB and FEMLAB models. A conical approximation of the reservoir was then used to estimate the expected rate of drug release. Additional simulations were performed to explore the effects of incomplete reservoir opening and the presence of an unstirred layer at the reservoir opening.

2.6. Microscale lyophilization and drying of proteins

Another project was the development of microscale lyophilization and drying methods for the preservation of protein activity within the reservoirs of the drug delivery device. The project helped to develop familiarity with the techniques necessary for working with MEMS drug delivery devices and produced some interesting results. The study developed into an independent UROP project that led to a patent and a short research paper. Protein stability and formulation are not well understood, but simple *in situ* lyophilization and drying of enzymes within the device reservoirs was able to preserve a majority of enzyme activity with minimal formulation for the four enzymes studied. The results of the microscale lyophilization and drying processes were compared to the enzyme activity preserved after traditional bulk-scale lyophilization and drying. Highly sensitive fluorescence-based enzyme assays were used because of the very small volume of the MEMS reservoirs. The assays were modified to attain sufficient sensitivity to distinguish between enzyme activity preserved by the four processing methods. Judiciously chosen control experiments, meticulous attention to detail, and careful statistical data analysis were required to obtain reliable, reproducible assay results for the different enzymes and processing methods studied.

2.7. Summary

The goal of monitoring drug release from the MEMS drug delivery device *in vivo*, in real time and non-invasively, was accomplished. An impedance-based sensor was integrated into the MEMS device and characterized in terms of an equivalent circuit. Drug transport from the device was modeled with a finite element transport model and measured experimentally by detection of radiolabeled drug in the release medium and by the impedance sensor measurements. Model predictions and the two measurement methods were in good agreement. Devices were implanted subcutaneously in rats and activated and monitored up to 11 days post-implantation.

3. Device Microfabrication and Packaging

The process of fabrication, filling, sealing, and wiring of MEMS devices was complicated by the small size and fragility of the device features. The overall process can be divided into two main tasks: microfabrication, which was performed in the clean room facilities of the Microsystems Technology Laboratory (MTL), and packaging, which took place largely in the Langer laboratory. Two major hurdles had to be overcome to make possible the addition of impedance sensors. The first was the patterning of impedance sensors within the pyramidal reservoirs of the device, which required a nonstandard microfabrication technique because the surface was three dimensional rather than flat. The second was the making of electrical connections to both the top and bottom surfaces of the device; top connections for activation and opening of the device reservoirs, bottom connections for monitoring of release via the impedance sensors. The microfabrication problem was addressed by use of a shadow mask wafer technique, and the connections problem was solved by embedding the bottom connections in epoxy before flipping the device over to make top connections. Both solutions were sufficient for the making of prototype devices but would need significant improvement to allow device production on a large scale.

The chapter is divided into three main sections:

1. A detailed description of the microfabrication processing steps
2. Microfabrication details specific to the devices used in experiments, each of which came from one of two wafers
3. A detailed description of the packaging process

Packaging details specific to each electrochemistry or release experiment are given in the experimental section of the appropriate chapter.

3.1. Microfabrication procedure

The microfabrication process was adapted from that developed by John Santini and Rebecca Shawgo for the original MEMS drug delivery devices.[1,2] General clean room training as well as training specific to each machine was required for the microfabrication process, and all microfabrication steps were approved by the process technology committee in accordance with MTL policy.[3] The process was designed taking into account the limitations of the available equipment as well as the need to maintain strict separation of clean (designated by a green dot in MTL), gold contaminated (red dot), and potassium contaminated (yellow dot) wafers, working areas, and machines.

Patterning sensor electrodes within the reservoirs of the device was nontrivial because the electrodes are patterned onto a three dimensional surface, while traditional patterning methods are designed for flat surfaces. Three possible solutions to this problem were considered: electrochemically deposited photoresist, sprayed photoresist, and a shadow mask. Electrochemically deposited photoresist[4] produces a conformal coating of photoresist and is the most suitable of the three processes for large scale processing but is not approved for use in MTL, so was not attempted. Sprayed photoresist,[5,6] which is applied using an airbrush, was attempted and initially gave promising results. Although the sprayed resist covered the wafer surface as well as the bottom and sides of the reservoirs, the resist had difficulty wetting the obtuse angles of the edges of the reservoirs, as depicted in Figure 3.1. As a result, the shadow masking technique was adopted, in which a separate wafer is patterned with the electrode design and etched through its entire thickness, creating a mask.[7,8] The mask wafer was then aligned over the device wafer for gold deposition, shadowing the device wafer in the desired pattern, as described in detail in section 3.1.18 on masked gold deposition.

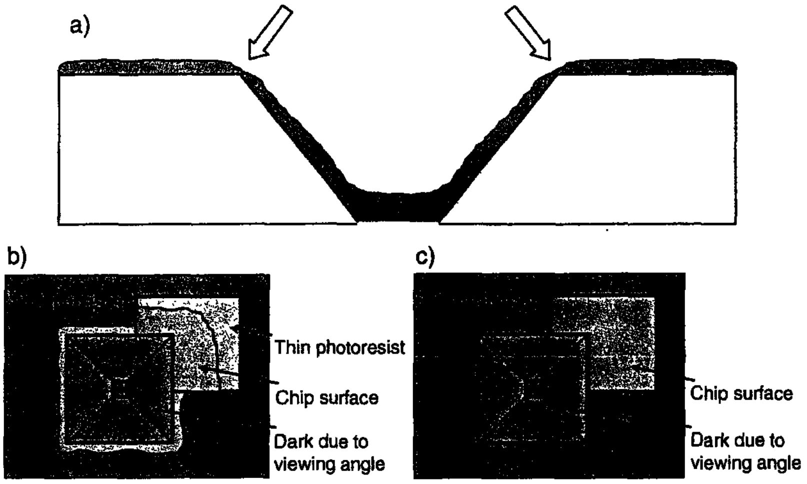

Figure 3.1. Schematics of sprayed photoresist test pattern results; **a)** side view showing the thickness of aerosolized photoresist with arrows showing thin resist over obtuse angles, **b)** top view of desired test pattern result after developing, as seen under mercury arc microscope in which organics glow red, **c)** top view of actual result of test pattern after developing, showing loss of thinned resist from edges prior to full removal of resist from patterned square.

The addition of sensors to the devices also significantly increases the number of microfabrication steps involved. Each additional step increases the attrition of wafers and individual devices due to breakage, imperfections in uniformity across wafers, processing errors, or machine malfunction. However, even with a more complex process, sufficient quantities of prototypes were produced due to the large number of devices per wafer. An overview of the final process is given in Table 3.1 and key process steps are illustrated in Figure 3.2. The shadow mask fabrication process is summarized in Table 3.2 and illustrated in Figure 3.3. Each processing step is described in further detail in the following subsections. In addition, detailed instructions for the operation and troubleshooting of each machine are given in appendix 10.1.

Table 3.1. Microfabrication process overview.

step #	processing step description
1	starting wafers are four inch, dsp <100> silicon
2	deposit nitride/oxide on both sides (done by staff)
3	pattern backside with AMJWELLS mask, positive resist
4	etch nitride/oxide pattern using plasmaquest
5	KOH etch through wafers to form wells
6	post-KOH clean to remove K^+ contamination
7	pattern frontside with AMJGOLD mask, image reversal resist
8	deposit gold onto frontside using ebeam
9	soak in acetone to lift off gold
10	clean wafer with Nanostrip
11	protect frontside with thick photoresist
12	etch nitride/oxide overhang on backside using plasmaquest
13	clean wafer with acetone and Nanostrip
14	protect frontside with thick photoresist
15	deposit oxide onto backside using plasmaquest
16	clean wafer using asher (optional)
17	align and mount shadow mask wafer onto wafer
18	deposit gold into wells using ebeam
19	dismount mask with acetone and clean wafer with Nanostrip
20	deposit oxide onto frontside over gold
21	pattern frontside with AMJOXIDE mask, positive resist
22	etch oxide on frontside using plasmaquest
23	etch titanium on frontside with HF dip
24	protect frontside with thick photoresist
25	dice wafers on diesaw
26	etch nitride/oxide on backside using plasmaquest
27	etch titanium on backside with HF dip

Table 3.2. Shadow mask fabrication process overview.

step #	processing step description
1	pattern with AMJSTS mask, thick resist
2	mount onto 6" quartz handle wafer
3	etch through wafer in sts2
4	dismount and clean

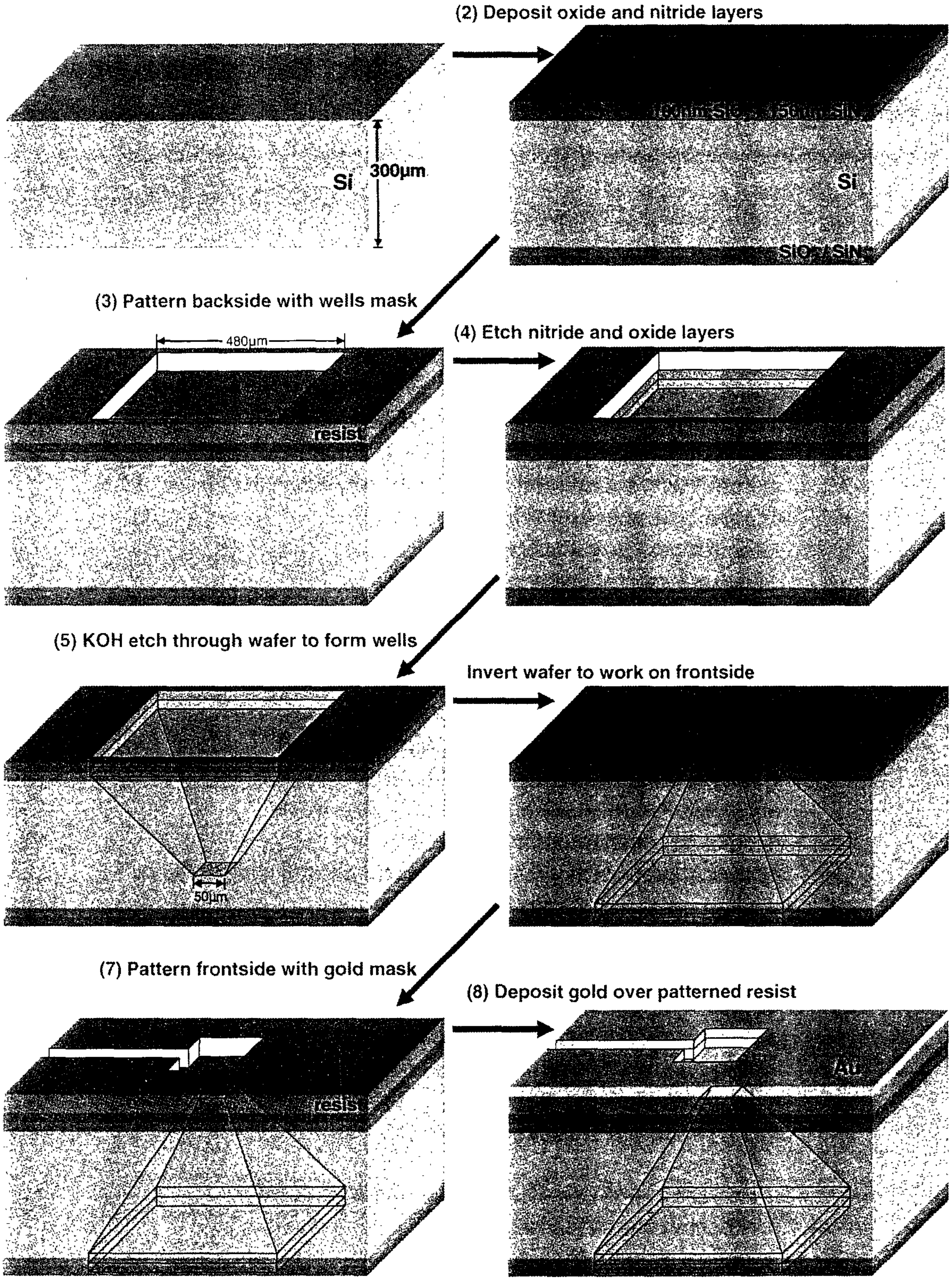

(2) Deposit oxide and nitride layers

(3) Pattern backside with wells mask

(4) Etch nitride and oxide layers

(5) KOH etch through wafer to form wells

Invert wafer to work on frontside

(7) Pattern frontside with gold mask

(8) Deposit gold over patterned resist

Figure 3.2. Illustrated process overview showing the effects of key process steps on the profile of a single reservoir (film thicknesses not to scale). Steps 1 through 8.

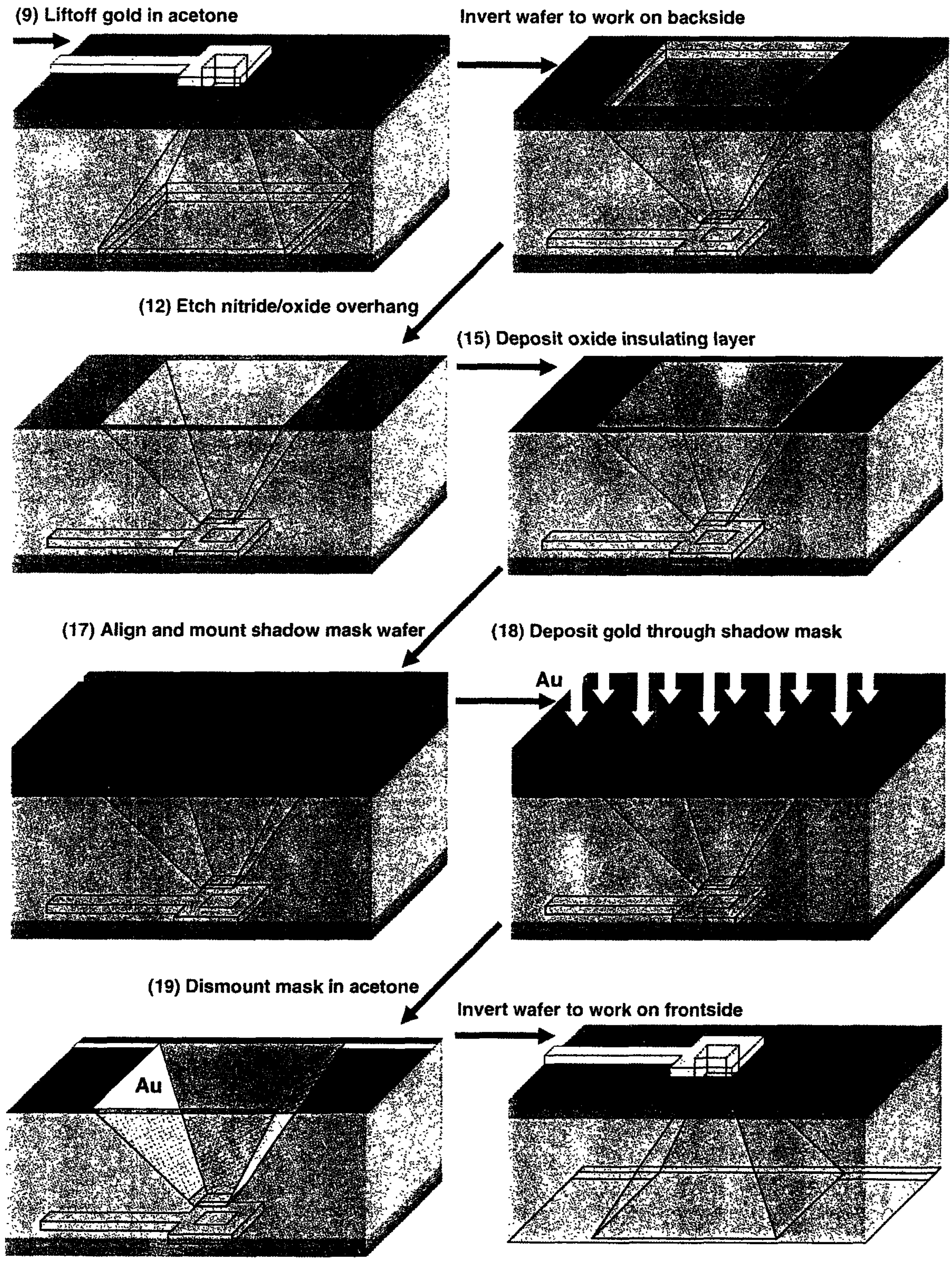

Figure 3.2. Illustrated process overview showing the effects of key process steps on the profile of a single reservoir (film thicknesses not to scale). Steps 9 through 19.

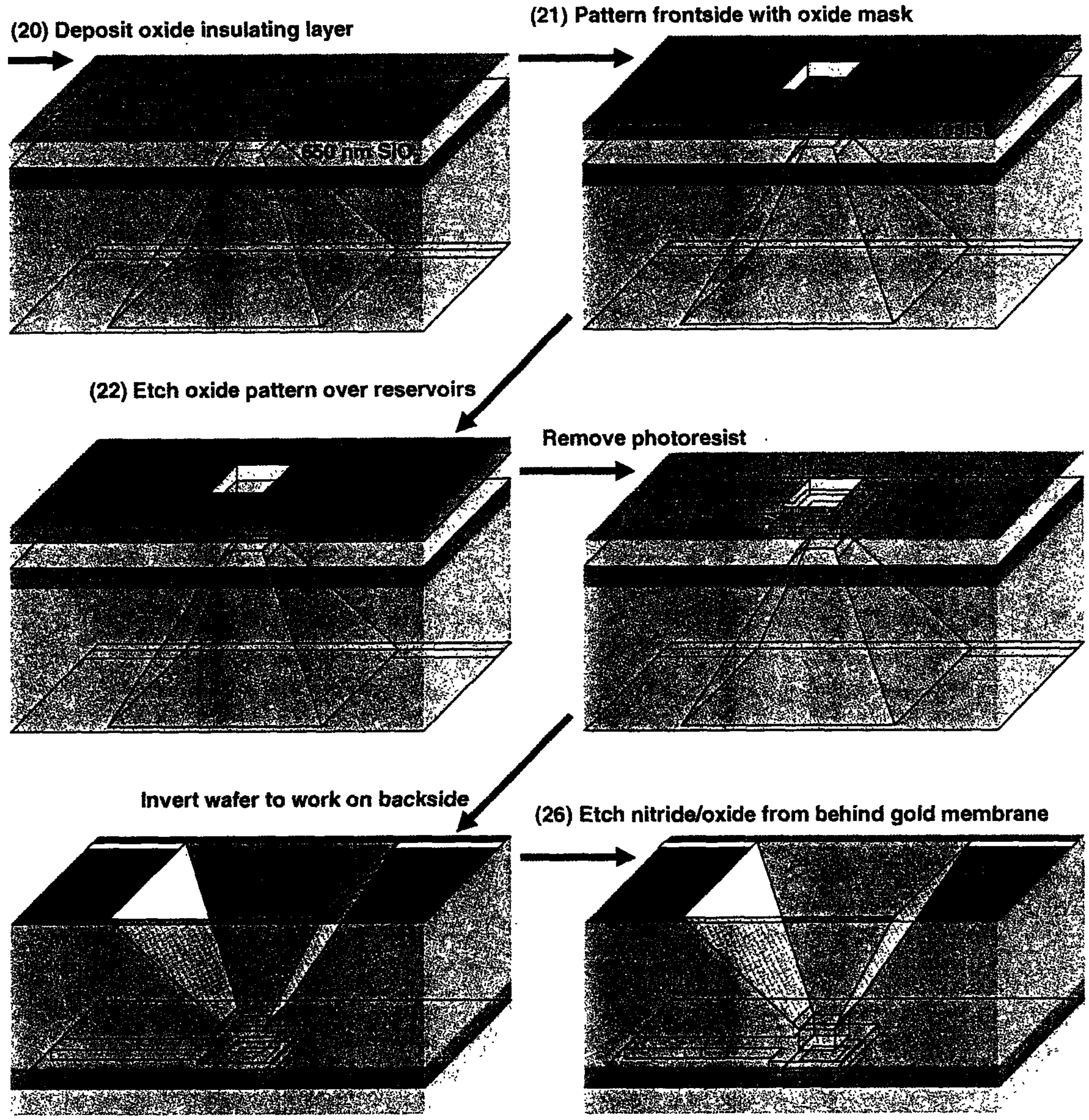

Figure 3.2. Illustrated process overview showing the effects of key process steps on the profile of a single reservoir (film thicknesses not to scale). Steps 20 through 26.

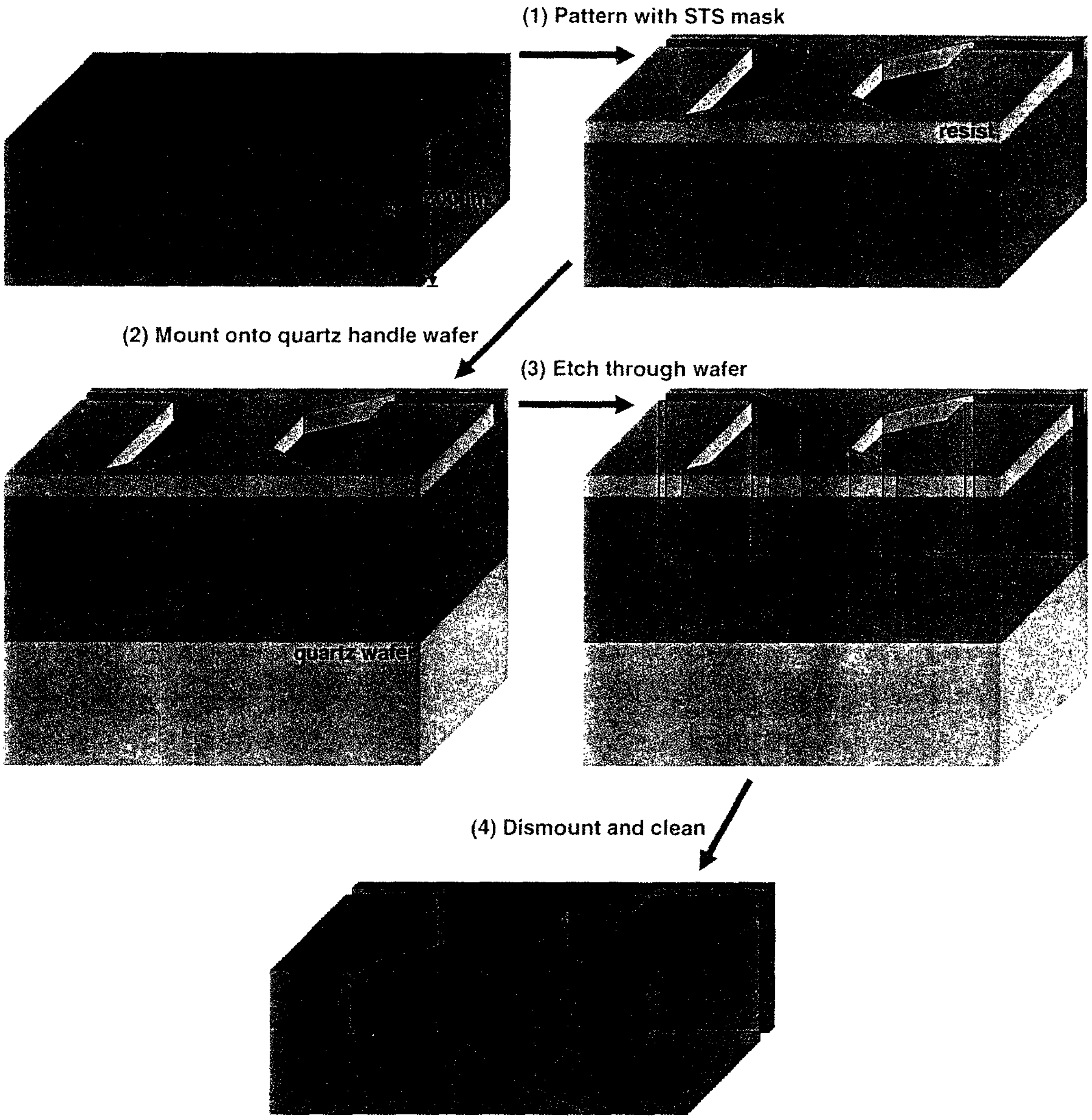

Figure 3.3. Illustrated overview of the shadow mask fabrication process showing results of key process steps on one section of the mask profile (film thicknesses not to scale).

3.1.1. Raw materials

Three types of wafers were used in the microfabrication process: test wafers, process wafers, and quartz handle wafers. Both test wafers and process wafers were 4 inch diameter, <100> silicon. Test wafers were single side polished (ssp), approximately 500 μm thick and were either p- or n- doped (purchased through MTL). As the name implies, test wafers were used to test process steps, for example, to test the adhesion or development of photoresist or the etch rate of the plasma etcher. Process wafers were double side polished (dsp), between 300 and 330 μm thick, p-type, boron doped, with resistivity of 1-10 Ω cm (WaferNet, San Jose, CA). All devices and shadow mask wafers were made from dsp process wafers. Six inch diameter quartz wafers were used as handle wafers for the sts2 DRIE etch of the shadow mask wafers.

3.1.2. Nitride/oxide deposition

Nitride is deposited onto both sides of the wafers to serve as an etch stop during KOH etching of the reservoirs. The KOH etch leaves a ~50 µm square nitride membrane covering the top of the well. In order that this membrane remain intact for gold to be deposited on it later, the membrane must have low stress. Originally, this meant that 1500 Å of 10:1 VTR (low stress) nitride was used. The VTR nitride machine motherboard short circuited in a flood in August 2001 and was not available for more than a year. As a substitute, 1000 Å of field oxide was grown on the wafer surface followed by deposition of 1500 Å of LPCVD (low pressure chemical vapor deposition) nitride in tubes A3 and A5, respectively (standard batch diffusion furnaces, Thermco 10K, La Porte, IN). The compressive stress of the oxide balanced the tensile stress of the nitride, stabilizing the membrane. MTL requires that even 'virgin' wafers undergo the standard RCA cleaning procedure before they can be processed in the diffusion furnaces. It was essential that all equipment, especially vacuum wands used to handle the wafers, be very clean for this step. Contaminants can lead to poor adhesion of the nitride layer and large vacuum wand-shaped holes in the wafer following the KOH etch.

Nitride/oxide protocol (performed by staff in ICL):

1. RCA clean
2. 1000 Å oxide deposited in tube A3
3. 1500 Å LPCVD nitride deposited in tube A5

3.1.3. Reservoir patterning

The next step is to pattern the wafer using photolithography. The photoresist covers all of the wafer except for the places that are to be KOH etched, which are the drug reservoirs (wells). Positive photoresist and a darkfield mask (AMJWELLS) are used. The mask pattern consists of an array of 16 reservoirs, 480 µm square, shown in Figure 3.4. Positive photoresist breaks down on exposure to light, so the light areas of the mask pattern were clear of photoresist after patterning. A four inch outer diameter, 3.5 inch inner diameter metal ring is placed on top of the mask to shield the edges from exposure. This creates a half inch ring of solid silicon around the wafer edge surrounding the etched parts of the wafer. Without the protection of the wafer edges, the wafers are exceedingly delicate after the KOH etch. The edges are further protected by the addition of an extra layer of photoresist to the edge of the wafer by careful manipulation of the spin coater nozzle. This repairs any damage to the photoresist at the wafer edge due to handling with tweezers. The HMDS oven treatment prevents undercutting of the resist during developing, and the baking steps drive off moisture from the photoresist.

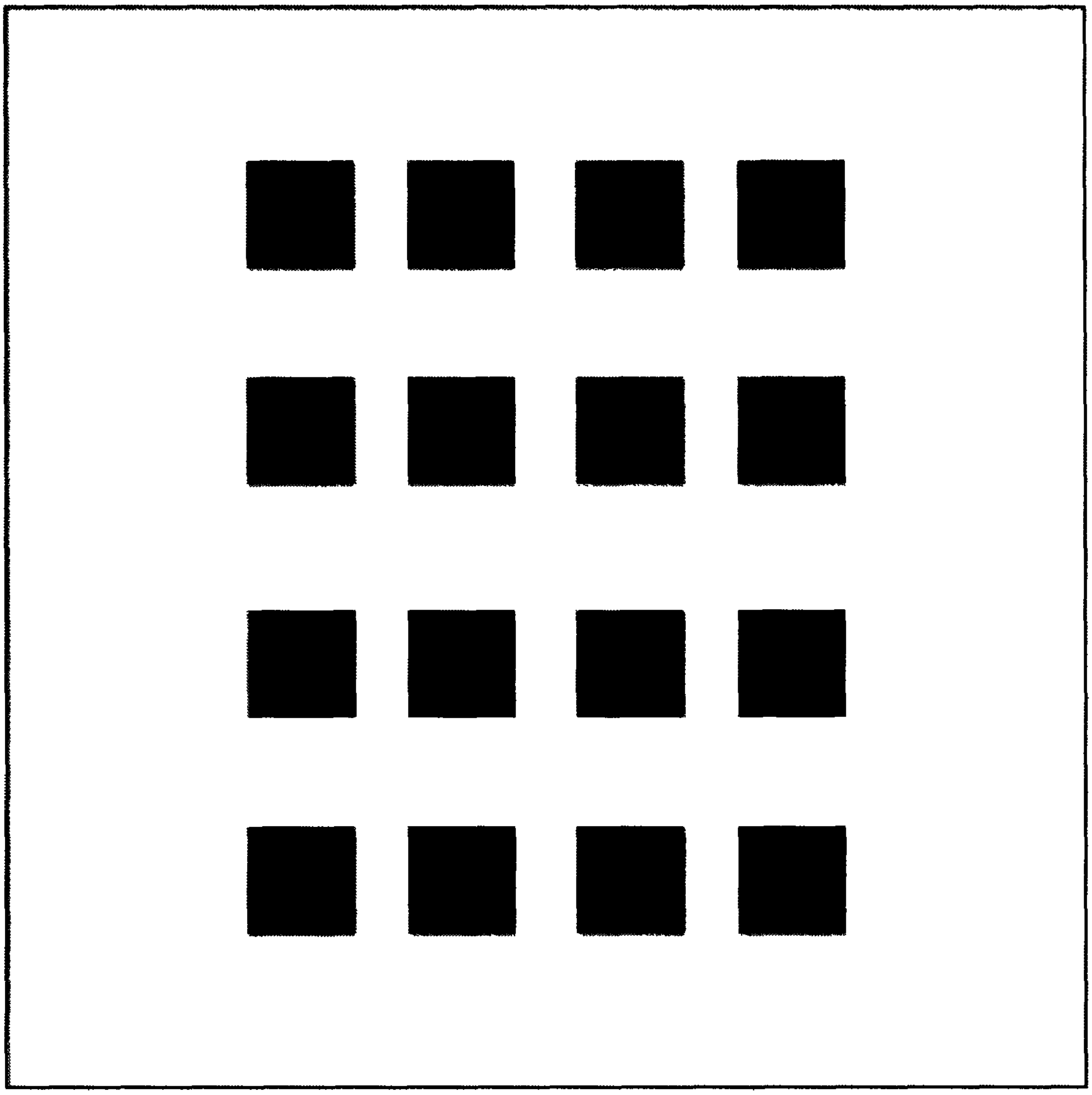

Figure 3.4. The darkfield mask AMJWELLS, for patterning an array of reservoirs across the back surface of the wafer. The light and dark regions of the mask are the reverse of that shown here, and the line around the edge is for reference and is not included in the actual mask. The pattern is 5x5 mm square and is repeated across the surface of the wafer every 5 mm.

Patterning protocol:

1. HMDS oven (approximately 20 minute cycle)
2. Coat wafers with positive resist (OCG825-20, Arch Chemicals, Norwalk, CT) using machine 'coater'
    a. 6-7 s @ 750 rpm during resist dispensing step
    b. 6-7 s @ 750 rpm spread step
    c. 30 s @ 3500 rpm spin step
3. Prebake for 30 min @ 90°C
4. Pattern using machine 'ksaligner2' and AMJWELLS mask
    a. Hard contact
    b. 32 s exposure time
    c. Use metal ring to prevent edge exposure
5. Develop in OCG934 (1:1) using machine 'Photo-wet-R'
6. Postbake for 30 min @ 120°C
7. Add ring of photoresist around edge
    a. 3 s @ 500 rpm
    b. 6 s @ 750 rpm
    c. 30 s @ 3500 rpm
8. Re-postbake @ 120°C for 15 min
9. Store wafer in light-tight box for up to 2 days

3.1.4. Nitride/oxide etch

In this step the nitride/oxide not covered by photoresist is plasma etched using the machine 'plasmaquest' (Plasmaquest Series II Reactor Model 145, MKS Instruments, Andover, MA). Note that the plasmaquest is gold contaminated (red dot), so the wafer becomes gold contaminated at this point. The standard recipes 'etchsin.rcp' and 'etchsio.rcp' are given in Tables 3.3 and 3.4, respectively. Each recipe consists of a gas stabilization step followed by an etching step. For reference, the approximate time required to etch 1500 Å nitride is 300 s, and the approximate time required to etch 1000 Å oxide is 300-350 s. Etch rates are variable and the machine is somewhat temperamental, as described in appendix 10.1.

The recipe etchsin.rcp is used first, until the nitride thickness is negligible, and then the recipe etchsio.rcp is used until the oxide thickness was negligible. Note that the nitride etching recipe will also rapidly etch oxide, but not vice-versa, since the nitride recipe actually is just the conversion of nitride to oxide by oxygen followed by removal of the oxide by CF_4. The thickness of the nitride/oxide may be measured in order to determine the etch rate using the machine 'nanospec'.

Table 3.3. Plasmaquest nitride etch recipe 'etchsin.rcp' settings.

parameter	step 1 setting	step 2 setting
gas1 O_2	2 sccm	2 sccm
gas2 He	15 sccm	15 sccm
gas10 CF_4	15 sccm	15 sccm
process pressure	20 mtorr	20 mtorr
chuck temperature	25°C	25°C
bath temperature	20°C	20°C
process time	45 s	according to thickness
ECR system	0 W	100 W
RF system	0 W	10 W

Table 3.4. Plasmaquest oxide etch recipe 'etchsio.rcp' settings.

parameter	step 1 setting	step 2 setting
gas2 He	15 sccm	15 sccm
gas10 CF_4	15 sccm	15 sccm
process pressure	20 mtorr	20 mtorr
chuck temperature	20°C	20°C
bath temperature	15°C	15°C
process time	45 s	according to thickness
ECR system	0 W	100 W
RF system	0 W	10 W

3.1.5. Potassium hydroxide (KOH) etch

Once the nitride is patterned, the wafer is etched in a KOH bath in the machine 'KOHhood' (machine is designated potassium contaminated, yellow dot) in the ICL packaging area. The recipe for the KOH bath is 1450 g KOH pellets in 5000 mL DI water (5.17 M) at 85°C. The etch is monitored under a microscope after 3 hours and then every hour until the wafers had been etched through, so that the bottom of the KOH pits is a nitride membrane. Although the etch is not entirely uniform across the entire wafer, the etch rate slows after the nitride membrane is reached, allowing the slower-etching pits to catch up. Etching is usually complete after 4-6 hours. There are several signs that an etch was complete. First, the color of the bottom of the pits changes from grey or yellowish (silicon) to purple (nitride). Second, it is possible to see through the wafer when it was held against the light. Finally, one can see a faint grid of dots on the reverse side of the wafer when it is held at an angle.

3.1.6. Post-KOH clean

Following the KOH etch the wafer must be cleaned to remove K^+ contamination before further processing in TRL. The standard cleaning procedure is performed in the machine 'acidhood'. For potassium and gold contaminated wafers, it is necessary to use red dot lab ware throughout the process, rather than the yellow dot lab ware prescribed for potassium contamination.

Cleaning protocol:

1. Rinse in running DI water 5 minutes
2. Piranha etch (3 parts H_2SO_4 added to 1 part H_2O_2) 10 minutes
3. Rinse in running DI water 5 minutes
4. Piranha etch 10 minutes
5. Rinse in running DI water 5 minutes
6. Dip in HF (1 part HF added to 50 parts water) 30 seconds
7. Rinse in running DI water 5 minutes
8. Spin rinse dry

3.1.7. Electrode patterning

In this step the frontside of the wafer is patterned with image reversal photoresist (AZ5214 E, Clariant, Somerville, NJ) using the brightfield mask AMJGOLD, shown in Figure 3.5. This pattern is for gold deposition and liftoff, to form the gold membrane caps of the wells. Image reversal resist hardens in response to light, so dark areas of the mask pattern are clear of photoresist. The photoresist covers all of the wafer except for the places where gold is to be deposited. The reason image reversal resist is used is because it works better for liftoff, which is the removal of resist with gold on top of it, leaving behind patterned gold on the wafer surface.[9] The shape of the edges of the patterned image reversal resist is better for liftoff because it forms a slight overhang over the surface of the wafer rather than sloping down to the surface. This overhang keeps the gold deposited on top of the resist separate from the gold deposited on the wafer surface. The separation between the gold layers allows the solvent to penetrate to the photoresist more easily and prevents any mechanical connection between the removed gold membrane and the wafer. Acetone dissolves the resist and the gold on top of it peels away, leaving the electrode pattern behind.

The additional step of protecting the backside (etched side) of the wafer with blue tape (available in MTL photoroom) during photoresist coating is to prevent damage to the nitride membranes due to the vacuum applied by the spin coater chuck. It also prevents seepage of photoresist through any possible holes in the wafer from imperfect nitride protection during the KOH etch. However, the blue tape does make it more difficult to get a good vacuum on the wafer for spin coating. It must be applied very carefully because the etched wafers are quite fragile, and care must be taken to avoid air bubbles which make the wafer surface uneven and prevent the formation of a good vacuum. It must be removed prior to the prebake step because it cannot withstand elevated temperatures.

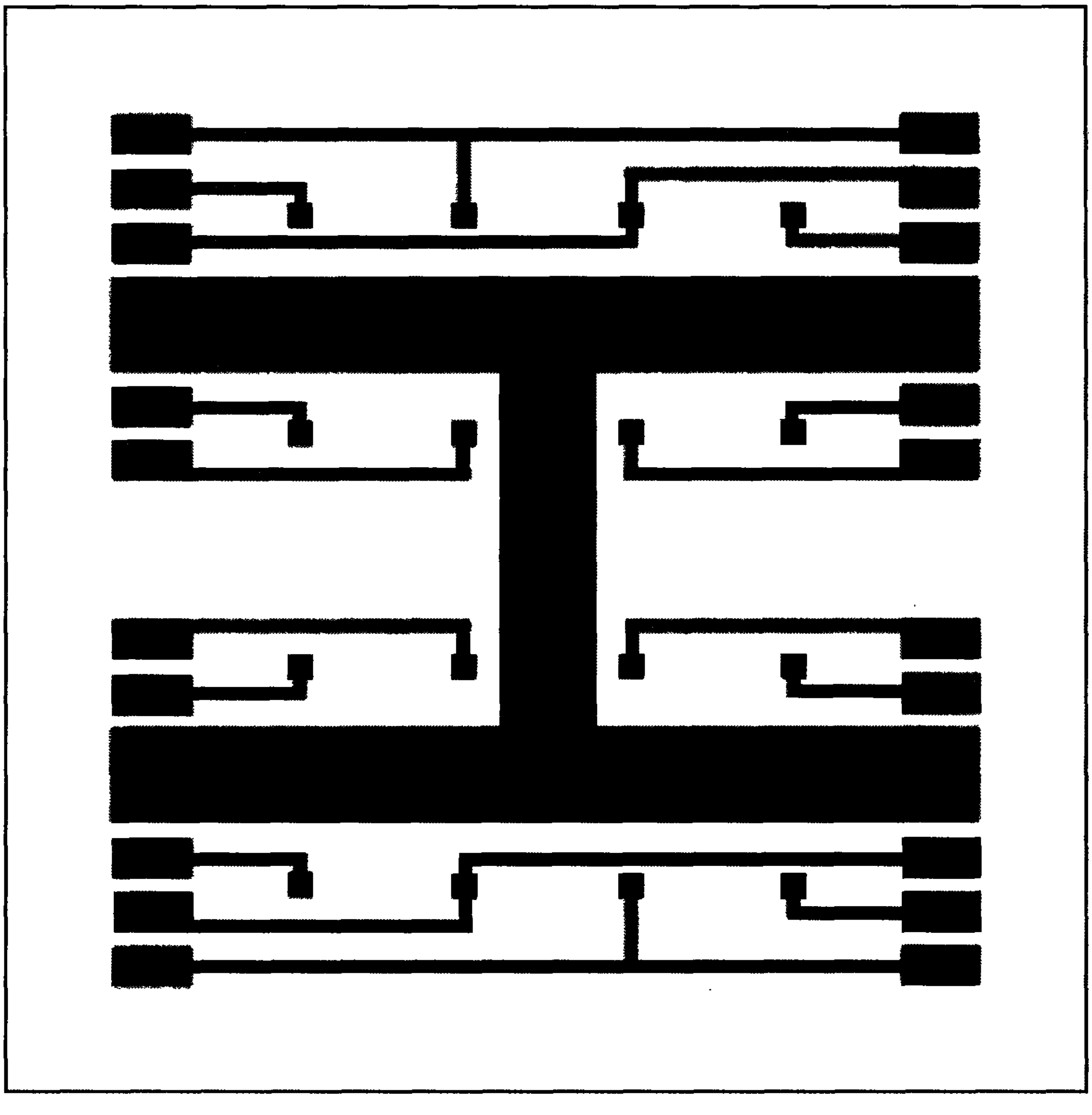

Figure 3.5. The brightfield mask AMJGOLD, for patterning the gold membrane caps and activation connections on the front surface of the wafer. The line around the edge is for reference and is not included in the actual mask. The pattern is 5x5 mm square and is repeated across the surface of the wafer every 5 mm.

Patterning protocol:

1. HMDS oven
2. Protect backside with blue tape, trim excess (opt)
3. Coat with image reversal resist (AZ5214E)
    a. 5 s @ 500 rpm during resist dispensing step
    b. 6 s @ 750 rpm spread step
    c. 30 s @ 4000 rpm spin step
4. Remove blue tape
5. Prebake for 30 min @ 90°C
6. Pattern using machine 'ksaligner2' and AMJGOLD mask
    a. Soft contact
    b. 40 s exposure time
    c. Do not use metal ring around edge
7. Hot plate bake @ 120°C for 90 s (timing critical)
8. Flood expose for 300 s
9. Develop in AZ422 using machine 'photo-wet-R'
10. Spin rinse dry
11. Store wafer in box for up to one day – if stored, bake briefly at 120°C just before deposition

3.1.8. Gold deposition

Gold is deposited onto the wafer using the machine 'e-beam-Au' (Model VES 2550, Temescal Semiconductor Products, Fairfield, CA). An electron beam evaporates the metal from a crucible under high vacuum. The chamber is pumped down to about 10^{-7} torr and then a layer of titanium is deposited, followed by a layer of gold, then another layer of titanium. The first titanium layer improves the adhesion of the gold to the wafer, while the second titanium layer improves the adhesion of the oxide insulating layer (deposited in step 20) over the gold. Previous devices used chromium as an adhesion layer, however, MicroCHIPS researcher John Maloney found that titanium is better for verifying the complete removal of the nitride layer underneath the gold/titanium membrane as described in step 26. The titanium layer is thicker than required for adhesion in order to provide a noticeable color change when the titanium is removed, as well as to carry current underneath corroded gold in the occasional case where the oxide insulation layer over the traces is imperfect. The stationary liftoff stage of the ebeam is used rather than the rotating planetary stage, which makes the deposition approximately unidirectional and preserves the gap between the gold layer on top of the photoresist and the gold on the wafer surface. For the electrode patterning and liftoff, any of the central wafer slots on the liftoff stage may be used. The titanium and gold deposition recipes are given in Tables 3.5 and 3.6, respectively.

Deposition specifications:

1. 500 Å titanium at 2 Å/s
2. 3000 Å gold at 1 Å/s
3. 500 Å titanium at 2 Å/s

Table 3.5. Ebeam titanium deposition recipe.

parameter	name	value
11	rise time	1.00 (min.sec)
12	soak time	2.00 min
13	predeposit time	0.50 (min.sec)
14	set point	0
15	soak power	17 %
16	predeposit power	16 %
17	maximum power	18 %
18	idle power	0 %
21	rate	2 Å/s
22	set point	0
23	thickness	0.5 kÅ
24	source/sensor	11
25	response	15
26	error limit	10 %
27	tooling	61.5 %
28	density	4.5
29	acoustic impedance	14.0
32	feed power	0
33	feed time	2 min
34	interlock input	24

Table 3.6. Ebeam gold deposition recipe.

parameter	name	value
11	rise time	2.00 min
12	soak time	2.30 (min.sec)
13	predeposit time	1.30 (min.sec)
14	set point	0
15	soak power	17 %
16	predeposit power	18 %
17	maximum power	20 %
18	idle power	0 %
21	rate	5 Å/s
22	set point	0
23	thickness	3.0 kÅ
24	source/sensor	11
25	response	15
26	error limit	10 %
27	tooling	55 %
28	density	19.3
29	acoustic impedance	23.18
32	feed power	0
33	feed time	20 min
34	interlock input	24
35	discrete	1

3.1.9. Gold liftoff

The wafer is then soaked in acetone in the hood 'photo-wet-Au' to lift off the gold that was deposited on top of photoresist, leaving the gold pattern behind. This step usually takes from 15 minutes to 1 hour. Mild agitation may be used to assist in peeling of the undesired gold, as well as squirting problem areas directly with acetone. The wafer is then rinsed with acetone, methanol, and isopropyl alcohol, and blow dried gently with an air gun. The air gun should be held at least one foot distant or the wafer may shatter from the applied stress.

3.1.10. Nanostrip clean

The wafer is cleaned using Nanostrip, which contains sulfuric acid and hydrogen peroxide, essentially a cold piranha etch (Cyantek Corp., Fremont, CA). This step is optional but helps to remove any residual gold particles that may cling to the wafer.

Cleaning protocol:

1. Rinse in running DI water 2 minutes

2. Nanostrip etch 10 minutes
3. Rinse in running DI water 5 minutes
4. Spin rinse dry

3.1.11. Photoresist protection

The gold electrodes are then covered with a layer of thick photoresist in order to protect them from scratches or other damage during the processing of the backside of the wafer. The HMDS oven step may be omitted because the resist will not be patterned, so adhesion of the photoresist is not as critical.

Protection protocol:

1. Apply blue tape to reservoir side of wafer, trim excess
2. Coat frontside with thick resist (AZP4620)
    a. 11 s @ 1.75 krpm
    b. 60 s @ 1.25 krpm
    c. 10 s @ 5.00 krpm, swab edge
3. Remove blue tape
4. Bake @ 90°C for 1 hour

3.1.12. Plasmaquest etch of nitride overhang

Due to slow undercutting of the nitride during the KOH etch, there is a small nitride/oxide overhang around the edges of the reservoirs. This is removed using the recipes 'etchsin.rcp' and 'etchsio.rcp' given in Tables 3.3 and 3.4 above. Removal is again monitored using the nanospec. If the overhang were not removed, there would be a gap between the gold deposited within the reservoirs and the gold traces and bond pads on the wafer surface.

3.1.13. Nanostrip clean

Following etching of the nitride/oxide overhang, the wafer is cleaned using Nanostrip. This is to remove any possible nitride or oxide fragments that might be created as the overhang is removed. It is first rinsed in acetone to remove the photoresist protective layer on the reverse side, which would contaminate the Nanostrip etch.

Cleaning protocol:

1. Acetone rinse to remove most photoresist
2. Rinse in running DI water 2 minutes
3. Nanostrip etch 10 minutes
4. Rinse in running DI water 5 minutes
5. Spin rinse dry

3.1.14. Photoresist protection

The gold electrodes are once again covered with a layer of thick photoresist in order to protect them from scratches or other damage during the processing of the backside of the wafer. The procedure is identical to the previous photoresist protection step described in section 3.1.11.

3.1.15. Oxide deposition

The backside of the wafer is then covered with a layer of oxide that will insulate the impedance electrodes from the silicon. The oxide is deposited using the plasmaquest with the recipe 'siodep.rcp', given in Table 3.7. The RF power is set to zero in order to get a non-directional, lower stress, conformal film of oxide. The thickness of the deposited oxide is about 1000 Å as measured with the nanospec and the rate of deposition is typically about 5 Å /s. It may be desirable to increase the thickness of this insulating oxide layer for future devices in light of the significant leakage current through the silicon substrate during impedance measurements. Also, the relatively poor adhesion of the impedance electrodes during wire bonding as described in section 3.3.2 may be due to poor adhesion of this oxide layer to the silicon. An alternative method of oxide film deposition or growth has the potential to greatly improve the device. However, any alternative must take into account the gold contamination of the wafers at this step and the need to avoid temperatures above approximately 300°C to avoid defect formation in the gold electrodes on the wafer frontside. Defects arise at higher temperatures because the diffusivity of gold atoms increases with temperature. Diffusion away from high energy grain boundaries in the thin film causes grooving at grain boundaries.[10] Yawen Li found that grain boundary grooving leads to defects in the gold films within an hour at 350°C, and within 4 hours at 300°C.

Table 3.7. Plasmaquest oxide deposition recipe 'siodep.rcp' settings.

parameter	step 1 setting	step 2 setting
gas1 O_2	12 sccm	12 sccm
gas6 SiH_4	80 sccm	80 sccm
process pressure	50 mtorr	50 mtorr
chuck temperature	80°C	80°C
bath temperature	80°C	80°C
process time	45 s	according to thickness
ECR system	0 W	200 W
RF system	0 W	0 W

3.1.16. Ash clean

The wafer is cleaned by a 5 minute ash as close to the time of mounting as possible, using the machine 'asher'. Ashing removes any organics from the surface of the wafer, improving the adhesion of the gold impedance electrode layer. The thick resist protecting the frontside electrodes is not significantly etched during such a short ash step.

3.1.17. Mask mounting

The shadow mask wafer is aligned and mounted onto the wafer using the machine 'ksaligner2' (Karl Suss MA4 Aligner, Suss MicroTec Inc., Waterbury Center, VT). Fabrication of the shadow mask wafer is described in section 3.1.28 below. The mask wafer takes the place of a photolithography mask and is aligned over the wafer with the aid of a special chuck belonging to the Jensen laboratory. The device wafer is dotted with a small amount of thick photoresist at the edges, and brought into contact with the mask wafer. The amount of photoresist should be minimal or the mask wafer may float out of position. After the wafers are contacted, they are baked horizontally at 90°C for 10 minutes to cure the photoresist. The wafers are then examined under the microscope to check for slippage or misalignment. If wafers are misaligned, they must be soaked briefly in acetone to separate them, then rinsed with acetone, methanol, and isopropyl alcohol and blow dried. The acetone also removes the protective photoresist over the frontside electrodes, which does not need to be reapplied. However, the ash cleaning step should be repeated before the mask mounting procedure is attempted again.

3.1.18. Masked gold deposition

Gold is deposited into the reservoirs by electron beam evaporation as in step 3.1.8. A titanium adhesion layer is deposited first to improve the adhesion of gold to the wafer, followed by a layer of gold. For this step it is desired to have the evaporated metal beam perpendicular to the face of the wafer to avoid skewing the shadow pattern. Figure 3.6 shows an example of a skewed shadow pattern, in which the electrodes within the reservoirs have been distorted, and the vertical portions of the traces on the face of the chip are thinned or broken due to shadowing. To get the correct angle, the wafer is placed on the liftoff stage in the wafer slot directly above the crucible. The correct positioning and pattern can be verified under the microscope for the traces, and by SEM for the electrodes in the reservoirs (see Figure 3.11 in the conclusions section at end).

Deposition specifications:

1. 100Å titanium at 2Å/sec
2. 3000Å gold at 1Å/sec

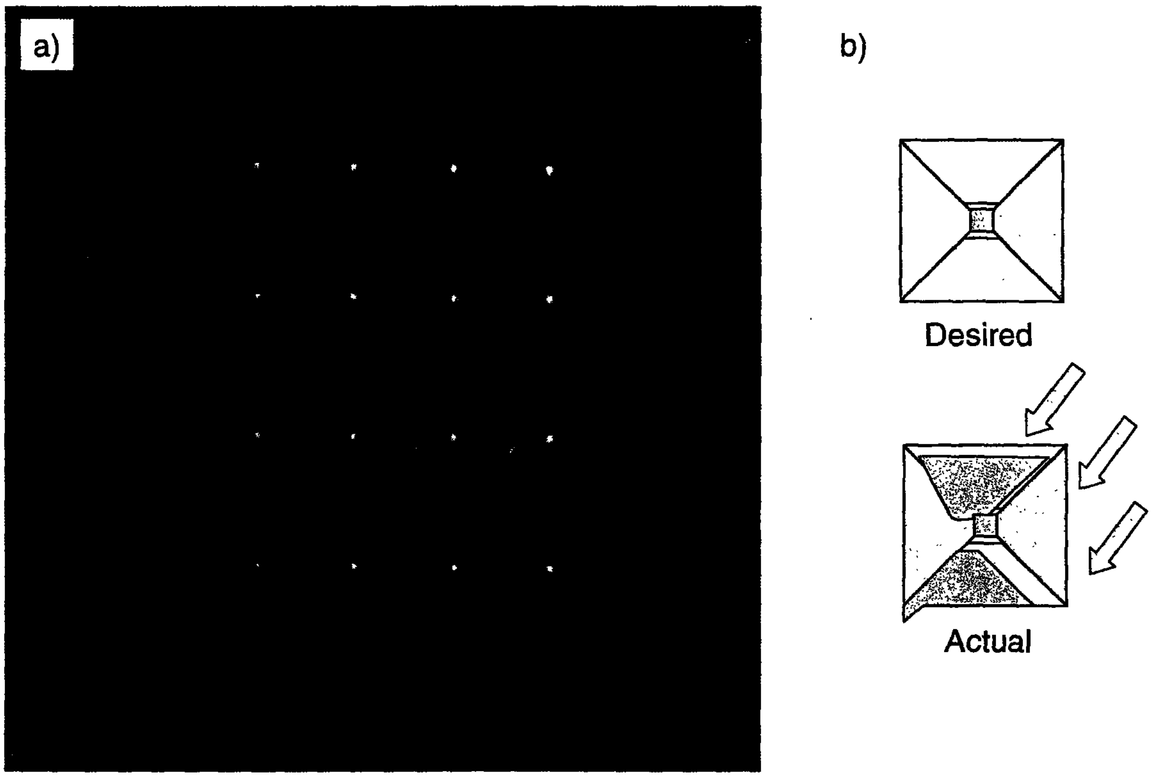

Figure 3.6. Example of a shadow pattern skewed due to the off-perpendicular orientation of the metal beam during deposition, **a)** picture taken under light microscope showing thinned and incomplete traces, area approximately 5x5 mm, **b)** schematic illustrating desired and actual shape of impedance electrodes within the reservoirs, which is obscured in the picture in part (a) by reflections from the reservoir sides.

3.1.19. Mask dismounting

The mask wafer is then removed by soaking the wafers in acetone overnight. The wafers may come apart much sooner due to the minimal amount of photoresist used in the mounting procedure. However, agitation of the wafers to speed to process should be avoided due to the fragility of both the mask and the device wafer. Once the wafers have come apart, they are cleaned by a 10 minute Nanostrip etch. The Nanostrip etch removes any contaminants from the acetone soak and ensures that the wafer surface is clean for good adhesion of the oxide layer deposited in the following step.

Dismounting protocol:

1. Soak in acetone overnight

2. Rinse in running DI water 2 minutes
3. Nanostrip etch 10 minutes
4. Rinse in running DI water 5 minutes
5. Spin rinse dry

3.1.20. Oxide deposition

A thick layer of oxide is deposited over the gold electrodes on the frontside of the wafer to insulate the traces during activation of the devices in saline or body fluid. Without a good insulation layer, the traces would corrode upon application of voltage and break the connection between the source and the caps over the reservoirs. The oxide layer must be sufficiently thick that it covers the sides of the deposited gold pattern, which is 3000 Å thick. The oxide layer is deposited using the plasmaquest recipe 'siodep.rcp' given in Table 3.7 in section 3.1.15. The machine nanospec cannot be used to determine the thickness of the oxide because there is no setting for measuring oxide on nitride on oxide. However, the deposition rate can be measured by depositing oxide on a plain test wafer and the measured rate can be used to determine the desired deposition time. The thickness of the oxide insulation layer is approximately 6500 Å.

The titanium adhesion layer deposited over the gold significantly improves adhesion of the oxide insulating layer to the gold electrodes. An alternative to oxide deposition in plasmaquest is deposition of oxide at 300°C in plasmatherm, in EML, as developed by Yawen Li. This may improve the density and uniformity of the oxide. However, the EML facility is not as clean as TRL, and wafers may not return from EML to the cleaner facilities. The subsequent patterning and etch steps must then also be performed in EML on inferior equipment, and a significant percentage of the devices on a wafer may be lost.

3.1.21. Oxide patterning

The oxide insulating layer is then patterned with positive photoresist using the darkfield mask AMJOXIDE, shown in Figure 3.7. The only parts of the device left exposed are the reservoir caps, the counter electrode, and the bond pads. For this patterning step, the protection of the backside of the wafer with blue tape is optional. The reservoir cap membranes are sufficiently strengthened by the oxide layer over them that they can usually withstand the vacuum applied by the coater chuck. Although some may break and the backside of the wafer gets slightly dirty, the application of blue tape carries the risk of breaking the wafer either during application or removal. In general, the blue tape protection step was usually skipped for this patterning step.

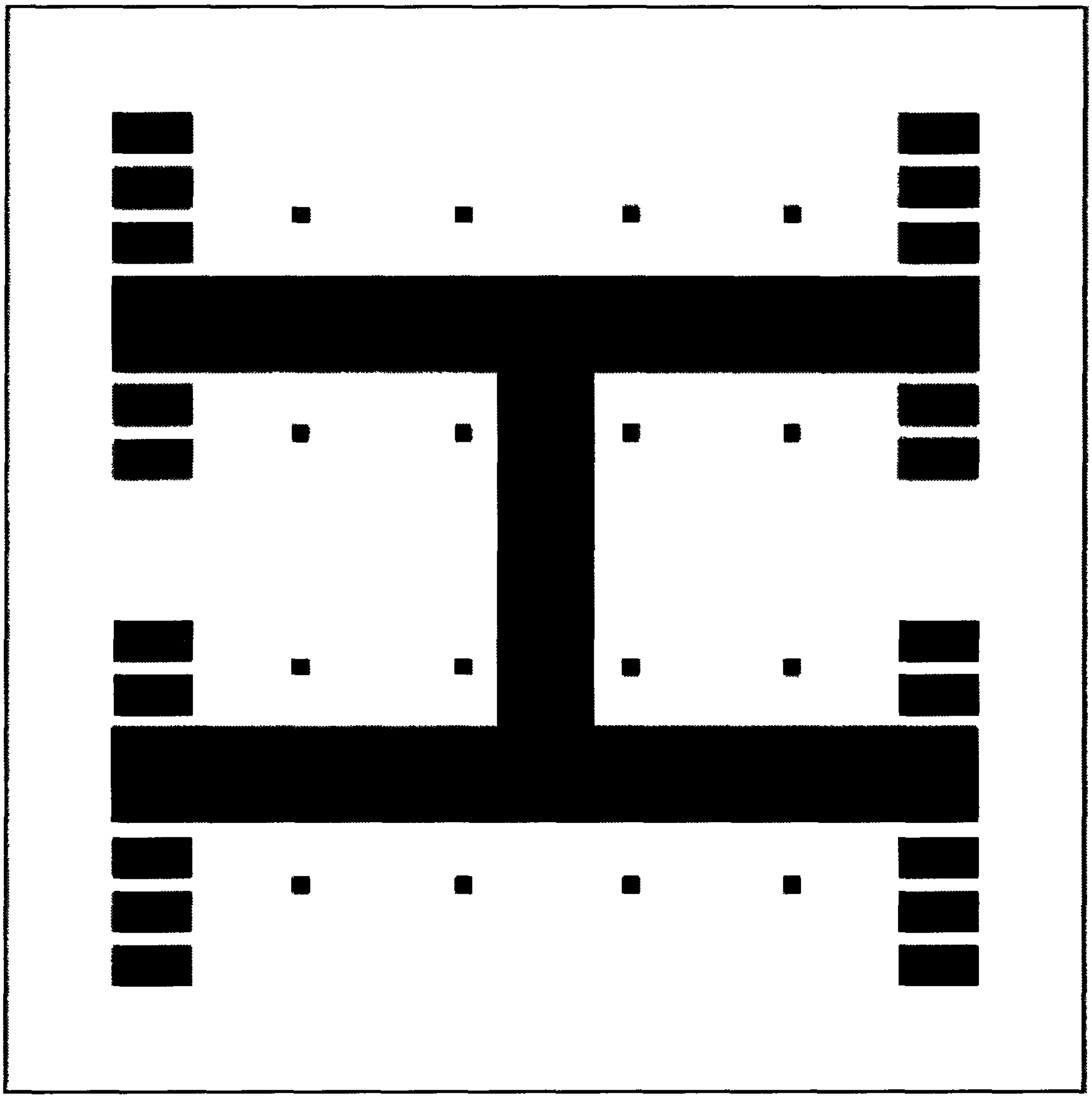

Figure 3.7. The darkfield mask AMJOXIDE, for patterning the oxide insulation layer over the gold activation electrodes on the front surface of the wafer. The light and dark regions of the mask are the reverse of that shown here. The line around the edge is included in the actual mask to serve as a guide for dicing the wafer. The pattern is 5x5 mm square and is repeated across the surface of the wafer every 5 mm.

Patterning protocol:

1. HMDS oven
2. Coat wafers with positive resist (OCG825-20, Arch Chemicals, Norwalk, CT) using machine 'coater'

   a. 6-7 s @ 750 rpm during resist dispensing step
   b. 6-7 s @ 750 rpm spread step
   c. 30 s @ 3500 rpm spin step
3. Prebake for 30 min @ 90°C
4. Pattern using machine 'ksaligner2' and AMJOXIDE mask
   a. Soft contact
   b. 32 s exposure time
5. Develop in OCG934 (1:1) using machine 'Photo-wet-R'
6. Postbake for 30 min @ 120°C

3.1.22. Oxide etch

The oxide pattern is then etched using the recipe 'etchsio.rcp' on plasmaquest, given in Table 3.4 in section 3.1.4. The etch rate is determined using the same test wafer that was used to determine the deposition rate for the oxide deposition in step 20. The device wafers are etched for slightly longer than the calculated time to ensure complete removal of the oxide over the reservoirs and bond pads. It is difficult to see the progress of the etch because oxide is transparent.

3.1.23. Titanium etch

The complete removal of oxide from the reservoir membranes and bond pads can be verified by etching the titanium adhesion layer that sits on top of the gold with a quick HF dip in acidhood2. If the oxide is not entirely removed, the titanium will be protected from the etchant. However, if the oxide etch is complete, the titanium will be rapidly removed and the color of the exposed metal will change from a faded yellow to a bright yellow. The color difference is readily apparent between the protected metal traces and the exposed metal bond pads. The HF etch also etches oxide, so it is essential that the wafer be dipped and rinsed quickly. In addition, the photoresist should be removed prior to the HF dip by rinsing the wafer in acetone in photo-wet-Au and spin rinsing to remove residual solvent.

Etching protocol:

1. Dip wafer in acetone to remove photoresist
2. Spin rinse dry
3. Dip wafer in 50:1 (water : 50% HF) for approximately 30 seconds
4. Rinse with DI water

5. Check for color change
6. Spin rinse dry

3.1.24. Photoresist protection

The gold membranes over the reservoirs must be protected prior to dicing the wafer. A layer of thick photoresist is used to protect them, as in steps 11 and 14 above.

Protection protocol:

1. Apply blue tape to reservoir side of wafer, trim excess
2. Coat frontside with thick resist (AZP4620)
    a. 11 s @ 1.75 krpm
    b. 60 s @ 1.25 krpm
    c. 10 s @ 5.00 krpm, swab edge
3. Remove blue tape
4. Bake @ 90°C for 1 hour

3.1.25. Wafer dicing

The wafer is diced into individual 5 x 5 mm devices on the machine 'diesaw', an automatic dicing saw (DAD-2H/6T dicing saw, Disco Hi-Tec America, Inc., Santa Clara, CA). Diesaw tape (#1064, Z index 0.25) is applied to the backside of the wafer taking care to avoid any bubbles which could interfere with the vacuum applied by the chuck. The 2060 (thick) silicon blade is used because the streets between devices are quite wide and the devices fit better in the metal frames used for packaging if they are slightly smaller. A slow cut speed (3) is used to avoid damaging the edges of the devices. The tape thickness is entered as 0.35 rather than the actual thickness of 0.25 to keep from cutting entirely through the wafer, because the cooling water jet of the diesaw has a tendency to knock devices loose after they have been cut. The thin silicon connecting the devices is broken by applying the slightest pressure to the wafer while it is still stuck to the tape. Individual devices are then peeled from the backing tape as needed. They are then cleaned of the photoresist protection layer by rinsing in acetone, methanol, and isopropyl alcohol and gently blow dried.

3.1.26. Nitride/oxide etch in reservoirs

The nitride/oxide layer underneath the gold membranes must be etched away or the membranes will not break when corroded. The individual devices are etched in plasmaquest using the modified 'etchsin.rcp' recipe in Table 3.8. The RF power is increased because the nitride to be etched is deep within the reservoirs. Devices are placed on top of a clean p-type test wafer in groups of 5 in the center of the wafer. A p-type wafer is used because n-type wafers are more likely to tip when they are transferred from the etching chuck to the load arm, due to the positions of the lifting pegs within the chamber. The etch rate within the reservoirs cannot be measured directly and is not necessarily the same as an etch rate measured at the wafer surface. The ideal etch time was determined by etching chips for 700, 800, 1100, and 1400 s, then corroding the chips in saline to see which ones open. The 1400 s etch time weakened the membranes so that some broke without being corroded. None of the 800-1100 s device membranes broke, and all opened when corroded, while some of the 700 s etched device membranes did not open. An etch time of 850 s was selected as optimal. It was observed that devices from a wafer that had not been subjected to this etching step had better gold adhesion to the wafer surface during wire bonding, as compared to devices that had been etched. It is possible that this etching step weakens the oxide layer between the gold impedance electrodes and the silicon, making wire bonding difficult. It would be very useful to change the process to improve the adhesion of the gold electrodes to the wafer surface, by modifying this etch step to avoid damaging the oxide under the gold, improving the adhesion of the oxide insulating layer deposited in step 15, or improving the adhesion of the gold on top of the oxide layer.

Table 3.8. Plasmaquest nitride etch recipe 'etchsin.rcp' settings for etching in bottom of reservoirs.

parameter	step 1 setting	step 2 setting
gas1 O_2	2 sccm	2 sccm
gas2 He	15 sccm	15 sccm
gas10 CF_4	15 sccm	15 sccm
process pressure	20 mtorr	20 mtorr
chuck temperature	25°C	25°C
bath temperature	20°C	20°C
process time	45 s	850 s
ECR system	0 W	100 W
RF system	0 W	20 W

3.1.27. Titanium etch

The final step is to etch the titanium from underneath the gold membranes with a quick HF dip, which is performed in the Langer laboratory rather than the clean room. The devices are submersed in 50:1 water:50% HF for approximately 30 s, then rinsed with DI water and gently blow dried. As in step 23, a color change is apparent under the microscope after removal of the titanium, from faded yellow to bright gold. If the nitride layer beneath the gold membranes was insufficiently etched in step 26, the etchant will not penetrate the remaining nitride to etch the titanium, and the color will not change. In the absence of a color change, the devices must be cleaned in acetone, methanol, and isopropyl alcohol before being returned to the clean room for additional etching in plasmaquest. Once the titanium layer has been etched, the devices are ready for packaging and testing.

3.1.28. Shadow mask fabrication

The shadow mask for patterning the gold impedance electrodes is fabricated separately in four steps: patterning, mounting, etching, and dismounting. The process is short but somewhat difficult because of the depth of the etch; the details of patterning and mounting are critical for a successful etch through the entire wafer thickness. The wafers for this step must be kept separate from the gold contaminated wafers for the device process because the DRIE etcher is not gold contaminated (green dot).

Patterning of reservoir electrodes.—Shadow mask wafers are fabricated from the dsp process wafers described in section 3.1.1. The first step is to pattern the wafer with thick resist (AZP4620, Clariant, Somerville, NJ) using the darkfield mask AMJSTS shown in Figure 3.8. The thick resist will be etched slowly during the DRIE etch so it is critical to make the resist sufficiently thick with good adhesion and uniformity. A ring around the edge of the mask protects the wafer edge and makes the etched wafer less fragile. An additional layer of photoresist around the wafer edge helps prevent over-etching of the resist at the edges of the wafer during the etch step. The thick resist must be baked for an extended period of time to remove excess moisture. Both the prebake and the postbake steps are at 90°C (the 'prebake' oven) because the thick resist cannot tolerate the higher temperature of the 'postbake' oven. The wafers are baked horizontally in a wafer carrier turned on end because the resist is thick enough to flow significantly before hardening.

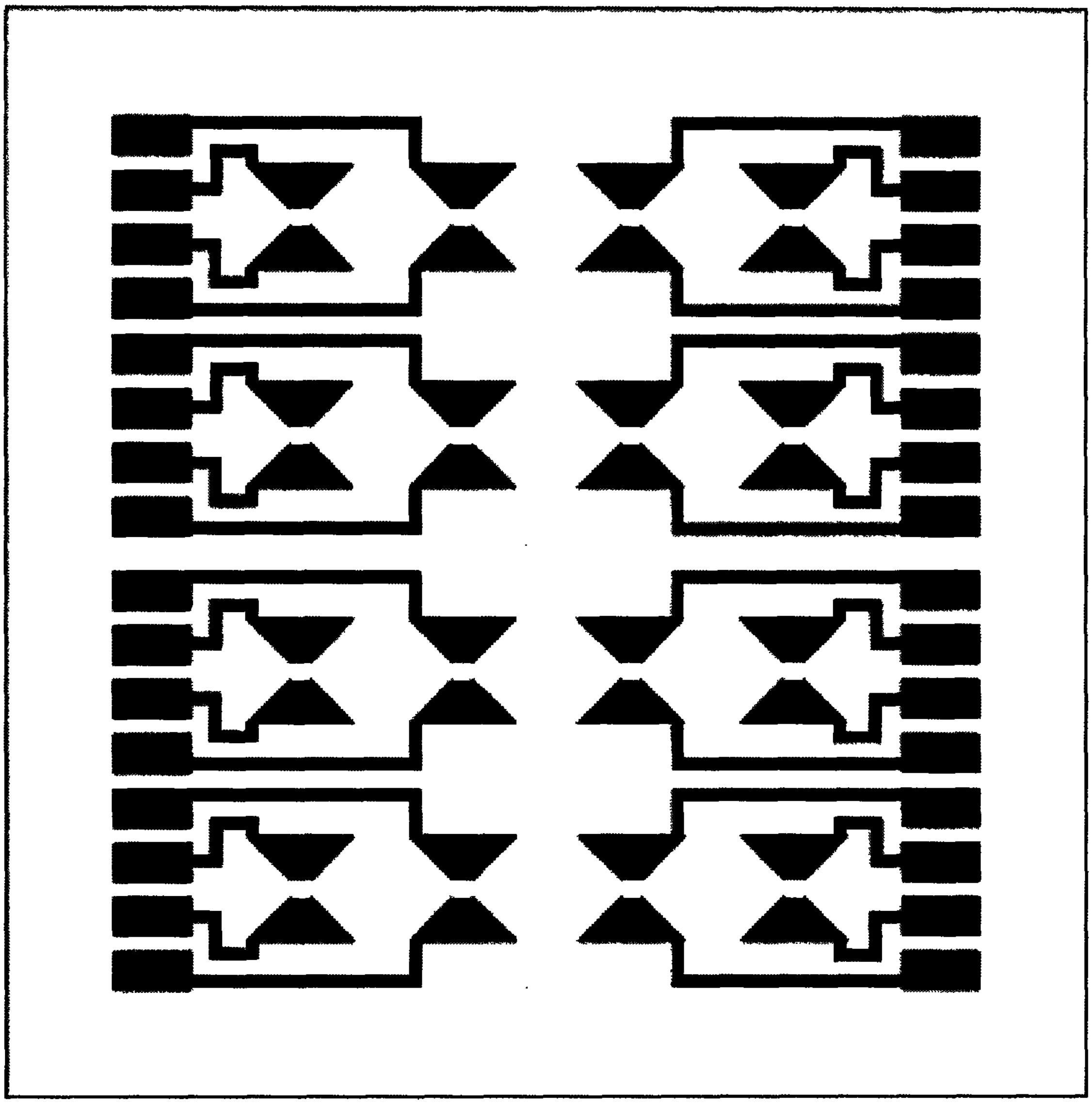

Figure 3.8. The darkfield mask AMJSTS, for patterning the impedance electrodes onto the shadow mask wafer. The light and dark regions of the mask are the reverse of that shown here, and the line around the edge is for reference and is not included in the actual mask. The pattern is 5x5 mm square and is repeated across the surface of the wafer every 5 mm.

Patterning protocol:

1. HMDS oven
2. Coat wafers with thick resist (AZP4620)
   a. 11 s @ 1.75 krpm during resist dispensing step; move nozzle to edge once
   b. 60 s @ 1.0 krpm spread step
   c. 10 s @ 5.0 krpm spin step, swab edge to remove excess
3. Prebake horizontally for 60 min @ 90°C

4. Pattern using machine 'ksaligner2' and AMJSTS mask
    a. Hard contact
    b. 650 s exposure time
    c. Use metal ring to prevent edge exposure
5. Develop in AZ440 until clear (3-4 min) using machine 'Photo-wet-R'
6. Postbake for 30 min @ 90°C
7. Add ring of photoresist around edge
    a. 5 s @ 1.75 krpm
    b. 30 s @ 1.0 krpm
    c. 10 s @ 5.0 krpm, swab edge to remove excess
8. Re-postbake @ 90°C for 15 min

Wafer Mounting.—The wafer must be mounted onto a 6 inch quartz handle wafer prior to the DRIE etch. The etcher is designed to handle 6 inch wafers, so all 4 inch wafers must be mounted onto a larger wafer. In addition, all wafers that will be through-etched (etched through the entire thickness of the wafer) must be mounted on top of another wafer to keep from etching through to the chuck. A layer of thick photoresist is applied to the quartz wafer using the coater and patterned into a modified bull's-eye pattern with acetone, as shown in Figure 3.9a. The mask wafer is pressed into place in the center of the pattern and the two wafers are baked together horizontally. The bull's eye pattern allows trapped air to escape in the etch chamber when vacuum is applied, while maintaining good contact between the two wafers. The etching chuck is cooled during the etch, and the photoresist pattern may burn without good heat transfer from the mask wafer through the photoresist to the quartz wafer on the chuck.

The photoresist flows during the baking step as depicted in Figure 3.9b and the pattern must be checked to ensure that there is good contact between the two wafers without blocking the air vents. A blocked air vent can cause the mask wafer to pop off the handle wafer when vacuum is applied. A poor mount must be soaked in acetone to dismount the quartz wafer, cleaned with acetone, methanol, and isopropyl alcohol, blow dried, and the mask wafer repatterned and remounted. The spin speed during the bull's eye patterning step and the width of the patterned rings may be adjusted to optimize the mount. Finally, the back of the quartz wafer is carefully scraped clean of stray photoresist with a clean razorblade, to help make better thermal contact between the etching chamber chuck and the quartz wafer.

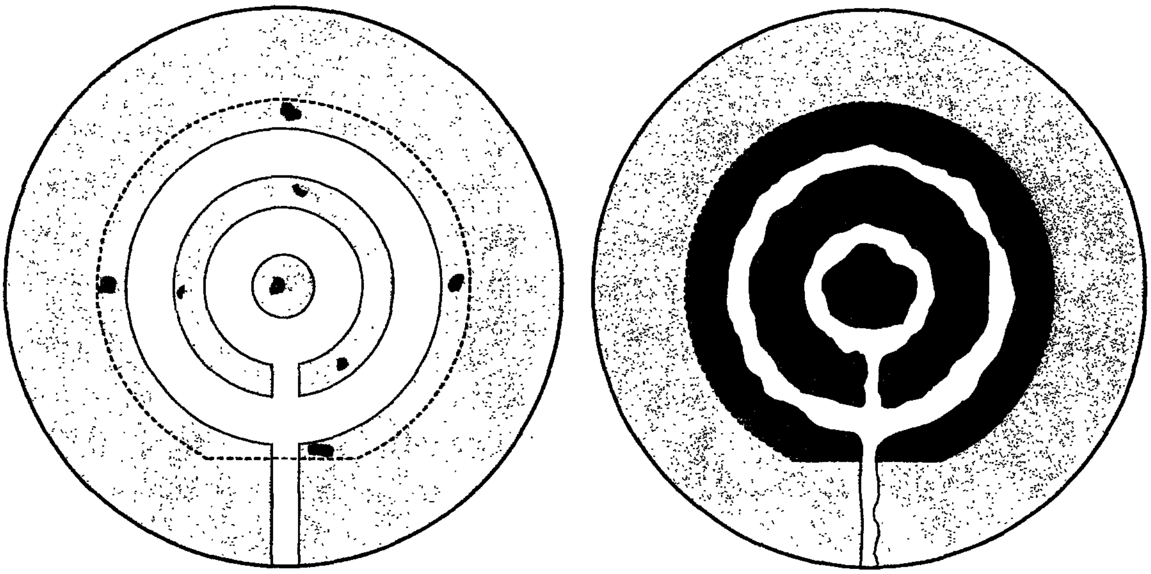

Figure 3.9. A typical bull's eye pattern used to mount the shadow mask wafer to the quartz handle wafer before etching, **a)** before baking, as patterned on the coater with the mask wafer pressed into place, **b)** after baking, which makes the patterned photoresist spread. Areas with good contact between the wafers appear darker.

Mounting protocol:

1. Spin quartz wafer continuously @ 1.8 krpm
   a. Coat quartz wafer with thick resist from center
   b. Remove all but center dot of resist with acetone
   c. Coat wafer with thick resist about ½" from center dot
   d. Remove all but center dot and ring of resist with acetone
   e. Coat wafer with thick resist from just inside diameter of coater chuck
2. Make air vents with acetone-dampened fabwipe
3. Align mask wafer in center of quartz wafer
   a. Drop wafer into place with double gloved hand
   b. Press edges down with clean pens at the four compass points
   c. Check back of wafer for good adhesion, indicated by darker spots where pressed with the pens
4. Bake horizontally @ 90°C for 10-15 minutes
5. Check bull's eye pattern for good contact (dark spots should have spread to most of the bull's eye pattern) without blocked vents
6. Scrape back of quartz wafer with fresh razorblade

DRIE Etch.—The wafer is deep reactive ion etched (DRIE) in the machine 'sts2', a DRIE Multiplex ICP (Surface Technology Systems, Portsmouth, NH). The DRIE etcher uses alternating etching and passivation phases to allow the etching of deep, straight-walled channels through the wafer. The wafer is etched using the standard recipe 'MIT59_A', which uses 10 second alternating phases and typically has an etch rate between 1.8 and 2.3 μm/min, which slows to approximately 1 μm/min as the etch progresses and the trenches get deeper. Smaller features etch more slowly than larger ones, and the center of the wafer etches more slowly than the edges. Some overetching of features is therefore unavoidable, and patterns with both very small and very large features are difficult to etch. The progress of the etch is checked under the microscope using the diffraction depth finder. It is important to handle the wafers very carefully when checking the trench depth because the etching makes the photoresist more fragile, and the contact between the mask and the handle wafer may be lost. Even if the two wafers do not come apart, loss of contact between them in one area will lead to poor thermal contact and burning of the photoresist pattern on the mask wafer when the wafers are etched further. Once the photoresist pattern is burned, the mask wafer is quickly etched away in the burned area and the wafer is ruined. Successful completion of the etching step is verified by examining both the center and the edges of the wafer under the microscope.

Wafer Dismounting.—The final step in the shadow mask wafer process is to dismount the mask wafer from the handle wafer. The wafers are soaked in acetone overnight in photo-wet-L, the green dot area of the photolithography hood. After the wafers have drifted apart, they are rinsed with acetone, methanol, and isopropyl alcohol, then gently blow dried. Finally, both wafers are cleaned in acidhood2 with a 10 minute Nanostrip etch and spin rinsed dry. The shadow mask wafer is then ready for use in steps 17-19 of the main fabrication process.

3.2. Microfabrication of devices used in experiments

The devices used in all experiments in this thesis came from two process wafers, designated #110601-5 and #020303-1. Wafer #110601-5 was fabricated earlier without any frontside patterning; the reservoirs had no gold membrane caps to seal them and the adhesion layer for the gold electrodes was chromium rather than titanium. The devices from #110601-5 were used for the equivalent circuit analysis experiments described in chapter 4. Wafer #020303-1 went through the full fabrication process of section 3.1 and had functional gold membrane caps as well as impedance electrodes. The devices from #020303-1 were used for the *in vitro* and *in vivo* experiments in chapters 6 and 7. The details of the processing steps performed on each wafer are given in Tables 3.9 and 3.10. The step number column refers to the step numbers given in the main process overview in Table 3.1 and the notebook page column refers to the page number in my TRL clean room laboratory notebook, which can also be found in electronic form in the file 'MTLhardcopyNotebook.doc'. In addition, the file 'MTLnotebook2002.doc' contains supplemental details concerning steps performed in the packaging area. The nitride/oxide and titanium etch steps that follow wafer dicing are detailed for each individual device in the experimental section of the appropriate chapters.

Table 3.9. Microfabrication process log details for wafer #110601-5.

step #	process step	date	notebook page	notes
1	starting materials	–	–	from wafers purchased by RS
2	nitride/oxide deposition	–	by staff	1000 Å oxide, 1500 Å nitride
3	positive resist	11/6/01	22	6s@0.5,6s@0.75,30s@3.5krpm
3	AMJWELLS pattern	11/6/01	22	32s, hard contact, ring at edge
4	nitride/oxide etch	11/6/01	22	275 s nitride etch, 350 s oxide
5	KOH etch	11/7/01	23	1450 g / 5000 mL, 85°C, 4:40 h
6	post-KOH clean	11/7/01	23	standard protocol
–	measure SiN_x on SiO_2	11/8/01	23	1287, 1277, 1308, 1304, 1284 Å
12	etch nitride overhang	11/8/01	23	275 s etch
–	measure thin SiO_2 on Si	11/8/01	23	607, 610, 597, 591, 607 Å
12	etch oxide overhang	2/6/02	25	200 + 80 s etch
–	measure thin SiO_2 on Si	2/6/02	25	<20 Å at all 5 points checked
13	Nanostrip clean	2/7/02	26	10 min
15	oxide deposition	2/7/02	26	20 W RF power, 195 s deposition
–	measure SiO_2 on Si	2/7/02	27	1114, 1076, 1079, 1081, 1081 Å
–	piranha clean	2/7/02	27	10 min
–	Nanostrip clean	2/13/02	27	10 min
17	mount shadow mask	2/13/02	27	mask #1, bake 10 min @ 90°C
18	gold deposition	2/15/02	28	100 Å chromium @ 2 Å/s, 100 + 100 + 2800 Å gold @ 5 Å/s
19	dismount shadow mask	2/19/02	29	soak until 2/21/02, rinse
–	blow dry	2/21/02	29	shattered while drying, pieced together onto blue tape
25	dice wafer (pieces)	3/11/02	–	diced largest pieces, speed = 4

Table 3.10. Microfabrication process log details for wafer #020303-1.

step #	process step	date	notebook page	notes
1	starting materials	10/18/01	–	box AMJ1 from WaferNet
2	nitride/oxide deposition	3/2002	by staff	1000 Å oxide, 1500 Å nitride
3	positive resist	2/3/03	37	6s@0.5,6s@0.75,30s@3.5krpm
3	AMJWELLS pattern	2/3/03	37	32s, hard contact, ring at edge
3	edge coat	2/3/03	37	3s@0.5,6s@0.75,30s@3.5krpm
4	nitride/oxide etch	2/3/03	38	800 s nitride etch, both layers
–	measure thin SiO_2 on Si	2/3/03	38	<20 Å at all 5 points checked
5	KOH etch	2/4/03	–	1450 g / 5000 mL, 85°C, 5 h
6	post-KOH clean	2/5/03	38	standard protocol
7	image reversal resist	2/10/03	39	5s@0.5,6s@0.75,30s@4.0krpm, blue tape, prebake 40 min
7	AMJGOLD pattern	2/10/03	39	40s, soft contact, no ring, hotplate bake 90 s, flood 300 s
8	gold deposition	2/10/03	40	100 Å titanium, 3000 Å gold, 100 Å titanium, all @ 1 Å/s
9	gold liftoff	2/11/03	40	swabbed stubborn edges
10	Nanostrip clean	2/11/03	40	10 min
11	thick resist protection	2/11/03	40	11s,60s@1.75,10s@5krpm,swab
12	nitride/oxide etch	2/12/03	40	450 s etch
–	measure thin SiO_2 on Si	2/12/03	41	<20 Å at all 5 points checked
13	Nanostrip clean	2/12/03	41	acetone 5 min, Nanostrip 10 min
14	thick resist protection	2/13/03	41	11s,60s@1.75,10s@5krpm,swab
15	oxide deposition	2/14/03	42	No RF power, 200s deposition
–	measure SiO_2 on Si	2/14/03	42	1041, 1013, 1039, 1043, 1011 Å
16	ash clean	2/19/03	42	5 min
17	mount shadow mask	2/19/03	42	mask #1, skewed after baking
–	remove skewed mask	2/19/03	42	acetone x 2, MeOH, IPA, SRD
17	mount shadow mask	2/19/03	42	mask #1, bake 10 min @ 90°C
18	gold deposition	2/20/03	42	100Å titanium,3000Å gold @1Å/s
19	dismount shadow mask	2/24/03	43	acetone, MeOH, IPA, blow dry
20	oxide deposition	4/30/03	47	1480s deposition, ~6500 Å oxide
21	positive resist	4/30/03	48	6s@0.5,6s@0.75,30s@3.5krpm
21	AMJOXIDE pattern	4/30/03	48	32s, soft contact, no ring, Hg lamp: not fully developed?
22	oxide etch	5/6/03	48	2000 + 1000 + 250 s etch
24	thick resist protection	5/12/03	49	11s,60s@1.75,10s@5krpm, broke while peeling off blue tape!
25	dice wafer (pieces)	5/12/03	–	diced largest pieces, speed = 3
26	nitride/oxide etch	various	49-51	700-1400 s nitride etch
27	etch titanium, HF dip	various	–	30 s dip, 1% HF

3.3. Packaging procedure

The packaging procedure for the impedance-sensing drug delivery devices was significantly different from the packaging scheme used for the original drug delivery devices. The impedance sensor MEMS devices require electrical connections to both the front and the back of the chip. This makes it quite difficult to adapt the compression sealing method developed by Rebecca Shawgo[2] to the impedance sensor devices. A workable alternative is the use of biomedical grade epoxy (MasterBond EP42HT) to seal the reservoirs and insulate the wires, with a small piece of glass slide to provide mechanical stability. The packaging process shown in Figure 3.10 (following pages), although somewhat crude and limited to systems with solid drug in the reservoirs, allows wire bonds to be made to both sides of the device while maintaining a hermetic seal and adequate insulation of the electrical components from the environment. The process can be broken down into four main tasks:

1. Filling and sealing the drug reservoirs, steps 1-4 in Figure 3.10
2. Making impedance sensor connections, steps 5-12
3. Making activation (anode and cathode) connections, steps 13-17
4. Preparing for *in vivo* implantation (adding reference electrodes, protecting wires with shrink tubing), steps 18-20

3.3.1. Reservoir filling and sealing

The drug reservoirs of each device were filled with mannitol, a sugar molecule often used as a model drug because of its simple pharmacokinetics.[11,12] Previous researchers used microinjection of drug solutions to fill the reservoirs with reproducible amounts of drug. However, the evaporation of the solvent after microinjection leaves the reservoirs mostly filled with air, with only a small residue of drug. This leads to highly variable drug release times because the drug may be trapped by the air bubble, which may dissolve quite slowly depending on the gas saturation of the release medium, as described in chapter 6. In such a case the impedance sensors would measure the rate of dissolution of the air bubble rather than the drug release rate. A melt process was developed to enable the filling of reservoirs entirely with solid drug. Although the dissolution of drug from a porous polymer matrix or gel should also give a measurable impedance change, the dissolution of a solid drug makes the system much simpler to understand and model.

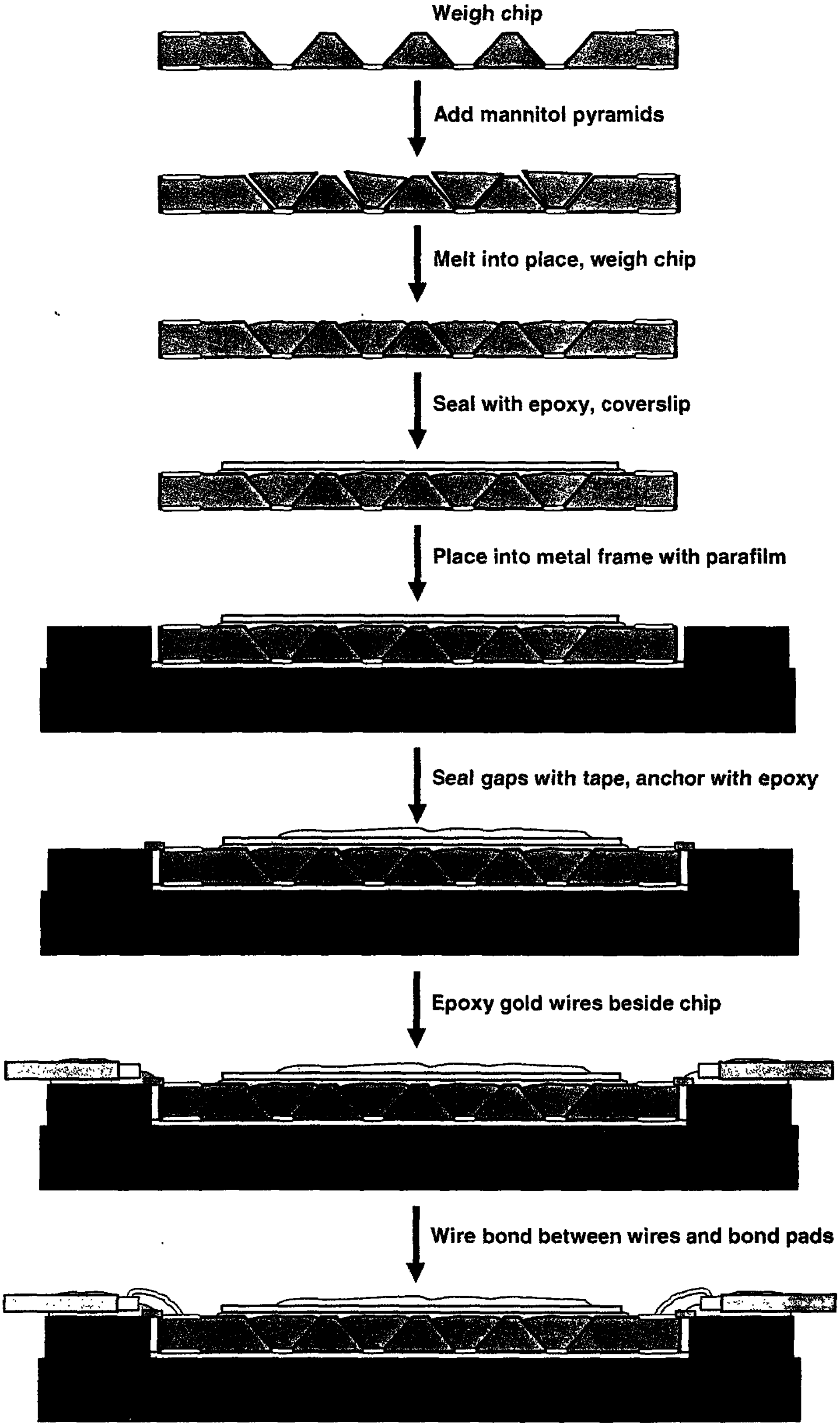

Figure 3.10. Illustrated overview of the packaging process. Steps 1 through 8.

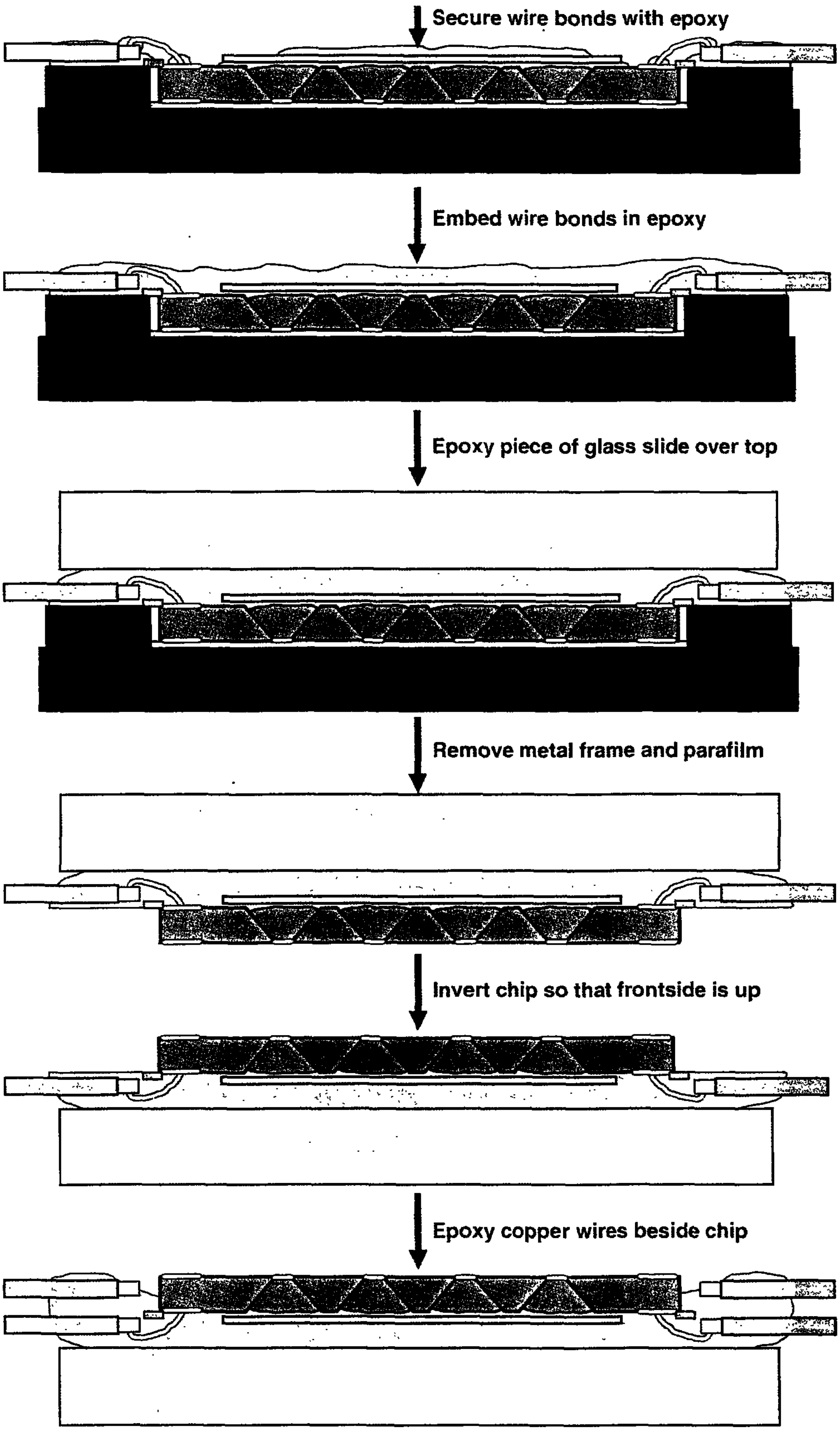

Figure 3.10. Illustrated overview of the packaging process. Steps 9 through 14.

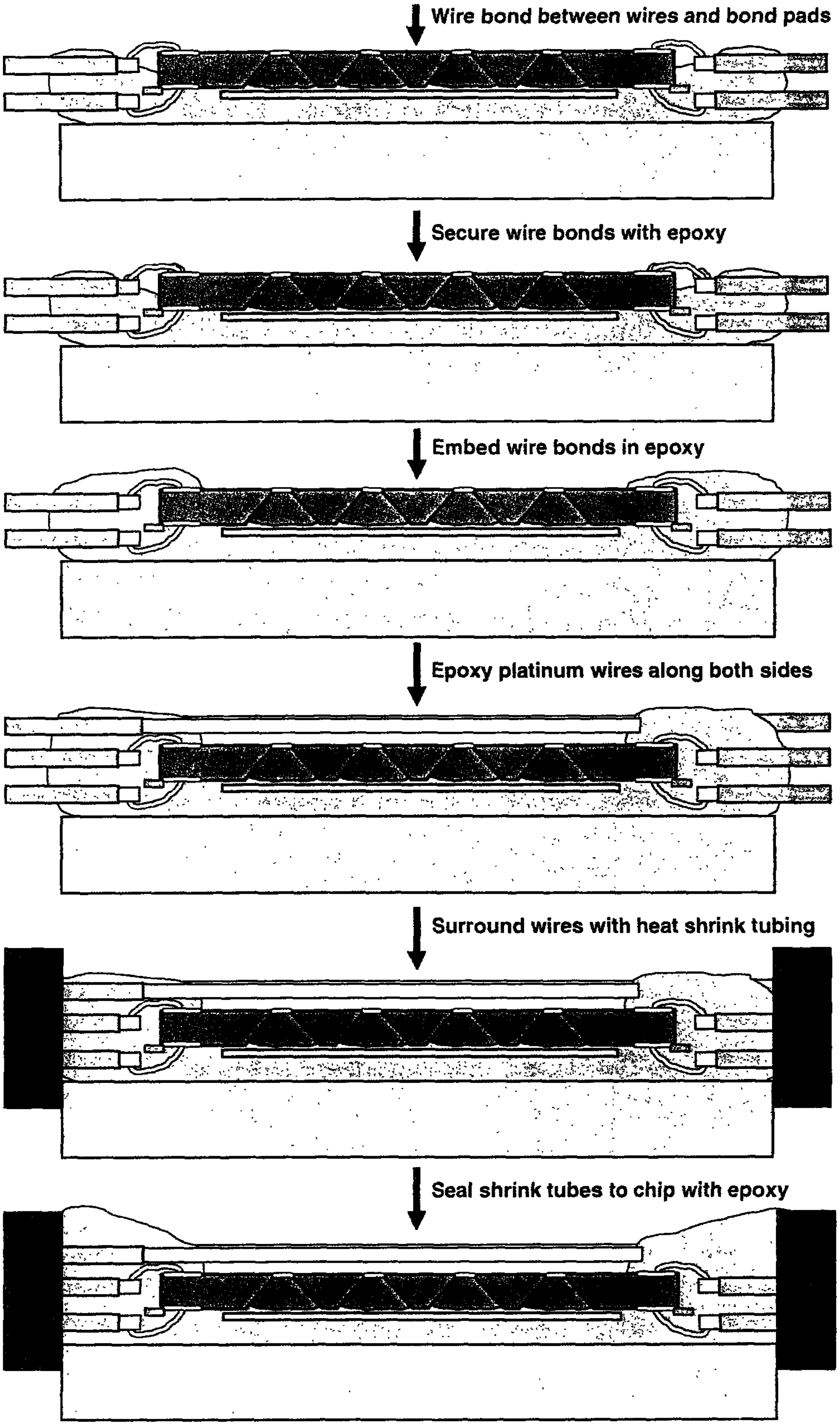

Figure 3.10. Illustrated overview of the packaging process. Steps 15 through 20.

In the melt filling process, powdered mannitol is spread over the reservoirs of a template device and heated, melting it into the reservoirs. Excess mannitol is removed with a razorblade, and the pyramid shaped mannitol pieces remaining are removed from the reservoirs. These pre-sized mannitol pieces, weighing approximately 30 μg each, are then placed into the reservoirs of the drug delivery MEMS device and heated to melt them in place. The MEMS device is weighed before and after the addition of mannitol to determine the amount loaded (AD-4 Autobalance, Perkin-Elmer, Boston, MA). The balance is calibrated with the 1 mg weight immediately prior to the experiment, and the weigh boats are treated with an anti-static gun every time the weighing chamber is opened. The reproducibility of the measurements was determined by repeated measurement of small standard weights over two successive days and found to be between 1 and 2 μg.

Most devices were filled with C^{14} radiolabeled mannitol. All steps must then be performed according to radiation safety requirements, as detailed in the official RPP protocol, given in appendix 10.2. The radiolabeled mannitol must be diluted by a factor of 100 with unlabeled mannitol prior to the melt process, in order to fill the reservoirs entirely with solid mannitol but avoid the use of excess radioactivity. This involves dissolution of C^{14} mannitol and unlabeled mannitol in a minimum of water followed by evaporation of the water and recrystallization. The dilution factor is such that a reservoir filled with mannitol contains on the order of 0.1 μCi of radioactivity.

The heating and cooling of the devices occasionally breaks one or more of the membranes of the device. Although some devices were filled, heated, and weighed after each reservoir was filled, this often led to the breakage of multiple membranes. Later devices were weighed before filling, filled with approximately equal amounts of mannitol in each reservoir, heated, and weighed just once at the end. If the membrane of a reservoir containing mannitol breaks while it is heated, capillary action can wick the mannitol out of the reservoir onto the front of the device and the glass slide underneath it. When the mannitol cools, the chip is then firmly attached to the glass slide. For this reason, two glass coverslips are placed about 3 mm apart on top of the glass slide and the chip is placed over the gap between them. Even if a membrane breaks, the mannitol stays within the reservoir and does not contaminate the front of the device or stick to the glass slide. Nevertheless, radioactive devices are always weighed with a piece of foil underneath them to prevent radioactive contamination of the microbalance.

After the device has been filled, it is sealed with epoxy and a small piece of glass coverslip that is cut to fit using the diesaw in MTL. It is essential to avoid spreading of the epoxy over the bond pads for the impedance electrodes. For this reason the chip is placed on a clean glass slide, reservoir side up, and the bond pads are covered with chemical resistant tape (1 mil polyester film with pressure sensitive silicone adhesive, 9144, ABI Tape, Lowell, MA). The tape also serves to hold the chip in place while it is epoxied and the coverslip is placed on top. After the epoxy has cured, the tape is carefully peeled away. The chemical resistant tape makes a sufficiently good seal with the chip surface so that epoxy cannot wick underneath, and the tape does not leave any residue behind that might interfere with wire bonding to the surface. The filled and sealed device is then ready for making electrical connections to the impedance sensors.

3.3.2. Impedance sensor connections

The impedance sensors are connected via traces along the surface of the device to bond pads along opposite edges of the backside of the chip. The chip is placed in a frame as diagrammed in Figure 3.10, step 5 to protect the frontside of the device while wire bonds are made to the backside bond pads. The frame is made from a stainless steel spacer plate originally designed for the compression sealing method used for the regular drug delivery MEMS devices. It is held on top of a glass slide with several layers of chemical resistant tape, double sided tape, and a 6 x12 mm piece of silicon wafer as a spacer. The frame is covered with chemical resistant tape to facilitate later removal of the frame from the chip. The frontside of the device is protected by a small square of parafilm placed underneath the device in the frame.

There is naturally a small gap between the frame and the device along all four edges. Small pieces of tape are cut to cover all parts of the gap to avoid wicking of the epoxy into the gap, which would permanently attach the chip to the frame. A layer of epoxy is spread over the center of the chip on top of the coverslip, extending (into and out of the page) over the frame on either side, as shown in Figure 3.10 step 6. Without this anchoring layer of epoxy, the chip is not stable and will be pushed down by the wire bonding tip, preventing good wire bond formation.

The next step is to epoxy bundles of insulated gold wires on top of the frame on either side of the device. Gold wire was chosen for the sensor connections to avoid complicating the impedance measurements with junction potentials between different conductors. Small diameter insulated gold wire is not readily available, so 0.2 mm diameter uninsulated gold wire (99.9% metals basis, Alfa Aesar, Ward Hill, MA) is used, insulated with liquid insulation (M-coat D and M-coat B, Vishay Micro-Measurements, Raleigh, NC). The insulation cures at room temperature to form a solid, flexible coating that is water and solvent resistant. The wire is cut into 4.5 cm lengths and insulated with 2 coats of M-coat D, an acrylic ester resin that is good for priming metals and has superior insulating properties. The wires are then colored with nontoxic ink to distinguish them from one another. Two layers of M-coat B, a nitrile rubber mixture, are applied over the ink to provide a saltwater-resistant, flexible coating over the wires. The wires are bundled together in groups of eight on glass slides covered with chemical resistant tape. About 7 mm of the tips of the wires are covered with epoxy in two coats, cured, then peeled from the glass slide using the tape. The tips of the wires are scraped free of epoxy under the microscope to prepare them for wire bonding. The wire bundles are then epoxied to the frame beside the device as shown in Figure 3.10, step 7.

The chip is wire bonded to the gold wires with gold wire bonds, 25 μm in diameter. This step is somewhat difficult because the gold bond pads often do not adhere well to the surface of the chip. Although a good bond is usually made between the wire bond and the chip surface, the wire bonding tip can easily tear the gold from the surface when it lifts. The optimal settings for wire bonding are usually power level = 6/7, time = 6, and force = 5/6. If the bonds have trouble sticking to the gold wires, re-scraping the wires to get a clean surface is usually effective. If the bonds do not stick to the chip surface, a gentle swab with acetone may be used to clean the bond pads. In the case of bond pads de-adhering from the chip surface, it is often necessary to make several attempts before a good bond is made.

The wire bonds are tested by impedance spectroscopy before they are sealed with epoxy. An impedance spectrum is measured across each reservoir between frequencies of 10^2 and 10^6 Hz. A good wire bond is indicated by a semicircular spectrum with resistance less than approximately 100 kΩ. It is generally true that the more attempts were made to make a good bond, the lower the measured resistance. This is because the wire bonding process damages the oxide layer that insulates the bond pads from the silicon beneath, increasing the leak current through the silicon substrate of the device. The semicircular spectrum is characteristic of a leaky capacitor, which is a capacitor and a resistor in parallel, as described in chapter 4. If one of the bonds is broken, the spectrum will show an open circuit and the bonds must be redone.

The successful wire bonds are then reinforced with a small drop of epoxy over each end as depicted in Figure 3.10, step 9. Once the reinforcing epoxy is cured, the wire bonds are embedded using several more coats of epoxy. Finally, a 6 x 12 mm piece of glass microscope slide (cut to size using the diesaw) is epoxied on top of the device. For devices that will be used *in vivo*, all edges and corners of the glass slide are first sanded down to avoid any sharp edges that might cause tissue damage. The epoxy is allowed to cure for a full 24 hours before the frame is removed from the chip, exposing the frontside of the device for wire bonding to the activation electrodes.

3.3.3. Activation electrode connections

Once the impedance electrode connections have been safely embedded in insulating epoxy and the frontside of the device has been exposed, the activation electrode connections can be made. It is not necessary to use gold wire for the activation electrode connections because they are used to apply the anodic potential to corrode the reservoir membranes, not for measurements. Insulated silver coated copper wire (30 AWG, 0.15 mm TFE, Alpha Wire, Elizabeth, NJ) is used for these connections. The wires are cut to 4.5 cm lengths and the ends are stripped of insulation, about 2 mm on the side toward the chip, and about 7 mm on the opposite end. The wires are bundled in groups of five on glass slides covered with chemical resistant tape, in the same manner as the gold wires were bundled together in section 3.3.2. Again, about 7 mm of the wire ends are covered with epoxy, removed from the slide using the tape, and the tips are scraped clear for wire bonding. The bundles are then epoxied on either side of the device as shown in Figure 3.10, step 14.

Wire bonds are made between the activation electrode bond pads and the copper wires. The adhesion of the bond pads to the chip surface is not problematic as with the impedance electrode connections. It is essential to scrape the copper wires with a clean razorblade immediately before wire bonding to remove the film of oxidized copper from the surface, or the wire bonds will not adhere well. Two wire bonds are made between each bond pad and the corresponding copper wire. Three or more bonds are made between the counter electrode (cathode) and the wire to ensure a good connection, because the cathode is essential to the activation of every reservoir. The ends of the bonds are secured with a drop of epoxy before they are embedded in more epoxy. Devices for use *in vitro* require no further preparation and can be tested as soon as the epoxy has cured.

3.3.4. Preparation for Implantation

Devices that will be used *in vivo* require the addition of reference electrodes and the encasing of the connection wires. Bright platinum wires (0.127 mm diameter, 99.9%, Alfa Aesar) are used as reference electrodes. The platinum wires are cut into 5.5 cm lengths and insulated in the same manner as the gold wires for the impedance connections, with two coats of M-coat D and two coats of M-coat B, but with no colored inks. One centimeter of the wire on the end toward the chip is left uninsulated to serve as a reference, and approximately 7 mm on the opposite side is left bare for connection to the potentiostat. One platinum wire is epoxied next to each set of copper wires, with the uncoated end extending alongside the edge of the chip face, as illustrated in Figure 3.10, step 18. The tip of the wire is epoxied in place to keep it from being accidentally bent out of position during implantation.

The gold, copper, and platinum wires are bundled together into two bundles, one on either side of the device. A sheath of shrink tubing (3M Very Flexible Polyolefin, 3/16", SFTW203 series, Digi-Key Corp., Thief River Falls, MN) is placed around each to protect the wires from the tissue and vice versa. The most flexible available tubing was chosen to try to avoid chafing of the tissue, which can be aggravated by very stiff wires. The tubing is heated with a hot air gun to shrink it into place, being careful to avoid excess heating of the chip (by avoiding heating continuously for long times, keeping the chip away from the hot air flow). The shrink tubing very near to the chip, approximately 5 mm, cannot be shrunk in this way without heating the chip. Instead, it is heated by application of a soldering iron, with care to avoid burning the tubing. The tubing is trimmed so that it just covers the tips of the longest wires. The tubing is affixed to the device with two coats of thick epoxy to seal any gaps between the embedded wires, the glass slide, and the tubing.

The devices are then ready for implantation. After the first *in vivo* test, it was found that many of the reservoir membranes broke, either during the implantation surgery or later during the implantation period, perhaps due to chafing of tissue against the surface of the chip. To avoid this problem during the second *in vivo* test, a small ring of epoxy was traced out around each reservoir that would be opened *in vivo*. The epoxy was applied using a monofilament brush in two separate applications with a curing step in between, to avoid spreading of the epoxy to cover the membrane. Far fewer reservoir membranes broke during implantation, indicating that this small ridge (<100 μm high) of epoxy may be effective in protecting the membranes from destructive mechanical forces. Although it was originally desired to have the reservoirs in direct contact with the tissue so that the transport through the tissue would be simpler, it was not possible with the fragile membranes and our current implantation techniques. However, this packaging method worked well enough to obtain *in vivo* release monitoring data from four devices at times up to 11 days post-implantation.

3.4. Conclusions

A microfabrication and packaging procedure was developed to enable the making of MEMS drug delivery devices with impedance sensors for real time release monitoring. The most challenging considerations were the patterning of electrodes within the three dimensional device reservoirs and the making of electrical connections to both the frontside and backside of each chip. Each of these challenges was successfully addressed by modification of the existing microfabrication and packaging protocols.

A shadow mask technique was adapted to our system to enable the patterning of the impedance electrodes within the reservoirs. A silicon wafer is through-etched with the electrode pattern and mounted on top of the device wafer to create a mask for metal deposition in the ebeam. With proper alignment of the wafers over the crucible, the electrode pattern is successfully transferred to the reservoirs of the device wafer, as shown in the SEM in Figure 3.11. The shadow masking technique is not easily scaled up to mass production but was sufficient for the production of prototype devices on a laboratory scale.

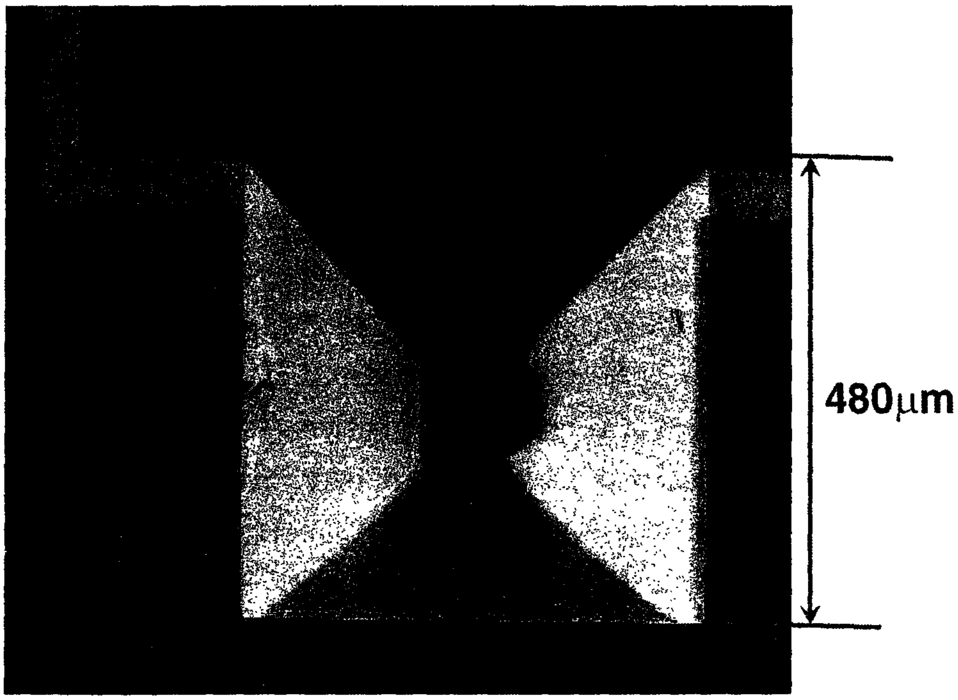

Figure 3.11. Scanning electron micrograph of impedance electrodes patterned within a reservoir on wafer #110601-5, using the shadow mask technique.

A simple packaging scheme was developed to allow electrical connections to be made to both the frontside and backside of the device. The device is placed in a frame to protect the frontside while the backside connections are made and embedded in epoxy. Upon removal of the frame, frontside connections can be made without disturbing the backside connections. The devices were shown to be hermetically sealed by this method, with the only leaks due to broken reservoir membranes. The electrical connections were well insulated and resistant to immersion in saline or implantation in tissue up to 2 weeks. Figure 3.12 shows typical packaged devices for *in vitro* and *in vivo* work.

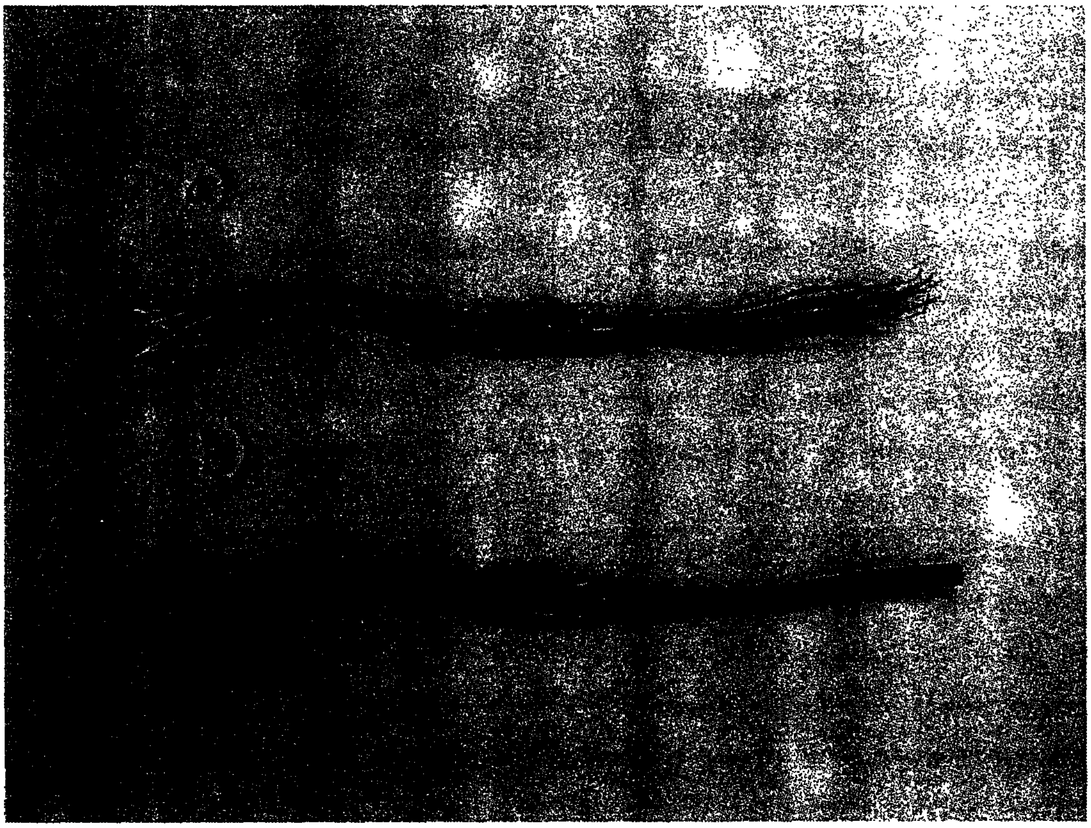

Figure 3.12. Fully packaged MEMS drug delivery devices with impedance-based sensors for real time, non-invasive monitoring of drug release, **a)** for *in vitro* experimentation, **b)** for *in vivo* implantation. Devices are approximately 10 cm in length.

3.5. Recommendations

For future microfabrication and packaging work, there are three main challenges: improvement of the adhesion of the gold impedance electrodes to the silicon substrate, improvement of the electrical insulation to allow long term implantation, and improvement of the activation technique for opening the reservoirs.

The impedance sensors are insulated from the silicon substrate of the device by a layer of silicon oxide. The current microfabrication procedure, while adequate, displays poor adhesion of the gold/oxide layers to the substrate. This makes wire bonding difficult, because the bond pads often detach from the device during bonding. It would be advantageous to improve this adhesion by properly adjusting the microfabrication procedure. The problem may lie in the adhesion of the oxide to the silicon, the adhesion of the gold to the oxide, or the etching of nitride in step 26, which may damage the oxide layer. Appropriate modifications to one or more of these steps could significantly reduce the time required for packaging the devices and improve the quality and reliability of the impedance connections.

The packaging technique is effective for devices that will be implanted up to 2 weeks, but not reliable for longer implantation times. It has been observed by Rebecca Shawgo and others that the EP42HT epoxy is not completely impermeable to water after an extended period of submersion. Some connections may last longer than 2 weeks, but significant attrition is noticeable among the activation connections, and the impedance electrode connections may give a false signal, measuring a solution resistance between the wires rather than through the reservoir. A substitute epoxy, an additional layer of electrical insulation over the wire tips or wire bonds, perhaps M-coat D or M-coat B, or even a completely new packaging scheme, could yield improved long term results.

Finally, the activation of the reservoirs by corrosion of the gold membrane was found to be somewhat unreliable *in vivo*, as described in chapter 7. MicroCHIPS, Inc. researchers have developed an entirely new method for opening the reservoirs, a so-called 'fuse chip'. A wide current path runs from the edges of the chip across the top of each reservoir, narrowing just above the reservoir opening. When current is applied, the bottleneck above the reservoir heats rapidly and melts within microseconds. The fuse method is much more reliable than the corrosion method and can open in air, saline, or tissue irrespective of the device environment.

In addition to making the opening of the device more reliable, the fuse method results in an opening of consistent size. The corrosion method causes the membrane to fail mechanically, which usually completely opens the reservoir but is somewhat inconsistent and may yield a variety of opening sizes and shapes. The variability in the degree of membrane opening interferes with the measurement of transport through the tissue by the impedance sensors, as a slow drug release rate may be due to either an incomplete reservoir opening or the transport characteristics of the surrounding tissue. While researchers using the traditional MEMS drug delivery devices typically open many reservoirs at once, monitoring drug delivery with the impedance sensors requires the activation of one reservoir at a time, making the reliability of activation a critical factor. Modifying the fabrication protocol to use the fuse activation method rather than corrosion would significantly improve the amount and quality of data collected with each device.

3.6. References

1. J. T. Santini Jr., A controlled release microchip, *Massachusetts Institute of Technology, Doctoral Thesis* (1999).
2. R. S. Shawgo, In vivo activation and biocompatibility of a MEMS microreservoir drug delivery device, *Massachusetts Institute of Technology, Doctoral Thesis* (2004).
3. Microsystems Technology Laboratories Handbook, *Massachusetts Institute of Technology* (1999).
4. R. Schnupp, R. Baumgartner, R. Kuhnhold, and H. Ryssel, Electrodeposition of photoresist: optimization of deposition conditions, investigation of lithographic processes and chemical resistance, *Sensors and Actuators A*, **85**, 310-315 (2000).
5. V. K. Singh, M. Sasaki, K. Hane, and M. Esashi, Flow condition in resist spray coating and patterning performance for three-dimensional photolithography over deep structures, *Japanese Journal of Applied Physics Part 1*, **43**, 2387-2391 (2004).
6. V. K. Singh, M. Sasaki, J. H. Song, and K. Hane, Heating effect on photoresist in spray coating technique for three-dimensional lithography, *Japanese Journal of Applied Physics Part 1*, **42**, 4027-4030 (2003).
7. G. T. A. Kovacs, Shadowing, Micromachined Transducers Sourcebook, p. 95, McGraw-Hill, Boston (1998).
8. G. J. Burger, E. J. T. Smulders, J. W. Berenschot, T. S. J. Lammerink, J. H. J. Fluitman, and S. Imai, High resolution shadow mask patterning in deep holes and its application to an electrical wafer feed-through, *Sensors and Actuators A*, **54**, 669-673 (1996).
9. G. T. A. Kovacs, Lift-off patterning, Micromachined Transducers Sourcebook, pp. 98-100, McGraw-Hill, Boston (1998).
10. E. Jiran and C. V. Thompson, Capillary instabilities in thin films, *Journal of Electronic Materials*, **19**, 1153-1160 (1990).
11. J. C. Cloyd, B. D. Snyder, B. Cleeremans, and S. R. Bundlie, Mannitol pharmacokinetics and serum osmolality in dogs and humans, *Journal of Pharmacology and Experimental Therapeutics*, **236**, 301-306 (1986).
12. M. F. Laker, H. J. Bull, and I. S. Menzies, Evaluation of mannitol for use as a probe marker of gastrointestinal permeability in man, *European Journal of Clinical Investigation*, **12**, 485-491 (1982).

4. Equivalent Circuit Analysis

A good understanding of how the physical characteristics of the reservoirs are related to the electrical measurements of the impedance sensors was necessary to interpret the impedance signal. An equivalent circuit was developed that describes the sensor as a combination of resistors and capacitors. The unusual electrode geometry and small size of the reservoirs made this a difficult problem; we therefore sought to understand the effect of electrode geometry separately by examining a macroscale model of a reservoir before moving to the full problem of a pyramidal microreservoir. The expected solution resistance and double layer capacitance were calculated from first principles and compared to the measured values obtained from the equivalent circuit analysis. There was very good agreement between our calculated and measured values, and the equivalent circuits fit the data well. The sensor was used to monitor the release of mannitol from a microreservoir to demonstrate how the observed electrical characteristics of the reservoir change during drug dissolution.

There are four categories of equivalent circuit analysis experiments:

1. Measurement of the conductivity of PBS solutions
2. Measurements of the impedance of the macroscale sensor model
3. Measurements of the impedance of the microreservoir sensors
4. Monitoring of microreservoir sensor output during mannitol dissolution

The expected solution resistance and double layer capacitance of the model and microreservoirs were calculated using the measured conductivities of PBS solutions. The macroscale model impedance measurements were used to obtain a simple equivalent circuit describing the electrical properties of a solution in a square pyramidal cavity. The simple equivalent circuit from the macroscale model was then used as a starting point for the equivalent circuit of the microreservoir sensors. The final microreservoir equivalent circuit was then used to fit the time varying data from the monitoring of mannitol dissolution from a reservoir. The results presented in this chapter were accepted for publication in the *Journal of the Electrochemical Society*[1].

4.1. Experimental

4.1.1. Materials

D-mannitol, potassium chloride, and eicosane (Sigma, St. Louis, MO) were used as received. Phosphate buffered saline, PBS, consisting of 0.137 M NaCl, 0.001 M KH_2PO_4, 0.01 M Na_2HPO_4, and 0.0027 M KCl at pH 7.4 when diluted to 1x concentration

(Roche, Indianapolis, IN) was purchased as a 10x solution and diluted to the appropriate concentration. Solutions were made with deionized water passed through a MilliQ (Millipore, Billerica, MA) system, resistivity above 17.8 MΩ cm. Wires and bond pads were insulated with EP42HT medical grade epoxy (MasterBond, Hackensack, NJ), cured for 24 h at room temperature.

4.1.2. Scale model of device reservoirs

A 100x scale model of a square pyramidal drug delivery device reservoir was fabricated from acrylic by the MIT machine shop. The pyramid was of base length 4.8 cm, height 3.0 cm, and base angle 54.4°. One side of the pyramid was removable to provide access to the pyramid interior. Gold foil electrodes (25 μm thick, 99.9+%, Sigma) were cut to cover two opposing interior sides of the pyramid with tabs extending from the top of the model for electrical connections, as shown in Figure 4.1. Detailed specifications for the model may be found in appendix 10.6.1.

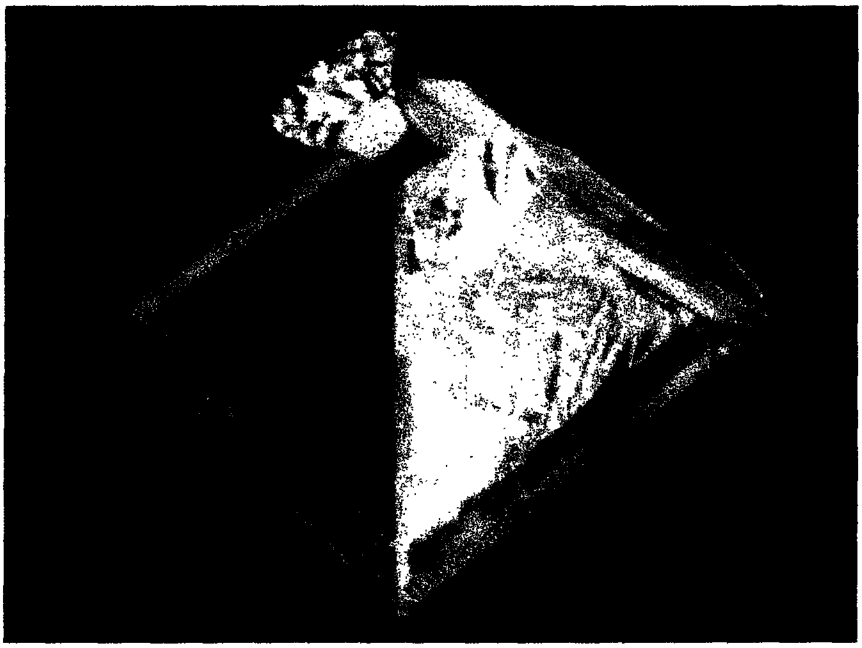

Figure 4.1. 100x scale model of a MEMS drug delivery device reservoir.

4.1.3. PBS solution conductivity measurements

The conductivities of PBS solutions were measured using a two-electrode conductivity cell (Industrial Instruments Inc., Cedar Grove, NJ) fully immersed in the solution to be measured. The impedance spectrum was recorded using a Solartron 1255B Frequency Response Analyzer with a SI1287 Electrochemical Interface. The impedance was measured for frequencies between 10^2 and 10^6 Hz, sufficient to reveal the critical point or 'notch' in the Cole-Cole plot. The critical point was independent of the magnitude of the ac excitation voltage, which was varied between 20-350 mV. The cell constant was determined using standard solutions of 0.01 D, 0.1 D, and 1.0 D potassium chloride. All solutions were kept at room temperature, 23.5°C. The measured value of the cell constant was then used to determine the conductivity of 0.01x, 0.1x, 0.5x, and 1.0x PBS solutions.

4.1.4. Impedance of reservoir scale model

The two-electrode impedance of the 100x scale model of a device reservoir was measured for frequencies between 10 and 10^6 Hz. An initial aliquot of 1.0x PBS was added to the model to make contact between the foil electrodes and the impedance measurement was repeated. The impedance measurement and addition of PBS was repeated in increments of 1 to 2 mL solution until the model was entirely full. The experiment was repeated using 0.5x PBS and 0.1x PBS solutions.

4.1.5. Impedance of microdevice reservoirs

A drug delivery MEMS device from wafer #110601-5 was packaged with open reservoirs for measurement of impedance submersed in PBS solutions. The impedance electrodes were connected by traces to bond pads along the edges of the device. Insulated gold wires were epoxied (MasterBond EP42HT) alongside the device and gold wire bonds, diameter 25 μm, were made between the bond pads and the wires. The wires, bonds, pads, and traces were covered with epoxy to insulate them. The two-electrode impedance of each of four reservoirs was measured for frequencies between 10 and 10^6 Hz. The device was then submersed in PBS solutions of 1.0x, 0.5x, and 0.1x concentration. The solutions were observed to entirely fill the reservoirs, and the impedance measurement across each reservoir was repeated in each solution.

4.1.6. Impedance during drug release

The reservoirs of a drug delivery MEMS device from wafer #110601-5 were filled with 20-30 μg solid mannitol per reservoir by the melt process described in chapter 3. For this set of experiments, non-water soluble eicosane wax was melted behind the mannitol to completely fill the remaining space within the reservoir. The device reservoirs were then sealed with a glass coverslip and epoxy, and gold wires were epoxied beside the bond pads. Wire bonds were made between the impedance electrodes of each reservoir and the wires, then insulated with epoxy. The two-electrode impedance of each reservoir was measured at frequencies between 10^3 and 10^6 Hz. The device was then submersed in 1.0x PBS solution and the impedance measurement was repeated. After each reservoir was opened, the reservoir impedance was measured every three minutes until the impedance did not change with time, to within approximately 1%. At this point it was assumed that the dissolution of the mannitol was complete.

4.2. PBS solution conductivity

A reported value for the conductivity of PBS solutions is not readily available in the literature, and PBS solutions vary depending on the manufacturer, so the first step in calculating the expected solution resistance was to measure the conductivity of PBS solutions of varying strength. A conductivity cell borrowed from Hammond lab was used for all conductivity measurements; however, the documentation accompanying the cell had been lost so it was first calibrated using standard KCl solutions to determine the cell constant. The cell constant, G, is the ratio of the effective length of the current path, ℓ, to the effective cross-sectional area of the current path[2], A

$$G = \ell / A$$

The cell constant relates the intensive property, conductivity, κ, to the extensive property, solution resistance, $R_{solution}$

$$\kappa = G / R_{solution}$$

The measured resistance, R_{meas}, is often slightly higher than the solution resistance due to a finite lead resistance[3], R_{leads}

$$R_{meas} = R_{solution} + R_{leads}$$

Substituting for $R_{solution}$ gives the following equation for R_{meas}

$$R_{meas} = G\,(1/\kappa) + R_{leads}$$

It is clear from the above equation that a plot of R_{meas} vs. $1/\kappa$ should have slope G and intercept R_{leads}. The conductivities of the standard solutions at room temperature were interpolated from values given by Wu and Koch[4]. The value of R_{meas} were taken from the Cole-Cole plot by taking the value of the real part of the impedance at the critical point, shown in Figure 4.2. The Cole-Cole representation of the impedance shows the imaginary (capacitive and inductive elements) vs. the real (resistive elements) part of the impedance. By taking the purely resistive part of the impedance at the critical point we can ignore the effects of capacitive elements of the cell, taking only the impedance that arises from the resistive elements $R_{solution}$ and R_{leads}. Plotting R_{meas} vs. $1/\kappa$, we obtained a value of 1.00 ± 0.01 cm^{-1} for the cell constant and 0.01 Ω for R_{leads}. The plot is sufficiently linear that the uncertainty in the cell constant arises almost entirely from the uncertainty in the temperature measurement.

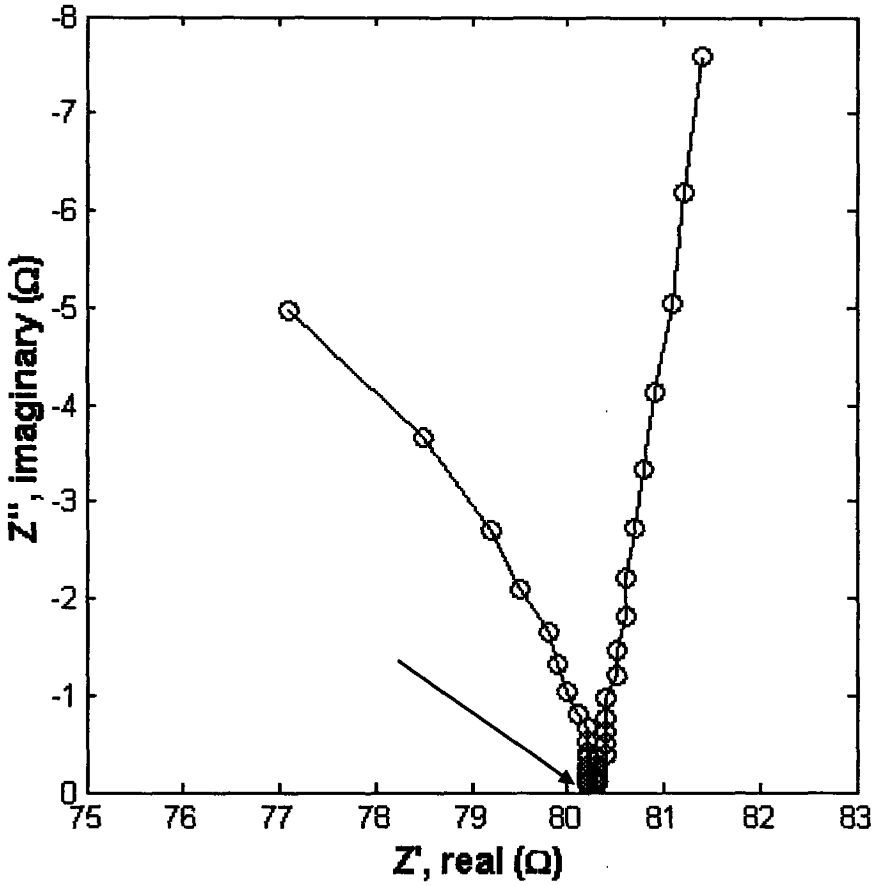

Figure 4.2. Cole-Cole plot of the impedance of a 0.1D KCl solution indicating the critical point where the impedance is purely resistive.

The cell constant was then used to determine the conductivity of the PBS solutions, neglecting the small contribution of the lead resistance. The measured values of the electrical conductivity of solutions of 1.0x, 0.5x, 0.1x, and 0.01x PBS at room temperature, 23.5°C, are given in Table 4.1.

Table 4.1. Conductivity of PBS solutions.

PBS concentration	calculated conductivity at 25°C (S cm^{-1})	measured conductivity at 23.5°C (S cm^{-1})
1.0x	1.59×10^{-2}	1.57×10^{-2}
0.5x	8.37×10^{-3}	8.32×10^{-3}
0.1x	1.81×10^{-3}	1.79×10^{-3}
0.01x	1.90×10^{-4}	1.88×10^{-4}

For comparison, the expected conductivity at 25°C can be estimated using Kohlrausch's law for strong electrolytes[5] and summing the contributions to the conductivity from the individual ionic species present in each PBS solution. The conductivity of an electrolyte solution is given by

$$\kappa = c\,\Lambda_m$$

where c is the concentration and Λ_m is the molar conductivity, which is itself a function of concentration. The molar conductivities of KCl and NaCl are tabulated as functions of temperature and concentration by Vanýsek[6] and may be interpolated to give the molar conductivity at each PBS concentration except for 0.137 M NaCl in 1.0x PBS, which must be extrapolated from the molar conductivity at 0.1 M. The extrapolation uses Kohlrausch's law

$$\Lambda_m = \Lambda^\circ_m - \mathcal{K} c^{1/2}$$

which says that a plot of the molar conductivity vs. the square root of concentration should be approximately linear with slope $\mathcal{K}$ and intercept equal to the limiting molar conductivity, Λ°_m. The coefficient $\mathcal{K}$ is a constant that depends on the stoichiometry of the ionic species. For Na_2HPO_4 and KH_2PO_4, no Λ_m values were available. However, the limiting molar conductivity can be calculated from the equation

$$\Lambda^\circ_m = \nu_+\lambda_+ + \nu_-\lambda_-$$

where ν is the number of positive or negative ions in the salt and λ is the limiting molar conductivity of the positive or negative ion, which is tabulated in both Atkins and Vanýsek. Values for $\mathcal{K}$ were estimated from several similar ionic species and the molar conductivity was extrapolated from the limiting value Λ°_m. Due to the relatively low concentrations of these two species, the uncertainty in $\mathcal{K}$ did not significantly affect the final values for the conductivity of the PBS solutions, which were calculated from the sum

$$\kappa = \Sigma_i\, c_i\, \Lambda_{m,i} \;;\; i = \mathrm{NaCl, KCl, Na_2HPO_4, KH_2PO_4}$$

The calculated values are given in Table 4.1 and are the same as the measured values of the conductivity to within 1-2%.

4.3. Impedance of 100x scale model

The scale model of the pyramidal reservoir was constructed to evaluate the effects of the unusual electrode geometry on the impedance. Figure 4.3 shows a typical series of impedance spectra obtained during filling of the pyramid model with PBS. The case of a pyramid with no solution is omitted because the impedance of the open circuit case is several orders of magnitude higher. The capacitance of a square pyramid in air is derived and compared to the measured open circuit capacitance in appendix 10.3. Each solution measurement is a line with a slight positive slope. As the model is filled, the x (real) intercept of the line decreases and the line becomes shorter and slightly more sloped. The data are qualitatively the same for each of the three PBS concentrations except for the scale of the axes, which increases as the conductivity of the solution decreases.

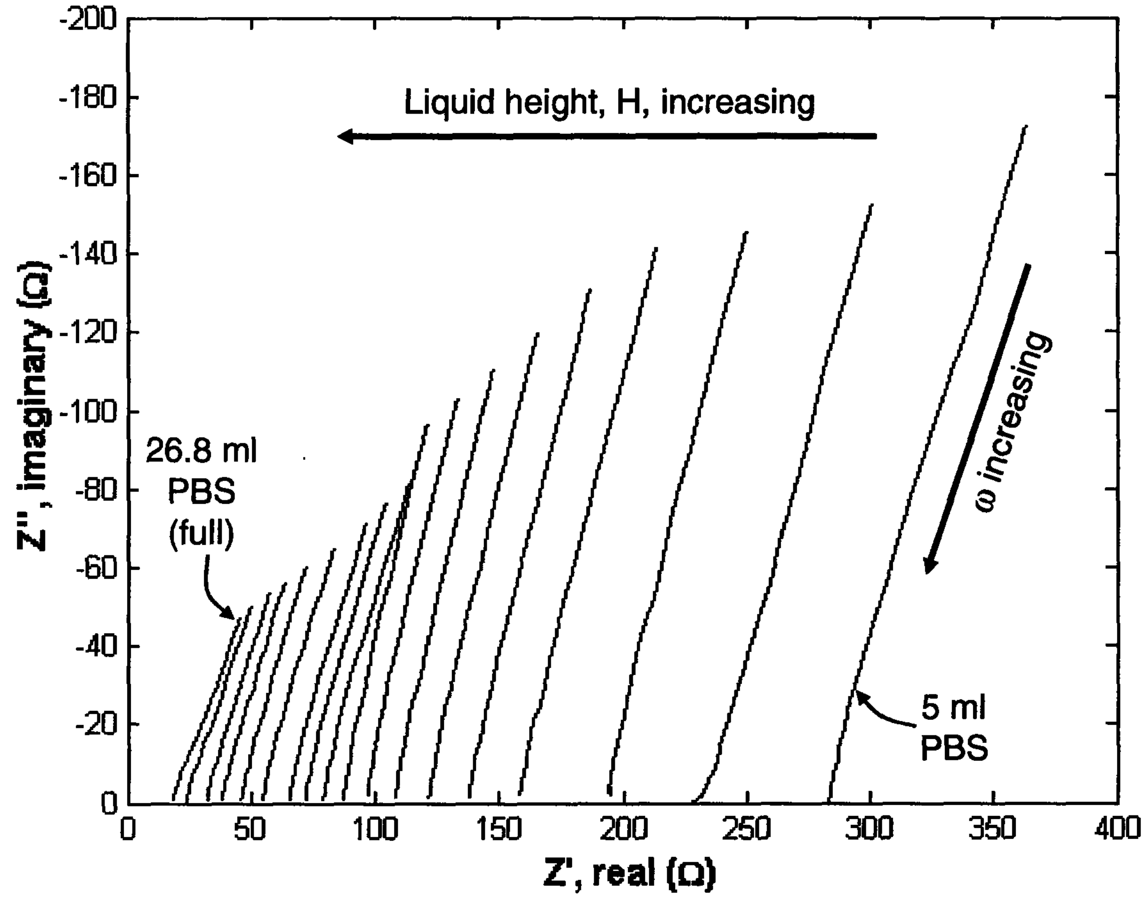

Figure 4.3. Cole-Cole plot of a series of impedance spectra obtained during incremental filling of the pyramidal model of a MEMS reservoir with 1.0x PBS.

To determine the appropriate equivalent circuit for the system, we began with the typical equivalent circuit for an electrochemical cell given in Bard and Faulkner[7], shown in Figure 4.4a. It consists of four elements: the solution resistance, the double layer capacitance, the charge transfer resistance, and the Warburg impedance. The solution resistance comes from the motion of charged species in solution and is related to the conductivity of the solution. The double layer capacitance is due to the arrangement of charged species in a layer adjacent to the electrode surface. The charge transfer resistance is the resistance associated with the chemical transfer of electrons between the electrode and the species undergoing oxidation or reduction. Finally, the Warburg impedance is a complex term arising from the transport of the oxidized/reduced charge carriers through the solution. For our system, the noble metal (gold) electrodes can be assumed to behave as ideal polarizable electrodes for these small voltages, so there are no Faradaic processes (oxidation or reduction reactions) occurring. The charge transfer resistance and Warburg impedance are therefore eliminated, leaving the very simple circuit shown in Figure 4.4b.

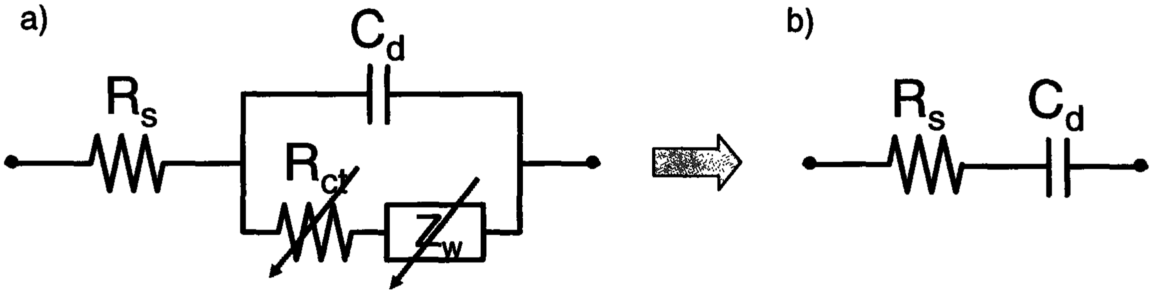

Figure 4.4. Equivalent circuits for **a)** a typical electrochemical cell, and **b)** an electrochemical cell with no Faradaic processes occurring.

The expected equivalent circuit is then simply the solution resistance and double layer capacitance in series. The Cole-Cole plot for such a system is a vertical line with real intercept equal to the solution resistance and height determined by the double layer capacitance. A comparison of the macromodel data and the equivalent circuit fit is shown in Figure 4.5. The only deviation is the slight positive slope of the data. In real systems it is generally observed that a constant phase element (CPE) fits the data better than a simple capacitor. If a CPE were substituted for the capacitor in the equivalent circuit in Figure 4.5, the data and the fit would be nearly identical. However, although it is generally assumed that some sort of dispersion of physical properties gives rise to CPE behavior, the physics behind this are not well understood[8]. We therefore chose not to resort to the inclusion of a CPE, as the simple capacitor gives a reasonably good fit to the data.

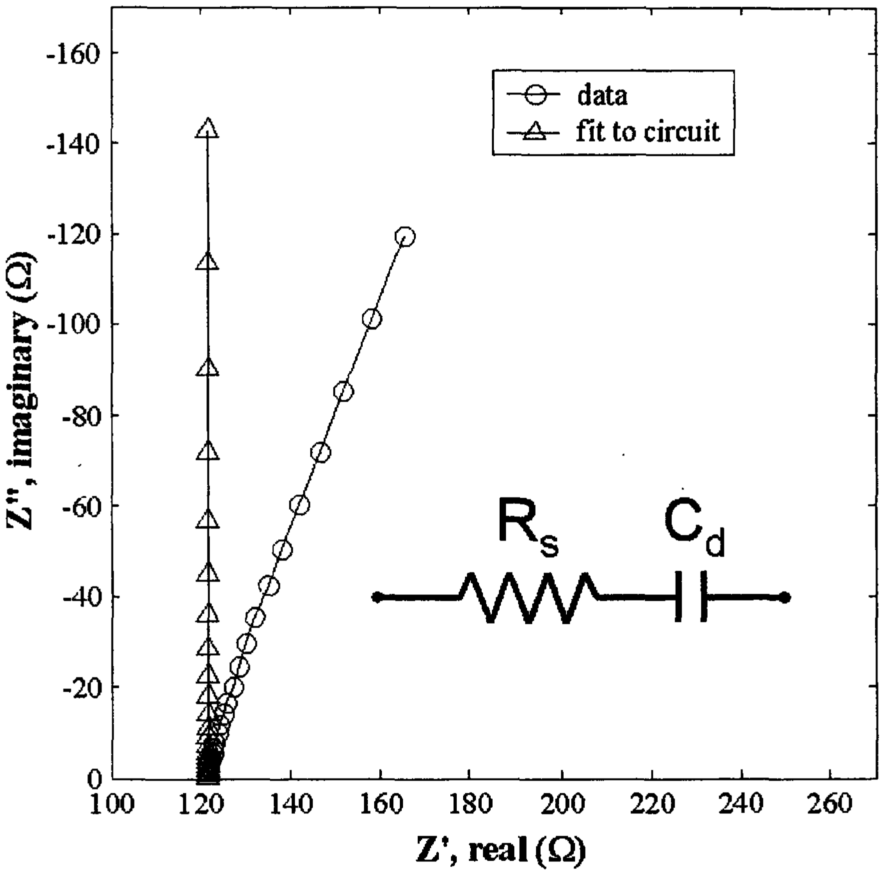

Figure 4.5. Equivalent circuit and Cole-Cole plot of experimental data and best fit to circuit for 100x scale model of a square pyramidal drug reservoir containing 10 ml of 1.0x PBS.

The series impedance spectra shown in Figure 4.3 can then be fitted to the equivalent circuit to obtain best fit values of the solution resistance and double layer capacitance. These measured values of resistance and capacitance can be compared to the values we would expect based on the geometry of the system and the conductivity of the solution. The resistance of a square pyramid can be calculated by starting with the formula for conductance, Y, of a solid

$$Y = A / \rho L$$

where A is the cross sectional area, ρ is the resistivity, and L is the length. By taking a differential horizontal cross section, we can integrate the conductivities of each slice from x=0 to x=H, where H is the height of the pyramid. In this case, A and L are both functions of x and of the base angle of the pyramid, as illustrated in Figure 4.6.

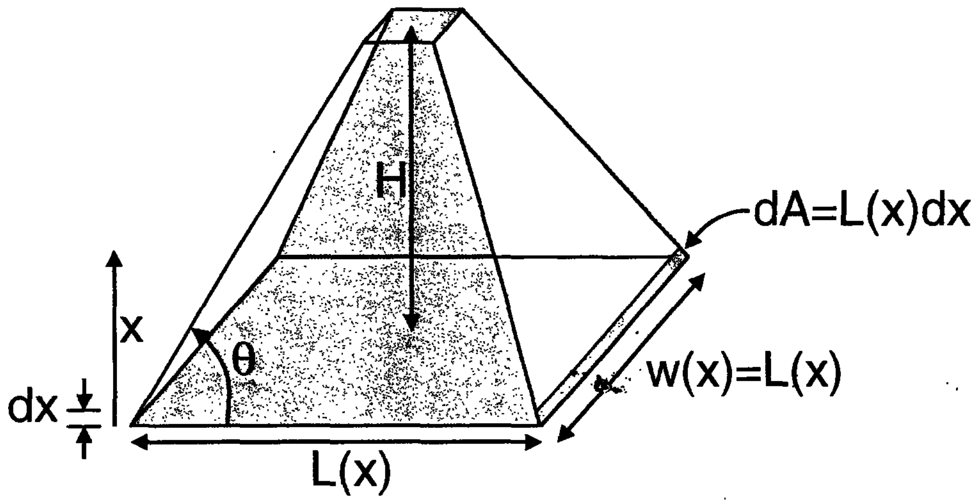

Figure 4.6. Coordinate system and discretization used for calculation of the resistance of a square pyramid.

For a square pyramid, at any height, x, the width of the electrode at the edge and the distance between the electrodes are the same function of x, L(x). This means that the differential area is given by

$$dA = L(x)\,dx$$

where L(x) is given by the following equation in terms of L_0, the width of the base, and θ, the base angle.

$$L(x) = L_0 - 2x / \tan\theta$$

Substituting into the equation for Y gives the formula

$$dY = L(x)\,dx / \rho\, L(x)$$

The L(x) cancel out and the equation is easily integrated from zero to H, yielding

$$Y = H / \rho\ ;\quad R = \rho / H$$

From this formula we see that for the special case of a square pyramid, the resistance scales with the inverse of the height of the pyramid. Therefore, as the pyramid model is filled with solution, the resistance should scale with the inverse of the height of liquid in the model. This matches the experimental findings as shown in Figure 4.7. In an ideal case the slope of the plot should be equal to the solution resistivity, which is the inverse of the conductivity measurements in Table 4.1. For our system the linear least squares slope for each solution differs from the resistivity by a factor of 0.95 ± 0.01, which yields an effective cell constant for this particular experimental setup of 0.95/H, very close to the theoretical cell constant of 1/H derived above. The experimental data agree very well with the predicted equivalent circuit and expected values for solution resistance. In addition, the double layer capacitance for an aqueous solution is expected to be on the order of 10 μF/cm^2, and the best fit capacitance for our data agrees with this estimate.

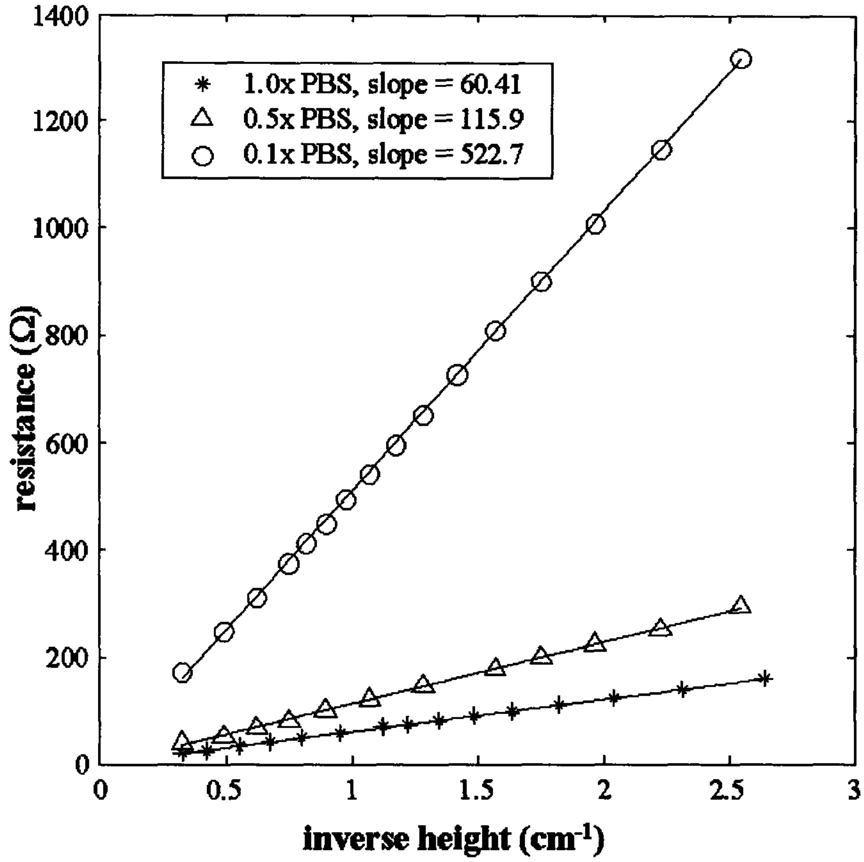

Figure 4.7. The dependence of the measured solution resistance in the square pyramidal model on height of the solution in the model and PBS concentration, with best fit lines through each data set.

4.4. Impedance of drug delivery MEMS reservoirs

Once the effects of electrode geometry were well understood from the macroscale pyramid model, experiments were conducted to investigate the electrochemical characteristics of the microreservoirs. Figure 4.8 shows the impedance spectra for each of the four reservoirs, measured in air and in three different PBS concentrations. Whereas the macromodel gave infinite resistance for air and a line when filled with solution, the microreservoirs yield a semicircle when filled with air and a double semicircle when filled with solution. The position of the inflection between the two semicircles is a function of the solution resistance and is approximately the same for each reservoir. The overall size of the graph is independent of the reservoir contents and is a function of which reservoir is being studied. The semicircular spectra indicate that there is an alternate current path, parallel to the one through the microreservoir.

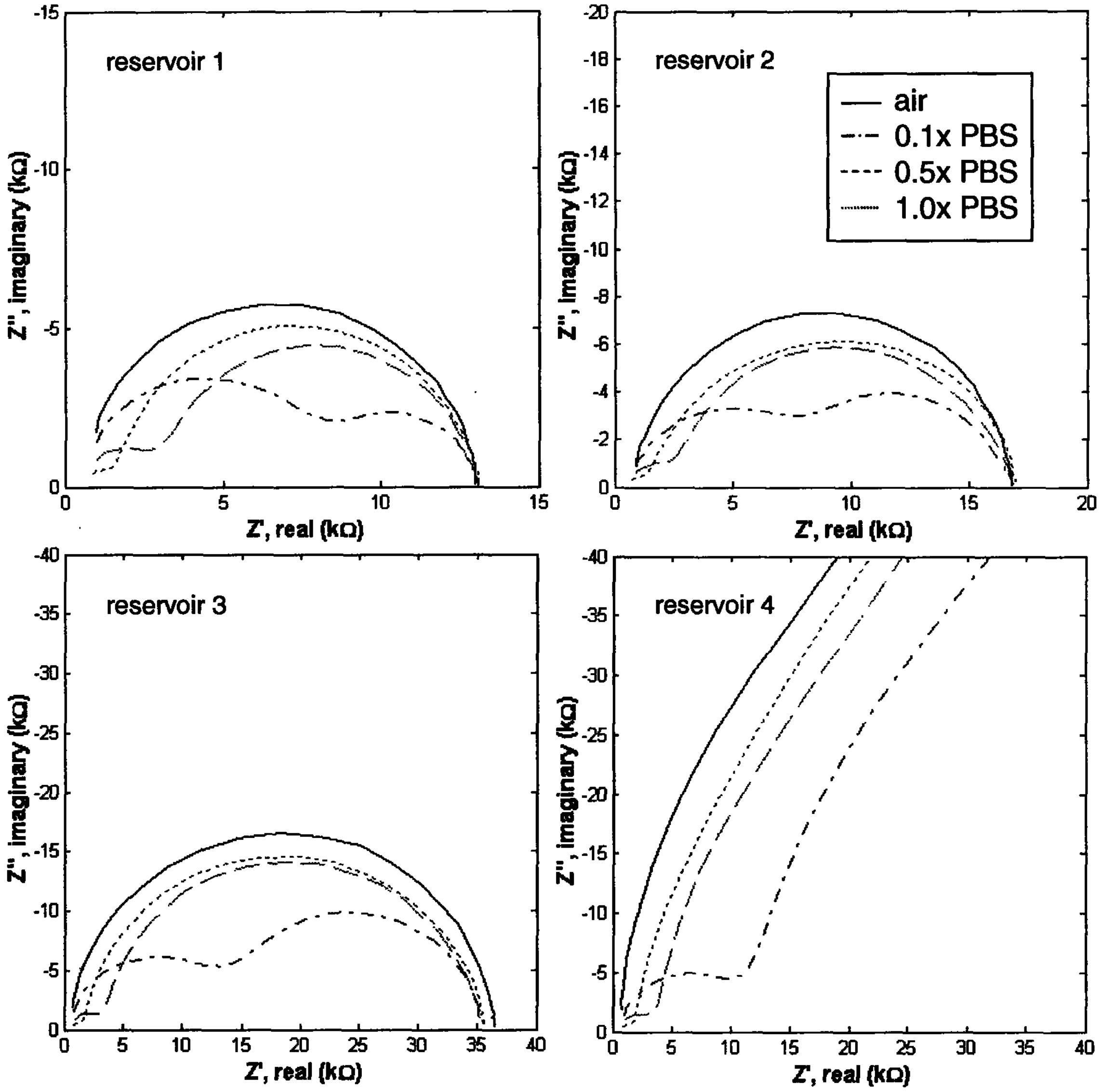

Figure 4.8. Cole-Cole plot of impedance spectra of four MEMS drug delivery device reservoirs, taken in air, 0.1x PBS, 0.5x PBS, and 1.0x PBS.

The alternate current path goes through the silicon substrate in which the reservoir is etched, and is due to leakage current from the electrodes through the silicon oxide layer beneath into the silicon. Such a leakage current should take the form of a parallel RC circuit, a so-called 'leaky capacitor'[9]. Adding a leaky capacitor to the equivalent circuit for the macromodel gives the more complex circuit shown in Figure 4.9, which fits the experimental data very well. The magnitude of the leak current is determined by the connection between the wire bonds and the bond pads. This varies from reservoir to reservoir due to the inconsistency of the wire bonding process. The greater the number of wire bonds made to the pad, the greater the damage to the silicon oxide insulating layer beneath the pad, and the lower the resistance of the path through the silicon. The magnitude of the silicon resistance determines the overall size of the spectrum, which fits well with the observation that the overall size of the spectrum depends only on which reservoir is being measured. For any particular reservoir the resistance and capacitance of the path through the silicon were found to be independent of reservoir contents, as expected. The best fit resistance for each reservoir remained constant within 3% during all experiments and the capacitance was constant within 10%.

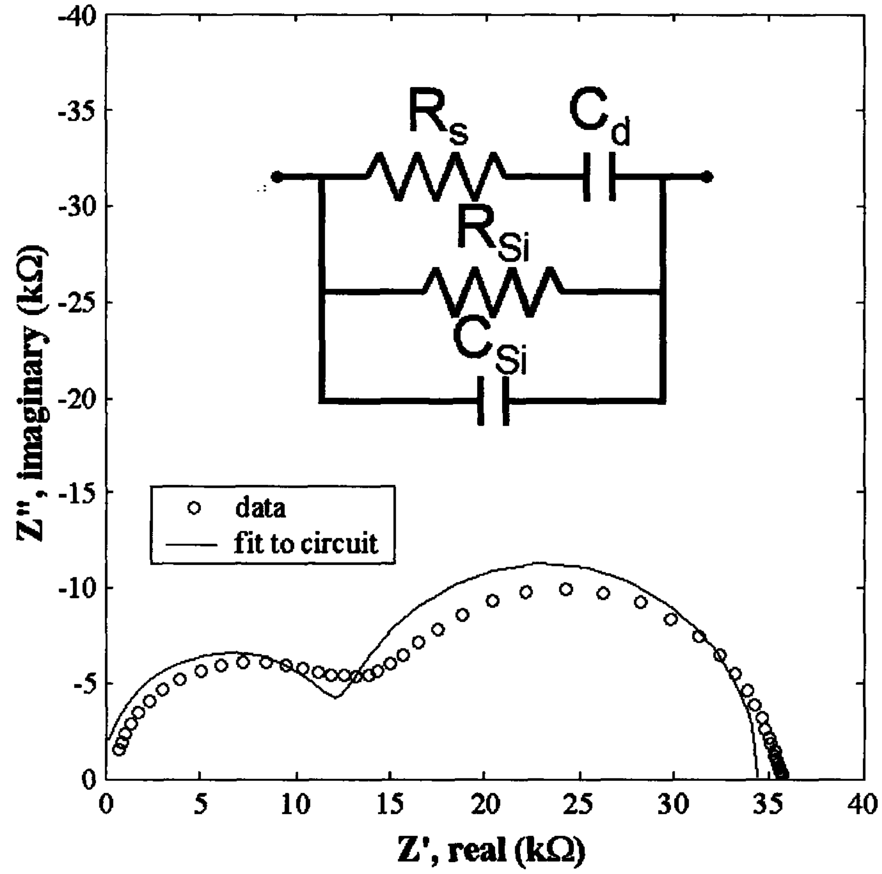

Figure 4.9. Equivalent circuit and Cole-Cole plot of experimental data and best fit to circuit for MEMS drug delivery device reservoir filled with 0.1x PBS.

The solution resistance depends on the ionic strength of the solution and determines the position of the inflection point between the semicircles. This fits well with the initial observation that the position of the inflection point depends only on the contents of the reservoir and not on which reservoir is measured. Some depression of the data from the ideal fit was observed, but again, a reasonably good fit was obtained without the substitution of a CPE for the capacitive elements. The average best fit solution resistance and double layer capacitance of the device reservoirs are given in Table 4.2. The double layer capacitance is of the correct order of magnitude, a factor of 10^4 smaller than that observed for the 100x scale model. The measured solution resistance is lower than that calculated using the formula for resistance of a square pyramid by a factor of 0.86 ± 0.02, as opposed to the factor of 0.95 ± 0.01 observed for the macromodel. This is likely due to fringing at the edges of the electric field, which is more significant in smaller systems. Taken together, these observations demonstrate the validity of the equivalent circuit of Figure 4.9, giving us a good understanding of the physical system.

Table 4.2. Solution resistance and double layer capacitance of microreservoirs filled with PBS.

PBS concentration	predicted solution resistance (kΩ)	measured solution resistance (kΩ)	measured double layer capacitance (nF)
1.0x	2.13	1.79 ± 0.12	3.54 ± 0.79
0.5x	4.01	3.68 ± 0.44	2.50 ± 0.62
0.1x	18.6	16.0 ± 4.7	1.9 ± 1.6

4.5. Monitoring drug release by impedance measurements

Once the equivalent circuit describing the physical system was well understood, it was desired to demonstrate that the sensors allow us to monitor the rate of drug release from a MEMS device reservoir in real time. The impedance measurement during release of mannitol, a model drug, from a device reservoir is shown in Figure 4.10a and b, as a succession of Cole-Cole and Bode plots. The impedance before opening the reservoir is similar to that observed for reservoirs full of air, which is expected because mannitol is a semicrystalline solid with negligible conductivity and there is no electrolyte present for conduction. After opening the reservoir, the impedance changes gradually from the single semicircle characteristic of the RC parallel circuit to the overlapping double semicircle characteristic of the circuit in Figure 4.9. The solution resistance drops as the saline solution provides an ever larger low resistance path between the electrodes, and the double layer capacitance increases as the area of the electrodes in contact with solution increases. Successive data fits to this circuit give the solution resistance and double layer capacitance vs. time shown in Figure 4.10c. This corresponds to the dissolution of the mannitol and the advance of the PBS solvent front into the reservoir. The dissolution is largely complete after 90 minutes.

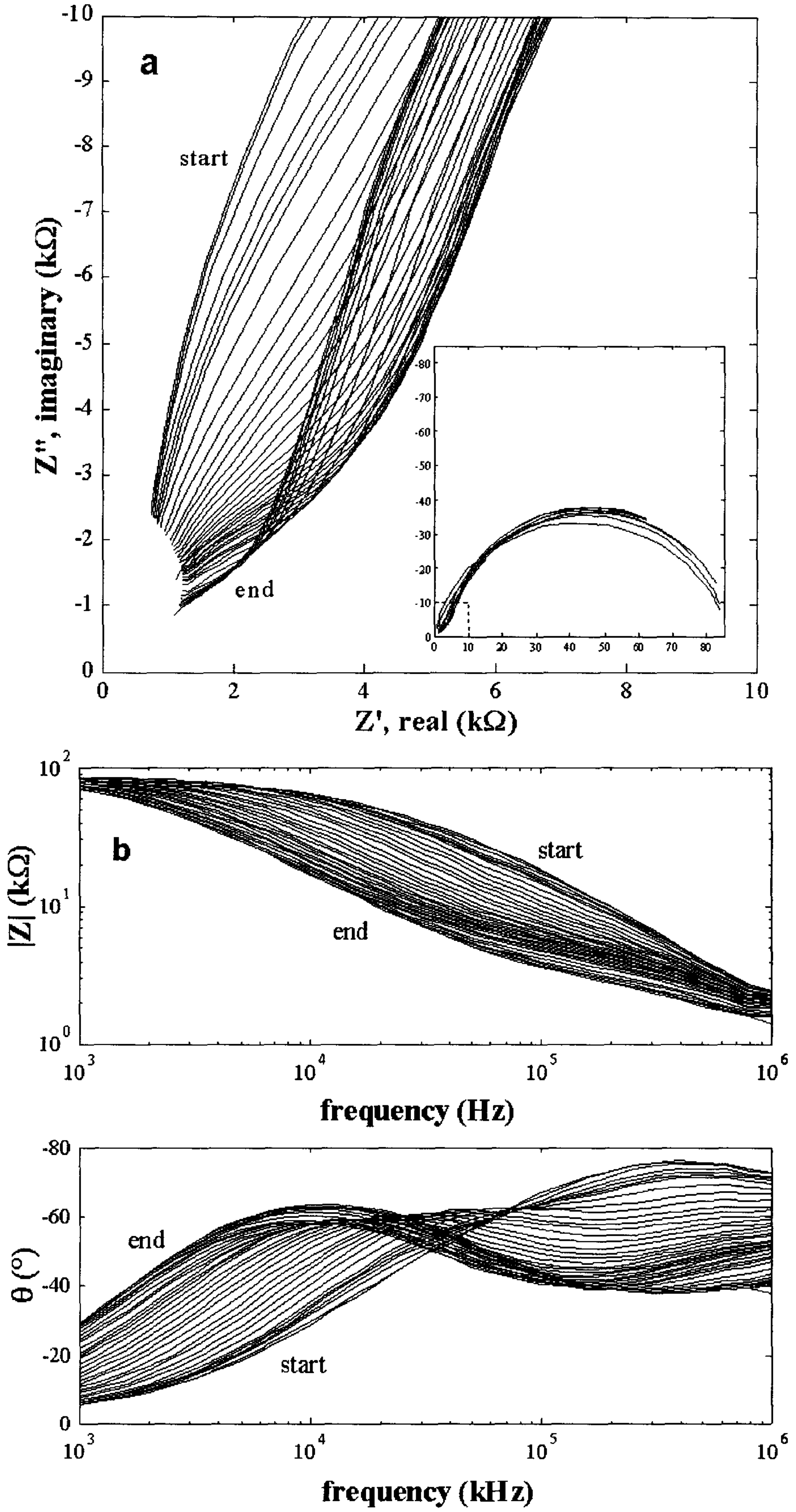
a
start
end
Z'', imaginary (kΩ)
Z', real (kΩ)
-10
-9
-8
-7
-6
-5
-4
-3
-2
-1
0
0
2
4
6
8
10
-80
-70
-60
-50
-40
-30
-20
-10
0
0
10
20
30
40
50
60
70
80
b
start
end
|Z| (kΩ)
10^2
10^1
10^0
10^3
10^4
10^5
10^6
frequency (Hz)
end
start
θ (°)
-80
-60
-40
-20
0
10^3
10^4
10^5
10^6
frequency (kHz)

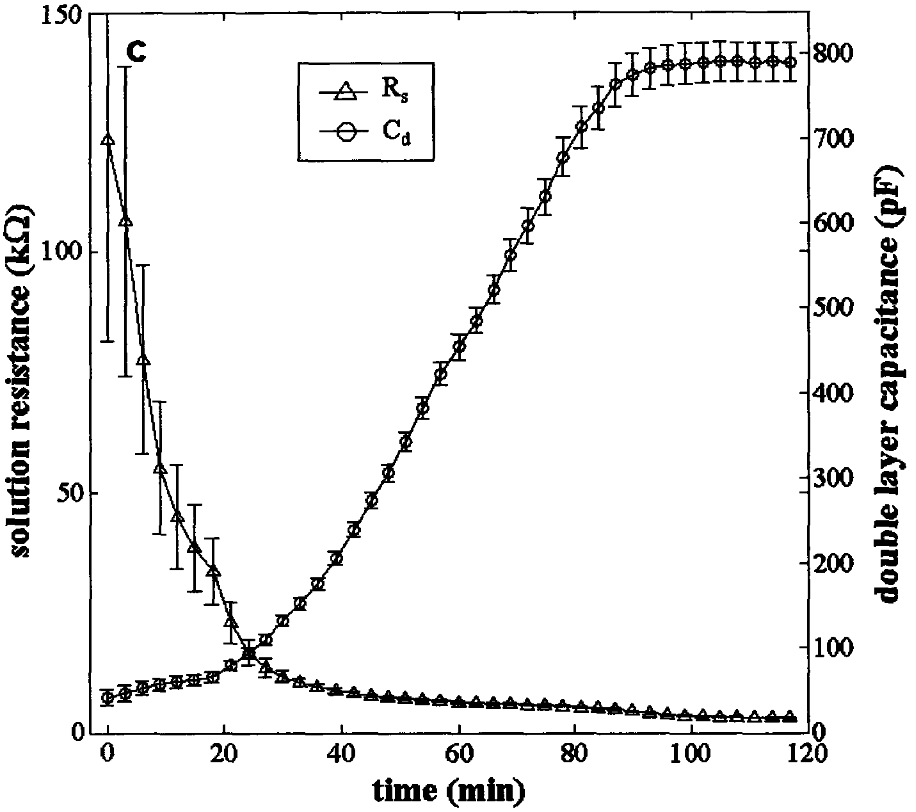

Figure 4.10. Impedance of MEMS device reservoir during release of mannitol into 1.0x PBS. **a)** series of Cole-Cole plots over time, **b)** series of Bode plots over time, and **c)** series of best fits of solution resistance and double layer capacitance over time.

Further *in vitro* release experiments with radiolabeled mannitol, described in chapter 6, show that the rate of drug release measured by the sensor corresponds well to the rate of drug released measured by scintillation counting of the release medium. A detailed transport model to predict dissolution rate and the corresponding solution resistance and double layer capacitance is presented in chapter 7. However, as an initial comparison, a first order estimate of the expected time for dissolution can be made by considering the dissolution and diffusion of a solid in one dimension[10,11]. The diffusion equation gives the following equation for C(x,t)

$$\partial C/\partial t = D\, \partial^2 C/\partial x^2;\quad C(x,0) = 0;\quad C(0,t) = C_{sat};\quad C(\infty,t) = 0$$

where C_{sat} is the solubility of the compound in solution and D is the diffusivity. This can be solved for the flux at the interface as a function of time[12],

$$N_x|_{x=0} = -D\, dC/dx|_{x=0} = C_{sat}\, (D/\pi t)^{1/2}$$

A mass balance at the interface between solid and liquid can be written as

$$-AD\, dC/dx|_{x=0}\, dt = AC_s dz$$

where A is the area exposed to solution, C_s is the density of the solid compound, and dz is the differential distance traveled by the interface in the time dt. Note that the equation for C(x,t) is only valid if the motion of the interface is slow compared to the formation of the concentration profile (pseudosteady state). If we substitute the expression for the flux at the interface into the interfacial mass balance, we obtain an expression for the distance traveled by the interface (the depth of penetration of solvent into the reservoir) as a function of time

$$z(t) = 2(C_{sat}/C_s)(Dt/\pi)^{1/2}$$

Substituting appropriate values for the physical parameters ($C_{sat} = 0.18$ g/cm^3, $C_s = 1.5$ g/cm^3, $D = 10^{-5}$ cm^2/s, $z \sim 200$ µm for a partially filled reservoir), we obtain an estimated time for dissolution of ~35 minutes, which is the same order of magnitude as the experimentally observed dissolution time. This initial release experiment demonstrated the ability of the equivalent circuit analysis to describe both static and dynamic sensor output for monitoring of release of drug from the device microreservoirs.

4.6. Conclusions

The drug delivery MEMS device with an impedance-based sensor successfully monitored the release of drug from a device reservoir. The sensor output was related to the drug release rate by a simple equivalent circuit whose elements correspond to the physical characteristics of the system. The equivalent circuit was developed in two stages, by using a macroscale model of the sensor to understand the effects of electrode geometry, then measuring impedance in the microreservoirs and adding elements to describe the bypass current through the silicon substrate. The equivalent circuit allowed us to extract the two key parameters, solution resistance and double layer capacitance, from the overall impedance spectrum. The solution resistance and double layer capacitance were measured as functions of time during release of the drug. These two parameters are functions of the degree of penetration of solution into the reservoir during drug release, which can be related to the rate of transport of drug from the device.

4.7. References

---

1. A. M. Johnson, D. R. Sadoway, M. J. Cima, and R. Langer, Design and testing of an impedance-based sensor for monitoring drug delivery, (accepted to *Journal of the Electrochemical Society*).
2. Y. C. Wu, W. F. Koch, W. J. Hamer, and R. L. Kay, Review of electrolytic conductance standards, *Journal of Solution Chemistry*, **16**, 985-997 (1987).

3. S. L. Schiefelbein, N. A. Fried, K. G. Rhoads, and D. R. Sadoway, A high-accuracy, calibration-free technique for measuring the electrical conductivity of liquids, *Review of Scientific Instruments*, **69**, 3308-3313 (1998).
4. Y. C. Wu and W. F. Koch, Absolute determination of electrolytic conductivity for primary standard KCl solutions from 0 to 50°C, *Journal of Solution Chem*istry, **20**, 391-401 (1991).
5. P. Atkins, *Physical Chemistry*, p. 834-837, W. H. Freeman & Co., New York (1994).
6. P. Vanýsek, Equivalent conductivity of electrolytes in aqueous solution, in *CRC Handbook of Chemistry and Physics*, 73rd ed., D. R. Lide, Chief Editor, p. 5-110, CRC Press, Boca Raton, FL (1992).
7. A. J. Bard and L. R. Faulkner, *Electrochemical Methods*, p. 376, Wiley, New York (1980).
8. Z. Lukacs, The numerical evaluation of the distortion of EIS data due to the distribution of parameters, *Journal of Electroanalytical Chemistry*, **432**, 79-83 (1997).
9. A. K. Jonscher, *Dielectric Relaxation in Solids*, p.81, Chelsea Dielectrics Press, London (1983).
10. A. van Hook, *Crystallization Theory and Practice*, p.130, Reinhold, New York (1961).
11. J. Christoffersen and M. R. Christoffersen, Kinetics and mechanisms of crystal growth and dissolution, in *The Experimental Determination of Solubilities*, G. T. Hefter and R. P. T. Tomkins, Editors, p.77-98, Wiley, New York, (2003).
12. W. M. Deen, *Analysis of Transport Phenomena*, p.91, Oxford University Press, New York (1998).

5. *In Vitro* Release Monitoring

Once a suitable equivalent circuit was found to describe the behavior of the impedance sensors, the sensors were used to monitor release of air and mannitol from device reservoirs *in vitro*. The *in vitro* tests provided a correlation between sensor output (solution resistance and double layer capacitance) and the rate of drug release and characterized the typical release profile and variability. A metric based on the rate of change of the solution resistance was developed to draw a consistent cutoff for the completion of release. Several experiments were performed, which can be grouped into five categories:

1. Release of air into deaerated PBS (4 experiments)
2. Release of mannitol, backed by eicosane wax, into PBS (2)
3. Release of radiolabeled mannitol into stirred PBS (3)
4. Release of radiolabeled and unlabeled mannitol into PBS in a laminar flow cell (3 radiolabeled, 1 unlabeled)
5. Release of radiolabeled mannitol into PBS during leak testing of devices prior to implantation (4)

The measured release times for all experiments were between 80 and 290 minutes, depending on the specific release conditions. The release of air and of mannitol into a stirred volume of PBS was the most reproducible, while release of mannitol in the flow cell and during leak testing were more variable. The variability of release times during leak testing was expected because release occurred through membranes that had been damaged during processing, not corroded open. The variability of release times between the different flow cell experiments is likely due to differences in the corrosion and opening of the membranes. It is thought that release into a stirred volume of PBS was more consistent because the rapid motion of the liquid around the membrane helped break the corroded membrane and fully open the reservoirs.

Scintillation counting of the release medium provided an independent measure of the release time. The sensors monitor the dissolution of solid mannitol, not the dilution of dissolved mannitol out of the reservoir, so some lag time was expected. For the release of mannitol into stirred PBS, the release times measured by the sensors were in good agreement with the release times measured by scintillation counting, differing by only 5-10 minutes. For release of mannitol in the flow cell, a significant lag time was observed, with the release time measured by scintillation approximately 1 hour longer (out of 3-5 hours) than the time measured by the sensors. The difference in lag times between the flow cell experiments and the experiments in a stirred volume of PBS is explained by the experimental setup. In the beaker, aliquots of PBS were removed for scintillation counting, while in the flow cell, fresh PBS continually flowed past the reservoirs. The end of the release during release in a beaker was when the concentration of radioactivity in the bulk solution did not change with time. The sensitivity of the measurements at high radioactivity concentrations meant that the release of the last 2-3% of mannitol from the reservoir was lost in noise. However, in the flow cell the end of release was when the concentration of radioactivity in the effluent decayed to background levels. The flow cell measurements were much more sensitive, capable of detecting as little as 0.01-0.1% of the total mannitol loaded into a reservoir. The flow cell scintillation measurements were therefore able to detect the slow dilution of very small amounts of mannitol from the reservoirs following the dissolution of the solid.

The *in vitro* release experiments are described in detail by category in the results sections below, and compared with one another in the discussion section. The results presented in this chapter and the *in vivo* results presented in chapter 6 are currently being prepared for publication.

5.1. Experimental

A total of seventeen separate release experiments are described, which are grouped into five categories: air dissolution into deaerated PBS, mannitol backed by eicosane into PBS, radiolabeled mannitol into PBS, radiolabeled and unlabeled mannitol into PBS in a flow cell, and radiolabeled mannitol into PBS during leak testing before implantation. The experimental protocols were relatively similar for each type of experiment, so it is convenient to divide the discussion of experimental details according to the type of procedure, as follows:

1. Packaging of devices
2. Release testing setup
3. Flow cell setup
4. Corrosion protocol
5. Impedance monitoring protocol
6. Data analysis

5.1.1. Device packaging

Devices were fabricated and packaged according to the protocols described in chapter 3. Table 5.1 lists the particular wafer, device, and reservoir numbers for each experiment. The air and mannitol/wax release experiments were performed using devices from wafer #110601-5, which had no gold membranes to seal the reservoirs. The reservoirs were sealed using small pieces of pressure sensitive 9144 tape. The tape was removed with tweezers to open the reservoirs.

For air release, empty reservoirs were sealed by spreading thin lines of epoxy between the reservoirs and pressing a piece of glass coverslip over the top. Care was taken to prevent the epoxy from spreading into the reservoirs. Devices for mannitol release experiments were loaded using the melt filling process described in section 3.3.1. Devices L4B3, L4B4, and Flow2 were weighed on the microbalance after each reservoir was filled with mannitol, giving a precisely known amount of mannitol in each reservoir, to within about ± 2 μg. Later devices F2, N4, N6, N8, N10, N14, and N16 were weighed after loading the entire device with mannitol to prevent damage to the membranes during multiple heating and cooling cycles. Each reservoir was filled with approximately the same amount of mannitol. The total loading was then divided by the number of reservoirs to give an approximate amount of mannitol per reservoir, to within about ± 7 μg. For the mannitol/wax device, small pieces of eicosane ($C_{20}H_{42}$, mp 36-38°C, Sigma) were melted over the mannitol in the reservoirs, and excess wax was removed with a razorblade.

Devices were then sealed with epoxy and a small piece of glass coverslip. Capillary action drew the epoxy into any reservoir spaces that had not been filled with mannitol or wax. Reservoirs were sufficiently filled that the amount of reservoir volume occupied by epoxy was less than 10%. In the case of L4B3, the amount of mannitol in the reservoirs was high enough (41.2 μg in well 7) that the coverslip did not fit flush with the back surface of the device. Additional epoxy was added to seal the reservoirs despite the slight mounding of the mannitol out of the back of the reservoirs.

Table 5.1. Wafer and device details for *in vitro* release monitoring experiments.

experiment	wafer #	device #	reservoir #'s	notes
air	110601-5	R4B3	B78,B56,A56,A78	sealed with tape, wax in other reservoirs
mannitol/wax	110601-5	L4B4	B12,A34	sealed with tape
C^{14} mannitol in beaker	020303-1	F2	white11, black15	nitride etched 900 s in Feb. 2004
	020303-1	Flow2	well10	nitride etched 800 s in July 2003
C^{14} / unlabeled mannitol in flow cell	020303-1	L4B3	well7	nitride etched 800 s in July 2003
	020303-1	N8	red2, blue7	nitride etched 900 s in Nov. 2003
	020303-1	N10	red3	nitride etched 900 s in Nov. 2003
C^{14} mannitol leak tests before implantation	020303-1	N4	red1	nitride etched 900 s in Nov. 2003
	020303-1	N6	black15	nitride etched 900 s in Nov. 2003
	020303-1	N14	blue6	nitride etched 900 s in Nov. 2003
	020303-1	N16	red3	nitride etched 900 s in Nov. 2003

5.1.2. Release testing setup

The release testing setup was similar for all but the flow cell release experiments. The device was connected to the potentiostat and immersed in a container of PBS. A reservoir was then opened and monitored until the impedance and/ or scintillation measurements stopped changing.

The dissolution of air required that the PBS be deaerated prior to the experiment. To prepare deaerated PBS, DI water was brought to a boil to reduce the dissolved gases. At the same time, 50 mL of 10x PBS was brought to a boil in a 500 mL volumetric flask. The DI water was added to the volumetric flask to make 1x PBS solution (the effect of the thermal expansion of water was neglected). The hot solution was immediately poured into an autoclavable orange cap culture medium flask (leaving no head space), tightly sealed, and allowed to cool to room temperature. For the release experiment, the device was connected to the impedance spectrometer and suspended in an empty beaker. One reservoir was opened by removing the tape seal over the top of the reservoir. At time zero, the deaerated PBS was unsealed and poured into the empty beaker to completely cover the device and nearly fill the beaker. The beaker was quickly covered with parafilm and a glass plate to slow the absorption of gases from the atmosphere during the release experiment. Of the four air release experiments, all but #B78 were performed by UROP Priya Shah.

The release of mannitol backed by eicosane wax was performed in a similar manner to the release of air. The device was connected to the impedance spectrometer and suspended in a beaker of PBS. At time zero, the tape seal was removed with tweezers and the device submersed in the PBS solution. The beaker was covered with parafilm and a glass plate to slow evaporation of the solution.

The release of radiolabeled mannitol into PBS was slightly different because the reservoirs were opened by corrosion (with the exception of F2 black15, which had no membrane when examined under the microscope, and therefore released immediately upon immersion in solution) and the solution was sampled regularly for scintillation counting. The volume of solution was carefully measured to allow calculation of total radioactivity released (20 mL solution for device Flow2 and 25 mL for device F2). The solution was stirred by a magnetic stir bar for the duration of the experiment. The device activation wires were connected to the potentiostat and a platinum wire was placed in the solution to act as a reference electrode. The device was submersed in the solution and the corrosion protocol was started at time zero. Once corrosion was complete, the impedance monitoring wires were connected to the impedance spectrometer and monitoring began, usually about 18 minutes after the beginning of the corrosion protocol. Concurrently, 0.5 mL samples were removed at 5 minute intervals, replaced by 0.5 mL fresh PBS solution. The scintillation sampling interval was extended to every 10-15 minutes after the first half hour of monitoring. The solution was covered with parafilm to prevent evaporation during the experiment. Monitoring continued until the sensor output stopped changing and the scintillation counts began to decline. Scintillation samples were mixed with 5 mL scintillation fluid (ScintiSafe Plus, Fisher Scientific, Pittsburgh, PA) and analyzed on a Packard 2200CA TriCarb Liquid Scintillation Analyzer (Perkin-Elmer Life Sciences, Downers Grove, IL) for 5 minutes each using protocol 3 for C^{14}.

The leak test monitoring experiments served two purposes. The primary purpose was to determine which reservoirs had membrane defects prior to implantation, in order to seal them with epoxy and prevent background leaks during the *in vivo* experiment. However, during the leak testing one reservoir on each device was connected to the impedance spectrometer to monitor the rate of mannitol release during the test. Examination of the devices under the microscope led to identification of reservoirs most likely to leak during the test. The data were expected show a wide range of release times because the reservoirs were open to varying degrees due to membrane defects. Also, the scintillation data was not expected to match the impedance monitoring because multiple reservoirs were leaking at the same time.

Devices were leak tested in petri dishes filled with either 30 mL (for device N4) or 40 mL PBS. Petri dishes were used instead of beakers to avoid bending the wires and causing work hardening of the metal before implantation. Devices were connected to the impedance spectrometer and submersed in the solution at time zero. Scintillation samples were taken at regular intervals, stirring the PBS solution slightly by flowing solution in and out of the pipette tip before each sample. Each sample was replaced by an equal volume of fresh PBS solution. Impedance monitoring continued until the impedance stopped changing with time, and scintillation sampling continued until the radioactivity leveled off.

5.1.3. Flow cell setup

Four release experiments were performed in the laminar flow cell depicted in Figure 5.1. PBS solution flowed through the channel over the face of the device. The device was clamped in place by a backing plate with four screws. A neoprene gasket (0.5mm uncompressed thickness, 50 durometer, O. G. Supply, Inc., Corona, CA) sealed the face of the device to the edge of the flow cell opening. Detailed schematic drawings of the flow cell are given in appendix 10.6.2.

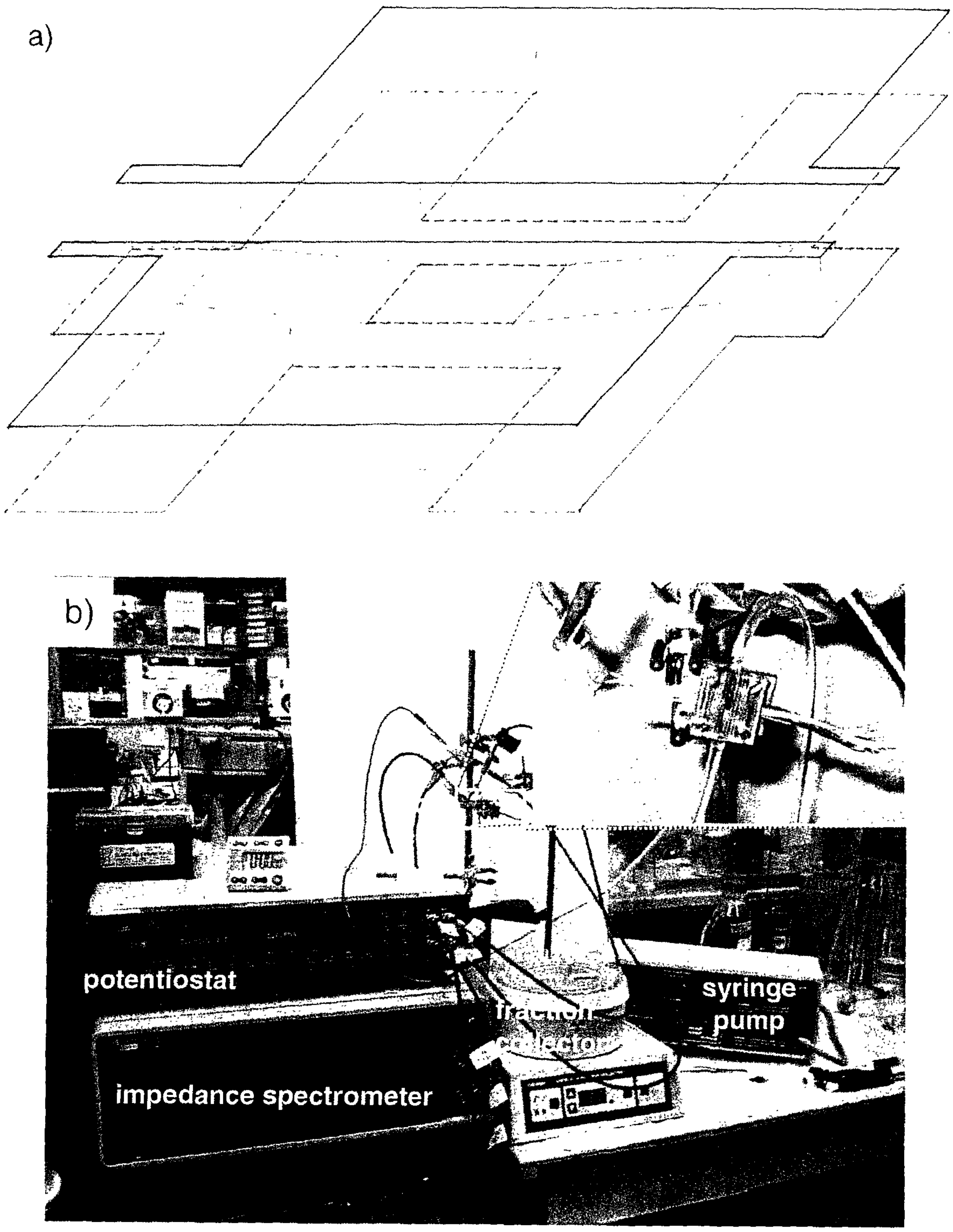

Figure 5.1. The laminar flow cell. **a)** schematic drawing of the flow cell channel, **b)** picture of the flow cell setup with magnified view of the flow cell with a MEMS device connected to the impedance spectrometer for monitoring.

The design allowed the eight reservoirs in the center of the chip to be wet while the rest of the device was not exposed to solution. The top of the cell was acrylic to allow observation of the chip face during testing and alignment. A platinum wire reference electrode was inserted into the effluent tube for the corrosion step. A steady flow of PBS was maintained by a syringe pump (Harvard Apparatus syringe infusion pump model 2620, with Beckman Dickenson plastipak 50 cc syringes) and the effluent was collected by a fraction collector (Bio-Rad fraction collector model 2110). An aliquot of 0.5 mL effluent was taken from each fraction for scintillation counting.

Four reservoirs were successfully opened and monitored in the flow cell. L4B3well7 released unlabeled mannitol into PBS flowing at 1.1 mL/min. The other three reservoirs, N8red2, N10red3, and N8blue7, released C^{14} radiolabeled mannitol into PBS flowing at 0.2 mL/min. Reservoir N8blue7 was partially obscured by the flow cell gasket and was ½ - ¾ exposed to solution rather than fully open, slowing the release. The scintillation data was adjusted to account for the length of time necessary for solution to travel from the chip face to the fraction collector. Difficulty aligning the flow cell and getting a good seal without cracking the device reduced the amount of data collected in the flow cell.

5.1.4. Corrosion protocol

The corrosion protocol for opening device reservoirs was developed by Rebecca Shawgo and adapted by Yawen Li. There are four inputs to the potentiostat for electrode connections: working, counter, reference 1 and reference 2. The reservoir membrane was connected to the working electrode, which was tied to reference 2. The counter electrode input was connected to the large gold counter electrode on the device surface. Finally, the reference 1 input was connected to a platinum wire immersed in the solution for reference.

The protocol had three stages: a precleaning step, a diagnostic scan, and a corrosion step. The precleaning step applied a triangle wave voltage between -0.8 and -1.3 V vs. platinum, to remove organics such as adsorbed proteins from the surface. The precleaning step can be skipped for tests in PBS but is essential for successful corrosion *in vivo* or in serum. Ten cycles were applied at a rate of 50 mV/s. Figure 5.2a shows a typical current and voltage vs. time plot for the precleaning step. As the surface was cleaned, the magnitude of the current decreased until each cycle was of similar magnitude. If the magnitude of the current was still decreasing after 10 cycles, another 10 cycles were applied before proceeding to the diagnostic scan. The precleaning step was performed on all reservoirs for consistency despite the lack of proteins in the PBS solution.

The diagnostic scan applied a triangle wave voltage between 0 and 1.5 or 1.75 V vs. platinum at a rate of 50 mV/s for 4 cycles, as shown in Figure 5.2b. The diagnostic scan revealed the position of the corrosion and depassivation peaks when plotted as current vs. voltage as depicted in Figure 5.2c. There was considerable variation in the size of the peaks between reservoirs and sometimes the depassivation peak was not observable. If the connections had broken or shorted, the diagnostic scan was Ohmic and no peaks were seen.

The corrosion step applied a square wave voltage between the depassivation and corrosion voltages observed in the diagnostic scan, typically 0-0.4 V to 0.8-1.2 V. It applied 600 cycles at a rate of 1 Hz. A typical corrosion current and voltage vs. time plot is shown in Figure 5.2d. The plots do not look like square waves because the sampling rate for the potentiostat I/O card was too slow to capture the shape of the curve – the equipment is capable of applying a voltage much faster than it can measure and record it. The shape of the corrosion curve is therefore difficult to examine for signs of reservoir opening. In some instances there was a sudden drop in the magnitude of the current, but in other cases there was no apparent drop when the reservoir opened.

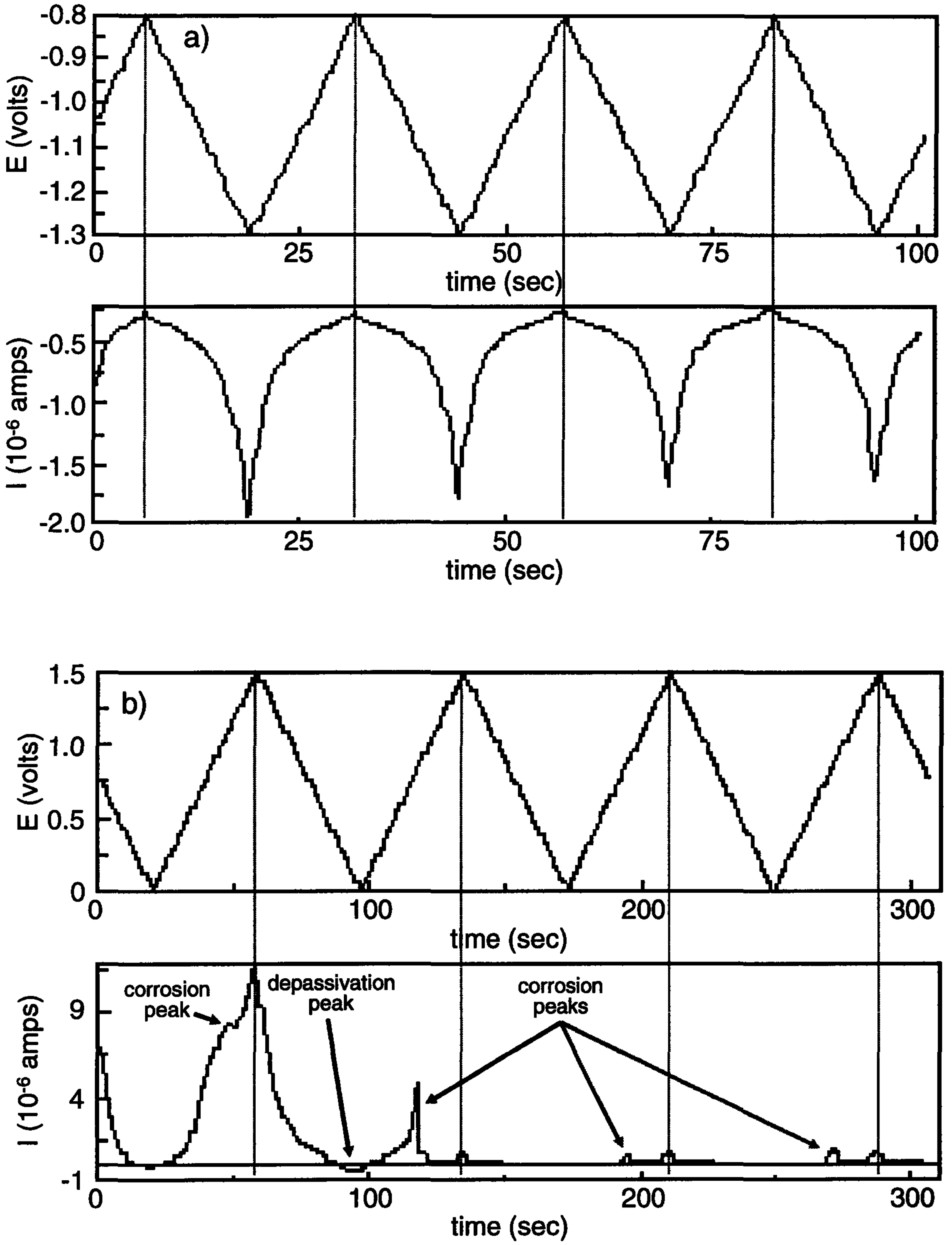

Figure 5.2a-b. The corrosion protocol for opening device reservoirs; **a)** precleaning step plotted as current and voltage vs. time, **b)** diagnostic scan plotted as current and voltage vs. time.

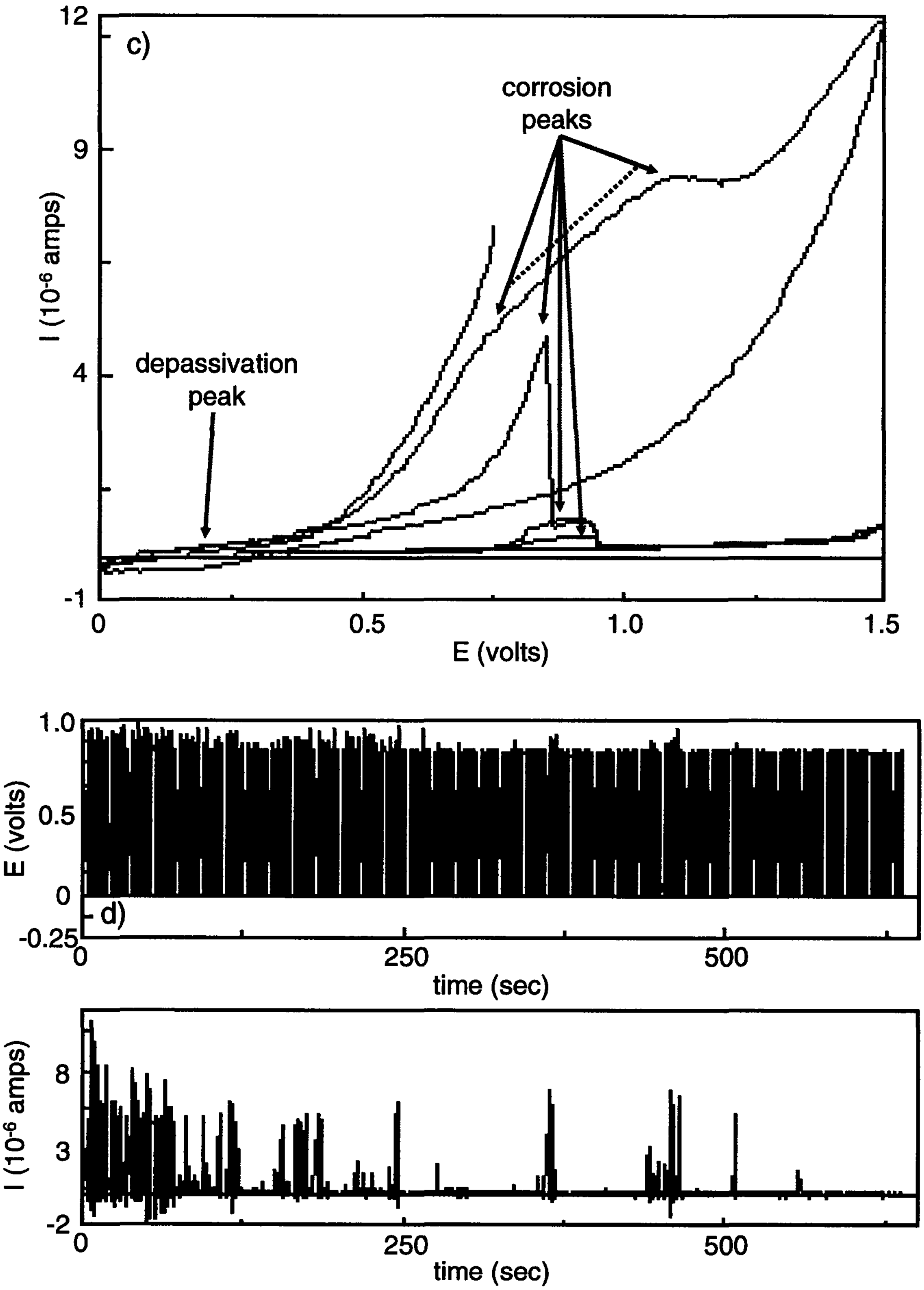

Figure 5.2c-d. The corrosion protocol for opening device reservoirs; **c)** diagnostic scan plotted as current vs. voltage showing corrosion and depassivation peaks, **d)** corrosion step plotted as current and voltage vs. time.

5.1.5. Impedance monitoring protocol

The impedance of the sensor in the reservoir was measured repeatedly during each release. The impedance spectrometer was connected via the potentiostat to the two electrodes within the reservoir. The reference 1 input was tied to the counter electrode input, and reference 2 input was tied to the working electrode input. The two-electrode impedance was then measured at frequencies between 1 and 1000 kHz, 10 logarithmic steps per decade. The dc offset was set to zero vs. open circuit and the amplitude of the applied ac voltage was 10 mV. The measurement at each frequency was integrated for 5 cycles with no delay between frequency measurements. Additional potentiostat settings included: current ranges = auto, transition frequency = 5000, bandwidth = C, low pass filter = on, bias rejection = on, and attenuator = auto. Additional gain phase analyzer (impedance spectrometer) settings included: source mode = V2/V1, current mode = V1, V1 (Channel 1) and V2 (Channel 2) range = auto, coupling = dc, input = single, outer = floating, and location = N/A.

An impedance measurement was taken before each reservoir was opened to provide a baseline impedance for determination of the silicon resistance and capacitance. Once the reservoir was open, the impedance measurements were run in batch mode so that the computer automatically began a new measurement as soon as the previous one finished. The equipment took 25 s to prepare for each measurement, and the total time for each measurement was 2.95 min, giving impedance measurements approximately 3 minutes apart. Once the impedance was no longer changing rapidly, the batch mode was changed to include a 15 minute or 1 hour pause between each measurement.

5.1.6. Data analysis

Each release gave a set of impedance sweeps vs. time. Each impedance measurement was fitted to the equivalent circuit developed in chapter 4 to determine the solution resistance and double layer capacitance of the reservoir over time. The first measured data point in each sweep, at 1000 kHz, was always excluded from fitting because it was at the high end of the measurable range and was often anomalously low.

First, the impedance of the unopened reservoir was fitted to a two element parallel RC circuit to determine the silicon resistance (R_{Si}) and silicon capacitance (C_{Si}). This gave a better fit to the unopened measurement than the four element circuit because the reservoir resistance is very high and the double layer capacitance is nonexistent. The best fit values from the two element circuit were then entered in the 4 element circuit as fixed values for subsequent data fits. The fitting program then gave the best fit values for solution resistance (R_s) and double layer capacitance (C_d) with time, as well as the fit error associated with each. These were recorded as the best fixed fit values and the fit errors.

Each impedance measurement was then also fit to the four element circuit while allowing the values of R_{Si} and C_{Si} to float to their best fit values. The best fit values of all four circuit elements were recorded as the best float fit values. The best float fit values of R_{Si} and C_{Si} were usually similar to the best two element fit values (within a factor of 2) but not the same. The values of R_s and C_d were then recorded as the best float fit values. The best float fit and fixed fit values were then averaged to give final values of R_s and C_d at each time point. The fixed vs. floating fit error associated with each value was calculated as the absolute value of $(R_{s,fixed} - R_{s,float})/2$ and $(C_{d,fixed} - C_{d,float})/2$ respectively. The reported error bars for each point were either the fixed vs. floating fit error or the fit error (reported by the fitting program during the fixed fits), whichever was larger. The error bars of the first few measurements were typically quite large because the fitting program does not work very well when R_s is very high and C_d is very low.

A metric was developed to make the determination of the time of completion of release consistent between all data sets. The intuitive endpoint of release is simply when the impedance stops changing, that is, when the derivative with respect to time is zero. However, the solution resistance and double layer capacitance never stop changing entirely, so it is necessary to determine an appropriate threshold value of d/dt below which the impedance is essentially not changing. The best fit capacitance values show some unusual behavior as discussed in the results section, so the solution resistance was chosen for the determination of the end of release. The rate of change of the solution resistance (dR_s/dt) over time was calculated for the air and mannitol/wax data sets. An example plot of dR_s/dt is shown in Figure 5.3. The initial value of dR_s/dt for all data sets was on the order of 10-100 kΩ/min. The end of release as judged by eye corresponded well to the point where dR_s/dt had dropped by three or four orders of magnitude from its initial value. The cutoff point for the end of release as measured by the impedance sensors was therefore set to $dR_s/dt < 0.01$ kΩ/min.

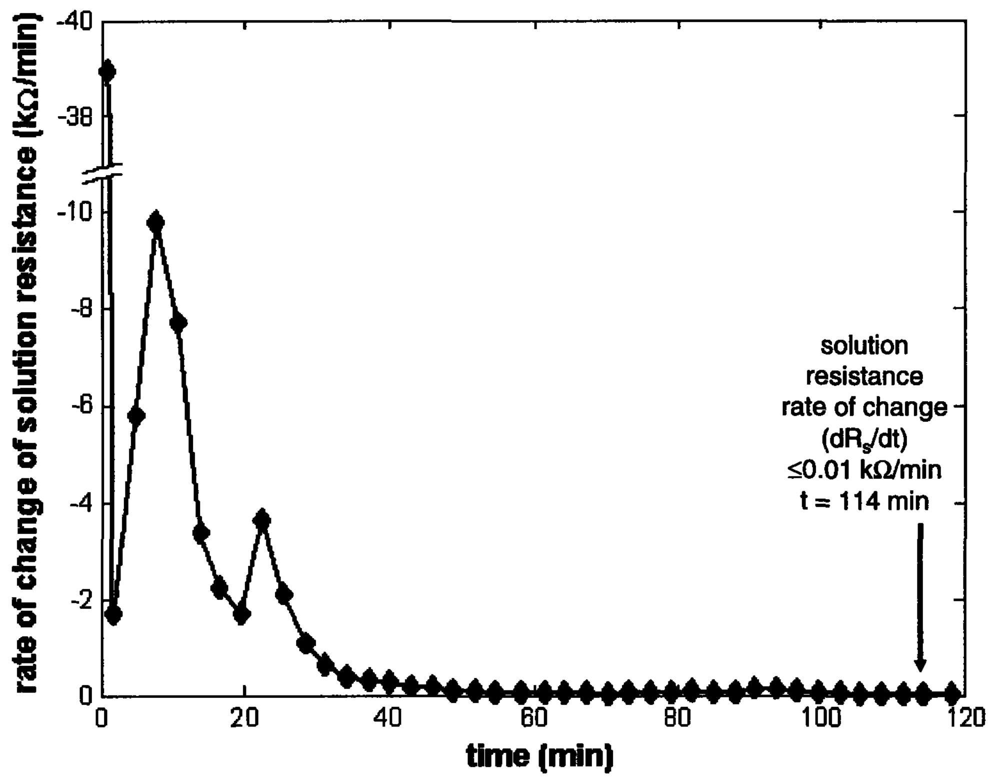

Figure 5.3. Rate of change of solution resistance (dR$_s$/dt) vs. time for device R4B3 reservoir B12 showing threshold for end of release.

5.2. Results and discussion

The results of each of the five categories of experiments are discussed below in separate sections, in the following order: dissolution of air into deaerated PBS, mannitol backed by eicosane into PBS, radiolabeled mannitol into stirred PBS, radiolabeled and unlabeled mannitol into PBS in the flow cell, and radiolabeled mannitol into PBS during leak testing before implantation.

5.2.1. Release of air into deaerated PBS

Four reservoirs full of air were released into deaerated PBS from device R4B3. Sets of impedance spectra for the each experiment may be found in appendix 10.4. Figure 5.4 shows the best fit solution resistance and double layer capacitance vs. time for each of the four experiments. The release times and the shape of the curves are similar for all four data sets, although the first data set, reservoir B78, is not as similar as the other three and has a shorter release time. This may be due to experimental differences since all but B78 were set up and monitored by Priya Shah. The degree of deaeration of the solution and the rate of adsorption of gases from the air would both affect the release time and could easily vary due to slight differences in procedure.

If the first release is excluded, the average release time for air into deaerated PBS is 108 ± 3 min (including all four it is 102 ± 13 min), which is remarkably consistent between runs. These reservoirs were opened by removal of tape from over the reservoir rather than corrosion, which may leave portions of the gold membrane behind. The tape release method may have made the release times more reproducible than in experiments using corrosion to open the reservoirs. Each reservoir was examined before and after release through the transparent coverslip over the wide end of the reservoir. Microscopic examination confirmed that each reservoir was dry before release and wet after release (air bubbles appear lighter than PBS).

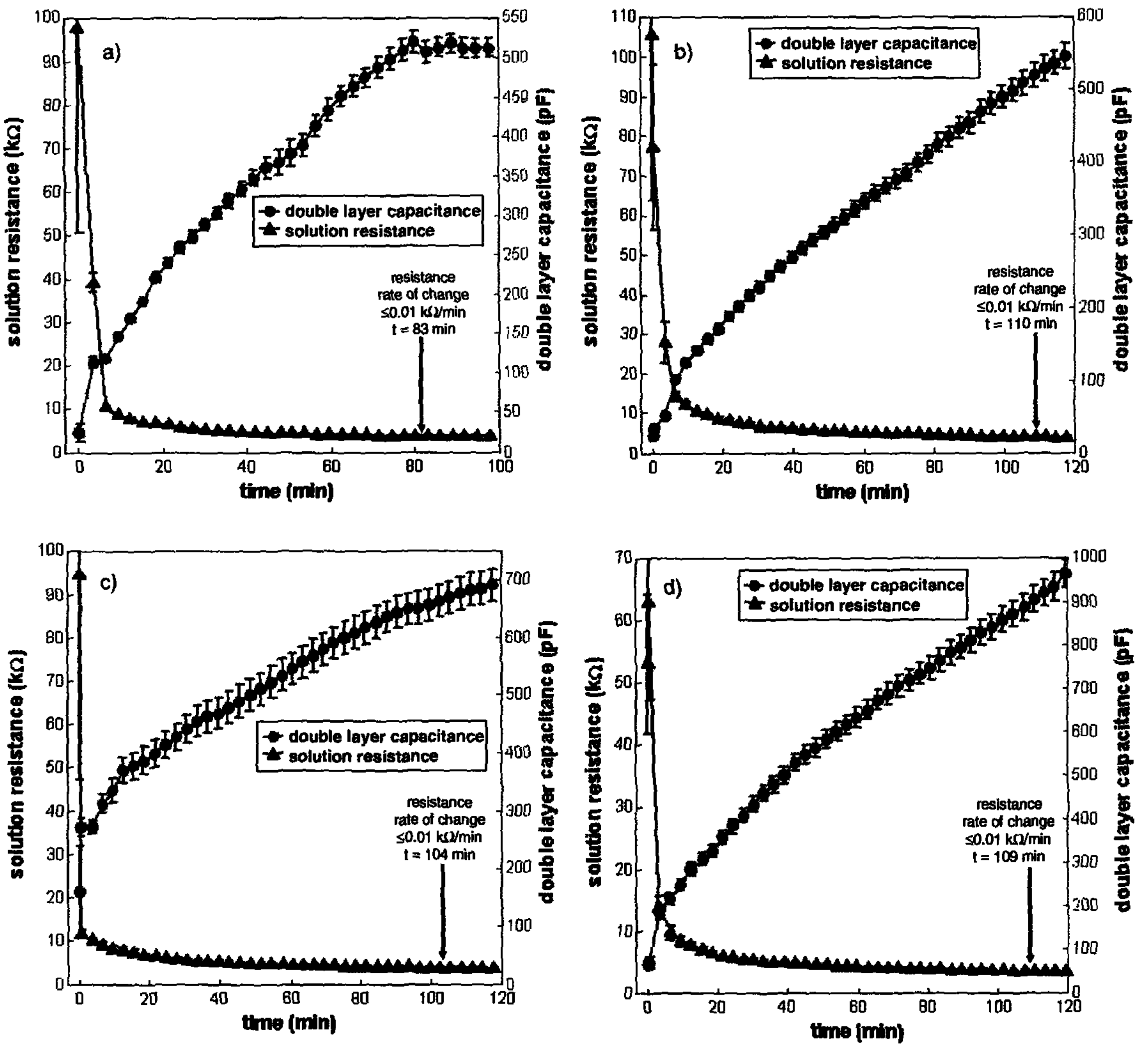

Figure 5.4. Best fit values of solution resistance and double layer capacitance during dissolution of air into deaerated PBS solutions from device R4B3, **a)** reservoir B78, **b)** reservoir B56, **c)** reservoir A56, **d)** reservoir A78.

Table 5.2 gives the electrical characteristics of each sensor and the measured release times. The 'end' values of the solution resistance and double layer capacitance are the values measured when the rate of change of the solution resistance drops below the threshold value of 0.01 kΩ/min. Despite the large variation in the silicon resistance and capacitance, which makes each set of impedance spectra appear quite different, the final solution resistance and double layer capacitance are relatively similar, with average values of 2.3 ± 0.1 kΩ and 650 ± 170 pF, respectively. The initial resistance and capacitance are more variable and have larger errors associated with them because of the difficulty in fitting the data to the 4 element circuit when the solution resistance is very high. Over the course of the experiment, the solution resistance was observed to decrease by two orders of magnitude and the double layer capacitance increased by one order of magnitude. The impedance of the reservoirs was monitored for a full 24 hours following the release, during which time the solution resistance did not change appreciably but the double layer capacitance slowly increased, over a period of 10-12 hours, by another order of magnitude to a value between 1100 and 1800 pF before leveling off. This gradual but significant increase in capacitance was not observed for any other type of release. However, the final capacitance values after 24 hours are much closer to the end values of capacitance seen for most other release experiments. One possible explanation for this behavior could be that small bubbles of air cling to the electrodes and do not dissolve immediately but are slowly displaced as the solution wets the gold surface.

Table 5.2. Reservoir sensor electrical characteristics and release times for the dissolution of air into deaerated PBS.

release	silicon resistance R_{Si} (kΩ)	silicon capacitance C_{Si} (pF)	solution resistance at start (kΩ)	double layer capacitance at start (pF)	solution resistance at end (kΩ)	double layer capacitance at end (pF)	release time (min)
B78	26	79	98	25	2.28	520	83
B56	41	81	110	24	2.40	519	110
A56	609	91	95	160	2.15	663	104
A78	49	94	63	68	2.28	887	109

5.2.2. Release of mannitol/wax into PBS

Two reservoirs were partially filled with mannitol and backfilled with insoluble eicosane wax before being released into a large volume of PBS. Figure 5.5 shows the best fit solution resistance and double layer capacitance over time for both release experiments and Table 5.3 gives the electrical characteristics and measured release times for each reservoir. The solution resistance decreases to a value of 3.21 ± 0.2 kΩ and the double layer capacitance rises steadily to 650 ± 150 pF. The release times are relatively consistent, averaging 100 ± 11 min. The solution resistance does not fall as far, and the double layer capacitance does not reach as high a value, as during most other release experiments. This is expected because the reservoir is partly full of insoluble wax, so only part of the reservoir electrodes are exposed to solution at the end of the release. Two additional device reservoirs were entirely filled with eicosane and monitored during immersion in PBS to show that the solution resistance and double layer capacitance would not change if the contents of the reservoir did not dissolve. The results of the eicosane wax 'release' experiments are discussed in appendix 10.4.1.

Table 5.3. Reservoir sensor electrical characteristics and release times for the dissolution of mannitol, backed by wax, into unstirred PBS.

release	amount mannitol (μg)	silicon resistance R_{Si} (kΩ)	silicon capacitance C_{Si} (pF)	solution resistance at start R_s (kΩ)	C_d, double layer capacitance at start (pF)	solution resistance at end R_s (kΩ)	C_d, double layer capacitance at end (pF)	release time (min)
B12	22.5	74	89	120	44	3.20	790	114
A34	23.2	25	87	42	48	3.23	501	92

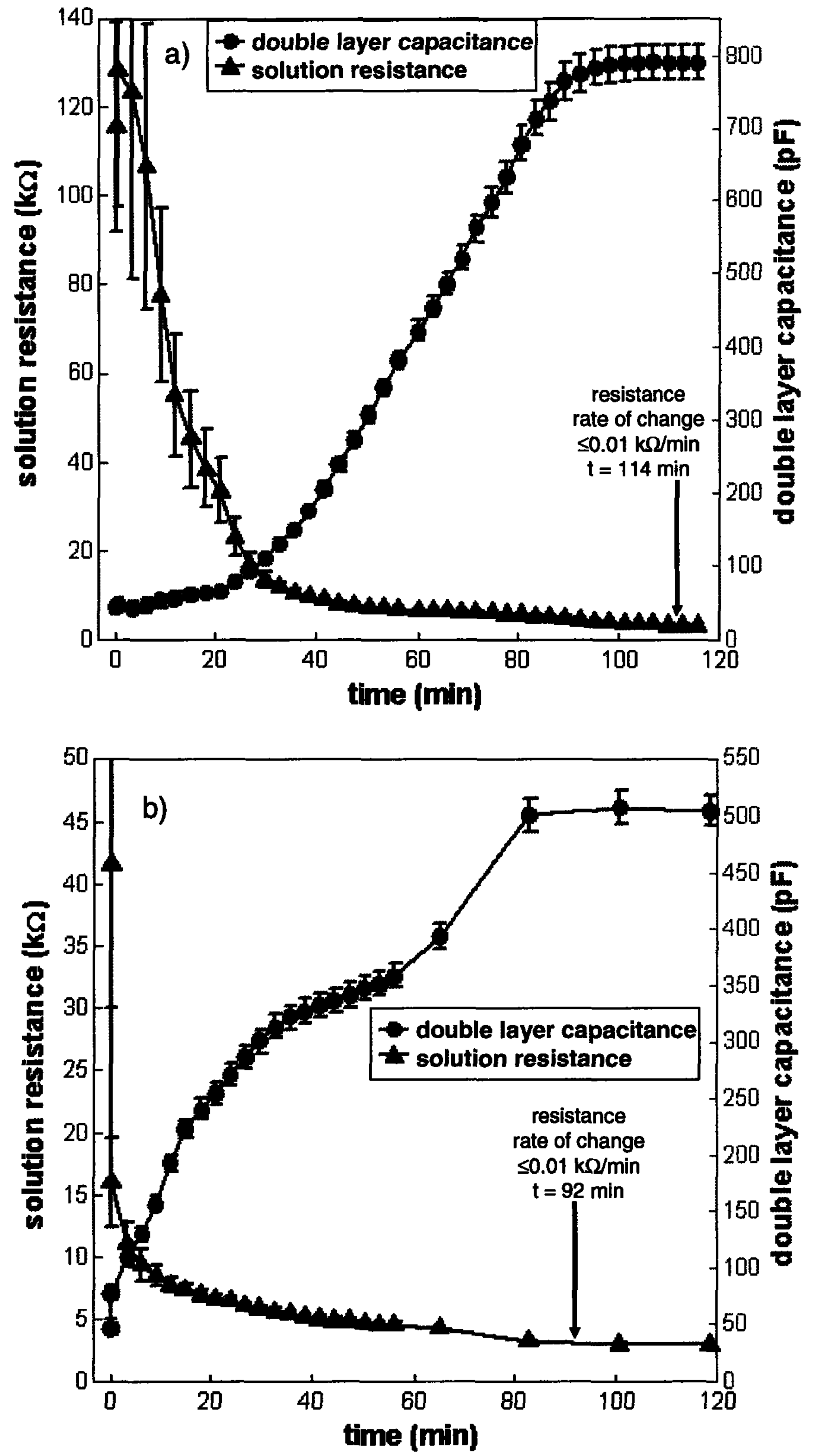

Figure 5.5. Best fit values of solution resistance and double layer capacitance during dissolution of mannitol backed by eicosane wax into PBS solutions from device L4B4, **a)** reservoir B12, **b)** reservoir B34.

5.2.3. Release of radiolabeled mannitol in stirred PBS

Three reservoirs were filled with radiolabeled mannitol and released into stirred PBS. Figure 5.6 shows the cumulative radioactivity released and the best fit solution resistance and double layer capacitance over time for each reservoir. The first two reservoirs, F2white11 and Flow2n10, were opened by corrosion of the gold membrane over the reservoir, and the third reservoir, F2black15, had no membrane covering the reservoir and began dissolving as soon as the device was immersed.

During the dissolution of mannitol from F2black15, it was observed that the solution resistance stopped falling and actually began to increase gradually. The double layer capacitance also stopped rising and fell slightly, and the scintillation measurements showed a delay in the release of radioactivity. Close inspection of the device through the wall of the beaker showed that an air bubble had lodged over the opening of the reservoir. Agitation of the solution with a pipette tip dislodged the bubble at 40 minutes post-immersion, and the solution resistance started to fall again. Although the release time is therefore longer and does not match the other experiments, the results clearly show the sensitivity of the impedance sensors to the release rate.

The two other release times agree quite closely, giving an average time of 115 ± 3 min, while F2black15 took an extra hour to finish dissolving. The release times measured by scintillation counting of the release medium agree well with the times measured by the sensors, although there is a 5-10 minute lag time. The lag time may be because the sensors detect the dissolution of solid mannitol, which is followed by dilution of the concentrated solution in the reservoir into the release medium. The release times are slightly longer compared to the release times observed for the dissolution of mannitol backed by eicosane although the difference is not statistically significant. The pyramidal shape of the reservoirs means that the depth of the mannitol within the reservoirs is not much greater than the depth of the mannitol in the mannitol/eicosane reservoirs despite the several additional micrograms of mannitol. Also, the earlier mannitol/eicosane release experiments were performed in unstirred solutions, which would be expected to slow the release.

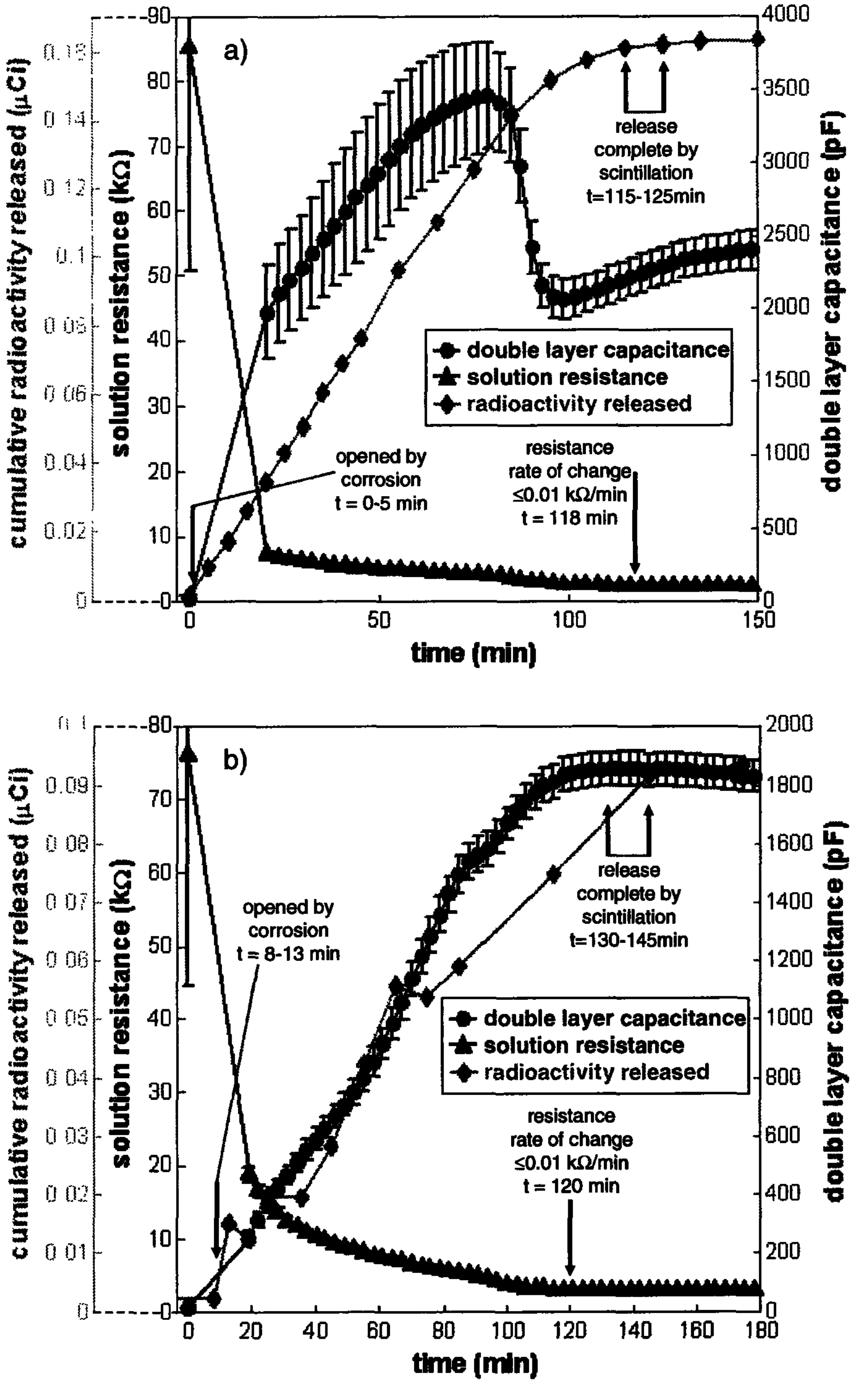

Figure 5.6a-b. Cumulative radioactivity released and best fit values of solution resistance and double layer capacitance during dissolution of radiolabeled mannitol into stirred PBS solutions from **a)** device F2 reservoir white11, **b)** device Flow2 reservoir 10.

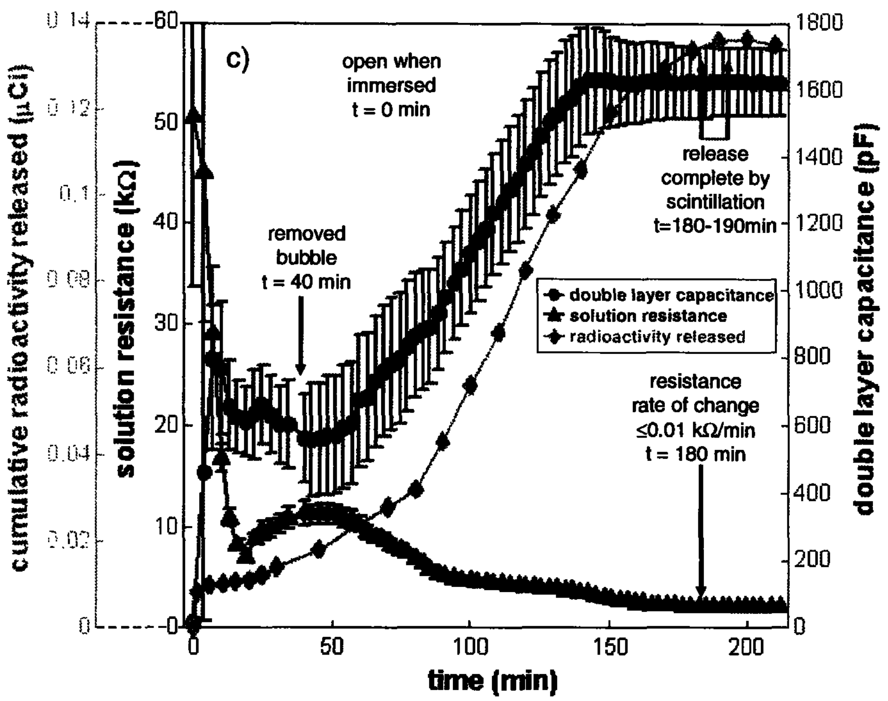

Figure 5.6c. Cumulative radioactivity released and best fit values of solution resistance and double layer capacitance during dissolution of radiolabeled mannitol into stirred PBS solutions from **c)** device F2 reservoir black15.

Device F2white11 (Figure 5.6a) also shows an unexpected maximum in the double layer capacitance partway through the release. The reason for this behavior is unknown, although similar maxima are seen in two of the leak tests and small maxima are seen in three out of four flow cell experiments. It may be that the electrodes have a tenuous connection to the remains of the membrane over the reservoir, which would provide additional surface area for an electrical double layer, and that during the release the membrane remnants break away. Though this theory cannot be substantiated, the fact that none of the air or mannitol/wax experiments showed a capacitance maximum lends some support because the devices used in those experiments had no membranes.

Table 5.4 gives the electrical characteristics and release times for each of the three experiments. The average final solution resistance and double layer capacitance were 2.4 ± 0.4 kΩ and 1900 ± 300 pF, respectively. The solution resistance is the same as at the end of the air release experiments and the end of a majority of flow cell and leak test experiments discussed below. The double layer capacitance is in agreement with the capacitance values reached at long times following the air experiments and with the capacitance values at the end of most flow cell and leak test experiments.

Table 5.4. Reservoir sensor electrical characteristics and release times for the dissolution of radiolabeled mannitol into stirred PBS.

release	amount mannitol (μg)	R_{Si} (kΩ)	C_{Si} (pF)	R_s at start (kΩ)	C_d at start (pF)	R_s at end (kΩ)	C_d at end (pF)	release time by dR_s/dt (min)	release time by C^{14} (min)
F2white11	31 ± 7	22	25	85	16	2.25	2210	118	115-125
Flow2n10	27.8	11	28	76	16	2.92	1830	112	120-135
F2black15	31 ± 7	3.7	12	51	15	2.10	1630	178	180-190

5.2.4. Release of radiolabeled and unlabeled mannitol in flow cell

Four reservoirs were filled with mannitol, successfully opened by corrosion and monitored in the flow cell. Device L4B3 contained unlabeled mannitol for a test run of the flow cell. Devices N8 (two reservoirs succesfully released) and N10 (one release) contained radiolabeled mannitol and were opened under the slower flow conditions. One of the reservoirs on N8, N8blue7, was partially covered by the flow cell gasket so that the opening was 50-75% as large as that for other reservoirs. Figure 5.7 shows the cumulative radioactivity released and the best fit solution resistance and double layer capacitance for each of the four flow cell experiments, while Table 5.5 gives the electrical characteristics and measured release times for each reservoir.

It is immediately apparent from the figure that all experiments took longer than those in stirred solutions and that the variability in release times is greater. The average release time for all four reservoirs in the flow cell is 200 ± 60 minutes. Reservoir L4B3well7 took the longest time despite the more rapid flow of PBS over the surface of the device. Reservoirs N8red2 and N10red3 should have comparable release times but differ by 50 minutes, and N8blue7 took only 20 minutes longer to release despite being partially covered by the gasket. All four reservoirs were opened by corrosion, so it is possible that the membranes were not completely removed during the reservoir opening step. The flow past the membrane is much slower than in a stirred beaker and less likely to mechanically remove any membrane remnants, making the chances of having partially intact membranes in the flow cell much greater.

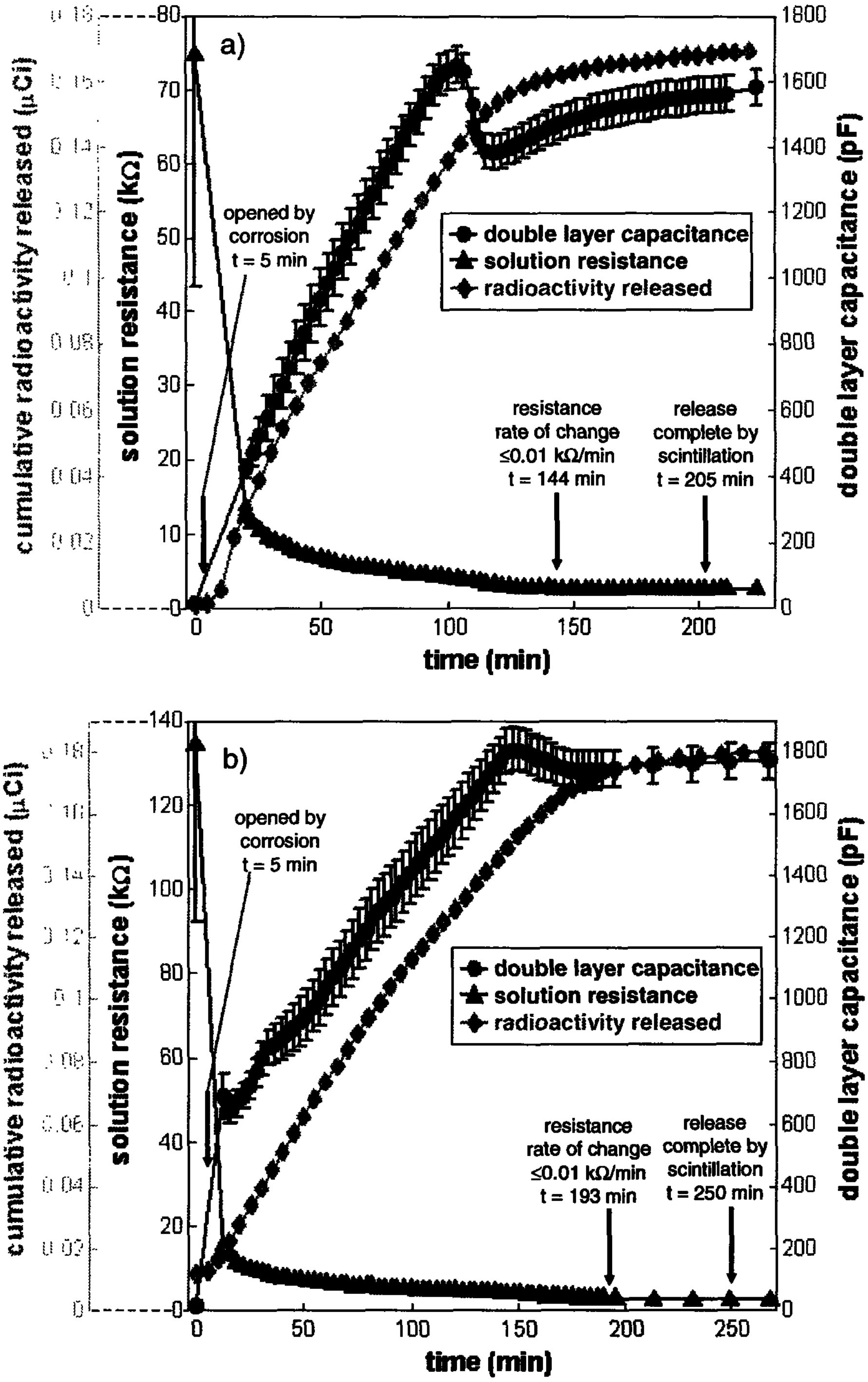

Figure 5.7a-b. Cumulative radioactivity released and best fit values of solution resistance and double layer capacitance during dissolution of radiolabeled and unlabeled mannitol into PBS in the laminar flow cell, from **a)** device N8 reservoir red2, **b)** device N10 reservoir red3.

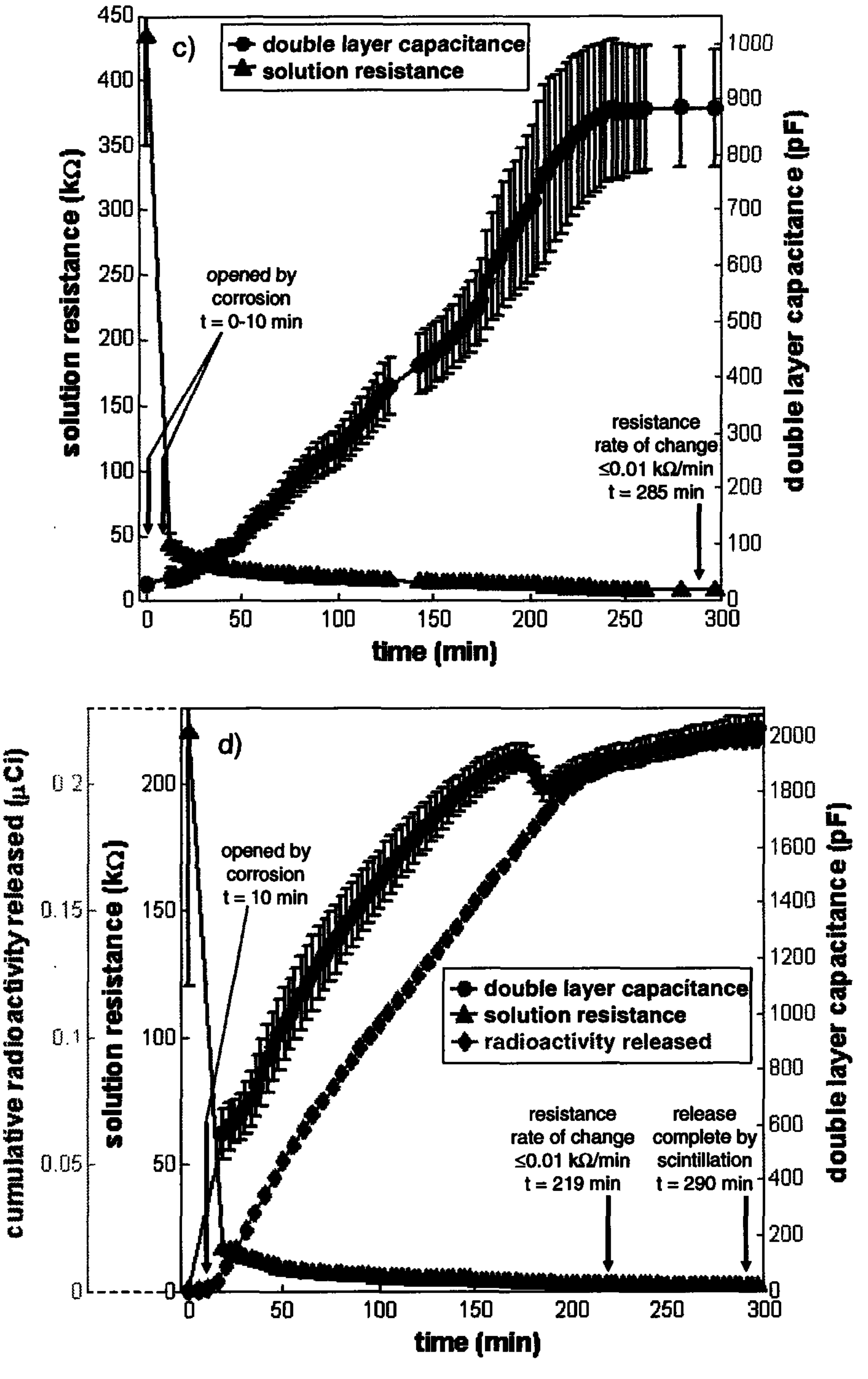

Figure 5.7c-d. Cumulative radioactivity released and best fit values of solution resistance and double layer capacitance during dissolution of radiolabeled and unlabeled mannitol into PBS in the laminar flow cell, from **c)** device L4B3 reservoir 7, **d)** device N8 reservoir blue7.

Another observation is that the release time measured by scintillation of the release medium lags the release time measured by the sensors by 60-70 minutes in all three cases. The consistent lag is thought to be due to the slow dilution of dissolved mannitol out of the reservoir as fresh PBS solution flows past. The lag time is much longer than that observed in the stirred beaker (5-10 min) because the scintillation measurements are much more sensitive in the flow cell setup. In a beaker, the measurement of the end of release is when the scintillation levels off at a high value. The scatter in the measurements means that the last 2-3% of mannitol released from the reservoir is lost in noise. In the flow cell, the end of release is the time at which the radioactivity measured in the effluent falls to background levels. The scintillation measurements are able to detect as little as 0.1% or less of the mannitol released from the reservoir, capturing more of the dilution phase of the release. If the end of release measured by scintillation counting is adjusted to be when 97-98% of the mannitol has been released, the lag time is reduced by 55-65 minutes, giving an identical lag time to the stirred beaker setup.

Table 5.5. Reservoir sensor electrical characteristics and release times for the dissolution of radiolabeled and unlabeled mannitol into PBS in the laminar flow cell.

release	amount mannitol (μg)	R_{si} (kΩ)	C_{si} (pF)	R_s at start (kΩ)	C_d at start (pF)	R_s at end (kΩ)	C_d at end (pF)	release time by dR_s/dt (min)	release time by C^{14} (min)
N8red2	36 ± 7	17	18	75	14	2.55	1470	139	200
N10red3	35 ± 7	90	20	130	16	2.61	1740	188	245
L4B3well7	41.2	14	19	520	28	6.76	885	275-285	—
N8blue7	36 ± 7	22	14	220	1.1	2.18	1910	209	280

Finally, examination of the final values of solution resistance and double layer capacitance in each reservoir reveals that reservoir L4B3well7 (Figure 5.7c and Table 5.5) was significantly different from the other three experiments. It appears that the impedance stopped changing before the reservoir was completely full of solution, because the solution resistance is much higher and the double layer capacitance is much lower than usual. With the absence of scintillation data it is difficult to be sure what caused this anomaly. One possible explanation is contamination of the mannitol with an insoluble substance. Occasionally during the melt filling process a stray piece of look-alike dust would make its way onto the slide of mannitol crystals. It is possible that an insoluble contaminant material was present in reservoir L4B3well7 that prevented the entire volume of the reservoir from filling with solution. Excluding L4B3well7, the average solution resistance and double layer capacitance at the end of release were 2.4

± 0.2 kΩ and 1700 ± 220 pF, respectively, in agreement with the final values measured for other release types.

5.2.5. Release of radiolabeled mannitol during leak testing

Four devices were prepared for the second *in vivo* study and leak tested prior to implantation. The impedance of one reservoir on each device was monitored during the leak test to acquire additional release profiles for reservoirs with membranes partially intact. Figure 5.8 shows the cumulative radioactivity released and the best fit values of solution resistance and double layer capacitance during each release. More than one reservoir was leaking during the test, so the release times measured by radioactivity measurements were not expected to match the release profiles measured with the sensors. Two of the four experiments showed significant maxima in the capacitance during release, which may be due to a tenuous connection to the reservoir membranes remaining as discussed in section 5.2.3. The observed release times have the greatest variation of any of the categories of release, as expected. Reservoir N16red3 was not monitored until the very end of release so that all leak tests could be finished prior to the scheduled *in vivo* experiments. Reservoir N4red1 released significantly faster than the rest and was the only reservoir that was observed under the microscope to have no membrane remaining at all prior to the leak test.

Table 5.6 gives the electrical characteristics and release times for each reservoir. As observed in the flow cell experiments, one reservoir, N6black15, shows a significantly higher solution resistance and low double layer capacitance at the end of release. It may be due to an insoluble contaminant present in the reservoir, although this cannot be verified. Reservoir N16red3 also has a slightly higher solution resistance but the release was not yet complete at the end of the measurement period. The other two reservoirs have final electrical characteristics very similar to those seen for other release types.

Table 5.6. Reservoir sensor electrical characteristics and release times for the dissolution of radiolabeled mannitol in PBS during leak testing, prior to implantation.

release	amount mannitol (μg)	R_{Si} (kΩ)	C_{Si} (pF)	R_s at start (kΩ)	C_d at start (pF)	R_s at end (kΩ)	C_d at end (pF)	release time by dR_s/dt (min)	release time by C^{14} (min)
N4red1	30 ± 7	14	12	190	12	2.77	1520	126	180
N6black15	32 ± 7	18	19	100	12	4.71	498	233	270
N14blue6	35 ± 7	54	23	110	13	2.27	1570	288	286
N16red3	27 ± 7	65	17	250	7.6	3.24*	1880*	>210	240

**End values reported for N16red3 are last measurements taken because monitoring stopped slightly before the release was complete*

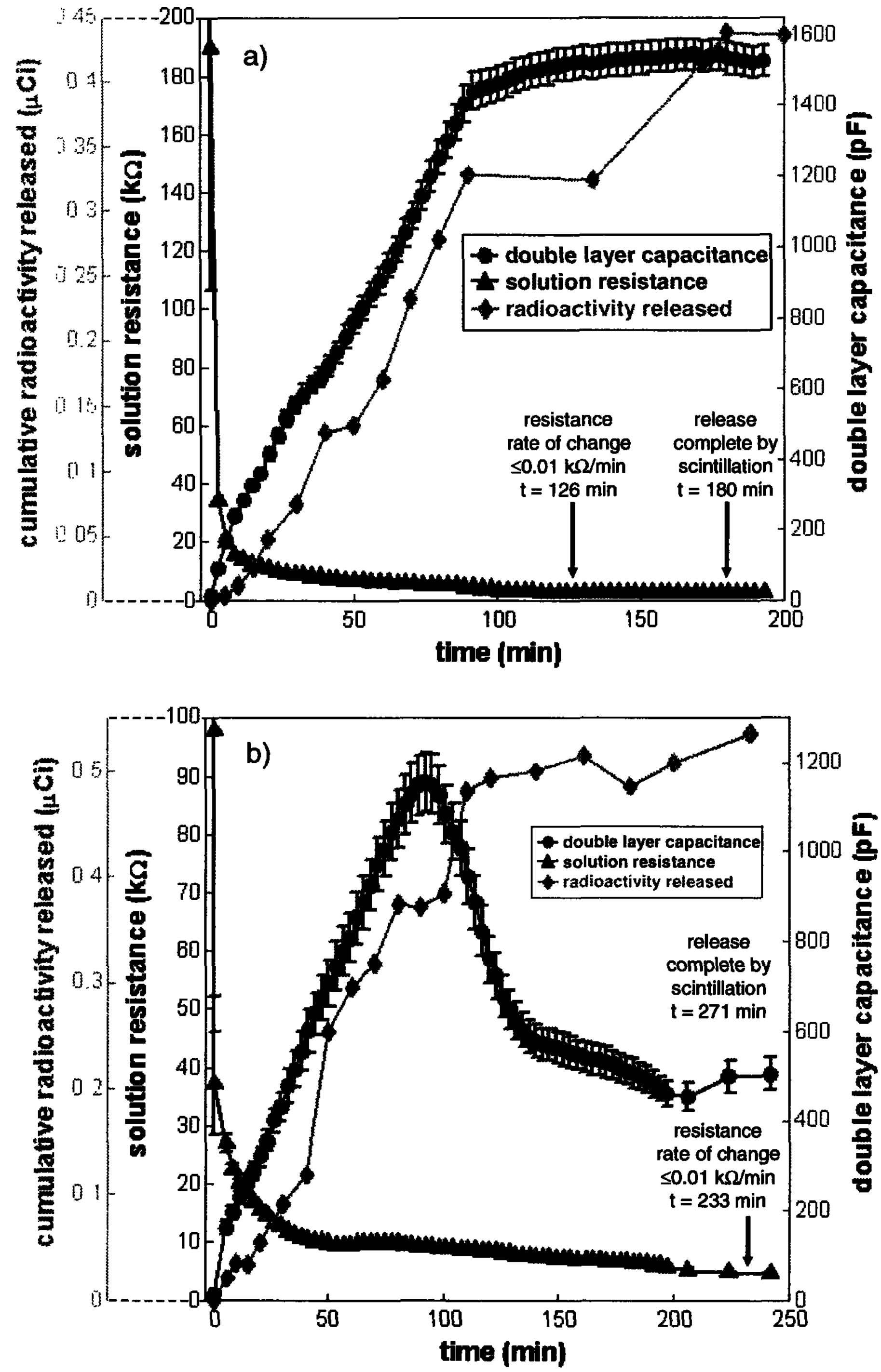

Figure 5.8a-b. Cumulative radioactivity released and best fit values of solution resistance and double layer capacitance during dissolution of radiolabeled mannitol into PBS during leak testing prior to implantation, from **a)** device N4 reservoir red1, **b)** device N6 reservoir black15.

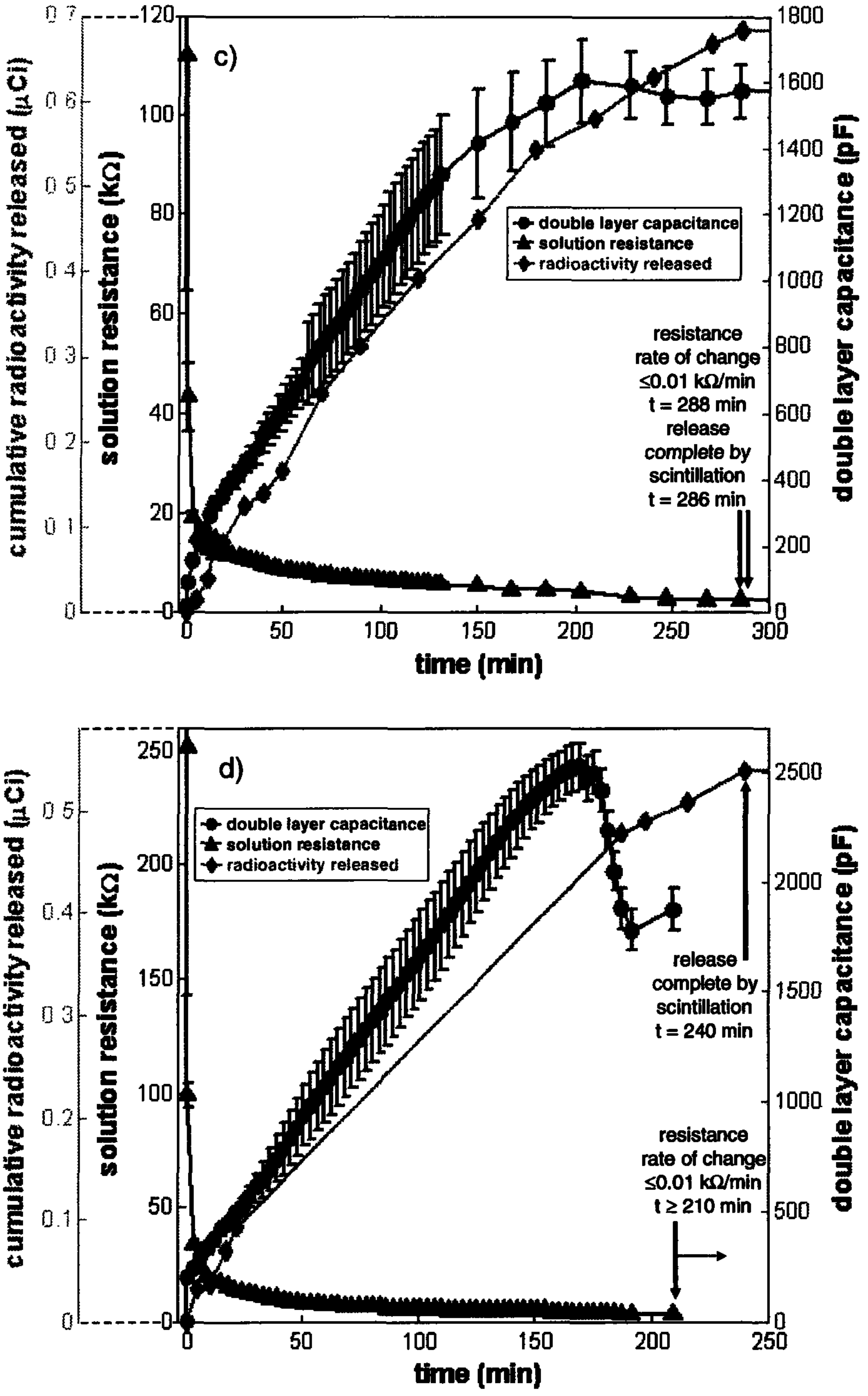

Figure 5.8c-d. Cumulative radioactivity released and best fit values of solution resistance and double layer capacitance during dissolution of radiolabeled mannitol into PBS during leak testing prior to implantation, from **c)** device N14 reservoir blue6, **d)** device N16 reservoir red3.

5.2.6. Summary

Five types of release experiments are described in this chapter: dissolution of air into deaerated PBS, mannitol backed by eicosane into PBS, radiolabeled mannitol into stirred PBS, radiolabeled and unlabeled mannitol into PBS in the flow cell, and radiolabeled mannitol into PBS during leak testing before implantation. The dissolution of air took 108 ± 3 min, the dissolution of mannitol backed by eicosane took 100 ± 11 min, and the dissolution of mannitol in stirred PBS took 115 ± 3 min, as measured by the sensor output. The pyramidal shape of the reservoirs means that the depth of mannitol in the reservoir was only slightly higher for the dissolution of full reservoirs (~30 μg in the release of radiolabeled mannitol into PBS) compared to the dissolution of partially filled reservoirs backed by eicosane (~23 μg). The shape factor and the fact that the dissolution of full reservoirs took place in a stirred medium make it unsurprising that the release time for full reservoirs was only slightly longer than for reservoirs 2/3 filled. Release times in the flow cell (200 ± 60 min) and during leak testing (220 ± 70 min) were slower and much more variable, likely due to partial blockage of the reservoir opening by membrane fragments.

Scintillation counting of the release medium provided a check on the release time measured by the sensors. In the stirred beaker setup, the release time measured by scintillation counting was 5-10 minutes longer than the time measured by the sensors. The sensors primarily measure the dissolution of solid mannitol, so the lag time is probably due to the time required for the concentrated mannitol solution within the reservoir to be diluted down to the concentration in the bulk volume. In the flow cell, the setup allows much more sensitive scintillation measurements of the effluent, detecting down to 0.1% or less of the mannitol released from the reservoir, as opposed to 2-3% in the stirred beaker setup. The time lag between the sensor and flow cell scintillation measurements of release time is consistently between 60 and 70 minutes because of the lower detection limit of the scintillation measurements. If the end of release in the flow cell is changed to the point when 97-98% of the mannitol has been released, the lag time is 5-10 minutes, the same as in the stirred beaker setup.

The time profile of the solution resistance and double layer capacitance was qualitatively similar for most experiments. The initial fit value of the solution resistance varied widely, largely because the circuit fitting program is unable to fit the circuit very well when the solution resistance element is very high. The resistance dropped rapidly at the start of each release, then tapered off as the release continued, as expected. The best fit double layer capacitance started very low and rose gradually throughout the release. Both the solution resistance and double layer capacitance showed a change of two orders of magnitude over the course of the release.

For three experiments (one release in stirred PBS and two leak tests), however, a maximum was observed in the double layer capacitance that is not easily explained. One possibility is that a tenuous connection exists between the remains of the reservoir membrane and an impedance electrode, increasing the surface area of the electrode until the connection is broken. Also, for two experiments (one in the flow cell and one leak test), the release appeared to stop before the solution resistance had dropped as far as usual and the double layer capacitance stopped rising at a lower value. There is a possibility that an insoluble contaminant was present in the reservoirs, preventing the solution from completely filling the reservoir at the end of release. The final values of solution resistance and double layer capacitance for the two release experiments were similar to the values observed for mannitol dissolution backed by insoluble eicosane.

The typical release profile has a starting best fit solution resistance on the order of 100 kΩ and double layer capacitance on the order of 10 pF. Of course, before the reservoir has been opened the 'solution resistance' element is actually a resistance of solid mannitol, which should be quite high, and the 'double layer capacitance' element is actually a capacitance of solid mannitol, which should be quite low. The best fit to the data is a two element circuit that includes only the silicon resistance and silicon capacitance, which is the same as setting the solution resistance to infinity and the double layer capacitance to zero. However, the best fit values are used for the starting solution resistance and double layer capacitance for simplicity. During the release, the solution resistance drops by two orders of magnitude to an average value of 2.4 kΩ (standard deviation = 0.3 kΩ, n = 12). The double layer capacitance increases by two orders of magnitude to an average value of 1600 pF (standard deviation = 310 pF, n = 12). If the reservoir is partly filled with an insoluble compound, as in the case of the two mannitol/eicosane release experiments, the final solution resistance is higher and the double layer capacitance is lower, as expected. For reservoirs containing 23 μg of mannitol backed by eicosane, the final solution resistance was 3.20 – 3.23 kΩ and the final double layer capacitance was 500 – 790 pF.

5.3. Conclusions

The *in vitro* release results show that it is possible to monitor the dissolution of compounds from the device reservoirs using the impedance sensors. The measured values of solution resistance and double layer capacitance change by two orders of magnitude during the dissolution of air or solid mannitol from the reservoirs. The end of the release, as determined by the rate of change of the solution resistance, was relatively consistent for similar conditions during dissolution of air and mannitol in PBS solutions. The release time was longer and more variable for experiments in the flow cell and during leak testing, likely because the reservoir openings were partially obscured by fragments of the gold membrane. Scintillation counting of the release medium gave release times that were 5-10 minutes longer than those measured by the sensors in the stirred PBS experiments, and 60-70 minutes longer than sensor release times in the flow cell experiments. The lag time arises because the sensors monitor the dissolution of solid mannitol, which is then followed by dilution of the concentrated mannitol solution in the reservoir into the bulk solution. In the stirred PBS experiments the dilution of the concentrated mannitol solution is largely lost in the noise of the scintillation measurements, while the high sensitivity of the scintillation measurements of the flow cell effluent enables the detection of the dilution process. If the scintillation measurements are adjusted to the same level of sensitivity, both setups give an identical lag time of 5-10 minutes. Finally, the release profiles of the solution resistance and double layer capacitance were relatively consistent from reservoir to reservoir although there were some exceptions.

5.4. Recommendations

It would be desirable to make the opening of the reservoir membrane consistent from reservoir to reservoir and to increase the number of experiments to increase the statistical significance of the results. The changing of the device design to the 'fuse chip' developed by MicroCHIPS, Inc. would address both these problems. The fuse chip membranes melt and are drawn to the edges of the reservoir opening by surface tension, creating a highly reproducible reservoir opening. Also, the fuse method of opening is much more reliable than the corrosion method, which would increase the yield of successfully opened and monitored reservoirs per device.

Once the variability in the size of the reservoir opening was reduced, it would be possible to examine how the transport conditions outside the device affect the rate of drug transport. The transport conditions could be varied systematically by casting agarose gel films with known thickness and density over the device surface before opening the reservoirs. In addition, a variety of drugs of differing solubilities and molecular weights could be released to determine how these results can be extended to a variety of therapeutic molecules.

6. *In Vivo* Release Monitoring

The impedance sensors were developed for the purpose of monitoring drug delivery from the MEMS device *in vivo* in real time, in order to understand how tissue reaction impacts drug transport. The devices were therefore implanted subcutaneously in rats and individual reservoirs were activated and monitored at various times post-implantation. Two *in vivo* studies were performed, using the results of the first study to improve the amount of data collected in the second. Seven subcutaneous release experiments were performed in total, at days 5, 6, 11, and 12 post-implantation.

The original intent was to implant several devices, each with 6-8 independently addressable reservoirs filled with C^{14} radiolabeled mannitol, and activate/monitor one reservoir each week for four weeks. The devices would then be explanted, and part of the fibrous capsule removed for histology to determine its thickness and density. The remaining reservoirs would be activated *in vitro* with the capsule still covering the surface, to see how *in vitro* transport through the capsule resembles *in vivo* transport. This ambitious plan was not possible because of device reliability issues – the yield of workable reservoirs per device was insufficient.

The theoretical yield of 8 reservoirs per device was reduced by several factors. The first was the difficulty of making good wire bonds to the impedance electrodes, which often reduced the number of monitorable reservoirs by one or two. Second was the fragility of the reservoir membrane caps, which often broke during packaging, reducing the number of properly sealed reservoirs by 2-4. These two factors meant that most fully packaged devices had between 4 and 6 good reservoirs. However, *in vivo* experiments took a further toll in three ways: 1) the corrosion method to open the reservoirs was not very reliable *in vivo*, often making it impossible to open the reservoirs for release monitoring, 2) the medical grade epoxy used to insulate the electrical connections was not entirely impermeable to water over long times, making implantation times longer than 2 weeks difficult, 3) chafing of the device surface against the tissue often broke some membranes, releasing reservoirs prematurely.

These factors put together meant that only one reservoir was successfully opened and monitored during the first 4 week *in vivo* study. The three mechanisms described above all took a heavy toll on the reservoirs, especially membrane breakage and the difficulty in getting reservoirs to open by the corrosion method. For the second study, devices were implanted for only 2 weeks to avoid degradation of the electrical insulation and breakage of device membrane caps over time. The shorter implantation time meant that histology of the fibrous capsule could not be performed, because the film deposited over the chip surface during that time was not cohesive enough to be removed and examined. A small ridge of epoxy was added around each reservoir to prevent chafing of the tissue directly against the membrane. The addition of epoxy to the device surface greatly improved the survival rate of the membranes during implantation. The corrosion method was slightly improved with the help of Rebecca Shawgo, but this problem could not really be solved, and the unreliable opening of device reservoirs was the greatest obstacle to data collection. Despite these difficulties, four reservoirs were successfully opened by corrosion and monitored *in vivo* and two further reservoirs were mechanically opened and then monitored *in vivo.*

The two *in vivo* studies showed that the impedance monitoring method can be used to observe the release of drug from the MEMS device in real time *in vivo.* The sensors work identically *in vitro* and *in vivo*, measuring the conductivity of the reservoir via the equivalent circuit developed in chapter 4. Scintillation counting of the C^{14} mannitol in the rats' urine confirmed the release of the reservoirs. The observed release times varied significantly between data points, although this could be due to either variability in the tissue reaction or variability in membrane opening. With improvements to the device packaging and the use of the 'fuse' method for opening reservoirs, the amount of data collected could be significantly improved in the future. A greater number of data points and longer implantation times could allow correlation of release times with the tissue reaction in different animals at different times post-implantation, yielding *in situ* information about transport of drugs from the implants *in vivo.*

6.1. Experimental

Two *in vivo* studies were performed at Johns Hopkins Medical Institute (JHMI) in Dr. Henry Brem's laboratory, with the collaboration of lab coordinator Betty Tyler. The first study took place in October 2003 and the second in March 2004. The experimental procedures used in each study were similar, with certain improvements made to the device preparation and activation protocols for the second study. The experimental procedure can be divided into three parts: device preparation, implantation, and release monitoring. The details of each study are described in the appropriate subsections below.

6.1.1. Device preparation

Devices for both studies came from wafer #020303-1. The devices were etched on plasmaquest for 850s to remove the nitride backing behind the gold membranes. Devices were loaded with C^{14} mannitol, packaged according to the protocol given in chapter 3, and leak tested prior to implantation. Devices for the first study were weighed after each reservoir was filled with mannitol to quantify the amount of radioactivity in each reservoir. The repeated heating and cooling involved in the filling process led to breakage of some reservoir membranes, which were epoxied over before the leak testing step. The device reservoirs for the second study were filled with approximately equal amounts of mannitol all at the same time, with a single heating and cooling step to melt the mannitol into place. This procedure reduced the number of broken membranes but did not give a precise value for the amount loaded in each reservoir.

Five devices and one control device were implanted during the first study. The control device was filled with radioactive mannitol and sealed, but had no electrical connections. Each device has 16 reservoirs, but the number that may be electrically connected is limited to eight, which are selected on the basis of which ones have fully intact membranes. Some devices had more than eight reservoirs filled because some membranes broke during filling, and others were filled to replace them.

After the devices were fully packaged, they were leak tested by immersion in PBS solution to allow radioactivity from reservoirs with broken membranes to leach out. The sensor connections were tested to ensure good electrical connections and to determine which reservoirs had leaked. All broken reservoirs were covered with epoxy after being removed from the solution. Table 6.1 gives the amount of radioactivity loaded in each reservoir and the approximate magnitude of the impedance spectrum for each reservoir. Also given are the amount of radioactivity leaked during immersion, the estimated amount of radioactivity remaining in the device before implantation, the amount of radioactivity detected in the urine, and the identity of the leaky reservoirs as indicated by the impedance sensors.

Table 6.1. Device loading and electrical characteristics for first *in vivo* study.

device	reservoir	impedance magnitude (kΩ)	radioactivity loaded (μCi)	leaked *in vitro*	notes
1	black2	100	0.18	N	leaked *in vivo* before day 28
	black3	44	0.13	N	would not open *in vivo*
	white6	bad bond	0.14	N	sealed with epoxy before implantation
	white7	60	0.15	N	leaked *in vivo* before day 15
	blue9	170	0.14	N	leaked *in vivo* before day 15
	10	no bond	0.17	N	sealed with epoxy before leak test
	blue11	70	0.15	Y	sealed with epoxy before implantation
	red14	22	0.13	Y	sealed with epoxy before implantation
	red15	2.4	0.14	N	leaked *in vivo* before day 15
	total radioactivity loaded:		1.33 μCi		in 9 reservoirs
	total radioactivity leaked:		0.28 μCi		from 2 reservoirs
	total radioactivity implanted:		1.05 μCi		mostly in 5 unsealed, 2 sealed reservoirs
	total radioactivity in urine:		0.49 μCi		and traces in 2 sealed reservoirs
2	red1	140	0.17	N	leaked *in vivo* before day 6
	2	no bond	0.04	N	sealed with epoxy before leak test
	black3	130	0.17	N	would not open *in vivo*
	blue6	180	0.20	N	would not open *in vivo*
	white7	82	0.19	N	sealed with epoxy before leak test
	white9	85	0.11	N	activated and monitored on day 6
	10	no bond	0.06	N	sealed with epoxy before leak test
	blue11	48	0.16	N	sealed with epoxy before leak test
	black13	80	0.16	N	sealed with epoxy before leak test
	red15	120	0.10	N	would not open *in vivo*
	total radioactivity loaded:		1.35 μCi		in 10 reservoirs
	total radioactivity leaked:		0 μCi		open reservoirs epoxied before leak test
	total radioactivity implanted:		1.35 μCi		mostly in 5 unsealed reservoirs and 5
	total radioactivity in urine:		0.49 μCi		sealed reservoirs
3	red2	50	0.14	Y	sealed with epoxy before implantation
	black3	125	0.11	N	leaked *in vivo* before day 15
	blue6	bad bond	0.14	?	sealed with epoxy before implantation
	white7	bad bond	0.15	N	sealed with epoxy before leak test
	white10	45	0.18	N	would not open *in vivo*
	blue11	90	0.19	N	leaked *in vivo* before day 15
	black14	10	0.16	N	would not open *in vivo*
	red15	35	0.14	N	would not open *in vivo*
	total radioactivity loaded:		1.21 μCi		in 8 reservoirs
	total radioactivity leaked:		0.14 - 0.29 μCi		from 1-2 reservoirs
	total radioactivity implanted:		0.93 - 1.07 μCi		mostly in 5 unsealed, 1-2 sealed
	total radioactivity in urine:		0.40 μCi		reservoirs, trace in 1-2 sealed reservoirs
4	black2	38	0.12	Y	sealed with epoxy before implantation
	black3	19	0.16	Y	sealed with epoxy before implantation
	white6	36	0.16	Y	sealed with epoxy before implantation
	white7	40	0.15	N	would not open *in vivo*
	blue10	70	0.18	N	leaked *in vivo* before day 28
	blue11	45	0.15	Y	sealed with epoxy before implantation

Table 6.1. (cont.) Device loading and electrical characteristics, first *in vivo* study.

device	reservoir	impedance magnitude (kΩ)	radioactivity loaded (µCi)	leaked *in vitro*	notes
4	red14	25	0.20	Y	sealed with epoxy before implantation
	red15	21	0.15	Y	sealed with epoxy before implantation
	total radioactivity loaded:		1.26 µCi		in 8 reservoirs
	total radioactivity leaked:		0.93 µCi		from 6 reservoirs
	total radioactivity implanted:		0.33 µCi		mostly in 2 unsealed reservoirs and
	total radioactivity in urine:		0.10 µCi		traces in 6 sealed reservoirs
5	black2	32	0.14	Y	sealed with epoxy before implantation
	black4	18	0.14	Y	sealed with epoxy before implantation
	white5	67	0.10	Y	sealed with epoxy before implantation
	6	no bond	0.04	N	sealed with epoxy before leak test
	white7	320	0.18	Y	sealed with epoxy before implantation
	blue10	100	0.17	N	leaked *in vivo* before day 15
	blue11	80	0.12	Y	sealed with epoxy before implantation
	red14	44	0.15	Y	sealed with epoxy before implantation
	red15	75	0.16	N	leaked *in vivo* before day 15
	total radioactivity loaded:		1.20 µCi		in 9 reservoirs
	total radioactivity leaked:		~0.5 - 0.83 µCi		from 6 reservoirs, not done releasing
	total radioactivity implanted:		~0.37 - 0.7 µCi		mostly in 2 unsealed reservoirs and
	total radioactivity in urine:		0.62 µCi		traces in 6 sealed reservoirs
6	1	control	~0.08	Y	sealed with epoxy before implantation
	2	control	~0.08	N	
	5	control	~0.12	N	
	6	control	~0.08	N	
	9	control	~0.12	N	
	10	control	~0.12	N	
	13	control	~0.12	N	
	14	control	~0.08	N	
	total radioactivity loaded:		~0.78 µCi		in 8 reservoirs
	total radioactivity leaked:		~0.08 µCi		from 1 reservoir
	total radioactivity implanted:		~0.70 µCi		mostly in 7 unsealed reservoirs and
	total radioactivity in urine:		0.07 µCi		traces in 1 sealed reservoir

Four devices were implanted for the second study. To reduce the attrition of membranes during the melt filling process, all eight reservoirs were filled with approximately the same amount of mannitol, heated to melt it in place, and weighed. The radioactivity loaded into the entire device is then divided by the number of reservoirs to determine the approximate amount of radioactivity in each reservoir. The devices were again packaged according to the protocol in chapter 3 and then leak tested by immersion in PBS solution. Table 6.2 gives the amount of radioactivity loaded in each device, the magnitude of the impedance spectrum for each reservoir, the amount of radioactivity leaked during immersion, and the identity of the leaky reservoirs as indicated by the sensors. All broken reservoirs were covered with epoxy, and a small ridge of epoxy was applied around each intact reservoir to moderate the contact between the membranes and the tissue after implantation. The devices were labeled to indicate which wires should point toward the head of the rat and which toward the tail and shipped to JHMI for implantation.

Table 6.2. Device loading and electrical characteristics for second *in vivo* study.

device	reservoir	impedance magnitude (kΩ)	leaked *in vitro*	notes
A1	red2	60	N	activated and monitored on day 11
	red3	75	Y	sealed with epoxy before implantation
	blue6	90	N	would not open *in vivo*
	blue7	9	N	mechanically opened, monitored day 5
	white10	35	N	would not open *in vivo*
	white11	110	Y	sealed with epoxy before implantation
	black14	>400	Y	sealed with epoxy before implantation
	black15	27	Y	sealed with epoxy before implantation
	total radioactivity loaded:		≥1.11 μCi	in 8 reservoirs (0.2459 mg +)
	total radioactivity leaked:		0.56 μCi	from 4 reservoirs
	total radioactivity implanted:		≥0.55 μCi	primarily in 4 reservoirs, some traces
	total radioactivity in urine:		0.28 μCi	remaining in the 4 sealed reservoirs
A2	red2	130	N	activated and monitored on day 5
	red3	10	N	leaked *in vivo* around day 8
	blue6	65	Y	sealed with epoxy before implantation
	7	not connected	Y	sealed with epoxy before implantation
	blue8	>500	N	would not open *in vivo*
	white10	24	N	leaked *in vivo* around day 8
	white11	>300	Y	sealed with epoxy before implantation
	black14	240	N	leaked *in vivo* around day 8
	black15	150	Y	sealed with epoxy before implantation
	total radioactivity loaded:		1.42 μCi	in 9 reservoirs (0.3153 mg)
	total radioactivity leaked:		0.64 μCi	from 4 reservoirs
	total radioactivity implanted:		0.78 μCi	primarily in 5 reservoirs, some traces
	total radioactivity in urine:		0.41 μCi	remaining in the 4 sealed reservoirs
A3	red2	35	maybe	leaked *in vivo* slowly over time
	red4	300	Y	sealed with epoxy before implantation
	blue6	42	N	activated and monitored on day 12
	blue7	40	maybe	leaked *in vivo* before day 12
	white10	10	Y	sealed with epoxy before implantation
	white11	62	N	would not open *in vivo*
	black14	5.4	N	would not open *in vivo*
	black15	18.5	Y	sealed with epoxy before implantation
	total radioactivity loaded:		1.15 μCi	in 8 reservoirs (0.2562 mg)
	total radioactivity leaked:		0.49 μCi	from 3-5 reservoirs
	total radioactivity implanted:		0.66 μCi	primarily in 3-5 reservoirs, some traces
	total radioactivity in urine:		0.32 μCi	remaining in the 3 sealed reservoirs

Table 6.2. (cont.) Device loading and electrical characteristics, 2nd *in vivo* study.

device	reservoir	impedance magnitude (kΩ)	leaked *in vitro*	notes
A4	red1	14	Y	sealed with epoxy before implantation
	3	not connected	Y	sealed with epoxy before implantation
	red4	44	N	activated and monitored on day 11
	blue6	27	N	mechanically opened, monitored day 6
	blue7	90	N	would not open *in vivo*
	white10	46	N	would not open *in vivo*
	white11	160	N	would not open *in vivo*
	black13	6.6	N	would not open *in vivo*
	14	not connected	Y	sealed with epoxy before implantation
	black15	60	Y	sealed with epoxy before implantation
	total radioactivity loaded:		1.34 μCi	in 10 reservoirs (0.2967 mg)
	total radioactivity leaked:		0.39 μCi	from 4 reservoirs
	total radioactivity implanted:		0.95 μCi	primarily in 6 reservoirs, some traces
	total radioactivity in urine:		0.28 μCi	remaining in the 4 sealed reservoirs

6.1.2. Device implantation and animal care

All animal procedures were carried out in compliance with MIT and JHMI animal care guidelines as described in the approved animal protocol for the Microchip project NIH grant. Animal care, surgery, and monitoring was performed by Betty Tyler in Dr. Brem's laboratory and in the main animal care facility at JHMI. Ten female Fischer 344 rats weighing between 150-200 g were used for the studies, six for the first and four for the second. Animals were housed individually in Nalgene metabolic cages[1] to allow quantification of radioactive mannitol in the urine. The metabolic cages automatically funnel feces to one collection compartment and urine to another. Urine was collected for at least 24 hours before implantation to allow measurement of baseline urine radioactivity. Animals were given standard rat chow and sugar water (4 tsp / 500 mL) *ad libitum*. The sugar water encouraged the animals to drink more, allowing more frequent collection of urine radioactivity time points[2]. Cages were cleaned every 3 days.

The devices were sterilized by gamma irradiation with a Cesium 137 source for a total dose of 40 Grey and implanted in a subcutaneous pocket in the flank, one device per rat. Rats were anesthetized by intraperitoneal injection of 0.6 mL xylaket (25 mg/mL xylazine, 2.5 mg/mL ketamine; 3-5 mL xylaket per kilogram animal weight). All instruments were autoclaved and sterile gloves were worn throughout the procedure. Animals were shaved and prepped for surgery with alcohol and betadine prior to surgical incision. An incision was made in the skin of the rear flank and a subcutaneous tunnel and pocket was made with sterile scissors. The sterilized MEMS device, with wires leading from both sides as shown in Figure 3.12, was inserted into the tunnel and pocket. A second incision was made toward the head of the animal and a tunnel opened between the incision and the first subcutaneous pocket. The device was then positioned so that the wires on each side were located in the tunnels with the device in the subcutaneous pocket between them and the ends of the wires near the incisions. The face of the microchip for drug release was oriented to face the fascia. The incisions were closed with autoclips. Following surgery the animals received a subcutaneous injection of 0.1 mg/kg buprenorphine, an analgesic. The day of implantation was designated as Day 1.

Following device implantation animals were returned to the metabolic cages. All urine was collected to be analyzed for C^{14} radiolabeled mannitol and feces were discarded. The collection time and volume of each urine sample was recorded and a 1 mL aliquot taken for scintillation counting. For samples with volumes less than 1 mL, all of the sample was taken for scintillation counting.

For device activation, animals were anesthetized and prepped as above. The autoclips were removed from one of the incisions and the wires were exposed. The shrink tubing covering the wires was removed with a sterile razorblade and the wires were connected to the potentiostat and impedance spectrometer for activation and monitoring of release. During the procedure anesthetic was boosted in 0.2 mL increments as necessary to keep the animal unconscious up to 6 hours. Once monitoring was complete or 6 hours had passed since the initial anesthetization of the animal, the wires were disconnected and the exposed ends clipped off. The incision was closed with autoclips and the animal placed in the metabolic cage for observation.

Following the final activation, animals were monitored for several days to ensure complete drug release. Animals were then euthanized by CO_2 inhalation and the devices were explanted. The first study ran for one month and the second for two weeks. After explantation, devices were immersed in isopropyl alcohol solution and shipped to MIT for examination. The encapsulation tissue over the face of the devices from the first study was removed prior to shipping and preserved in alcohol for future histological analysis. The short duration of the second study led to a less cohesive encapsulation layer that could not be removed from the devices in one piece.

6.1.3. Device activation and monitoring of release

The wires for electrical connections were exposed through either the head side or the tail side incision as described in section 6.1.2 above. Every sensor on that side of the device was tested with the impedance spectrometer to determine whether each reservoir was still sealed or had already opened. After initial sensor readings were recorded, one reservoir was selected for activation and connected to the potentiostat. The reservoir was then activated using the standard corrosion protocol[3] developed by Rebecca Shawgo, described in chapter 5. Following the corrosion protocol, the sensor leads were connected to the impedance spectrometer and monitored. If the impedance still indicated an unopened reservoir, the corrosion protocol was repeated, either on the same reservoir or on another unopened reservoir. If the sensor indicated that the impedance was decreasing with time, a series of impedance measurements was recorded. The measurements were continued until the impedance stopped changing, indicating completion of release, or until the time limit for safe anesthetization of the rat was reached. One reservoir (Device #2 white9) was successfully opened and monitored on day 6 in the first study, and four were successfully opened and monitored in the second study on days 5, 11, and 12 (A1 red2, A2 red2, A3 blue6, A4 red4).

In the second study, two reservoirs (A1 blue7, A4 blue6) were also opened mechanically after the corrosion protocol failed. For those two devices, the device was pulled out through the open incision and the desired reservoir was scratched with the tip of a needle. The device was then returned to the subcutaneous pocket and the impedance was monitored as described above. Data from the mechanically opened reservoirs was collected until the safety time limit was reached, due to the long time spent attempting to open the reservoirs by corrosion.

6.2. Results and discussion

The first and second *in vivo* studies yielded seven sets of release monitoring data in total. Radioactivity measurements confirmed the release in each case, showing an increase in radioactivity released following each successful activation. Figure 6.1 shows the cumulative radioactivity released measured by scintillation counting of urine samples. Scintillation data in CPM was converted to microcuries using the standard curve of C^{14} mannitol in baseline rat urine prepared by Rebecca Shawgo, which yields a conversion factor of 1.851×10^6 CPM/μCi, as described in appendix 10.5. Complete scintillation data for the animals in the first study with devices that were not successfully activated is also given in the appendix.

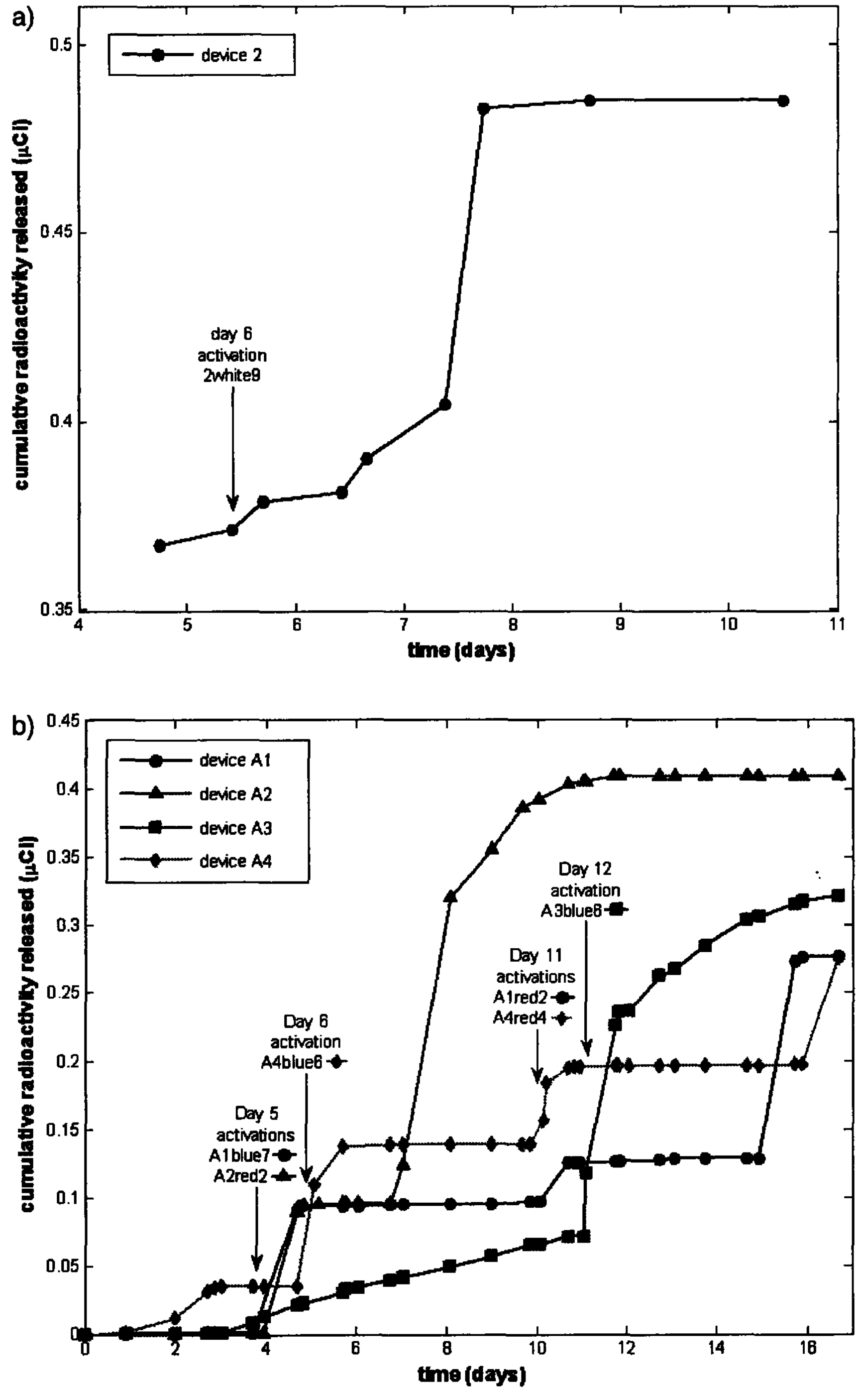

Figure 6.1. Cumulative radioactivity (C^{14} mannitol) released from implanted devices as measured by scintillation counting of urine samples; **a)** data for device 2 from the first study, **b)** data for all four devices from the second study. The x axis label in days is the time elapsed following implantation, where the implantation time is time zero, while the 'day' labels on the activations refer to the day of the study as recorded by Dr. Brem's laboratory, where the day of implantation is day one.

Successful activations, followed by drug release monitoring using the impedance sensors, are indicated by black arrows. In all cases except device 2 white9 from the first study, the mannitol comes out in a spike in the first urine sample taken after activation. This is expected because mannitol partitions rapidly to the urine[4] and the rats were not catheterized, so that the mannitol was removed from the bloodstream and present in the urine before the rats recovered from the anesthetic. Each device shows additional mannitol release at various times due to leakage of other reservoirs, but the release following each successful activation is clear. Additionally, every time wires from one side of a device were exposed for a new activation, each sensor/reservoir was tested to determine whether the reservoir was still full or had leaked. In each case, sensor readings were in agreement with the scintillation data, i.e., at least one reservoir was found to have leaked by sensor readings whenever the scintillation data indicated that a leak had occurred.

Device 2 white9 is unique because the mannitol came out very slowly for two days before finishing rapidly on the third day post-activation. The sensor readings from monitoring this release also indicated an unusually slow release rate compared to all other experiments. It has been observed by other researchers that on occasion the corrosion protocol may lead to a pinhole defect in the gold membrane sealing the device, giving very slow drug release. It is likely that device 2 white9 opened only partially through some such small defect, releasing slowly over two days until the rest of the membrane gave way to release the rest of the mannitol on the third day.

The sets of impedance spectra taken *in vivo* showed no significant differences from the spectra taken *in vitro* discussed in chapter 5. The spectra are plotted in appendix 10.5 for reference. Each spectrum was fitted to the four-element equivalent circuit developed in chapter 4 to give values of the solution resistance and double layer capacitance at each time point. Figure 6.2 gives the best fit values of solution resistance and double layer capacitance during each of the seven mannitol release experiments *in vivo.* It is not possible to directly compare the radioactivity data to the sensor data due to the time lag involved in collection of urine samples. However, for device 2 white9, shown in Figure 6.2g, it is clear that the release is unusually slow. The solution resistance was still above 30 kΩ and the double layer capacitance was only 500 pF even after 160 min, while during other experiments the resistance dropped below 30 kΩ within 10-50 minutes (often before the first time point) and the capacitance rose an order of magnitude higher before the end of the monitoring period.

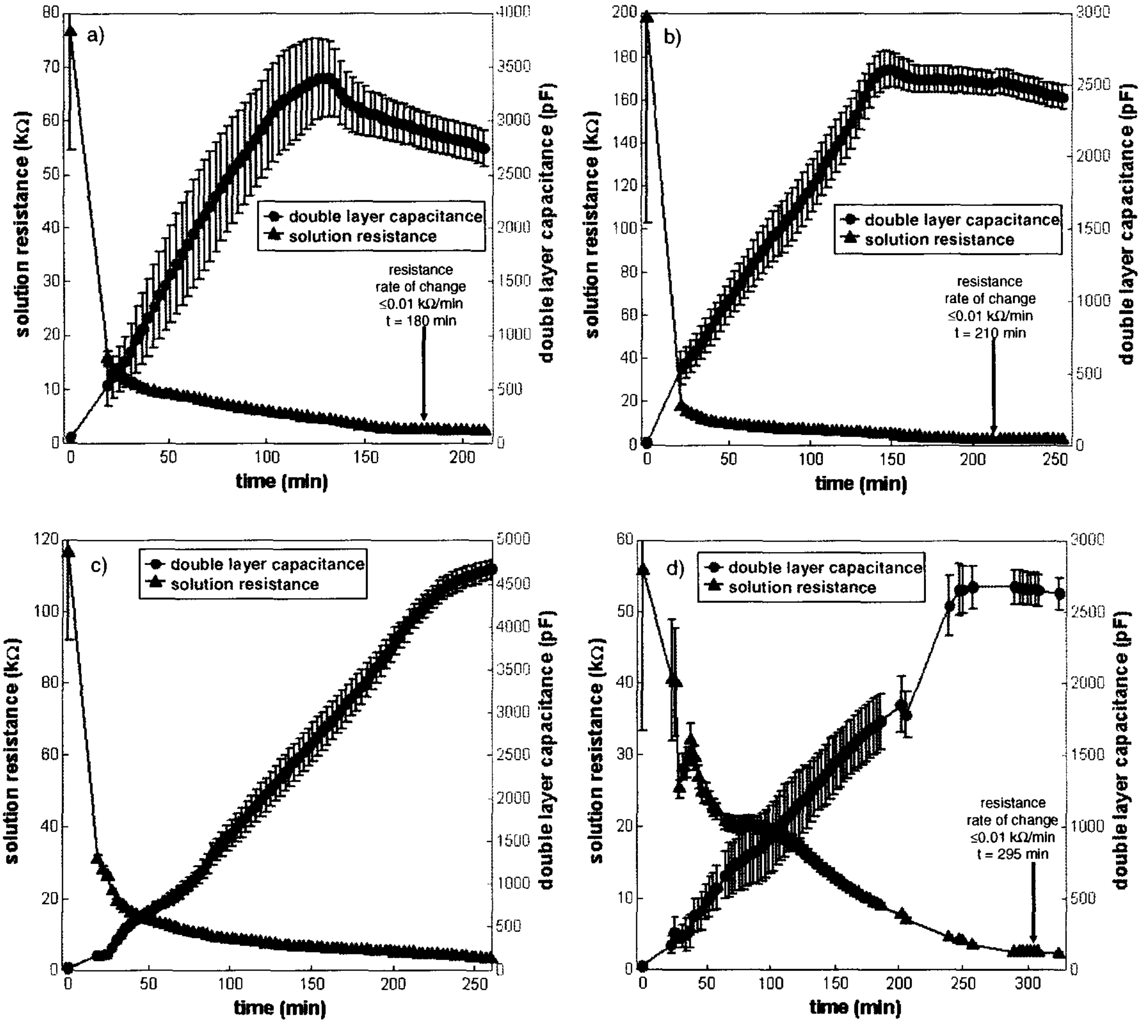

Figure 6.2a-d. Best fit values of solution resistance and double layer capacitance of device reservoirs during monitoring of release of C^{14} mannitol *in vivo*, with end of release marked if reached; **a)** device A2 reservoir red2 release on day 5, **b)** device A4 reservoir red4 release on day 11, **c)** device A1 reservoir red2 release on day 11, **d)** device A3 reservoir blue6 release on day 12.

]

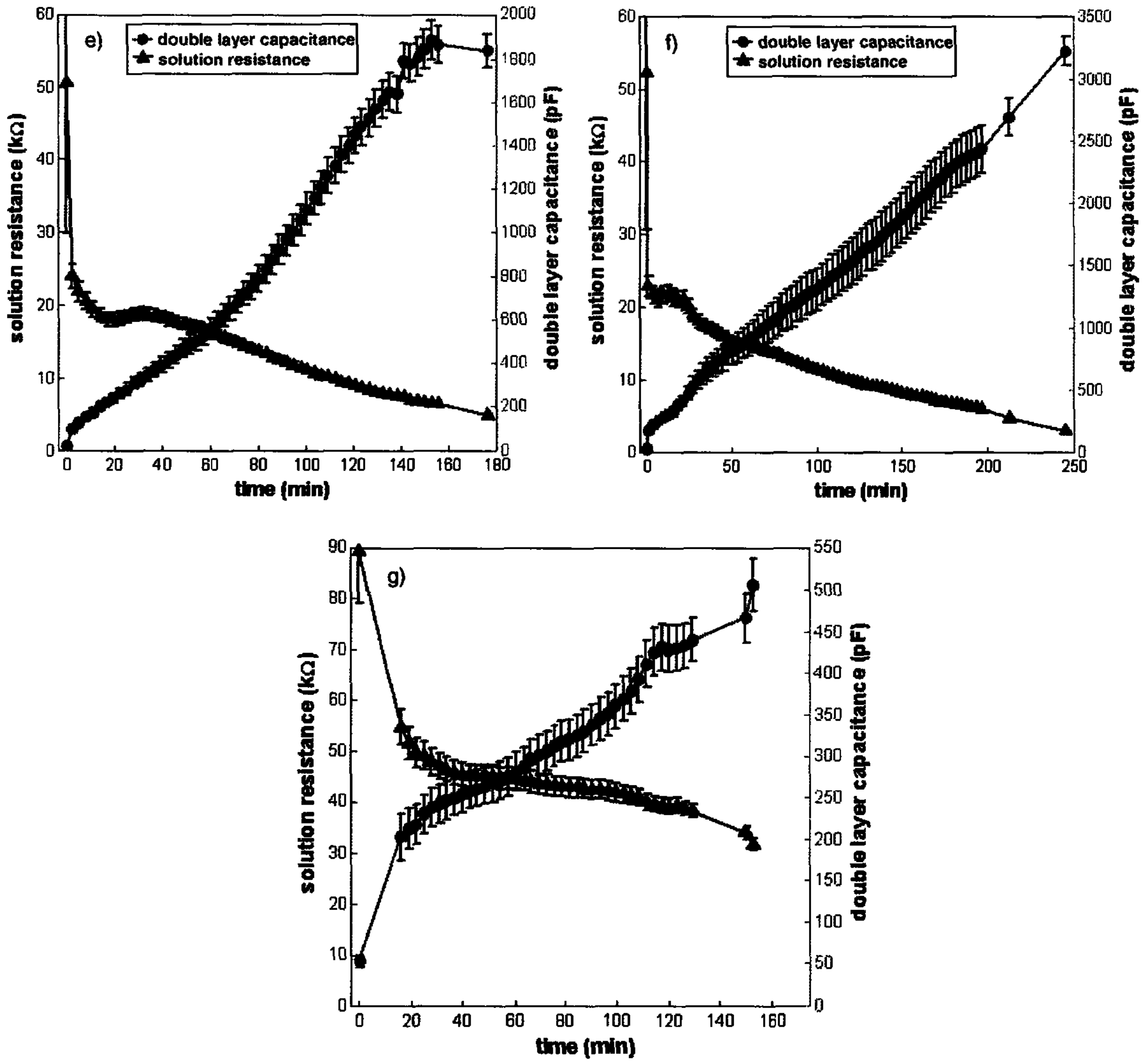

Figure 6.2e-g. Best fit values of solution resistance and double layer capacitance of device reservoirs during monitoring of release of C^{14} mannitol *in vivo*, with end of release marked if reached; **e)** device A1 reservoir blue7 released mechanically on day 5, **f)** device A4 reservoir blue6 released mechanically on day 6, **g)** device 2 reservoir white9 release on day 6 during first *in vivo* study showing very slow release.

The release profiles are qualitatively similar but show a wide range of release rates. As during the *in vitro* experiments in chapter 5, some but not all of the experiments showed an unexplained peak in the double layer capacitance. Three experiments also show brief reverses in the rate of change of the solution resistance during the beginning of monitoring. They are qualitatively similar to the uneven *in vitro* release experiments that were affected by obstruction of bubbles around the reservoir opening. It is possible that a similar phenomenon was responsible for the uneven release of mannitol *in vivo*, especially considering that both of the mechanically assisted release experiments (that had been exposed to air during opening) showed this reversal.

Table 6.3 summarizes the electrical characteristics and release times for each data set. Three release experiments were complete within the measurement period as determined by the rate of change of the solution resistance threshold method described in chapter 5. The observed release time varied between 3 and 5 hours for the completed experiments. Three of the incomplete experiments were nearing completion at the end of monitoring, as can be seen from the final solution resistance and the slowing of the rate of change of resistance. As mentioned above, device 2 white9 released significantly more slowly than the rest and may have taken up to 50 hours to fully release as measured by the slow rise in radioactivity released in the urine. For the three experiments that were complete within the monitoring period, the average final solution resistance and double layer capacitance were 2.5 ± 0.2 kΩ and 2700 ± 200 pF, respectively. The resistance value is in agreement with those measured for *in vitro* release, but the double layer capacitance is significantly higher by about one third. One possible explanation for the higher observed capacitance is the presence of proteins and other biological materials in the *in vivo* environment.

Table 6.3. Reservoir sensor electrical characteristics and release times for the seven *in vivo* release experiments.

release	day	silicon resistance (kΩ)	silicon capacitance (pF)	solution resistance at start (kΩ)	double layer capacitance at start (pF)	solution resistance at end* (kΩ)	double layer capacitance at end* (pF)	release time (min)
A2red2	5	112	44.9	77	48.9	2.41	2910	180
A4red4	11	32.7	22.6	198	11.7	2.68	2520	210
A1red2	11	34.6	27.2	117	29.1	3.02	4660	>260
A3blue6	12	21.2	36.4	56	19.7	2.41	2680	295
A1blue7	5	9.00	26.0	51	19.1	4.91	1840	>175
A4blue6	6	15.4	29.8	52	21.9	2.84	3230	>245
2white9	6	60.0	25.9	89	53.2	31.8	507	>>195

**End values of resistance and capacitance are at the end of release if it was reached; otherwise the values given are the last values recorded during the monitoring period.*

The variation in the release times, the low number of data points, and the short implantation times are such that a correlation between implantation time and release rate cannot be made from these data. It was expected that there should be a high degree of variability between experiments due to the variability in the tissue response between animal subjects. During the monitoring experiments, significant differences were observed in the amount of tissue irritation, fluid exudate, and type of exudate around the devices. These variations could be caused by the amount of movement of the animal, the range of motion of the device within the subcutaneous pocket, and the possibility of some degree of infection of the incisions. The wide range of release times helps to demonstrate the utility of the sensors in evaluating device performance in the face of inherent tissue response variability.

6.3. Conclusions

The impedance sensors were able to monitor release of the radiolabeled model drug mannitol from MEMS device reservoirs *in vivo* in real time. Sensor output was qualitatively similar to results obtained *in vitro*, as measured by the shape of the impedance spectra, the behavior of the solution resistance and double layer capacitance over time, and the final values of the solution resistance and double layer capacitance. Of the seven release experiments, three finished releasing during the monitoring period, within 3-5 hours. Three further devices were near the end of the release, giving an approximate range of release times of 3-7 hours, significantly longer than the 2 hour release times generally observed *in vitro* (with the exception of incompletely opened reservoirs in the flow cell and leak tests). One device showed significantly slower release, likely due to formation of a very small opening in the reservoir membrane. Scintillation counting of urine samples confirmed each release and showed the slow release to be complete after approximately 50 hours.

The amount of data collected was significantly limited by the breakage of membranes during packaging and during implantation, the unreliability of the corrosion protocol to open the reservoirs, and the limitation of the implantation time to two weeks due to degradation of the packaging *in vivo*. It was not possible to correlate the observed release times with the duration of device implantation due to the low number of data points and the limited implantation time. However, the variability in the release times shows the utility of the release sensors for evaluating drug release *in vivo*.

6.4. Recommendations

For future studies, it would be very interesting to have multiple release experiments per device at different times post-implantation to see how implantation time and the formation of a fibrous capsule around the device influence drug release. Histological examination of the fibrous capsule post-implantation and *ex vivo* release of drug through explanted capsule would yield information on how the structure of the tissue affects release rate. In addition, the release of drugs with more complex pharmacokinetics could yield new insights into *in vivo* transport barriers since the drug release rate from the device would be precisely known. Finally, the sensors could be used to evaluate different implant sites or biocompatible coatings *in vivo* to see how they affect the degree of implant isolation by the tissue.

All of these future studies would hinge on the ability to improve the packaging method to avoid membrane breakage and leaking and to increase the durability of the package *in vivo*. For longer implantation times, it would also be desirable to increase the flexibility of the wires connected to the device because stiff wires irritate the animals' skin and may start to erode through it. Although animal health remained good throughout both studies, it would be improved by the development of a more flexible package, especially for implantation times of three weeks or more. Also critical is the implementation of a more reliable activation method such as the 'fuse' chip developed at MicroCHIPS Inc. to achieve the necessary degree of device reliability for collection of a large and statistically significant data set.

6.5. References

---

1. E. Eriksson, F. Royo, K. Lyberg, H. E. Carlsson, and J. Hau, Effect of metabolic cage housing on immunoglobulin A and corticosterone excretion in faeces and urine of young male rats, *Experimental Physiology*, **89**, 427-433 (2004).
2. S. Roysommuti, T. Khongnakha, D. Jirakulsomchok, and J. M. Wyss, Excess dietary glucose alters renal function before increasing arterial pressure and inducing insulin resistance, *American Journal of Hypertension*, **15**, 773-779 (2002).
3. R. S. Shawgo, G. Voskerician, H. L. Ho Duc, Y. Li, A. Lynn, M. McEwan, R. Langer, J. M. Anderson, and M. J. Cima, Repeated in vivo electrochemical activation of MEMS drug delivery device and the biological effects, (accepted to *Journal of Biomedical Materials Research*).
4. J. C. Cloyd, B. D. Snyder, B. Cleeremans, and S. R. Bundle, Mannitol pharmacokinetics and serum osmolality in dogs and humans, *Journal of Pharmacology and Experimental Therapeutics*, **236**, 301-306 (1986).

7. Mathematical Simulation of Drug Release

The dissolution and diffusion of drug from the device reservoirs was simulated by finite differences and finite elements and compared to the release rates measured experimentally. Although the problem involves only diffusion without convection, the geometry of the reservoirs is sufficiently complex that an analytical solution is not possible. The dissolution of the solid mannitol creates a moving boundary within the problem that further complicates the simulation. Figure 7.1 shows a schematic of the dissolution of drug from a pyramidal reservoir.

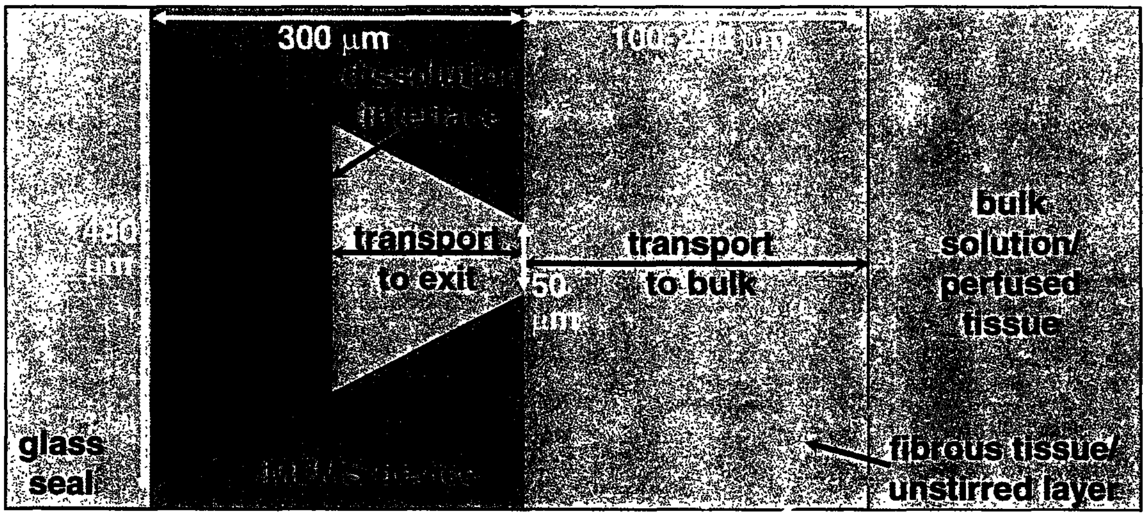

Figure 7.1. Dissolution of drug from a pyramidal drug reservoir through an unstirred layer or avascular fibrous capsule, in cross section.

Three models were developed: a cylindrical approximation of the reservoir programmed in MATLAB with finite differences, a finite element model in FEMLAB with the same geometry as the MATLAB model, and a conical approximation of the reservoir using finite elements in FEMLAB. The MATLAB model uses a mass balance at the interface and a stretch factor to track the dissolution interface as the simulation progresses. The FEMLAB programming environment is unable to cope with a moving boundary, so a concentration dependent diffusion coefficient was used to create a moving boundary within the simulation. The MATLAB and FEMLAB models of the same cylindrical geometry provide a check on one another to help ensure that the model results are valid, while the simulation of a conical geometry provides a close approximation to the actual pyramidal geometry of the reservoirs.

The conical reservoir model sheds light on the time lag observed between the sensor measurements and the scintillation measurements. The sensors detect the percentage of the reservoir filled with conductive solution, which is a function of the amount of solid drug that has dissolved. However, the scintillation measurements detect the amount of drug released, which is not the same as the amount dissolved because the dissolved drug must then exit the reservoir. Once all of the solid drug has dissolved, the sensor signal essentially stops changing, to within the limits of measurement error. The conical reservoir model predicts that about 10% of the mannitol remains in the reservoir in dissolved form after the solid drug is gone.

The time lag between the sensor measurements and the scintillation measurements should be equal to the time required to dilute the concentrated solution within the reservoir to the detection limit of the scintillation measurement. The detection limit of the flow cell measurement was approximately 0.1% of mannitol originally present in the reservoir, and the stirred beaker measurement could detect down to 2-3% of the original loading. Using these detection limits we obtain an expected lag time of 15 min for the stirred beaker setup and 45-65 min for the flow cell, compared to the 5-10 min and 60-70 min time lags observed experimentally.

The model gives an expected release time of 70 minutes, of the same order of magnitude as the experimentally measured release time of 115 minutes in the stirred beaker setup. One of the most useful aspects of the model is that it allows predictions to be made as to how changes in drug solubility, drug density, reservoir geometry, and transport conditions outside the reservoir should be expected to impact drug release. The conical reservoir model was also used to explore the effects of incomplete membrane removal and of unstirred layers of varying thickness outside the reservoir.

7.1. Numerical methods

The system to be modeled is difficult for two primary reasons: the presence of a moving boundary at the interface between solid and dissolved drug, and the complexity of the geometry of the reservoir. The FEMLAB programming environment is ideal for solving problems with complex geometry but not well suited to problems with moving boundaries. For this reason, the dissolution interface is simulated in FEMLAB by specifying the diffusion coefficient as a function of concentration. At concentrations less than or equal to the solubility of drug, the diffusion coefficient takes its normal value, but at higher concentrations (the solid drug) it is zero. An arctangent function smoothes the diffusion coefficient step change. However, a steep change in diffusion coefficient can lead to problems in the simulation if the mesh is not fine enough, and an extremely fine mesh makes the simulation time impractically long. The MATLAB model provides a check on the FEMLAB moving boundary, because the MATLAB model is able to use a mass balance at the interface to calculate the appropriate boundary position. However, it is difficult to program a complex geometry in the MATLAB model because it is discretized by hand. The MATLAB model therefore calculates the dissolution of drug from a cylindrical reservoir.

The problem of dissolution of drug from a complex geometry with a moving boundary was broken down into three parts:

1) A MATLAB finite differences model of a cylindrical reservoir with a mass balance at the interface to simulate the moving boundary
2) A FEMLAB model of the same cylindrical reservoir with the diffusion coefficient as a function of concentration to simulate the moving boundary
3) A FEMLAB model of a conical reservoir that closely resembles the actual geometry of the reservoir, with the diffusion coefficient as a function of concentration to simulate the moving boundary

The cylindrical FEMLAB model can then be compared to the MATLAB model to make sure that they give the same result. The diffusion coefficient step function and the mesh size are adjusted to simulate the behavior of the interface in the MATLAB model. The appropriate diffusion coefficient function and mesh size are then used in the conical FEMLAB model to evaluate the effects of the pyramidal reservoir geometry on dissolution time.

7.1.1. MATLAB model of cylindrical reservoir

A MATLAB finite differences model of dissolution and diffusion of a drug from a cylindrical reservoir into a dead space was developed as a part of Dr. Ken Beers' class on numerical methods in chemical engineering. The model geometry, boundary conditions, and initial conditions are shown in Figure 7.2.

Diffusion Equation:

$$\partial C/\partial t = (D/r)\ \partial/\partial r(r\ \partial C/\partial r) + D\ \partial^2 C/\partial z^2 + \Phi$$

Mass Balance at Interface:

$$\partial\lambda/\partial t = [-D/(C_{sat}-C_{solid})]^{*}\partial C/\partial z(z=\lambda)$$

Boundary Conditions:

$\partial C/\partial r=0,\ r=0,\ z\in[0,H+\delta]$

$\partial C/\partial r=0,\ r=R,\ z\in[\lambda,H]$

$C=0,\ r=R_0,\ z\in[H,H+\delta]$

$\partial C/\partial z=0,\ r\in[R,R_0],\ z=H$

$C=0,\ r\in[0,R_0],\ z=H+\delta$

Initial Conditions:

$C=0,\ r\in[0,R],\ z\in[\lambda_0,H]$

$C=0,\ r\in[0,R_0],\ z\in[H,H+\delta]$

$C=C_{solid},\ r\in[0,R],\ z\in[0,\lambda_0]$

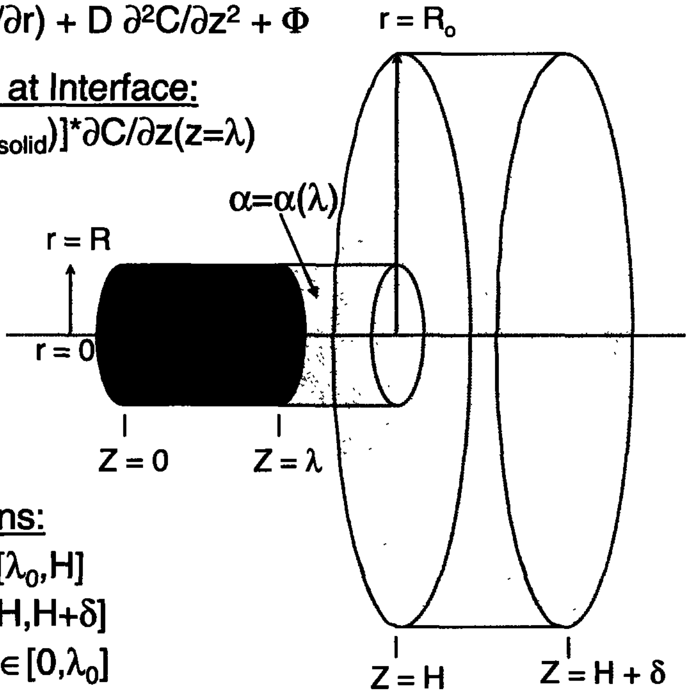

Figure 7.2. MATLAB finite differences model of drug dissolution from a cylindrical reservoir: geometry, differential equations, boundary conditions and initial conditions.

The simplified cylindrical system can be completely described by the geometric parameters H, R, R_o, δ, and λ, and the additional compound-specific parameters C_{solid}, C_{sat}, and D_{liquid}, defined in Table 7.1. The equations were scaled prior to simulation using R and C_{sat}, yielding the nondimensional variables concentration θ, radial coordinate η, axial coordinate ζ, and time τ as defined in Table 7.1. The differential equations were discretized by hand and solved using a MATLAB PDE solver routine written by Dr. Beers. The discretization introduces the additional parameters N_η, N_ζ, N_{ro}, and N_{zo}, which define the number of discrete points in the simulation in each direction and in each region.

Table 7.1. Definitions and values of variables used in MATLAB finite differences simulations.

variable / parameter	value / definition	description
R	25 μm	radius of cylindrical reservoir
H	300 μm	depth of cylindrical reservoir
R_o	150 μm	radius of unstirred layer at the reservoir opening
δ	200 μm	thickness of the unstirred layer at the reservoir opening
λ	—	distance between the dissolution interface and the back of the reservoir
λ_0	270 μm	position of the dissolution interface at time zero (90% full)
C_{solid}	1.489 g/cm^3	density of solid drug (mannitol)[1]
C_{sat}	0.182 g/cm^3	solubility of drug in water (mannitol)[2]
D_{liquid}	6.5×10^{-6} cm^2/s	diffusivity of drug in water (mannitol)[3]
τ	t^*D_{liquid}/R^2	dimensionless time
η	r/R	dimensionless radial coordinate
ζ	z/R	dimensionless axial coordinate
θ	C/C_{sat}	dimensionless concentration
θ_s	$C_{solid}/C_{sat}=8.18$	dimensionless concentration of the solid drug (mannitol)
N_η	10	number of discrete points in the radial direction between $\eta = 0$ and $\eta = 1$, for 1x mesh
N_ζ	20	number of discrete points in the axial direction between $\zeta = \ell/R$ and $\zeta = H/R$, for 1x mesh
N_{ro}	10	number of discrete points in the radial direction between $\eta = 1$ and $\eta = R_o/R$, for 1x mesh
N_{zo}	20	number of discrete points in the axial direction between $\zeta = H/R$ and $\zeta = (H+\delta)/R$, for 1x mesh
α	—	axial stretch factor for discrete points in the reservoir

The problem of a moving boundary is solved by the introduction of a stretch factor, α, into the discretization of the volume inside the reservoir. A mass balance at the dissolution interface determines how far the interface should move at each time step, and increases the value of α appropriately. The structure of the simulation means that the reservoir cannot be entirely full at the start of the simulation ($\alpha = 0$ is not allowed), so an initial interface position, λ_0, must be chosen. Once the interface has reached the back of the reservoir, the boundary becomes stationary with a no flux condition. The MATLAB m-files used in the simulation are given in appendix 10.7.

The simulation results described in this chapter use the parameter values given in Table 7.1, which were chosen to match the solubility, density, and diffusivity of mannitol. The diameter of the cylindrical reservoir is equal to the width of the square opening of a drug delivery MEMS reservoir. The initial interface position gives a reservoir 90% full of mannitol at the beginning of the simulation. The simulation was run with the discretization parameter values given in the table (1x mesh simulation) as well as with each parameter doubled (2x mesh simulation), to ensure that the 'mesh' or grid of points was sufficiently fine to capture the true behavior of the system. The time steps were adjusted by trial and error to keep the motion of the interface small with each time step, and the final values of time step size were sufficiently small that simulation output was independent of time step size to within 2-3%. Both the 1x and the 2x mesh simulations took 1000 steps of size 0.0001, then 100 steps of 0.01, and finally several thousand steps of 0.1 to complete the simulation.

7.1.2. FEMLAB model of cylindrical reservoir

A FEMLAB (finite elements) model was developed to mimic the MATLAB finite differences model described above. The geometry, diffusion equation, initial conditions, and boundary conditions are all identical to those shown in Figure 7.2 for the MATLAB model. The FEMLAB environment is not equipped to handle moving boundaries, so a concentration-dependent diffusion coefficient was used to effectively create a moving boundary within the reservoir subdomain. The diffusion coefficient equation uses an arctangent function to make a step change in the diffusion coefficient at the saturation concentration of mannitol, C_{sat}. Above C_{sat}, the diffusion coefficient drops to zero, while below C_{sat} it is equal to the diffusion coefficient for mannitol, D_{liquid}. The diffusion coefficient, D, is given by

$$D(C) = (D_{liquid}/\pi)\ \{\ \pi - (\pi/2 + \arctan[A_0(C-C_{crit})])\}$$

where C_{crit} and A_0 are parameters used to empirically adjust the step change position and steepness, respectively. A value of 0.1825 g/cm^3 was chosen for C_{crit}, just above the saturation concentration of mannitol.

The steepness of the step change, A_0, must be adjusted based on the fineness of the mesh. If the width of the step change is much smaller than the size of the elements, the simulation is not accurate. Likewise, if the step change is too wide, diffusion occurs in the solid and the dissolution interface is not sharp. A finer mesh can handle a steeper step change but takes longer to run. For this reason, two mesh sizes were selected and the value of A_0 was adjusted for each mesh size, to obtain the same dissolution time predicted by the MATLAB model. Both FEMLAB meshes used the following parameters: normal predefined mesh size, regular refinement method, r and z scale factors = 1, resolution of narrow regions =1, and resolution of geometry = 10.

The default time dependent solver was used for all simulations, with a relative tolerance of 0.01, an absolute tolerance of 0.001, and time steps determined automatically by the solver. The solution form was general, and the time dependent solver used a direct (UMFPACK) linear system solver at each step, with a 0.1 pivot threshold and 0.7 memory allocation factor.

The FEMLAB format is not well suited to output the interface position vs. time, but it can be calculated by analyzing the concentration profile along the centerline and reservoir wall at each time point. The concentration profiles at these boundaries were exported to MATLAB to extract the interface position as a function of time. An additional variable, C_{int}, was defined to track the amount of drug remaining in the reservoir as a function of time. The definition and variable type for C_{int} and other variables in the FEMLAB simulation are given in Table 7.2.

Table 7.2. Definitions and values of variables used in FEMLAB simulations.

variable	value	type	description
D_{liquid}	0.039 mm^2/min	constant	diffusivity
C_{solid}	1.489 mg/mm^3	constant	solid density
C_{crit}	0.1825 mg/mm^3	constant	step change parameter
A_0	500-10,000 mm^3/mg	constant	step change parameter
D(C)	$(D_{liquid}/\pi)\{\pi-(\pi/2+\arctan[A_0(C-C_{crit})])\}$	expression variable	diffusivity step change
C_{int}	$2\pi\int rCdr$ ($2\pi rC$ in FEMLAB)	integration coupling variable	amount of drug remaining

7.1.3. FEMLAB model of conical reservoir

The FEMLAB simulation was then modified to more closely approximate the geometry of a drug delivery MEMS reservoir. The reservoir is represented by a cone, with a reservoir opening of area equal to that of the square openings of actual devices. The angle and depth of the actual pyramidal reservoirs and the angle and depth of the cone are equal. The basic simulation imposes a boundary condition of zero concentration at the reservoir opening, with no dead space. The other boundaries have no-flux conditions, and the initial condition specifies that the reservoir is entirely filled with mannitol at concentration C_{solid}. The mesh size and steepness of the diffusion coefficient step change are identical to the best values found by trial and error using the cylindrical models. All parameters other than the geometry of the reservoir are the same as those listed for the cylindrical models. The radius of the reservoir opening is 0.028 mm, the radius of the back of the reservoir is 0.27 mm, and the reservoir depth is 0.3 mm.

Several additional simulations were performed using the conical reservoir geometry. Two of the simulations imposed a no flux condition on a portion of the reservoir opening, to simulate the effects of incomplete removal of the membrane cap from the reservoir. The center portion of the reservoir opening remained open with a boundary condition of C = 0, while the surrounding annulus had a no flux boundary condition. The radius of the central opening was chosen so that the area of the membrane-obscured reservoir opening was 10% or 25% of the original area of the reservoir opening. Several further simulations included an unstirred boundary layer outside the reservoir opening. The radius of the unstirred layer was 300 μm, and the barrier thicknesses were between 10 and 200 μm. The barrier thicknesses were chosen to be of the same order of magnitude as the ~100 μm fibrous capsule observed to form around drug delivery MEMS devices *in vivo.*[4]

7.2. Results and discussion

The results of each of the three simulations are given separately: the MATLAB finite differences model of dissolution of drug from a cylindrical reservoir with mass balance at the interface, the FEMLAB model of dissolution from a cylindrical reservoir with a concentration-dependent diffusion coefficient, and the FEMLAB model of dissolution from a conical reservoir with the optimized concentration-dependent diffusion coefficient.

7.2.1. MATLAB model results

The MATLAB model gave an expected dimensionless dissolution time of $\tau = 690 \pm 10$, which corresponds to a dissolution time t_{diss} of 11 ± 0.2 min. The dissolution time is defined as the time elapsed between the start of the simulation and the time when the dissolution interface reaches the back of the reservoir. Both the 1x and the 2x mesh simulations gave the same time to within 2%, indicating that the grid was sufficiently fine that the discretization did not significantly affect the results. The reported error in the predicted dissolution size was based on comparison of simulation results using the two mesh sizes. Figure 7.3 shows surface plots of the dimensionless concentration outside the reservoir at 7 snapshots in time. It is difficult to plot the concentration over the inside and outside areas in the same plot in the MATLAB environment. Figure 7.4 shows the position of the interface as a function of time, converted to dimensional parameters for simpler comparison with the FEMLAB model results.

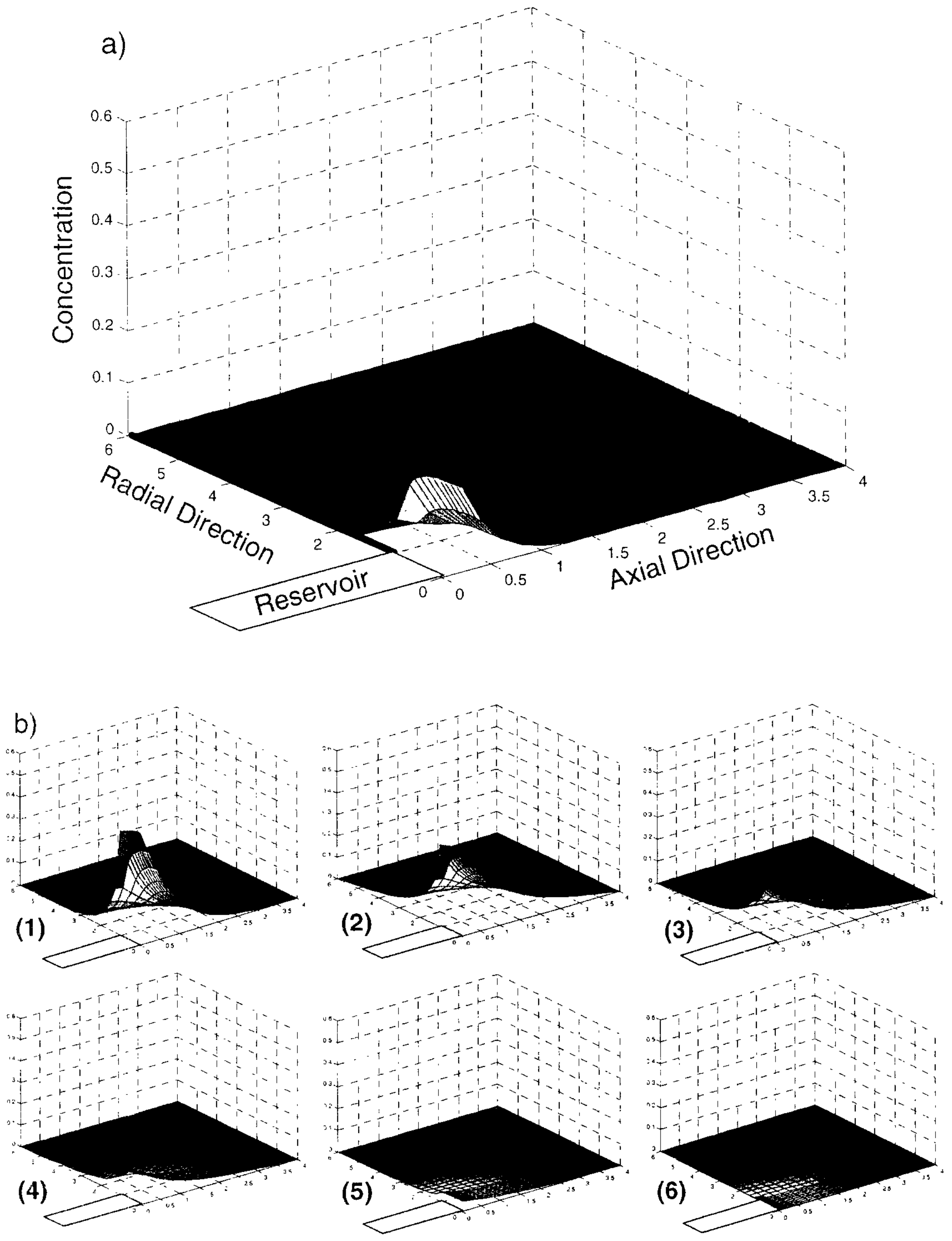

Figure 7.3. Dimensionless concentration of drug in the unstirred layer at the mouth of the reservoir, **a)** closeup view showing reservoir position and axis labels just after the start of dissolution, **b)** sequence of snapshots in time as the drug dissolves, showing how the concentration profile develops and then decays away. All axes have the same scale.

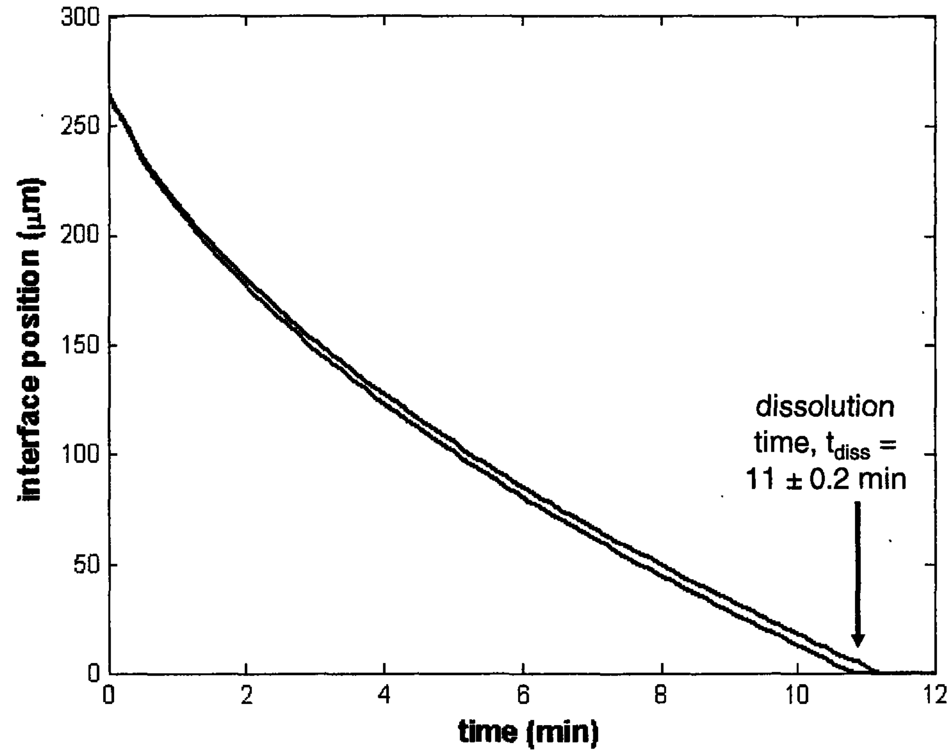

Figure 7.4. The distance between the dissolution interface and the back of the reservoir as a function of time for both the 1x and 2x mesh simulations, indicating the total dissolution time, t_{diss}.

7.2.2. FEMLAB cylinder model results

The rate of drug dissolution from cylindrical reservoir in the FEMLAB simulation was highly dependent on the size of the mesh elements compared to the steepness of the step change, A_0. Table 7.3 gives the calculated dissolution time for simulations using a variety of mesh sizes and steepness parameters. The first four simulations varied the mesh size while keeping the step change very steep. The dissolution time was heavily dependent on the mesh size and approached the dissolution time predicted by MATLAB as the mesh was progressively refined. These results indicated that the step change in diffusion coefficient was too steep with respect to the mesh size, causing nonphysical artifacts at the dissolution interface. Examination of the concentration profile at the interface showed an anomalously high concentration (higher than the solid concentration) at the interface when the step change was too steep.

The steepness parameter was then adjusted to obtain a dissolution time in agreement with the dissolution time predicted by the MATLAB simulation, which used a mass balance to move the interface. The optimal value of A_0 was determined for a 1x and a

2x refined mesh. The 1x mesh simulations run in a matter of minutes but are noticeably coarse, while the 2x simulations run over the course of several hours but give more detailed results. As expected, the coarser 1x mesh requires a lower value of A_0 (less steep step change), while the finer 2x mesh can handle a higher A_0 value. One cannot simply use a very gradual step change in diffusion coefficient because the interface would be nonphysically diffuse rather than sharp.

Table 7.3. Dissolution time calculated by FEMLAB simulation of drug dissolution from a cylindrical reservoir, as a function of mesh size and step change steepness parameter A_0.

mesh size	A_0 (units)	t_{diss} (min)	% drug remaining at t_{diss}	1% lag time (min)
normal	10,000	101	1.9	0.8
refined 1x	10,000	55.8	2.5	1.1
refined 2x	10,000	30.5	3.2	1.4
refined 3x	10,000	16.9	5.2	1.8
refined 1x	1000	14.0	6.1	2.0
refined 1x	700	12.0	6.7	2.1
refined 1x	550	11.0	7.0	2.1
refined 1x	500	10.7	6.9	2.1
refined 2x	2000	12.9	6.1	2.0
refined 2x	1200	11.0	6.6	2.0
refined 2x	1000	10.5	7.1	2.1

Also listed in Table 7.3 is the time lag between full dissolution of the solid and the time when only 1% of the drug remains within the reservoir. When the solid has dissolved, approximately 2-7% of the mannitol originally present in the reservoir remains inside the reservoir in dissolved form. The discrepancy between the release time measured by the sensors and that measured by scintillation counting of the release medium (described in chapter 5) is thought to be due to the fact that release is not complete when the solid has fully dissolved. The sensors measure the dissolution of solid mannitol within the reservoir, while the scintillation counting of the release medium measures the release of mannitol from the reservoir. The time lag between the two measurements should be the time between the dissolution of the last of the solid drug, t_{diss}, and the time when the amount of mannitol remaining in the reservoir reaches the detection limit of the scintillation measurement. The time lag for a detection limit of 1% is given for reference. The lag time is relatively invariant with the mesh size and A_0, supporting the idea that the variation in dissolution time is caused by poor simulation of the interface, not by the simulation of diffusion in the liquid.

According to the results in Table 7.3, a 1x refined mesh should use a steepness parameter of 550 and a 2x refined mesh should use a steepness parameter of 1200, in order to match the dissolution time predicted by the MATLAB model. The finer mesh yields smoother, more detailed results but takes significant computation time. Figure 7.5 shows the interface position over time for both the MATLAB and FEMLAB simulations of drug dissolution from a cylindrical reservoir. The discrete jumps in the interface position seen in the FEMLAB plot occur at the nodes of the mesh. The agreement between the two models is reasonably good.

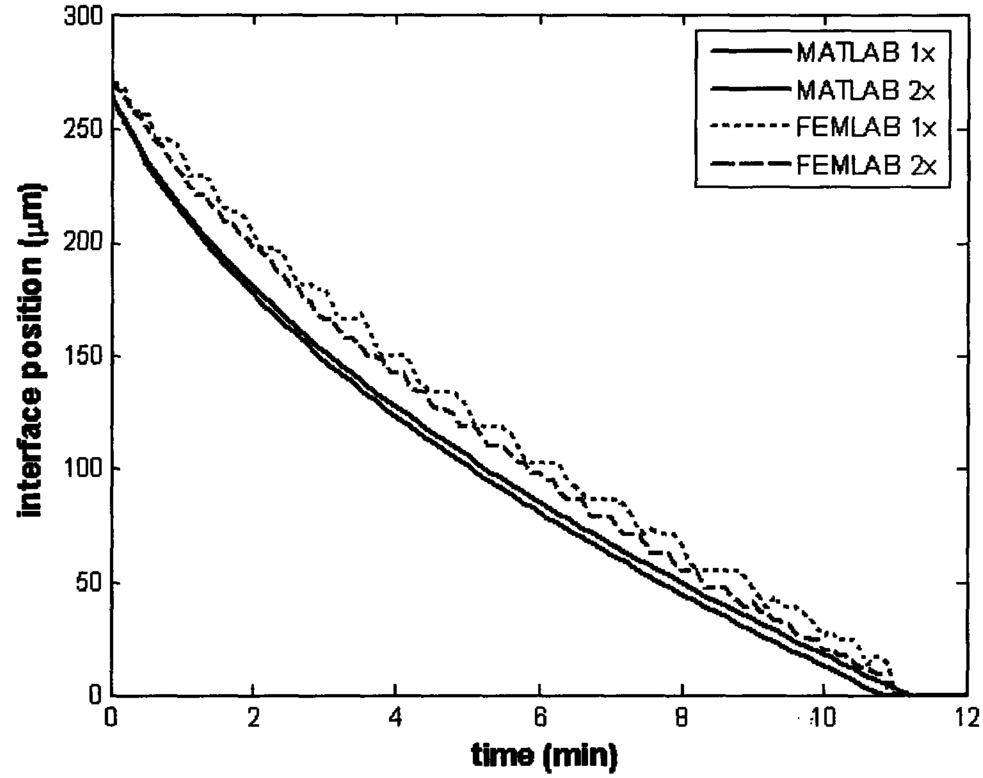

Figure 7.5. Comparison of the interface position profile calculated by the MATLAB simulation using a mass balance at the interface and by the FEMLAB simulation using a concentration-dependent diffusivity.

Figure 7.6 shows a series of surface plots of the concentration profile in the simulation space over the course of the simulation for a 1x refined mesh. White areas of the reservoir are filled with solid drug, which has a concentration in excess of the limits of the scale bar. The concentration profiles are reasonable despite the roughness of the dissolution boundary. Analysis of individual concentration profiles along an axial cross section of the reservoir indicate that there is some artificial buildup of drug at the boundary due to the step change in diffusivity. Decreasing the steepness parameter or increasing the resolution of the mesh alleviate this artifact but do not eliminate it entirely.

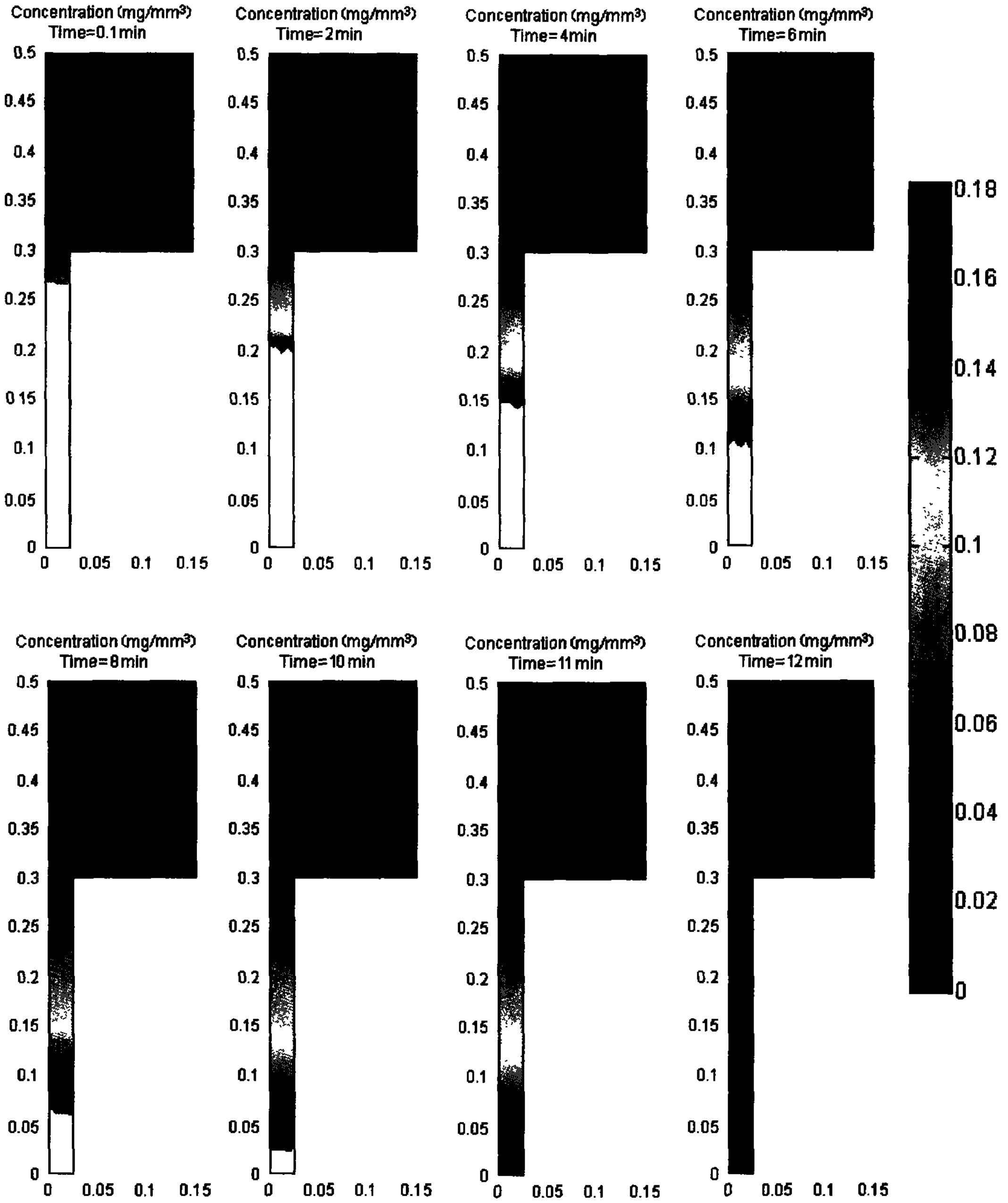

Figure 7.6. Concentration of mannitol in the cylindrical reservoir and unstirred space as a function of time, as calculated by the FEMLAB model.

7.2.3. FEMLAB conical model results

The simulation of drug dissolution from a conical reservoir should approximate the experimentally observed dissolution times for pyramidal reservoirs. Figure 7.7 shows a series of surface plots of concentration in the reservoir during drug dissolution for a simulation using a 2x refined mesh with $A_0 = 1200$ (the optimal steepness parameter as discussed in 7.2.2). The dissolution of solid is complete after 71.9 minutes.

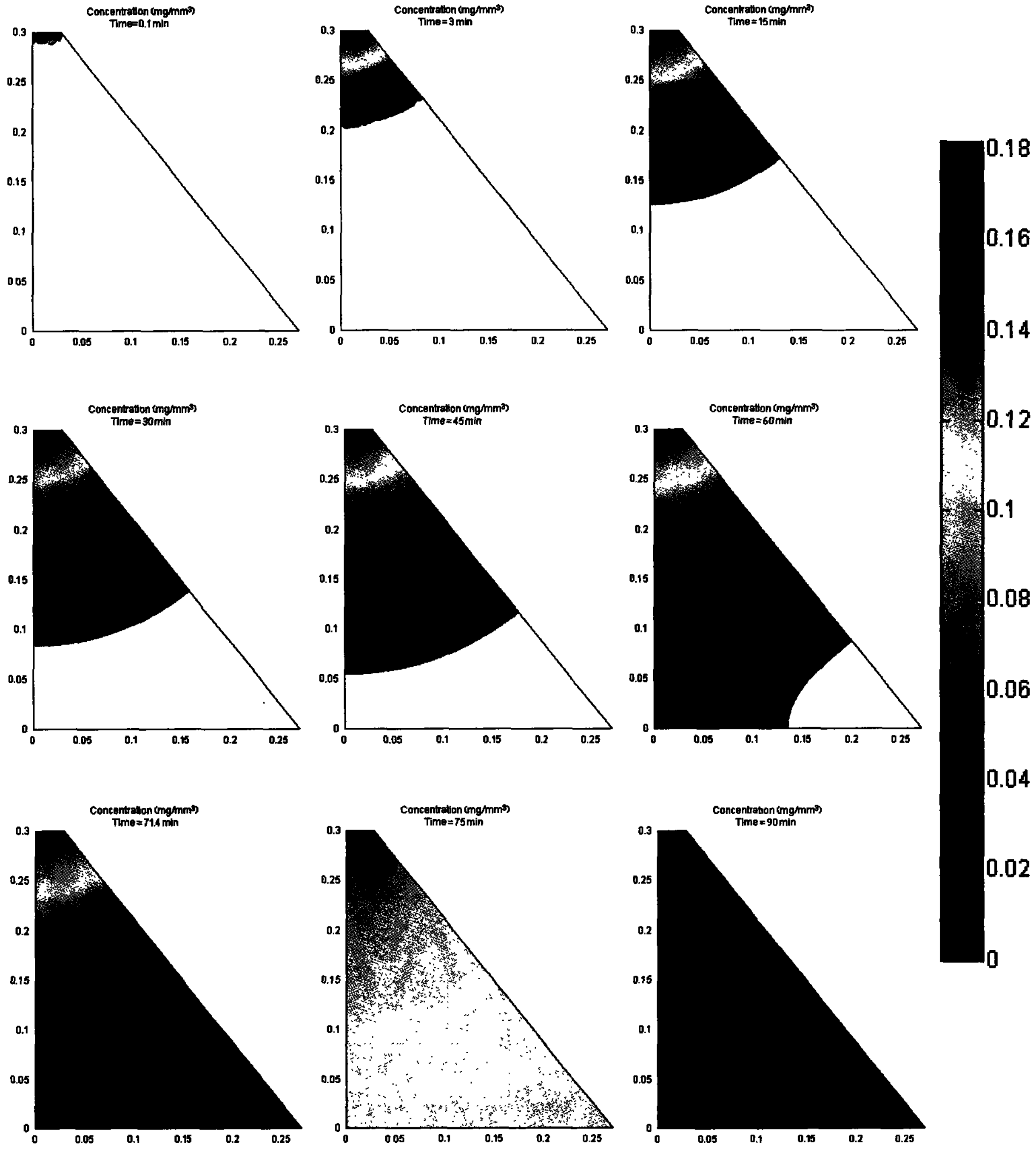

Figure 7.7. Concentration of mannitol in the conical reservoir FEMLAB simulation as a function of time.

It is interesting to see that the dissolution interface is curved because of the reservoir wall angle. The curvature of the interface makes the prediction of solution resistance and double layer capacitance difficult. Figure 7.8 shows estimated profiles of solution resistance, double layer capacitance, and amount of mannitol released over time. The resistance and capacitance values are estimated using the position of the interface along the wall of the reservoir. The inflection in the capacitance is due to the increased rate of dissolution as the interface reaches the back of the reservoir along the centerline. The model predictions are in qualitative agreement with the impedance sensor and scintillation measurements of drug release.

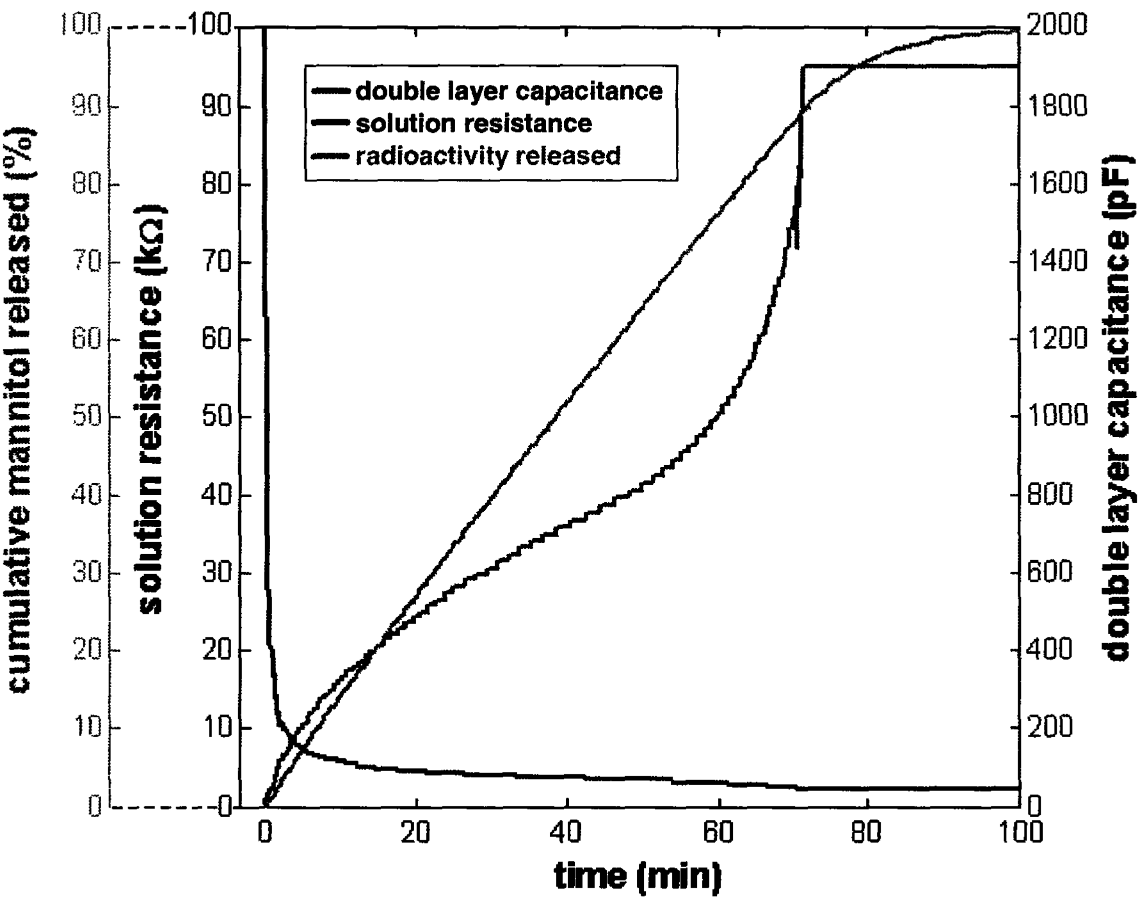

Figure 7.8. Solution resistance, double layer capacitance, and the amount of mannitol released as a function of time, as predicted by FEMLAB simulation of dissolution of drug from a conical reservoir.

The solid dissolves completely after approximately 72 min, on the same order of magnitude as the dissolution time of 115 min measured by the impedance sensors for release in stirred PBS solution. The model allows us to calculate the amount of mannitol remaining within the reservoir after the dissolution of solid is complete, which is approximately 10% of the total amount of mannitol in the reservoir at time zero. It is theorized that the lag time between the end of release measured by the sensors and the release time measured by scintillation of the release medium is due to the dilution of concentrated mannitol solution out of the reservoir following dissolution of the solid. The stirred PBS solution experiments gave a 5-10 min time lag for a 2-3% detection limit, while the flow cell experiments gave a 60-70 min time lag for a detection limit between 0.01-0.1%. The model predicts that the time between the dissolution of the last of the solid phase and the time when only 2-3% of the original amount of mannitol loaded remains in the reservoir should take approximately 15 min. The dilution of the dissolved mannitol to 0.1% of the original amount loaded is predicted to take approximately 45 min. Dilution to 0.01% takes more than 57 min, the end of the simulation. The simulated and experimental lag times agree very well, lending support to the idea that they arise from the dilution of mannitol out of the reservoir after dissolution of the solid.

Additional simulations were performed to explore the effects of incomplete membrane removal during reservoir opening. Table 7.4 shows the expected dissolution time for reservoirs with an impermeable membrane over a portion of the reservoir opening. As expected, incomplete removal of the gold membrane cap from the reservoir opening can significantly delay the release.

Table 7.4. Dissolution time calculated by FEMLAB simulation of drug dissolution from a conical reservoir with part of the reservoir opening obscured by an impermeable barrier (incompletely removed membrane).

reservoir opening (% original area)	t_{diss} (min)	% drug remaining at t_{diss}	1% lag time (min)
100% (not obscured)	71.9	10.3	22.1
50%	83.8	10.6	25.9
25%	108.1	10.8	34.1
10%	150.6	11.2	48.5

Finally, the model was used to see how an unstirred layer over the reservoir opening would affect the dissolution time. This provides a prediction of how sensitive the impedance measurement method would be to the formation of a fibrous tissue barrier layer over the device. Table 7.5 gives the predicted dissolution time for a mannitol-filled reservoir with an unstirred layer 10-200 μm thick over the opening. The release time slows as the barrier layer becomes thicker, but the release time is not as sensitive to barrier thickness as the layers become thicker than approximately 50 μm. These results, in combination with the results in Table 7.4, suggest that the reservoir opening is sufficiently small that it limits the rate of drug release. A larger reservoir opening would allow faster release, and a faster release would be more sensitive to the thickness of the fibrous capsule barrier layer outside the reservoir. Therefore, if the sensors were to be used to monitor fibrous capsule formation *in vivo*, it would be advisable to make the reservoir opening larger than the current 50 × 50 μm opening on current devices. However, if it was desired to make the drug release rate independent of the fibrous capsule thickness for reproducible release rates during an extended implantation time, a smaller reservoir opening could be used.

Table 7.5. Dissolution time calculated by FEMLAB simulation of drug dissolution from a conical reservoir with an unstirred barrier layer over the reservoir opening.

barrier thickness (μm)	t_{diss} (min)	% drug remaining at t_{diss}	1% lag time (min)
0 (none)	71.9	10.3	22.1
10	85.8	10.6	26.2
20	93.8	10.6	28.8
50	103.8	10.8	32.2
100	108.6	10.7	33.4
200	110.8	10.8	34.4

7.3. Conclusions

The dissolution of solid drug from the reservoirs of the MEMS device was simulated in MATLAB and FEMLAB for a cylindrical reservoir, and in FEMLAB with the pyramidal geometry simplified to a cone in cylindrical coordinates. The MATLAB program used a mass balance at the interface and an axial stretch factor to track the moving dissolution boundary over time. In FEMLAB the dissolution interface was simulated by a step change in the diffusivity at the saturation concentration. The predicted dissolution time was very sensitive to the steepness of the diffusivity step change in relation to the mesh size. If the step change occurs over a distance much shorter than the element size, the model predicts a concentration peak at the dissolution interface. The steepness parameter was empirically adjusted in the cylindrical FEMLAB model to give the same dissolution kinetics as predicted by the MATLAB program with a mass balance at the boundary. The steepness parameter was adjusted to 550 for a 1x refined mesh, and 1200 for a 2x refined mesh.

The optimal mesh and steepness parameter were then used in the FEMLAB simulation of a conical reservoir that closely approximates the actual pyramidal reservoir geometry. The predicted release time of 72 min for mannitol dissolution is of the same order of magnitude as experimentally measured release times. The lag time between the end of dissolution of the solid and the dilution of the concentrated solution in the reservoir to the detection limit was approximately the same as the lag between the release times measured by the impedance sensors and those measured by scintillation of the release medium. The model therefore supports the assumption that the sensors are most sensitive to the dissolution of solid drug rather than the dilution of concentrated drug solution. Simulations of dissolution through unstirred barrier layers of varying thicknesses suggest that the current opening size of 50 × 50 μm is small enough that it begins to limit the rate of drug release, and that incomplete removal of the gold membrane cap over the reservoir can significantly affect release time. The reservoir opening could be made larger to make the drug release rate more sensitive to the formation of a fibrous capsule over the reservoir, to facilitate measurements of fibrous capsule formation *in vivo*. Alternatively, the a smaller reservoir opening could be used to limit the rate of drug release and make it independent of the properties of the external surroundings during long implantation times.

7.4. Recommendations

The current MEMS drug delivery sensing device is limited in its sensitivity to the transport characteristics of the tissue surrounding the implant by the variability in the size of the reservoir opening. The variability in reservoir opening size arises from incomplete corrosion and removal of the membrane over the reservoir. The opening size could be made more consistent by changing the membrane cap over the reservoir to a fuse, similar to the 'fuse chips' developed by MicroCHIPS, Inc. In addition, the reservoir opening size should be increased to make the drug release rate more sensitive to the thickness of the fibrous capsule. Simulations indicate that the current 50 × 50 μm opening is sufficiently small that it begins to limit the rate of drug release.

The conical approximation of a drug reservoir is sufficient to describe the approximate rate of drug release observed experimentally. The presence of simulation artifacts at the moving boundary due to the diffusivity step change could be alleviated by simulations with a finer mesh. The steepness parameter for the step change would need to be adjusted using the cylindrical models to give accurate dissolution kinetics in the finer mesh. The FEMLAB conical model could then be used to predict drug release rates under a variety of conditions. The potential effects of wider reservoir openings or deeper reservoirs could be modeled to predict how fabrication changes would affect drug release. The expected release rates for different compounds of interest could be predicted as well as the possible effects of different drug formulations. The model could also be used in conjunction with *in vivo* data on drug release through fibrous capsules to model drug transport through the fibrous tissue layer.

7.5. References

---

1. D. R. Lide, ed., Physical constants of organic compounds, in *CRC Handbook of Chemistry and Physics*, 73rd ed., p. 3-314, Boca Raton, FL (1992).
2. M. Windholz, ed., *The Merck Index*, 10th ed., Merck & Co., p. 818, Raway, NJ (1983).
3. P. E. Liley, R. C. Reid, and E. Buck, Physical and chemical data, in *Perry's Chemical Engineers' Handbook*, 6th ed., R. H. Perry and D. W. Green, Editors, p. 3-259, McGraw-Hill, New York (1984).
4. G. Voskerician, M. S. Shive, R. S. Shawgo, H. von Recum, J. M. Anderson, M. J. Cima, R. Langer, Biocompatibility and biofouling of MEMS drug delivery devices, *Biomaterials*, **24**, 1959-1967 (2003).

8. Microscale Lyophilization and Drying of Proteins

Concurrently with the development of the impedance sensors, we developed methods for drying and lyophilizing proteins from solution within nanoliter scale reservoirs of a drug delivery MEMS device. The goal of this side project was to enable the loading of reproducible amounts of active proteins within the drug reservoirs of the device. The activity of the serine proteases trypsin, elastase, and collagenase, and of the cysteine protease papain, was studied before and after 'micro drying' and 'micro lyophilization' within device reservoirs by means of fluorogenic peptide substrate assays. To better understand what aspects of the microscale processes affect protein stability, the enzymes were also lyophilized and dried from bulk solution with the same formulation components. For papain and trypsin, the micro drying process preserved the most enzyme activity of all four processes studied. For elastase and collagenase, the traditional method of lyophilization from bulk solution preserved the most activity of the four processes. For all of the enzymes studied, it was possible to preserve at least 60% of the enzyme activity after processing in the MEMS reservoirs by means of either micro drying or micro lyophilization. The results presented in this chapter were submitted to the journal *Pharmaceutical Research* for publication as a note[1], and the microscale lyophilization and drying methods were submitted to the US Patent office[2].

8.1. Introduction

The development of stable drug formulations is crucial to the efficacy of drug delivery devices. Protein pharmaceuticals constitute a class of therapeutic compounds that it would be useful to be able to deliver in the complex profiles achievable in the MEMS drug delivery platform. It was desired to fill the microreservoirs with a reproducible amount of dry, stable protein formulation. Working with small, precise amounts of dry powders is difficult, so methods were developed to dry or lyophilize proteins from solution within the microscale reservoirs (herein referred to as 'micro drying' and 'micro lyophilization' processes). It was unknown what effect the small solution volumes and high reservoir wall surface areas would have upon the proteins, since obtaining active protein formulations is difficult and the complexity of proteins means that formulation is often a matter of educated guesswork combined with trial and error[3,4].

To explore the effects of the 'micro drying' and 'micro lyophilization' processes on the activity of proteins, a series of experiments was conducted using the proteolytic enzymes trypsin, papain, collagenase, and elastase[5,6,7,8]. The activity of these enzymes may be quantified by assays involving fluorogenic peptide substrates[9,10,11,12,13]. The use of fluorescence-based assays rather than colorimetric or other assays provided the increased sensitivity necessary to detect the activity of very small amounts of protein contained within the MEMS microreservoirs. To better understand the effects specific to the microscale drying and lyophilization processes, the enzymes were also dried and lyophilized from bulk solution under similar conditions. For two of the enzymes studied, micro drying preserved the most activity of any of the processes studied, while for the other two, traditional lyophilization proved best. It was surprising to find that the simple drying from nanoliter scale droplets in the reservoirs was in some cases better than lyophilization. In all cases, it was possible to add excipients to preserve at least 60% of the original enzyme activity in the drug delivery MEMS device using either the micro drying or the micro lyophilization process. Several additional experiments were conducted to try to understand what aspects of the microscale processes were most important in determining the amount of enzyme activity preserved.

8.2. Experimental

8.2.1. Materials

Trypsin (bovine pancreatic, twice crystallized lyophilized), elastase (porcine pancreatic, twice crystallized aqueous suspension), and collagenase type II (clostridium histolyticum, lyophilized) were purchased from Worthington Biochemicals, Lakewood, NJ. Papain (papaya latex, twice crystallized lyophilized) was purchased from Sigma, St. Louis, MO.

The trypsin substrate rhodamine 110 bis-(benzyloxycarbonyl-L-arginine amide) dihydrochloride (BZAR), the elastase substrate rhodamine 110 bis-(benzyloxycarbonyl-L-alanyl-L-alanyl-alanine amide) dihydrochloride (BZTAlaR), and the papain substrate 7-amino-4-methylcoumarin benzyloxycarbonyl-L-phenylalanyl-L-arginine amide hydrochloride (AMCFA) were purchased from Molecular Probes, Eugene, OR. The collagenase substrate rhodamine 110 bis-(glycine-proline-leucine-glycine-prolyl-amide), (GPLGP) was purchased from Beckman-Coulter, Miami, FL.

Tromethamine buffer as Trizma preset pH 8.8 crystals, N-[2-hydroxylethyl] piperazine-N'-[2-ethanesulfonic acid] (HEPES), Tween-20, 0.1% Brij-35 in water, dimethyl sulfoxide (DMSO), dimethyl formamide (DMF), sodium phosphate monobasic monohydrate, potassium phosphate monobasic, DL-dithiothreitol, ethylenediaminetetraacetic acid

(EDTA), 1 M calcium chloride, 1 N HCl and 1 M NaOH solutions were purchased from Sigma.

8.2.2. Drug delivery MEMS devices

The fabrication of the drug delivery MEMS devices is described in chapter 3. The devices used in this study were a simplification of the full device, consisting of pyramidal reservoirs etched into silicon, without the activation electrodes. Instead of reservoirs etched entirely through a 300 µm double side polished wafer, the reservoirs used for the enzyme activity studies were etched partially through a 500 µm test wafer. The anisotropic etching method leaves the <111> crystal planes of the silicon exposed on the sides of the reservoir. The bottoms of the reservoirs were silicon rather than the gold membranes of a fully processed device. However, the majority of the surface area within the reservoirs is the <111> silicon crystal plane in both cases, so results should be quite similar. Devices were loaded by microinjection of solution into the wide end of the reservoir. The devices were left unsealed after filling and submersed in solution to effect release.

8.2.3. Processing methods

Each of the four enzymes was subjected to each of four procedures: micro drying, micro lyophilization, drying, and lyophilization. Prior to each procedure, a solution of the enzyme was prepared, consisting of enzyme and 0.0005% Tween-20 in DI water. The enzyme concentrations in the solutions were 4 mg/ml trypsin, 266.7 µM elastase, 1 mg/ml collagenase, and 4 µM papain. In addition, the trypsin solution was acidified with 1 mM hydrochloric acid, according to standard practice [3,14]. These solutions are the basis for the results in Table 1. The solutions used for the additional results in Table 2 were identical in composition except for the specific modifications noted in the table. Each of the four procedures – micro drying, micro lyophilization, drying, and lyophilization – was performed using a freshly prepared enzyme solution.

Micro drying consisted of 3 steps: microinjection of the enzyme solution into drug delivery MEMS device reservoirs at a rate of 20 nl/s, 29.1 nl per reservoir; air drying of the solution in the reservoirs at room temperature; storage under vacuum until the activity assay. An UltraMicroPump II microinjector (World Precision Instruments, Sarasota, FL) was used for all microinjection steps, with a 50 µl glass syringe and a 32 gauge metal needle (Hamilton, Reno, NV). Air drying of the solution took approximately 10 s for these small droplets.

Micro lyophilization consisted of 4 steps: microinjection of the enzyme solution into drug delivery MEMS device reservoirs in contact with a metal block at approximately 5°C at a rate of 20 nl/s, 29.1 nl per reservoir; transfer of the devices to a frozen copper block at approximately –80°C to allow the solution to freeze; transfer of the devices and frozen block to vacuum to sublimate the water; storage under vacuum until the activity assay. The cold injection temperature was necessary to prevent rapid drying of the solution during microinjection. The solution froze within seconds following contact of the device with the frozen block. Sublimation of the water under vacuum took place in less than 30 minutes.

For the drying procedure, an aliquot of 2.5 ml of enzyme solution was placed in a 22 ml glass scintillation vial. The solution was evaporated at room temperature under a stream of dry argon gas over a period of 30 hours, then stored under vacuum until the activity assay.

For the lyophilization procedure, an aliquot of 2.5 ml of enzyme solution was placed in a 22 ml glass scintillation vial. The vial was brought into contact with a frozen copper block at approximately –80°C to allow the solution to freeze. The freezing step took between 1-2 minutes. The vial and frozen block were then placed in a lyophilization flask and placed on a FreezeMobile 25EL Lyophilizer (Labconco, Kansas City, MO). The enzyme was then stored under vacuum until the activity assay.

8.2.4. Enzyme activity assays

The activity of each enzyme was measured after processing and compared to the activity of unprocessed enzyme as received from the vendor. For trypsin, elastase, and papain, eight cuvettes with enzyme concentrations spanning two orders of magnitude were prepared and an aliquot of substrate was added to each cuvette at time zero. For collagenase, eight cuvettes were prepared with a range of substrate concentrations and an aliquot of enzyme was added at time zero. The fluorescence of each cuvette was measured following incubation using a PTI fluorescence system (Photon Technology Inc., Lawrenceville, NJ).

The trypsin assay solution contained 20 mM calcium chloride, 10 mM HEPES, 0.0005% (v/v) Tween-20, 10% (v/v) DMSO, and 0.1 µg/ml BZAR in DI water adjusted to pH 7.50 with sodium hydroxide. Trypsin at concentrations from 0 to 1000 ng/ml was incubated with the substrate for 10 minutes and the fluorescence measured at excitation and observation wavelengths of 492 and 523 nm, respectively. The elastase assay solution contained 20 mM calcium chloride, 10 mM Trizma, 0.0005% (v/v) Tween-20, 18% (v/v)

DMF, and 0.9 mM BZTAlaR in DI water adjusted to pH 8.8 with hydrochloric acid. Elastase at concentrations from 0 to 100 nM was incubated with the substrate for 20 minutes and the fluorescence measured at excitation and observation wavelengths of 492 and 523 nm. The collagenase assay solution contained 20 mM calcium chloride, 10 mM HEPES, 0.0005% (v/v) Tween-20 and 0.1µg/mL collagenase in DI water adjusted to pH 7.50 with sodium hydroxide. The collagenase was incubated with GPLGP concentrations from 0.0 to 0.7 nmol/ml for 3 hours in a water bath at 37 ± 2°C and the fluorescence measured at excitation and observation wavelengths of 492 and 523 nm. The papain assay solution contained 0.1 M sodium potassium phosphate, 2 mM dithiothreitol, 0.09 mM EDTA, 0.1% (w/v) Brij-35, 1% (v/v) DMSO and 3 µm AMCFA adjusted to pH 6.8 with sodium hydroxide. Papain at concentrations from 0 to 20 nM was incubated with the substrate for 10 minutes and the fluorescence measured at excitation and observation wavelengths of 380 and 460 nm.

8.2.5. Data analysis

The fluorescence data were plotted vs. the enzyme concentration for trypsin, elastase, and papain. The reaction rates were linear with slope proportional to the enzyme activity as expected for initial rate data with substrate in excess[15]. The percentage of enzyme activity lost after processing is equal to the percentage difference in the slopes of processed and unprocessed enzyme. For collagenase, an analysis of data taken at different substrate and enzyme conditions showed that $K_M >> S$, giving a nearly flat Hanes plot (S/v vs. S) and linear plot of v vs. S, where K_M is the Michaelis-Menten constant, S is the substrate concentration, and v is the reaction velocity. In this case, a plot of fluorescence vs. substrate concentration is linear, with the slope proportional to the enzyme activity. Although the x axis of the plot is different, it is again true that the percentage of enzyme activity lost after processing is equal to the percentage difference in the slopes of processed and unprocessed enzyme.

Each assay was performed in triplicate or more to allow calculation of the error associated with the measurement. Several processing experiments and assays were repeated on different days and combined to assess the variability in the measurement. Two types of error analysis were performed. For the first, the standard deviation of the three or more measured slopes was calculated and propagated through the calculation. For the second, the standard deviation associated with the best fit slope was calculated for each slope and propagated through the calculation. The reported error is the greater of the two calculated standard deviations.

8.3. Results and discussion

The percentage of original enzyme activity remaining after the enzyme was subjected to each of the four processing methods is shown in Table 1. In each case, the formulation was very simple, including a small amount of surfactant in all cases and acidified solution for trypsin. It was desired to avoid the complications inherent in choosing appropriate excipients for the initial experiments, in order to more closely study the effects of microscale processing vs. processing in bulk. Although the long term stability of protein formulations is also important, only stability during processing is considered here.

Table 8.1. Percent of original enzyme activity remaining post-processing by both microscale and bulk processing methods.

process	papain	trypsin	elastase	collagenase
micro drying	57 ± 3	88 ± 2	62 ± 1	76 ± 4
micro lyophilization	38 ± 2	74 ± 2	73.4 ± 0.8	56 ± 3
drying	32.0 ± 0.3	25 ± 3	59.5 ± 0.6	85 ± 2
lyophilization	39.8 ± 0.4	77 ± 2	80 ± 1	99 ± 2

The results vary significantly for the different enzymes studied according to their particular structures and sensitivities. Interestingly, the micro drying process preserved the maximum amount of enzyme activity for papain and trypsin. For both enzymes, the lyophilization and micro lyophilization processes produced similar results, and the drying process yielded the least amount of activity. These results suggest that these enzymes are not particularly sensitive to the increased surface contact[16,17] and microinjection shear forces[18,19] inherent in the microscale processing. The dramatic difference between micro drying and drying is likely due to the much shorter time required for drying (10 s vs. 30 hours), and perhaps related to the tendency of both these enzymes to self-digest in solution[5,6,12]. The improved performance of micro drying as opposed to bulk lyophilization may be due to the fact that lyophilization causes both freezing and drying damage[1].

Due to the low amount of papain activity preserved during most of the processing steps, several excipients were added to the solution to attempt to stabilize the enzyme, shown in Table 2. However, the addition of mannitol, acetate or dithiothreitol did not improve the enzyme stability in this case. To study the effect of microinjection on trypsin, trypsin solution was microinjected into cold MEMS reservoirs and assayed without drying or lyophilizing the solution. The amount of activity preserved was the same as that for micro lyophilization. Interestingly, the activity preserved was lower than that preserved during micro drying, which involves the same microinjection procedure but with room temperature reservoirs. Unfortunately, it was not possible to microinject enzyme into room temperature reservoirs without drying the solution because evaporation is rapid, so it is difficult to directly study the effect of low temperature reservoirs on enzyme activity. Although the underlying mechanisms are not clear, the data show conclusively that micro drying was the least damaging of the processes studied for trypsin and papain.

Table 8.2. Percent of enzyme activity remaining post-processing under modified conditions (excipients, surfactants).

process	enzyme	% activity remaining
micro drying, 0.01% Tween	elastase	60 ± 1
micro drying, 10% (w/w) mannitol	elastase	72.0 ± 0.9
micro lyophilization, 10% (w/w) mannitol	elastase	82 ± 1
micro drying, 0% Tween	collagenase	39 ± 2
micro injection into cold reservoirs	collagenase	60 ± 4
micro injection into cold reservoirs	trypsin	72 ± 4
lyophilization, 10% (w/w) mannitol	papain	12.7 ± 0.9
lyophilization, 10 mM acetate	papain	15.5 ± 0.2
lyophilization, 8 mM dithiothreitol	papain	23.4 ± 0.5

On the other hand, it was found that elastase and collagenase both retained the most activity after lyophilization. In fact, collagenase lost no activity during lyophilization, and only a small percentage during drying, while showing a significant decrease in activity during both of the microscale processes. This implies that collagenase is remarkably resistant to freezing and drying damage, but sensitive to either surface denaturation or the shear forces involved in microinjection. Two additional experiments, shown in Table 2, support this hypothesis. The activity retained during micro drying was significantly reduced by removal of surfactant, which helps protect against surface denaturation. Also, when collagenase was subjected to microinjection into cold MEMS reservoirs, similar to the first step of the micro lyophilization process, but then assayed immediately without drying or lyophilizing, the retained activity was the same as for micro lyophilization. This indicates that microinjection caused the majority of the denaturation, and that future formulation improvements should target surface and shear denaturation mechanisms.

Elastase, like collagenase, retained the greatest amount of enzyme activity during the lyophilization process. However, for elastase the microscale lyophilization process preserved only a little less activity, and the micro drying and drying processes were very similar, preserving about 60% of the original activity. This indicates that lyophilization was less harsh on elastase than drying, and that the differences in time constant and shear/ surface denaturation between the macro and micro processes are not as important for this enzyme. This is supported by the fact that additional surfactant made no difference to the enzyme activity during micro drying, as shown in Table 2. Finally, addressing elastase's sensitivity to drying by adding mannitol as a lyoprotectant increased the amount of enzyme activity preserved during micro drying and micro lyophilization by about 10% each.

For each enzyme studied, we were able to preserve at least 60% of the enzyme activity with either the micro drying or micro lyophilization technique, enabling delivery of these proteins from the drug delivery MEMS platform. As expected, each enzyme displayed its own unique sensitivities to the processing conditions, depending on its particular structure. Surprisingly, the very simple technique of micro drying preserved more activity than traditional lyophilization for some enzymes, which may indicate that microscale processing could be useful for other applications. The comparison between macroscale and microscale processes allowed some basic hypotheses to be made about the mechanisms underlying protein stability during the microscale processes. For therapeutic proteins whose key degradation processes are known, these results could be used to determine which therapeutic proteins would be most easily micro dried or micro lyophilized, as well as which excipients would be most likely to stabilize the protein during processing. The degradation mechanisms and formulations considered here could be used as a starting point for in depth studies to determine the optimal formulation for therapeutic proteins in drug delivery MEMS reservoirs.

8.4. Conclusions

The micro drying and micro lyophilization processes for loading micro reservoirs with protein formulations affected the enzymes differently according to which degradation mechanisms were most important for each enzyme. Micro drying preserved the most enzyme activity of the processes studied for trypsin and papain, perhaps because it avoids freezing damage and takes place rapidly. Collagenase and elastase activities were best preserved by lyophilization, and collagenase especially was sensitive to the increased surface and shear forces inherent in microscale processing. However, for all enzymes at least 60% of the enzyme activity could be retained following microscale processing. The results presented here could be used as a starting point for the development of stable micro formulations for therapeutic proteins.

8.5. References

1. A. M. Johnson, I. Sherifi, R. Lau, M. J. Cima, and R. Langer, Microscale lyophilization and drying of proteins in a MEMS drug delivery device, (submitting to *Pharmaceutical Research*).
2. A. M. Johnson, M. J. Cima, and R. Langer, Microscale lyophilization and drying methods for the stabilization of molecules, US Patent Application 10/308,579.
3. W. Wang, Lyophilization and development of solid protein pharmaceuticals, *International Journal of Pharmaceutics*, **203**, 1-60 (2000).
4. J. L. Cleland, M. F. Powell, and S. J. Shire, The development of stable protein formulations: a close look at protein aggregation, deamidation, and oxidation, *Critical Reviews of Therapeutic Drugs*, **10**, 307-377 (1993).
5. P. Desnuelle, Trypsin, in *The Enzymes*, Vol. 4 Part A, P. D. Boyer, H. Lardy, and K. Myrback, Editors, Academic Press, New York, p. 119-132 (1960).
6. R. Arnon, Proteolytic enzymes: papain, in *Methods in Enzymology*, Vol. 19, C. P. Sydney, N. O. Kaplan, G. E. Perlmann, and L. Lorand, Editors, Academic Press, New York, p. 226-244 (1970).
7. S. Seifter and E. Harper, The collagenases, in *The Enzymes*, Vol. 3, P. D. Boyer, H. Lardy, and K. Myrback, Editors, Academic Press, New York, p. 649-697 (1970).
8. B. S. Hartley and D. M. Shotton, Pancreatic elastase, in *The Enzymes*, Vol. 3, P. D. Boyer, H. Lardy, and K. Myrback, Editors, Academic Press, New York, p. 323-373 (1970).
9. S. P. Leytus, L. L. Melhado, and W. F. Mangel, Rhodamine-based compounds as fluorogenic substrates for serine proteases, *Biochemical Journal*, **209**, 299-307 (1983).
10. M. Szabelski, K. Stachowiak, and W. Wiczk, Influence of Me_2SO and incubation time on papain activity studied using fluorogenic substrates, *Acta Biochimika Polska* **48**, 995-1002 (2001).
11. C. G. Knight, Fluorometric assays of proteolytic enzymes, in *Methods in Enzymology*, Vol. 248, C. P. Sydney, N. O. Kaplan, G. E. Perlmann, and L. Lorand, Editors, Academic Press, New York, p. 18-34 (1995).
12. K. Kojima, H. Kinoshita, T. Kato, T. Nagatsu, K. Takada, S. Sakakibara, A new and highly sensitive fluorescence assay for collagenase-like peptidase activity, *Analytic Biochemistry*, **100**, 43-50 (1979).

13. A. F. Johnson, M. D. Struthers, K. B. Pierson, W. F. Mangel, and L. M. Smith, Nonisotopic DNA detection system employing elastase and a fluorogenic rhodamine substrate, *Analytic Chemistry*, **65**, 2352-2359 (1993).

14. M. L. Anson and A. E. Mirsky, The equilibrium between active native trypsin and inactive denatured trypsin, *Journal of General Physiology*, **17**, 393-398 (1993).

15. H. W. Blanch and D. S. Clark, *Biochemical Engineering*, Marcel Dekker, New York, p.5-19 (1996).

16. W. Norde and J. Lyklema, Why proteins prefer interfaces, *Journal of Biomaterials Science Polymer Edition*, **2**, 183-202 (1991).

17. R. A. Edwards and R. E. Huber, Surface denaturation of proteins: the thermal inactivation of β-galactosidase (Escherichia coli) on wall-liquid surfaces, *Biochemistry and Cell Biology*, **70**, 63-69 (1992).

18. P. D. Virkar, T. J. Narendranathan, M. Hoare, and P. Dunnill, Studies of the effects of shear on globular proteins: Extension to high shear fields and pumps, *Biotechnology and Bioengineering*, **23**, 425-429 (1981).

19. M. Tirrell and S. Middleman, Urease oligomerizes in a linear pattern: further hydrodynamic evidence from intrinsic viscosity theories and measurement, *Biopolymers*, **18**, 59-72 (1979).

9. Conclusions and Recommendations

9.1. Conclusions

The goal of monitoring drug delivery from an implant *in vivo*, in real time and without disturbing the tissue environment, was accomplished. An impedance based sensor was designed to measure the change in conductivity of the contents of a drug delivery MEMS device reservoir as the drug dissolves. MEMS devices with impedance sensors in each drug reservoir were microfabricated by means of a shadow masking technique for patterning of 3D surfaces. A four element equivalent circuit was developed to describe the impedance spectrum of the reservoirs in terms of physical components of the system. The solution resistance and double layer capacitance depend on the amount of drug that has dissolved and were used to measure the drug release rate in real time. Drug release was monitored *in vitro* in stirred saline and in a laminar flow cell. The flow cell releases showed significant variability, likely due to incomplete opening of the reservoir membranes. Radioactive tracer measurements of the release rate were in agreement with the release rates measured by the sensors. A finite element model of the system, simplified to a cone in cylindrical coordinates, also gave predicted release times in agreement with the sensor and radioactivity measurements of release times in stirred saline. MEMS devices with impedance sensors were implanted subcutaneously in rats and activated after 3-11 days post-implantation. Release of radiolabeled mannitol was monitored by the sensors *in vivo* in real time and by scintillation of urine samples. Significant release rate variability was seen between animals, demonstrating the utility of sensors for noninvasive monitoring of drug release rate *in vivo.*

9.1.1. Device microfabrication and packaging

A microfabrication and packaging procedure was developed to enable the making of MEMS drug delivery devices with impedance sensors for real time release monitoring. The most challenging considerations were the patterning of electrodes within the three dimensional device reservoirs and the making of electrical connections to both the frontside and backside of each chip. Each of these challenges was successfully addressed by modification of the existing microfabrication and packaging protocols.

A shadow mask technique was adapted to our system to enable the patterning of the impedance electrodes within the reservoirs. A silicon wafer was through-etched with the electrode pattern and mounted on top of the device wafer to create a mask for metal deposition in the ebeam. With proper alignment of the wafers over the crucible, the electrode pattern was successfully transferred to the reservoirs of the device wafer. The shadow masking technique is not easily scaled up to mass production but was sufficient for the production of prototype devices on a laboratory scale.

A simple packaging scheme was developed to allow electrical connections to be made to both the frontside and backside of the device. The device was placed in a frame to protect the frontside while the backside connections are made and embedded in epoxy. Upon removal of the frame, frontside connections could be made without disturbing the backside connections. The devices were shown to be hermetically sealed by this method, with the only leaks due to broken reservoir membranes. The electrical connections were well insulated and resistant to immersion in saline or implantation in tissue up to 2 weeks.

9.1.2. Equivalent circuit analysis

The drug delivery MEMS device with an impedance-based sensor successfully monitored the release of drug from a device reservoir. The sensor output is related to the drug release rate by a simple equivalent circuit whose elements correspond to the physical characteristics of the system. The equivalent circuit was developed in two stages, by using a macroscale model of the sensor to understand the effects of electrode geometry, then measuring impedance in the microreservoirs and adding elements to describe the bypass current through the silicon substrate. The equivalent circuit allows us to extract the two key parameters, solution resistance and double layer capacitance, from the overall impedance spectrum. The solution resistance and double layer capacitance were measured as functions of time during release of the drug. These two parameters are functions of the degree of penetration of solution into the reservoir during drug release, which can be related to the rate of transport of drug from the device.

9.1.3. In vitro *release monitoring*

The *in vitro* release results show that it is possible to monitor the dissolution of compounds from the device reservoirs using the impedance sensors. The measured values of solution resistance and double layer capacitance change by two orders of magnitude during the dissolution of air or solid mannitol from the reservoirs. The end of the release, as determined by the rate of change of the solution resistance, was relatively consistent for similar conditions during dissolution of air and mannitol in PBS solutions. The release of mannitol into stirred PBS took approximately 2 hours. The release time was longer and more variable for releases in the flow cell and during leak testing, likely because the reservoir openings were partially obscured by fragments of the gold membrane. Scintillation counting of the release medium gave release times that were 5-10 minutes longer than those measured by the sensors in the stirred PBS experiments, and 60-70 minutes longer than sensor release times in the flow cell experiments. The lag time arises because the sensors monitor the dissolution of solid mannitol, which is then followed by dilution of the concentrated mannitol solution in the reservoir into the bulk solution. In the stirred PBS experiments the dilution of the concentrated mannitol solution is largely lost in the noise of the scintillation measurements, while the high sensitivity of the scintillation measurements of the flow cell effluent enables the detection of the dilution process. If the scintillation measurements are adjusted to the same level of sensitivity, both setups give an identical lag time of 5-10 minutes. Finally, the release profiles of the solution resistance and double layer capacitance were relatively consistent from reservoir to reservoir although there were some exceptions.

9.1.4. In vivo release monitoring

The impedance sensors were able to monitor release of the radiolabeled model drug mannitol from MEMS device reservoirs *in vivo* in real time. Sensor output was qualitatively similar to results obtained *in vitro*, as measured by the shape of the impedance spectra, the behavior of the solution resistance and double layer capacitance over time, and the final values of the solution resistance and double layer capacitance. Of the seven monitored releases, three finished releasing during the monitoring period, within 3-5 hours. Three further devices were near the end of the release, giving an approximate range of release times of 3-7 hours, significantly longer than the 2 hour release times generally observed *in vitro* (with the exception of incompletely opened reservoirs in the flow cell and leak tests). One device showed significantly slower release, likely due to formation of a very small opening in the reservoir membrane. Scintillation counting of urine samples confirmed each release and showed the slow release to be complete after approximately 50 hours.

The amount of data collected was significantly limited by the breakage of membranes during packaging and during implantation, the unreliability of the corrosion protocol to open the reservoirs, and the limitation of the implantation time to two weeks due to degradation of the packaging *in vivo*. It was not possible to correlate the observed release times with the duration of device implantation due to the low number of data points and the limited implantation time. However, the variability in the release times shows the utility of the release sensors for evaluating drug release *in vivo.*

9.1.5. Mathematical simulation of drug release

The dissolution of solid drug from the reservoirs of the MEMS device was simulated in MATLAB and FEMLAB for a cylindrical reservoir, and in FEMLAB with the pyramidal geometry simplified to a cone in cylindrical coordinates. The MATLAB program used a mass balance at the interface and an axial stretch factor to track the moving dissolution boundary over time. In FEMLAB the dissolution interface was simulated by a step change in the diffusivity at the saturation concentration. The predicted dissolution time was very sensitive to the steepness of the diffusivity step change in relation to the mesh size. If the step change occurs over a distance much shorter than the element size, the model predicts a concentration peak at the dissolution interface. The steepness parameter was empirically adjusted in the cylindrical FEMLAB model to give the same dissolution kinetics as predicted by the MATLAB program with a mass balance at the boundary. The steepness parameter was adjusted to 550 for a 1x refined mesh, and 1200 for a 2x refined mesh.

The optimal mesh and steepness parameter were then used in the FEMLAB simulation of a conical reservoir that closely approximates the actual pyramidal reservoir geometry. The predicted release time of 72 min for mannitol dissolution is of the same order of magnitude as experimentally measured release times. The lag time between the end of dissolution of the solid and the dilution of the concentrated solution in the reservoir to the detection limit was approximately the same as the lag between the release times measured by the impedance sensors and those measured by scintillation of the release medium. The model therefore supports the assumption that the sensors are most sensitive to the dissolution of solid drug rather than the dilution of concentrated drug solution. Simulations of dissolution through unstirred barrier layers of varying thicknesses suggest that the current opening size of 50 × 50 μm is small enough that it begins to limit the rate of drug release, and that incomplete removal of the gold membrane cap over the reservoir can significantly affect release time. The reservoir opening could be made larger to make the drug release rate more sensitive to the formation of a fibrous capsule over the reservoir, to facilitate measurements of fibrous capsule formation *in vivo.* Alternatively, the a smaller reservoir opening could be used to limit the rate of drug release and make it independent of the properties of the external surroundings during long implantation times.

9.1.6. Microscale lyophilization and drying of proteins

New methods were developed for loading MEMS device reservoirs with a reproducible amount of a dry, stable protein formulation. The micro drying and micro lyophilization processes for loading micro reservoirs with protein formulations affected the enzymes differently according to which degradation mechanisms were most important for each enzyme. Micro drying preserved the most enzyme activity of the processes studied for trypsin and papain, perhaps because it avoids freezing damage and takes place rapidly. Collagenase and elastase activities were best preserved by lyophilization, and collagenase especially was sensitive to the increased surface and shear forces inherent in microscale processing. However, for all enzymes at least 60% of the enzyme activity could be retained following microscale processing. The results presented here could be used as a starting point for the development of stable micro formulations for therapeutic proteins.

9.2. Recommendations for future work

The findings of this thesis provide a solid foundation for a number of *in vivo* drug transport studies that would be difficult or impossible to perform with previous technologies. Noninvasive measurement methods for evaluating drug transport *in vivo* are very limited. The impedance sensors could be used with a wide variety of therapeutic compounds to measure drug transport in the immediate vicinity of the implant *in vivo* in real time. Factors such as implant site, duration of implantation, inter-animal variability, drug solubility and diffusivity, and the effects of biocompatibility-enhancing coatings could be evaluated in a controlled fashion. Multiple drug transport measurements could be made over time with each device, eliminating the need for separate animals and implants for each time point. This would not only eliminate the variability in the data due to differences between individual animals and implants, but would also reduce the number of animals necessary for a long term study. The impedance sensors make possible the measurement of drug transport *in vivo* and *ex vivo* through the same fibrous capsule, providing a measure of how well current *ex vivo* diffusion studies reflect *in vivo* transport measurements. The devices could also be used in conjunction with blood and urine measurements to help measure complex pharmacokinetics of different drugs and the effects of other *in vivo* transport barriers, because the drug release rate from the device would be precisely known.

All of the potential future applications are dependent on making the devices more reliable. Changing to the 'fuse' chip format developed by MicroCHIPS should solve the problem of unsuccessful or incomplete reservoir opening that contributes to highly variable release times. A more water resistant package is necessary to evaluate implants after implantation times longer than 2 weeks. For applications involving conductive drugs or porous formulations, the equivalent circuit would need to be modified to include the conductivity of the solid and dissolved drug, and the transport model would need to accurately reflect the mode of drug dissolution.

9.2.1. Device microfabrication and packaging

For future microfabrication and packaging work, there are three main challenges: improvement of the adhesion of the gold impedance electrodes to the silicon substrate, improvement of the electrical insulation to allow long term implantation, and improvement of the activation technique for opening the reservoirs.

The impedance sensors are insulated from the silicon substrate of the device by a layer of silicon oxide. The current microfabrication procedure, while adequate, displays poor adhesion of the gold/oxide layers to the substrate. This makes wire bonding difficult, because the bond pads often detach from the device during bonding. It would be advantageous to improve this adhesion by properly adjusting the microfabrication procedure. The problem may lie in the adhesion of the oxide to the silicon, the adhesion of the gold to the oxide, or the etching of nitride in step 26, which may damage the oxide layer. Appropriate modifications to one or more of these steps could significantly reduce the time required for packaging the devices and improve the quality and reliability of the impedance connections.

The packaging technique is effective for devices that will be implanted up to 2 weeks, but not reliable for longer implantation times. It has been observed by Rebecca Shawgo and others that the EP42HT epoxy is not completely impermeable to water after an extended period of submersion. Some connections may last longer than 2 weeks, but significant attrition is noticeable among the activation connections, and the impedance electrode connections may give a false signal, measuring a solution resistance between the wires rather than through the reservoir. A substitute epoxy, an additional layer of electrical insulation over the wire tips or wire bonds, perhaps M-coat D or M-coat B, or even a completely new packaging scheme, could yield improved long term results.

Finally, the activation of the reservoirs by corrosion of the gold membrane was found to be somewhat unreliable *in vivo*, as described in chapter 7. MicroCHIPS, Inc.

researchers have developed an entirely new method for opening the reservoirs, a so-called 'fuse chip'. A wide current path runs from the edges of the chip across the top of each reservoir, narrowing just above the reservoir opening. When current is applied, the bottleneck above the reservoir heats rapidly and melts within microseconds. The fuse method is much more reliable than the corrosion method and can open in air, saline, or tissue irrespective of the device environment.

In addition to making the opening of the device more reliable, the fuse method results in an opening of consistent size. The corrosion method causes the membrane to fail mechanically, which usually completely opens the reservoir but is somewhat inconsistent and may yield a variety of opening sizes and shapes. The variability in the degree of membrane opening interferes with the measurement of transport through the tissue by the impedance sensors, as a slow drug release rate may be due to either an incomplete reservoir opening or the transport characteristics of the surrounding tissue. While researchers using the traditional MEMS drug delivery devices typically open many reservoirs at once, monitoring drug delivery with the impedance sensors requires the activation of one reservoir at a time, making the reliability of activation a critical factor. Modifying the fabrication protocol to use the fuse activation method rather than corrosion is critical to improve the amount and quality of data collected with each device.

9.2.2. Equivalent circuit analysis

The equivalent circuit works well for a nonconductive solid drug such as mannitol, but the impedance analysis would need to be modified to properly describe other systems. As long as the conductivity of reservoirs filled with drug is different than the conductivity of reservoirs full of body fluid, the release could be monitored. Additional elements might need to be added to account for resistance and/or capacitance of the drug. For an ionic species, the conductivity of the solution would depend on the concentration of drug. The solution resistance would need to be modified to account for the effects of drug concentration on solution conductivity. Also, if the reservoirs were filled with a porous drug or with a drug-containing polymer matrix, the equivalent circuit elements would need to be changed to reflect the complex nature of the reservoir contents during dissolution.

9.2.3. In vitro release monitoring

It would be desirable to make the opening of the reservoir membrane consistent from reservoir to reservoir and to increase the number of monitored releases to increase the statistical significance of the results. The variability in the opening of the reservoirs could be addressed by changing to the 'fuse' chip format described in the microfabrication section. Once the variability in the size of the reservoir opening is reduced, it would be possible to examine how the transport conditions outside the device affect the rate of drug transport. Further releases in the laminar flow cell would provide a controlled transport environment for release. Scintillation counting of the flow cell effluent is extremely sensitive and provides a good independent measure of release rates. The transport conditions could be varied systematically by casting agarose gel films with known thickness and density over the device surface before opening the reservoirs. In addition, a variety of drugs of differing solubilities and molecular weights could be released to determine how these results can be extended to a variety of therapeutic molecules.

9.2.4. In vivo release monitoring

For future *in vivo* studies, it would be very interesting to have multiple monitored releases per device at different times post-implantation to see how implantation time and the formation of a fibrous capsule around the device influence drug release. Histological examination of the fibrous capsule post-implantation and *ex vivo* releases of drug through explanted capsule would yield information on how the structure of the tissue affects release rate. In addition, the release of drugs with more complex pharmacokinetics could yield new insights into *in vivo* transport barriers since the drug release rate from the device would be precisely known. Finally, the sensors could be used to evaluate different implant sites or biocompatible coatings *in vivo* to see how they affect the degree of implant isolation by the tissue.

All of these future studies would hinge on the ability to improve the packaging method to avoid membrane breakage and leaking and to increase the durability of the package *in vivo* as recommended in the microfabrication and packaging section. For longer implantation times, it would also be desirable to increase the flexibility of the wires connected to the device because stiff wires irritate the animals' skin and may start to erode through it. Although animal health remained good throughout both studies, it would be improved by the development of a more flexible package, especially for implantation times of three weeks or more. Also critical for future *in vivo* studies is the implementation of a more reliable activation method such as the 'fuse' chip developed at MicroCHIPS Inc. to achieve the necessary degree of device reliability for collection of a large and statistically significant data set.

9.2.5. Mathematical simulation of drug release

The current MEMS drug delivery sensing device is limited in its sensitivity to the transport characteristics of the tissue surrounding the implant by the variability in the size of the reservoir opening. The variability in reservoir opening size arises from incomplete corrosion and removal of the membrane over the reservoir. The opening size could be made more consistent by changing the membrane cap over the reservoir to a fuse, similar to the 'fuse chips' developed by MicroCHIPS, Inc. In addition, the reservoir opening size should be increased to make the drug release rate more sensitive to the thickness of the fibrous capsule. Simulations indicate that the current 50 × 50 µm opening is sufficiently small that it begins to limit the rate of drug release.

The conical approximation of a drug reservoir is sufficient to describe the approximate rate of drug release observed experimentally. The presence of simulation artifacts at the moving boundary due to the diffusivity step change could be alleviated by simulations with a finer mesh. The steepness parameter for the step change would need to be adjusted using the cylindrical models to give accurate dissolution kinetics in the finer mesh. The FEMLAB conical model could then be used to predict drug release rates under a variety of conditions. The potential effects of wider reservoir openings or deeper reservoirs could be modeled to predict how fabrication changes would affect drug release. The expected release rates for different compounds of interest could be predicted as well as the possible effects of different drug formulations. The model could also be used in conjunction with *in vivo* data on drug release through fibrous capsules to model drug transport through the fibrous tissue layer.

9.2.6. Microscale lyophilization and drying of proteins

The microscale lyophilization and drying methods were used to preserve at least 60% of enzyme activity after processing for each enzyme studied. Another key formulation parameter that would need to be examined before proteins could be reliably delivered with the MEMS device is protein stability after storage. For an implanted chip, the long term storage of proteins in the microreservoirs at body temperature should be established. Future studies could also attempt to establish more definitively which mechanisms are truly responsible for the differences in protein activity seen between bulk scale and microscale drying and lyophilization.

10. Appendix

10.1. Microfabrication machine notes

The following notes are an adjunct to the microfabrication process descriptions, intended to provide the details of day to day operation and troubleshooting of the various machines used in the microfabrication process.

10.1.1. Diffusion furnaces (ICL)

The diffusion furnaces in ICL are available for use by regular fab users with the exception of the VTR nitride machine. When the VTR nitride machine went down, the substitute process of field oxide deposition in tube A3 and LPCVD nitride deposition in tube A5 was implemented. Since all of the other machines used in this process are in TRL, it was much simpler to continue to have the MTL staff perform the initial deposition of nitride/oxide. Both processes require that wafers first be cleaned with the standard RCA cleaning procedure in the machine RCA. The cleaning process was also performed by staff.

All processes performed by staff were arranged through Paul Tierney.

10.1.2. HMDS (TRL photoroom)

The HMDS machine runs a set program in which it deposits HMDS onto the wafers. This improves the adhesion of photoresist on the wafers. It takes about 20 minutes to run. The program can be adjusted if necessary for different types of photoresist. However, for the drug delivery MEMS the pattern is not detailed enough that it matters. It is used for both gold and green-dot processing, depending on the wafer holder used. Green-dot holders are in or on top of the machine, while the gold contaminated holder is in the room next door with the other red-dot labware.

Procedure:

1. Place wafers in metal wafer carrier, place in oven
2. Close door
3. Press 'Start'
4. At end, machine beeps very loudly, press 'Reset'
5. Remove wafer carrier to glass dish on machine 'coater'

Training on HMDS was provided by Kurt Broderick.

10.1.3. Coater (TRL photoroom)

The coater is used for dispensing photoresist onto wafers. It can be used for either gold contaminated or green-dot wafers, either 4 or 6 inch, with the appropriate wafer chuck, found on pegs on the wall beside it. It is also used for the mounting procedure described in section 3.1.28, for mounting the shadow mask wafer onto a 6 inch quartz wafer prior to etching in sts2.

Procedure:

1. Turn on the machine (power = top left button with no lettering left)
2. Press 'Vacuum' to release dummy wafer, red light goes on
3. Remove dummy wafer, set aside
4. Check that the chuck is the correct one for the process, if necessary, change it out. Make sure it slides all the way down the post.
    a. Small green-dot chuck for new wafers
    b. Small red-dot chuck for gold contaminated wafers
    c. Large green-dot chuck for sts2 mounting procedure with quartz wafer
5. Place dummy wafer onto chuck, press 'Vacuum' (if using gold contaminated chuck, be sure to use gold contaminated dummy wafer)
6. Make sure 'Resist', 'Spread', and 'Spin' buttons are lit
7. Select the appropriate type of resist
    a. pump 1 = OCG825-20, positive resist
    b. pump 2 = AZ5214E, image reversal resist
    c. pump 3 = AZP4620, thick resist
8. Check that the resist toggle is set to 'Off'
9. Set the time for each step to a high value in order to adjust the spin speed
10. Press 'Start' (bottom left button with no lettering left)
11. Use knob to adjust spin speed of each step according to recipe
12. Set times for each step according to recipe
13. Replace dummy wafer with first wafer to be coated
14. With resist toggle off, hit 'Start' to check that wafer is centered, hit 'Stop'
15. Switch resist toggle to 'Auto', move nozzle to one side, hit 'Start', let resist flow for a little while to clean out any old resist, hit 'Stop'
16. Center nozzle over wafer, hit 'Start', wiggle nozzle if necessary to coat center
17. Move nozzle to side after the resist step just in case it drips
18. When all are coated, replace the 4 inch green dot chuck and dummy wafer
19. While wafer is spinning, squirt acetone, then methanol over the wafer until basin is clear of resist.

20. Clean wafer carrier and wand if necessary – use only methanol, because acetone will dissolve them!
21. Turn machine off

Notes:

- Spin step time has the decimal point in a different place than the other two steps
- Keep hands to one side, never over the wafer

Training on coater was provided by Kurt Broderick. The wafer mounting procedure was based on the advice of veteran sts2 users Yoav Peles, Leonel Arana, and Dennis Ward.

10.1.4. Prebake Oven (TRL photoroom)

The prebake oven is for curing photoresist before the patterning step. It is kept at a constant temperature of 90°C. Wafers are placed in the oven in the white plastic wafer carriers, either green-dot or red-dot. For wafers with thick resist, the wafer carriers are placed on their sides, to keep the wafers horizontal during baking. The handles cannot be used for this procedure, so users double glove before touching the carrier, and strip the extra glove after placing it in the oven.

10.1.5. Postbake Oven (TRL photoroom)

The postbake oven is for curing photoresist after the patterning step. It is kept at a constant temperature of 120°C. The same white plastic wafer carriers are used for both the prebake and postbake oven, although in the past they were segregated. Thick resist cannot withstand the elevated temperature of the postbake oven and is instead postbaked in the prebake oven at 90°C.

10.1.6. Ksaligner2 (TRL photoroom)

The ksaligner2 is a Karl-Suss aligner for photolithography. It can be used for either 2 inch or 4 inch wafers, for red or green-dot processes, with the appropriate wafer chuck and mask holder. An alternative machine is the EV1, which requires much shorter exposure times and can handle either 4 or 6 inch wafers. The ksaligner2 is also used for mounting the shadow mask wafer onto the device wafer in step 17 of the main microfabrication process. The shadow mask mounting procedure is listed below after the general photolithography procedure.

Procedure:

1. Turn the machine on by pressing the ‘Power’ button
2. Press ‘Align’ to get the chuck to slide out

3. Load the appropriate wafer chuck
    a. Get the wafer chuck from the shelves next to the ovens
    b. Slide tray out, place wafer chuck in slot (remove old chuck if necessary)
    c. Slide connector piece onto the two pins on the side of the tray
    d. Attach vacuum hoses to the three connectors, matching numbers
4. Load the appropriate mask and mask holder
    a. Get the mask holder from the shelves next to the ovens
    b. Set mask holder upside down on machine table
    c. Attach vacuum hose for mask vacuum to connector on mask holder
    d. Place mask onto holder upside down (when placed in the machine it should be right side up)
    e. Flip mask vacuum toggle to 'On'
    f. Pick up mask holder and turn upside down, keeping fingertips over mask edges just in case, slide into slot on machine, tighten knobs on left side to hold in place
5. Adjust the wafer tray position so that it is dead center according to the crosshairs on the right hand side of the machine
    a. The knob on the left side of the machine moves it in and out
    b. The knob on the right side of the machine, toward the back, moves it left and right
    c. The knob on the right side of the machine in the front changes the angle (theta)
6. Press 'Set Exposure Time' and use the up and down arrow keys to adjust exposure time according to recipe (press 'Fast' to change time more quickly), press 'Set Exposure Time' again
7. Check that the pressure gauges point to the regions marked with tape for 4 inch wafer processing
8. Choose hard or soft contact according to recipe
9. Slide tray out, place wafer onto chuck, slide back
10. Pull back smoothly on the silver lever on the left hand side of the machine just until it clicks to bring the wafer and mask into contact
11. If not aligning the mask and wafer (if this is the first mask), skip to step 23
12. Slide the white lever (behind the silver lever) forward to take the mask and wafer slightly out of contact

13. Turn on microscope light (and camera and monitor, if desired)
14. Focus microscope by moving the large focus knob in the back of the assembly
15. Focus individual eyepieces using the larger knobs directly above each eyepiece
    a. If turned past a certain point, the eyepiece focus knobs will move the eyepieces left to right relative to one another
    b. The small knobs next to the eyepiece focus knobs will lock the eyepieces in position
    c. The small knobs above the eyepiece focus knobs (with the arrows marked in next to them) adjust whether the view is from the left, right, or both eyepieces
16. Use arrow keys to move eyepieces around over wafer
17. With eyepieces on opposite sides of the wafer, align the pattern through one eyepiece using the x and y controls
18. Look at the pattern through the other eyepiece, and adjust alignment using the theta control until the pattern is halfway between where it started and true alignment
19. Go back to the first eyepiece and again align the pattern using x and y; then use the second to adjust theta halfway
20. Repeat steps 18 and 19 until both sides are perfectly aligned
21. Slide the white lever back to put the mask and wafer back in contact
22. Check the alignment over the whole wafer
23. If recipe calls for a metal ring to protect the wafer edge from exposure, take metal ring from red box on top of aligner labeled 'Arturo ks jigs' and place on top of mask
24. Press 'Expose' to start process
25. Wafer chuck slides back out at end, slide tray out and remove wafer

Special Procedure: Shadow Mask alignment

1. Obtain the special shadow mask jig from the Jensen lab shelf (with permission)
2. Place the jig in the mask holder instead of a mask, turn on mask vacuum
3. Connect the jig to the house vacuum by removing the vacuum wand from its connection and substituting the jig vacuum hose
4. Place the shadow mask wafer onto the jig and align
5. Use valve on jig vacuum hose to turn on vacuum to hold shadow mask wafer securely in place (check by pushing an edge with tweezers)

6. Very carefully slide the mask holder (with the jig and shadow mask) into the slot on the machine, keeping hoses out of the way
7. Place the device wafer on the wafer chuck and slide the wafer tray into place
8. Pull back smoothly on the silver lever on the left hand side of the machine just until it clicks to bring the device wafer and shadow mask wafer into contact
9. Slide the white lever forward to take the shadow mask wafer and the device wafer slightly out of contact
10. Focus the eyepieces on the shadow mask wafer as described above. This is just at the lower edge of their focusing ability, so be very careful. The eyepiece apparatus can fall off its adjustment screw if lowered too far.
11. Align the two wafers as described in the basic procedure, and bring them back into contact using the white lever.
12. Press 'Chuck down' to drop the device wafer out of contact
13. Slide the wafer tray out without pulling it all the way out, which would release the vacuum and ruin the alignment
14. Dab the edges of the wafer with a minimal amount of thick photoresist using a swab from the coater
15. Slide the wafer tray back in and pull back smoothly on the silver lever just until it clicks to bring the wafers into contact
16. Check the alignment and adjust slightly if necessary (remember to bring them out of contact using the white lever first if adjusting)
17. Once again, pull back smoothly on the silver lever. It has already 'clicked' but very gently pull it slightly further, to press the two wafers together, and hold it for several seconds
18. Release the vacuum on the shadow mask wafer by closing the valve on the jig vacuum hose
19. Press 'Chuck down' to drop both wafers away from the mask holder
20. Remove the wafers carefully and place horizontally on a white wafer carrier
21. Bake 10-15 minutes at 90°C to cure the photoresist
22. Check alignment under microscope; if good, store for ebeam deposition, if wafers have slipped out of alignment, dismount in acetone, clean, and retry another day
23. Put away jig and reconnect house vacuum to wand

Training on ksaligner2 was provided by Kurt Broderick, and the shadow mask procedure was demonstrated by Leonel Arana in Klavs Jensen's laboratory.

10.1.7. Photo-wet-R and Photo-wet-L (TRL photoroom)

The right side of the photo-wet hood is designated for gold contaminated processing. The left is reserved for green-dot processes. It is used primarily for development of photoresist. Developers and solvents are located under the table in the middle of the room. Green-dot labware is on shelves to the right of the hood, and red-dot labware is in the room next door in a cabinet.

Photoresist developing procedure:

1. Obtain small glass dish from either red or green dot labware, pour ~0.5cm of the appropriate developer into bottom
2. Slide wafer into developer and swirl until clear
3. Rinse wafer in dish under DI water tap, filling and draining dish repeatedly for about 1 minute
4. Remove wafer from water with tweezers, use air gun to dry
    a. It is advisable to blow a quick jet of air with the gun before pointing it at the wafer to clear the line
    b. dry wafer from the center outwards, then blow edge drops toward tweezers
5. At end, rinse out dish, place back on shelf (dish does not need to be dry)

Training on the photo-wet hoods was provided by Kurt Broderick.

10.1.8. Plasmaquest (TRL ballroom)

The plasma etcher is a gold contaminated machine – all wafers placed in it become gold contaminated. It can be used for either deposition or etching. Deposition should always be followed by a cleaning etch to leave the chamber clean for the next user. Problems with this machine are quite frequent due to the age of the machine, the variety of processes, and the number of users. Etch rates vary widely and reproducibility tends to be low.

General operation procedure:

1. Set water bath temperature (left of the machine) according to recipe
    a. Press 'Next Enter', SP flashes
    b. Use up/ down buttons to adjust set point
    c. Wait for it to reach temperature before the first run (heating from 20 to 80°C may take as long as 1 ½ hours)
2. Log in to the machine, click on 'Edit'
3. Click on recipe name, choose a recipe from the box that pops up
4. Compare all settings to recipe in notebook as they may have been changed

5. To change a setting:
   a. Use the arrow buttons at bottom left until the step to be changed is in the first column
   b. Click on the button of the setting to be changed
   c. Enter the new value
6. For tuning the microwave and RF reflected during the first run, set the step 2 time to about 200s
7. When recipe is set, click on 'Close Editor' button at top
8. Check the turbo, the LCD display located below the keyboard near the floor. It should read about 800, with a green light. If it's not on or has a red light, call a technician.
9. Check the RF controller below the keyboard, marked as 'Load' and 'Tune'. It should be on, and the toggles should be set to automatic. Before the controller was adjusted by Bob Bicchieri in 2003, it was necessary to set it to manual and use the +/- toggles to set 'Load' and 'Tune' to the optimal starting positions noted with the recipe in the notebook.
10. Click 'Run', then click on the buttons '700W Microwave' and 'RF Generator' to get the detail windows to pop up
11. Check the position of the dummy wafer. There should be only one in the machine, sitting on the load arm. Look through the window to check that there is no wafer in the etch chamber. If there is, unload it onto the load arm by clicking on 'Unload'. If there is no dummy wafer in the machine, get one from the blue box labeled 'Transfer Pucks' on the counter opposite the machine. Click on 'LL→ATM' to vent the load lock, then place the dummy onto the load arm.
12. Click 'Start' to begin the run. Click 'Start Recipe with Wafer on Load Arm'. The load lock pumps down, then the wafer is loaded into the chamber. During step 1, the gas flows and process pressure equilibrate.
13. During step 2, adjust the microwave and RF to minimize the 'Reflected' readings. Wait until readings are mostly stable before adjusting (about 30s after step 2 has started).
   a. Microwave reflected is reported on the screen and above the etch chamber on the left LCD display on the black box. Adjust the black Max, Mid, and Min knobs (one at a time, and in that order) to minimized the reflected readout on

the LCD. It is usually possible to reduce it to less than five, but values up to 12 or so are also acceptable.

   b. RF reflected is reported on the screen. If the controllers are set to automatic mode, it is not necessary to adjust the RF reflected. Check to make sure that neither 'Load' nor 'Tune' have maxed out in either direction (a red light comes on). If the controllers are maxed out or if the recipe was started in manual mode, adjust the 'Load' and 'Tune' toggles to minimize the reflected readout. It is usually possible to then put 'Load' and 'Tune' into Auto mode for best control now that the RF controller has been adjusted. However, it is possible to run it entirely in manual mode if the controller is unstable, keeping an eye on the RF reflected reading.
   c. If the recipe ends before the microwave and RF are properly adjusted, re-run the recipe on the dummy wafer. Click 'No' when it asks whether to unload the wafer, then click 'Start' and 'Start Recipe with Wafer Already in Chamber'.

14. If the recipe is running well, click 'Yes' when it asks whether to unload the wafer, then click 'Yes' when asked whether to vent the load lock
15. Place the dummy wafer in the Transfer Puck box and place a test wafer onto the load arm
16. Click 'Edit' and adjust the recipe step 2 time
17. Click 'Run', then the microwave and RF detail buttons, to run the recipe
18. When it is finished, use the machine 'nanospec' to check film thickness and adjust the recipe time accordingly
19. Run the recipe on the rest of the wafers, checking each on 'nanospec'
20. When finished, place dummy wafer on load arm
21. If running a deposition recipe:
    a. Set water bath back to 20°C (never leave it hot, it evaporates)
    b. Use the editor to choose the etchcln recipe
    c. Run etchcln on the dummy wafer for at least 600s
    d. At the end of the recipe, unload the wafer but do not vent the load lock
22. If running an etch recipe:
    a. Load the dummy wafer into the chamber so that the load lock is under vacuum
    b. Unload the dummy wafer back onto the load arm but do not vent the lock

Notes:

- Machine instructions 'drift' over time as the machine breaks/ is fixed. Currently (2004) there are problems with the overvoltage light for the Microwave power (at the very bottom of the instruments under the screen). If the overvoltage light comes on, the microwave power turns off. To get around this, hit the button to turn the microwave power to manual, and turn the knob so that the power is zero. Then turn the power back to automatic, and slowly ramp up the power using the knob. You don't have to stop at the power you want, just turn it up past it and the machine will automatically adjust. If the overvoltage light is coming on during test runs, it is best to turn the power down to zero before the start of step 2. Then when step 2 starts, slowly ramp up the power. This avoids triggering the overvoltage light during the runs.
- Avoid using n-type wafers if possible because the n flat often causes the lifting pegs on the wafer chuck in the chamber to miss the wafer, tilting it or even dumping it off the load arm and chuck entirely so that it falls down into the chamber (often breaking it). If this happens, the chamber must be opened, the wafer/devices retrieved, and the chamber cleaned. This can only be done by the staff member in charge of the machine.
- It is not advisable ever to skip the adjustment of parameters on a dummy wafer or measurement of etch/deposition rates on a test wafer, due to machine variability.
- Keep an eye on all readings. Occasionally a gas flow will become blocked, or the RF will go out of tune, or the process pressure fluctuate, etc.
- If the RF is not in tune during a run, the etch rate will slow down to near zero.
- The DC Bias reading on the RF Generator is a measure of the etch rate: it should usually be at least 200V, most often 250 or close to 300V. If lower, etching doesn't work very well.
- If the microwave does not turn on during step 2, check the buttons under the keyboard at the very bottom of the panel. It may be on local instead of remote control.
- Check the last recipe run before your reservation. If it was a deposition, the last user did not run etchcln like they were supposed to. Before running any etch recipes, run etchcln to clean the chamber.
- Check more than one point on the wafer for film thickness, as the etch and deposition rates are not uniform (faster in center).

- For some reason, the nitride deposition is relatively difficult to tune and the deposition tends to be very non-uniform across the wafer.

Training on plasmaquest was provided by Wayne Price, and further troubleshooting information was gleaned from Joe Walsh. Bob Bicchieri is the (lucky) staff member currently in charge of the plasmaquest.

10.1.9. Nanospec (TRL)

The nanospec is an ellipsometer used to measure thicknesses of various films. The microscope stage has two wafer holders. The left holds a reference wafer, while the right holds the sample. A wafer is provided to the left of the machine for placement underneath gold contaminated samples.

Procedure:

1. Place sample wafer on microscope stage on red dot wafer spacer
2. Press and hold 'Calibrate' button until it prints * NANOSPEC/AFT *
3. Press 'No' when it asks PRINT FILM MENU? (the film menu is taped to the machine)
4. When it says ENTER FILM TYPE select the appropriate number from the film menu, press 'Enter'
    a. For oxide below about 800 Å, use 'thin SiO_2 on Si' (number 7)
    b. For oxide thicker than 800 Å, use 'SiO_2 on Si' (number 1)
    c. For nitride on oxide, use 'SiN_x on SiO_2' (number 6)
    d. For unknown oxide thicknesses or those very close to 800 Å, compare both the 'thin SiO_2 on Si' and the 'SiO_2 on Si' film types
5. For oxide measurements, select the 10x objective (number 1), press 'Enter'
6. Make sure the filter is in place for oxide measurements, but it should be slid to one side for nitride measurements
7. Press 'Yes' when it asks NEW REF WAFER?
8. Focus microscope on reference wafer, push 'Measure'
9. Press any number when it says ENTER SAMPLE #, then press 'Enter'
10. For nitride on oxide, enter the oxide thickness, press 'Enter'
11. Press 'Enter' when it says ENTER REFR INDEX to use the default setting
12. Press 'Enter' when it says ENTER DATA BANK # to disable the data bank
13. Focus microscope on sample wafer, push 'Measure'
14. After the measurement is printed, the measurement may be repeated without recalibration until a new type of measurement is desired

Notes:

- When focusing on the reference wafer, use the edges of the turret (the octagon) to focus. If the turret is not visible, narrow the field of view by rotating the knob next to the filter. All measurements should be made with the narrowest field of view.
- The filter is usually left pushed into position (above the eyepieces and back a little). Slide it to the right to remove it for the nitride measurement. It is easy to tell if the filter is in by looking through the scope – it's yellowish with the filter, brighter without it.
- It seems that the approximate cutoff for using the 'thin SiO_2 on Si' measurement rather that 'SiO_2 on Si' is about 800 Å. The thin measurement will start giving the value 865 Å repeatedly as the film gets thicker, and if the film thickness is much higher than 800 Å it will give seemingly random readings. Below 800 Å, the 'SiO_2 on Si' measurement overestimates the film thickness by 100-200 Å.
- Typically, I took five measurements per wafer. If the wafer flat is counted as south, the measurement order is: center, north, east, south, west. Unless otherwise stated in my notebook, the five reported numbers correspond to this measurement order.

Training on nanospec was provided by Gwen Donahue.

10.1.10. KOHhood (ICL packaging area)

The KOHhood is a wet lab hood, located in the packaging area, which is significantly less clean than the actual clean room and requires only booties and gloves rather than a full clean room suit. Potassium contamination must be kept outside of the clean rooms and wafers brought back after the KOH etch must be immediately decontaminated using the KOH cleaning procedure. The left bath in the back of the hood is designated for use with KOH. Full protective gear (sleeve guards, apron, rubber gloves, and face mask) should be worn and red dot labware is used throughout.

Procedure:

1. Thoroughly rinse the bath using the DI water spray gun, drain using toggle switch on left side of hood, close drain
2. Fill bath with 5000 mL DI water, measured with a 2 liter graduated cylinder
3. Turn on stirrer by flipping toggle switch on front of hood
4. Turn on heater using console above hood, enter setpoint of 85°C
5. Measure out 1450 g KOH pellets (from bottom rack to left of hood) into white plastic cup on balance

6. Add pellets to bath, avoiding splashing; bath will heat up significantly as pellets dissolve
7. Place wafers in plastic wafer carrier with one empty slot between them
8. When bath has reached 85°C, add wafer carrier; bath will temporarily cool down but should recover within a few minutes
9. Check wafers after 3 or 4 hours
    a. Remove carrier from bath and place in dump rinser
    b. Run the dump rinser for at least 3 full cycles (using console above hood)
    c. Place wafer on fabwipes on microscope in adjoining room and examine for completion of etch (see section 3.1.5)
10. If necessary, return wafers to carrier and place back into bath; if finished, place in KOH contaminated wafer box and return to TRL for cleaning procedure
11. Drain KOH bath, rinse walls thoroughly with DI water

Notes:

- The recipe used for our wafers is more concentrated than the standard KOH bath to avoid exceedingly long etch times
- Avoid any contact between the wafer carrier and the stirrer, because the stirrer may break the wafers.
- The wafer carrier is place in the bath on its side, which if done carelessly may cause the wafers to slide out of their slots.
- The wafers become *significantly* more fragile after this step.
- Despite the stirrer, the bath is not always well mixed and has a tendency to be more concentrated toward the bottom. If there is much distance between the highest and lowest wafer the difference in etch rates may be significant.
- The bath does become more concentrated over time due to evaporation, slowly increasing the etch rate, but this is not generally a problem.
- The etch slows significantly when the nitride membrane on the opposite side of the wafer has been reached, allowing slower reservoirs to 'catch up' to fast ones. However, significant overetching increases the size of the membrane openings, making them more fragile, undercuts the nitride layer on the backside of the wafer, and makes the wafer itself more fragile by etching more of the wafer edges, so should be avoided.

Training on KOHhood was provided by Wayne Price.

10.1.11. Acidhood (TRL ballroom)

The acidhood is a wet hood designated for use with aqueous chemicals (no solvents allowed, unlike the photo-hoods). It can be used for either red dot or green dot processes with the appropriate labware. The dump rinser is only for green dot processes, while red dot DI water rinses must be performed manually in a plastic bucket in the sink. A variety of cleaning protocols and wet etches may be performed in acidhood. Spin rinse dryers are to the left of the hood. All acidhood work requires full protective gear over the clean room suit: rubber gloves, sleeve guards, apron, and face shield.

Training on acidhood was provided by Kurt Broderick.

10.1.12. Asher (TRL ballroom)

The asher is a furnace for cleaning organics from the surface of wafers by ashing. It can improve the deposition of metal onto the wafer surfaces. The asher should be kept under vacuum at all times except when loading or unloading wafers. The proper settings for ashing are circled on the machine.

Procedure:

1. Vent nitrogen to make it possible to open the chamber; the pressure readings disappear above a certain threshold pressure
2. To open, unfold the knob, then turn and pull
3. Load wafers into boat, making sure to handle the boat with a fresh set of clean gloves or a new fabwipe
4. Close door and turn on vacuum
5. When vacuum has pumped down to about 0.0020, turn on oxygen; the pressure should increase to about 0.5
6. When stable, turn on RF generator and ramp up the power until it is in the range marked on the knob
7. After the desired ash time, turn the power off, then turn the oxygen off
8. Turn the vacuum off and vent to retrieve wafers
9. Make sure to return the system to vacuum when finished

Training on asher provided by Kurt Broderick.

10.1.13. E-beam (TRL)

The ebeam uses an electron beam to evaporate metal from a crucible onto wafers. Deposition is highly directional, which is essential for good patterning using either the liftoff or the shadow mask method. These instructions are specific to directional deposition using the stationary liftoff plate, rather than the rotating planetary plate. The ebeam is a large machine with freestanding banks of controls to the right and left of the main chamber, which are referred to here as the 'left box' and 'right box' control panels. There is also a small controller for adjusting the position and oscillation of the beam that sits on top of the main chamber.

Procedure:

1. At the left box of controls:
    a. Flip the breaker to turn the main power on
    b. Make sure the key lock is on
    c. Check the filament current on Gun 1 by holding down the toggle; it should be about 0.3 A (note that only Gun 1 works)
    d. Turn left box off again
2. At the right box of controls:
    a. Check the pump temperature on the bottom; it should be ~10K, if it is as high as 20K report it to Paudley Zamora, Dave Terry or current technician in charge of machine
    b. Check that the pressure reading at the top of the box is less than approximately 10^{-6} torr; ion tube 1 should be lit
    c. Press auto pump stop; a gurgling noise will start (the power light must be lit)
    d. Switch the auto vent toggle on
3. Get the titanium and gold crucibles and some gold pellets from the plastic box on top of the main chamber
4. At the right box, press 'Parameter' '36' to see the % crystal health; if it is above 85, it should last for the whole deposition, if not, replace it with a new one
    a. Get the package of new crystals from the crucible box
    b. Pull out the crystal holder from inside the chamber, toward the top on the left
    c. Turn it over to let the old crystal drop in the trash, then drop a new crystal from the package directly into the holder
    d. Replace the holder in the chamber
5. Open shutter 1 using the toggle on the right box and load the crucibles
    a. Turn to the 'B' turret using the knob; the turrets rotate slowly so be patient
    b. Check the hole and clean it with the shop vacuum to remove any particles

    c. Drop the titanium crucible into the hole, and make sure it drops in all the way and is well filled (more than ¾ full but not higher than the edge of the crucible
    d. Change to turret 'D' and vacuum it clean
    e. Always add a few gold pellets to the gold crucible (~6) to get good melting
    f. Drop the gold crucible into turret 'D'
    g. Change to turret 'B'
6. Switch the shutter toggle to 'Auto' (not 'Close'); it will close
7. Vacuum any flakes or particles from the rest of the chamber
8. Get the liftoff plate down from the wall and place it over the chamber
9. Replace any dummy wafers that are flaky from repeated depositions; put them in the e-beam dummy box, and vacuum flakes if necessary
10. Check the O-ring around the edge of the chamber for flakes or particles, wipe with a fabwipe
11. Load device wafers into empty slots; they do not need to be clamped if the plate will not be rotating
12. Close the cover and pump down the chamber
    a. Turn off the auto vent toggle and press 'Auto pump start'
    b. Hold the lid down a little until the vacuum pulls it down into place
    c. The 'Rough' pump light should go on
    d. Wait for the chamber to pump down to 100 mtorr (indicated by the sticker on the top gauge)
    e. When it reaches 100 mtorr it automatically switches to the hivac cryo pump and the filament light goes on
13. Program the first deposition recipe in process 1, film 1 (right control box)
    a. Press 'Set Process #' '1' 'Film' '1'
    b. Use the 'Enter key to scroll through parameters
    c. Unlock the program with the keylock
    d. Enter appropriate values for each parameter
    e. Lock the program with the keylock for safety
14. Once the vacuum is about 2 x 10^{-6} torr, turn on the left box using the breaker and the keylock
    a. Look at the beam sweep control and ensure it is set to remote
    b. Frequency should be 2 for both longitude and latitude (it can also be 1 but should never be 0 or the beam will not oscillate)

   c. On the high voltage control, all lights on the left hand side should be on
   d. On the electron gun control, all lights on the left hand side but the bottom two should be on
15. Press 'Reset' to clear display before the run
16. Turn off room light, turn the HV and the Gun on
17. Press 'Start' to begin deposition; the recipe clock will start
18. When power has increased to ~10% the beam should start to be visible; look into chamber and adjust beam
   a. Open viewing shutter and scroll film a little to get a clear view
   b. Use remote control box to adjust the beam position and amplitude of oscillation so it doesn't hit the edges of the crucible
   c. Make sure the beam is centered in the heart of the crucible before the power gets too high to prevent damage to the machine (hit 'Abort' if necessary)
   d. Shut viewing shutter to prevent metal buildup on film when not observing the beam
19. When clock stops, turn off Gun and HV and change to turret 'D'
20. Enter the next deposition recipe in process 1, film 1 as in step 13
21. Turn on Gun, HV and press 'Start' to begin deposition
22. Check the beam position again and adjust if necessary; the pellets will sparkle until they melt and become smooth, but the metal should not be boiling
23. Once the recipe is at the cooling stage, turn off the Gun, HV, and keylock
24. When the timer stops:
   a. Press 'Auto pump stop' and turn the 'Auto vent' toggle on
   b. Turn the left box main power off
25. When the lid lifts and opens:
   a. Remove device wafers
   b. Put liftoff plate away on the wall
   c. Open shutter #1, pry crucible out and vacuum turret clean
   d. Rotate to 'B', pry crucible out and vacuum turret clean
   e. Close shutter #1 and put away crucibles
26. Close the lid, turn the 'Auto vent' toggle off, press 'Auto pump start', and hold lid down until the vacuum sucks it down into place
27. Wait for the vacuum to pump down and switch to the hivac cryo pump

Notes:

- The electron beam can burn a hole in the machine if not properly aimed and must oscillate constantly to prevent extreme heating at just one point.
- The are many process numbers and film numbers, but at some point the machine became incapable of reading anything but 1,1 and so all recipes must be programmed one at a time.
- Occasionally another user somehow manages to contaminate a crucible, leaving a film of unknown composition on the surface. Notify the appropriate staff member.
- The pressure should stay in the 10^{-6} torr range, and should increase to no more than 5×10^{-6} at any time during the run
- The feed time parameter (#33) determines the length of the cooling period after deposition. The chamber should not be opened until the metal has cooled, at least 20 minutes after the end of deposition. The feed time can be set to any value, but it is a good way to make sure that the metal is cooled by the time the clock stops running.
- If it is necessary to abort a run, make sure to press 'Reset' to be able to start a new recipe again.
- If the crystal fails (the health reading drops dramatically), hit 'Abort' and start over with a new crystal.
- It is also possible to change the mode to manual and do a dry run of the recipe (the beam does not turn on).

Training on ebeam was provided by Joe Walsh.

10.1.14. Photo-wet-Au (TRL)

Photo-wet-Au is a solvent hood in the room next to the photo room for use with gold contaminated labware and processes. It is the appropriate place to do overnight acetone soaks or liftoff, and may also be used for spray resist coating of wafers.

Training on photo-wet-Au was provided by Dave Terry.

10.1.15. Diesaw (ICL packaging area)

The diesaw is an automatic dicing saw for cutting wafers into devices at the end of a process. It is located in the packaging area near the KOHhood. Dicing is a messy process that creates a lot of silicon particulates. The diesaw blades are cooled by a continuous stream of water that also washes away the particulates. The wafer is mounted on tape, then cut in one direction, rotated 90°, and cut in the other. During the second set of cuts, the wafer should be monitored to ensure that the devices do not delaminate from the tape and wash away in the water jet. A set of instructions is generally posted on the wall behind the machine for quick reference.

Procedure:

1. Turn the machine on using the breaker switch on the right hand side
2. Push C to clear all data
3. A red light will blink over the parameter to be entered
4. Enter Cut Stroke = 1, (0 for square cut, 1 for round), press 'W' to enter
5. Enter wafer size = 100 mm (for a 4" wafer), press 'W'
6. Enter cut speed: slow = 3, fast = 7, press 'W'
7. Enter Y-index = 5 mm (the distance between cuts on the 1st side), press 'W'
8. It shows 'Block 2', enter 5 mm, the distance between cuts on 2nd side, press 'W'
9. Enter Z-index = tape thickness, never less than 0.05 (usually 0.25 mm, plus a margin of 0.1 mm to prevent delamination), press 'W'
10. Enter Theta-index = 90 (the desired degrees of rotation between the sets of cuts), press 'W'
11. Cut Number has no meaning in A mode, enter any number and press 'W'
12. Check the blade on the spindle and replace if necessary (see notes)
    a. Unscrew cover using the small screw on the top
    b. Use the driver tool to unscrew the chuck (to loosen, hold the handle and turn the center piece to the right)
    c. Remove blade by grabbing the holder by the indentation with your fingertips
    d. Remove blade from the holder and place on fabwipe
    e. Replace with appropriate blade, replace holder, and spin it a little to check alignment
    f. Tighten holder, then tighten cover
13. Press 'Illumination', 'Spindle', and 'Vacuum' (blade will start rotating)
14. Press 'Setup' and observe the blade as it moves over and descends to just barely touch the chuck, calibrating the blade height
15. Press 'Vacuum' to turn the vacuum off
16. Ensure Y is on the index setting and move blade to the back using the arrow key
17. Mount the device wafer onto backing tape
    a. Cut a piece of tape off the roll but leave a half inch uncut and tear it off
    b. Pull the backing off and put the tape on a fabwipe on the diesaw

    c. Hold the wafer in your left hand and press it against the edge of the table on the tape with your right thumb
    d. Gently press the tape across the back of the wafer using the edge of the table to smooth out any bubbles
    e. Trim tape to ~½ inch around edge
18. Place wafer in center of diesaw chuck and press 'Vacuum'
19. Move microscope to center of wafer using Y index, focus
20. Change Y index to jog/scan mode and move to the edge of a street
21. Use the Theta control in the jog/scan mode to adjust the angle until the streets in both eyepiece views are parallel
22. Change Y to index mode and move to near wafer flat to make a practice cut
23. Press 'Semi-auto' to start the water flow
24. Press either Y arrow key to start cutting
25. Press 'Semi-auto' again to take it out of automatic mode; the machine will then stop after making only one cut
26. Check under the microscope after the cut is finished to make sure that the hairline in the microscope view is lined up with the center of the cut
    a. To adjust the hairline, loosen it with the small knob on the scope
    b. Move the hairline with the large knob at the bottom of the scope
    c. Retighten the small knob
27. Adjust the lines on the screen on the left side of the machine to frame the cut
28. Move to wafer center, change Y to jog/scan mode, and put hairline in the center of the streets
29. Use Y in index mode to scan over wafer, checking that hairline is centered
30. Move blade to bottom edge, press 'Semi-auto', press back arrow key to start cutting
31. During last cut, press 'Semi-auto' so that the machine stops at the end of the cut
32. Change Theta to rotation mode, then press curly arrow key to rotate 90°
33. Repeat steps 28-31 for the second set of cuts
34. Press 'Spindle' and 'Illumination', move blade to back
35. Dry wafer with compressed air gun
36. Press 'Vacuum' to release wafer and turn off main power

Notes:

- If some devices do come off the tape, lift up the shield to retrieve them before they go down the drain.
- Water flow rate should be such that the floats are halfway up the meter.
- For silicon wafers with wide streets, use the 220 µm thick Z60 blade labeled 2060, known as the 'thick Si blade'. There is also a 'thin Si blade', a 32 µm thick Z50 blade labeled 2050, that is more fragile than the regular thick Si blade. For glass or quartz wafers use the black 240 µm glass blade.
- If it is difficult to tell which street the blade is aligned to cut, check the position by putting a fabwipe under the microscope to make the green spots show up.

Training on diesaw was provided by Dan Adams.

10.1.16. Sts2 (TRL ballroom)

The sts2 is a DRIE etcher for use in green dot processes only. It uses alternating etch and protection steps to make straight walled etch channels through the wafer thickness.

Procedure:

1. In the 'Select' box at left, click on recipe 'MIT59_A'
2. Set the etch time and save the recipe, leaving the standby step alone
3. Click on the load lock to pump down the lock
4. Load the wafer onto the load arm
5. Click 'Load' on the wafer side, wait until the wafer is on the chuck and the door is closed
6. Click 'Process' on process control box
7. When recipe finishes, unload wafer and vent lock
8. Check depth, estimate etch rate, and etch again if necessary
9. When finished, click 'Load' to keep the lock under vacuum

Notes:

- If the machine gives an error message when the process starts, either press 'Accept' or abort the run and unload and reload the wafer.
- One can press 'Abort' at the end of an etch to make sure it ends on an etch step (SF6) so that the wafer won't have Teflon on it. Alternatively, one could also run the alignment mark process to remove the Teflon after the etch is done.

Training on sts2 was provided by Dennis Ward.

10.2. Radiation Protection Program protocol

MIT Radiation Protection Program (RPP)

Attachment to Authorization to Possess and Use Radioactive Material

Section 8: Principle Procedures

Experimental Protocol

1. Title or Description: Release of radiolabelled chemicals from microchip devices
2. Name(s) of Individual(s) performing experiment or "entire lab:"
   Audrey Johnson, Priya Shah
3. Please mark any other handling hazards (waste issues can be addressed later)
   - ☐ Biological (BL2 material or greater)
   - ☐ Chemical (toxic, carcinogenic, ...)
   - ☐ Animal (attached is DCM "Protection and Control" protocol, update as necessary
4. List the following

Isotope:	^{14}C
Stock activity ordered (mCi):	Up to 0.5 mCi
Total activity used in the experiment (mCi):	Up to 0.15 mCi
Registered radiation lab where material is used:	E25-325, E25-326
Location of stock material storage	E25-326

5. Brief description of the experiment

The experiment will be divided into three parts: 1) preparation of the radiolabeled mannitol in small solid pieces of a precise shape, weight, and labeling concentration, 2) loading the solid radiolabeled pieces into a microchip device, hermetically sealing the device, and preparing the electrical connections to the sealed device, 3) Release of the radiolabeled mannitol into saline solution flowing over the device, which is collected in scintillation vials and counted.

1) Preparation of radiolabeled mannitol as 50 μg, 0.2 μCi pyramid-shaped pieces:

Mannitol will arrive from the supplier as 250 μCi dissolved in ethanol/water solution. Up to half of the solution will be pipetted into a vial. Due to the low labeling frequency desired, an appropriate amount of unlabeled mannitol will be added to the solution to dilute the radiolabel by a factor of approximately 100. The solution will be evaporated slowly over low heat to obtain a damp solid.

A portion of the solid will be scooped out with a spatula and placed on top of a microchip device (consisting of an array of pyramid-shaped reservoirs) on a glass slide. The slide will be placed on a hot plate and heated to a temperature of ~250°C to melt the mannitol down into the microchip reservoirs. The slide will be allowed to cool to room temperature and placed onto the stage of a microscope covered with a paper towel. The excess mannitol will be scraped from the surface of the device with a razorblade. The mannitol in the device reservoirs will be removed with micro-tweezers and placed into a plastic storage container. The melting process will be repeated to obtain the desired number of mannitol pieces.

2) Filling and sealing the device and making electrical connections:

A pyramid-shaped piece of mannitol will be placed into a reservoir of a microchip device on a glass slide. The slide will be placed on a hot plate and heated to a temperature of ~250°C to melt the mannitol in place. The slide will be allowed to cool to room temperature and the microchip device will be placed onto a microbalance pan and weighed. This procedure will be repeated until the desired number of reservoirs are filled (up to 16 reservoirs, 0.2 μCi each = 3.2 μCi maximum per device).

Once filled, the device will be placed on a glass slide on the stage of a microscope. Epoxy will be applied around the reservoirs and a glass coverslip will be placed on top, hermetically sealing the mannitol inside the reservoirs. The device will then be checked for any leakage of radioactivity, and re-sealed and/or cleaned if necessary.

The device will be epoxied to a set of wires for external connections. It will then be transported to room 39-312 within a secondary container and wire bonds will be made between the device and the wires. Following wire bonding, the wire bonding machine and area will be checked for contamination. The device will then be brought back to E25-325 and a second set of wires will be epoxied to the device. These will also be wire bonded in 39-312 in the same manner as the first set. The device will then be stored in E25-325 in a plastic storage container.

3) Release of radiolabeled mannitol into saline solution:

The device will be clamped into a sealed flow cell and the reservoirs will be opened with an electric signal, one at a time. Saline solution will be pumped through the flow cell and collected in a series of scintillation vials. The radioactivity in each vial will be measured using the scintillation counter in E25-326.

6. Survey and monitoring during experiment and close down survey procedure:
A GM counter (pancake) counter will be used to monitor for ^{14}C exposure and contamination after each of the three stages of the experiment, as well as after wire bonding step in building 39.

7. Types of waste generated, activity and volume, and where it is disposed. Examples of the various types of waste are listed below. Many mixed wastes are very difficult to dispose of so please call RPP at 3-2180 if you have any questions regarding mixed waste.

- Solid

Paper towels	from microscope stage, up to ~10µCi of powder
Gloves	

- Sharps

Needles	none
Pipette tips	up to ~10 µCi
Glassware	microscope slides and microchip devices (silicon), ~50 µCi
Razor blades	up to ~2 µCi, disposal in radioactive sharps containers in E25-326

- Aqueous Liquid

Sink Disposal	up to ~50 µCi
RPP collection container	none

- Organic Waste

Acidic	none
Alcohol	none

- Liquid Scintillation Waste

Vials	Up to 500 7 mL scintillation vials, <1 µCi ^{14}C per vial, disposal in liquid scintillation vial drum in E25-326
Five gallon carboy	none

- Mixed Waste

Biological contamination	none
Hazardous chemicals	none
Animal tissue or waste	none

10.3. Capacitance of a square pyramid

In the case where the square pyramid shaped sensor model is full of air (open circuit), there is still a measurable capacitance and a finite, if high, resistance. The resistance is finite (approximately 10kΩ) because some current goes through either the acrylic the model is made from, or the latex gasket used to seal the removable fourth side of the pyramid. The resistance is sufficiently high that the current is low and the measured impedance is noisy, as shown in Figure 10.1. The impedance has the same shape as for a pyramid filled with solution, a near vertical line, and can again be described by a series RC circuit, although the resistance is now a resistance of the solid model, not of solution, and the capacitance is from the charging of the electrodes, not from a solution double layer. Fitting the data to a series RC circuit gives a measured capacitance of 2.9 pF. When the model is even partly filled with solution, the model resistance is essentially infinite compared to the solution resistance, and the double layer capacitance is large enough to drown out any contribution from charging the electrodes.

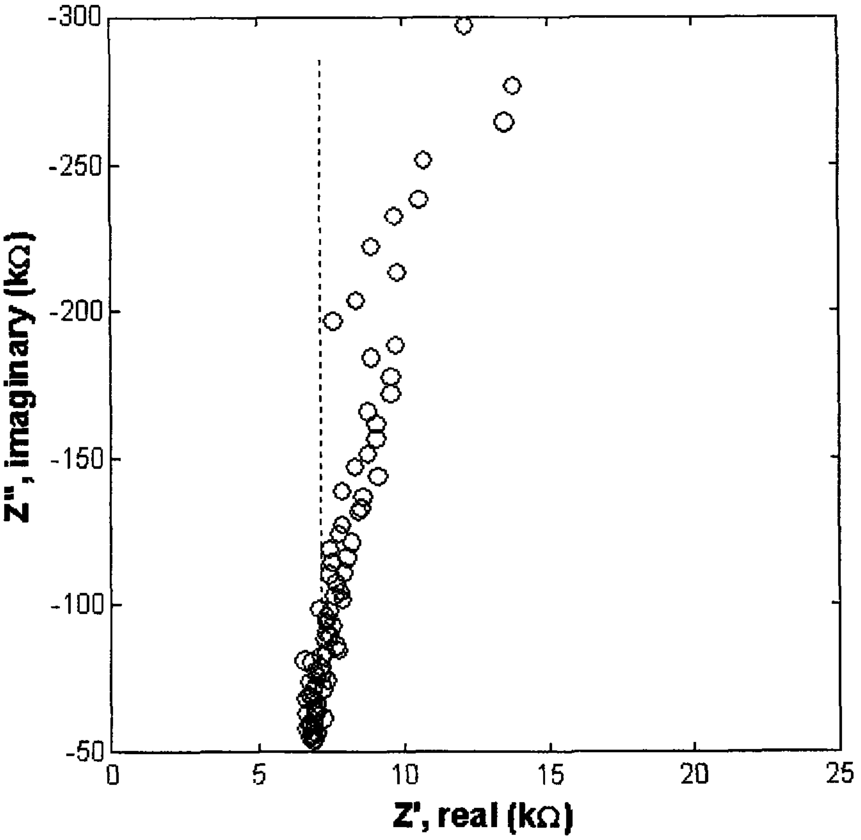

Figure 10.1. Impedance of 100x scale model of pyramidal microreservoir in air. Data points are shown by open circles and the best fit to the equivalent circuit is given as a dashed line.

The expected capacitance of a square pyramid shaped capacitor can be calculated using Maxwell's equations, in order to compare it to the measured capacitance. The pyramidal geometry is most easily described in spherical coordinates, with the approximation of the top and bottom plate edges as arcs rather than straight lines. The pyramid can be described completely by three parameters: one angle and two lengths. The discussion in chapter 4 made use of the base angle of the pyramid, the height, and the base length. In spherical coordinates, it is easier to deal with the pyramid angle, α, and the distances R_1 and R_2, where R_2-R_1 is the length of the side of the pyramid, ℓ, as illustrated in Figure 10.2. The plates (electrodes) of the capacitor are planes of constant ϕ, one at $\phi = 0$ and one at $\phi = 2\alpha$. The width of the plates is the same as the distance between them, so that θ spans an angle 2α as well. However, if θ were to run from 0 to 2α the plates would touch, so the plates are defined between $(\pi/2 - \alpha) \leq \theta \leq (\pi/2 + \alpha)$.

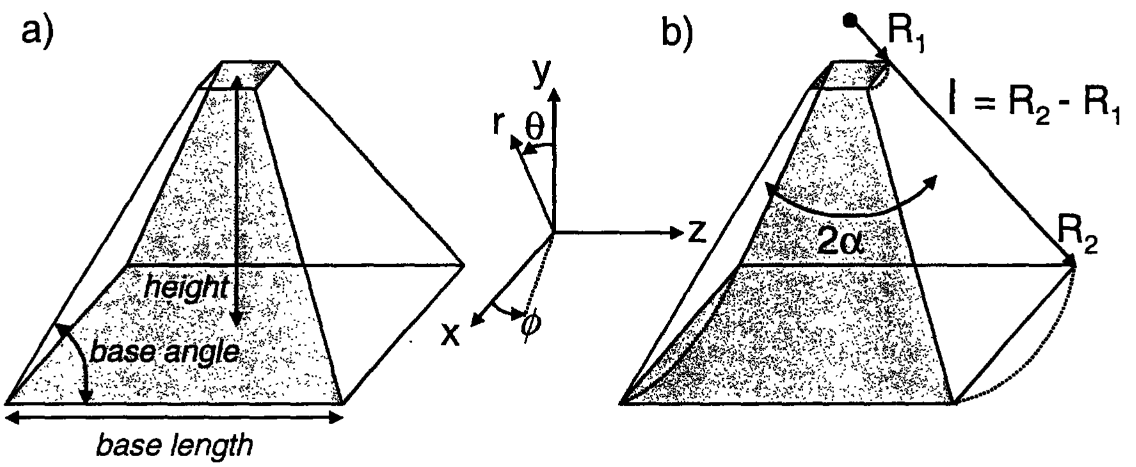

Figure 10.2. Square pyramid geometry in Cartesian and spherical coordinate systems. **a)** The three defining parameters used in calculations in Cartesian coordinates are the height, base length, and base angle. **b)** The three parameters convenient to spherical coordinates are the radii R_1 and R_2 and the top pyramid angle, α. Dashed lines indicate the approximation of the top and bottom edges of the plates as arcs rather than lines.

The plates of the capacitor are assumed to be perfect conductors and are therefore isopotential surfaces. Once the geometry of the system has been defined, we can then calculate the capacitance of the plates using four equations: Laplace's equation, the relationship between electric field and electric potential, Gauss' law, and the definition of capacitance. In the gap between the plates, the electric potential Γ is governed by Laplace's equation

$$\nabla^2 \Gamma = 0$$

which in spherical coordinates becomes

$$(1/r^2)\ \delta/\delta r\ (r^2\ \delta\Gamma/\delta r) + 1/(r^2 \sin\theta)\ \delta/\delta\theta\ (\sin\theta\ \delta\Gamma/\delta\theta) + 1/(r^2 \sin^2\theta)\ \delta^2\Gamma/\delta\phi^2 = 0$$

Because the plates are isopotential surfaces of constant ϕ, all surfaces of constant ϕ between the plates are also isopotential surfaces. That means that the derivatives of the electric potential Γ with respect to r and θ are zero, and Laplace's equation simplifies to

$$\delta^2\Gamma/\delta\phi^2 = 0$$

The solution is

$$\Gamma = A\phi + B$$

where A and B are constants. Using the boundary conditions

$$\Gamma(\phi = 0) = 0\ ;\ \Gamma(\phi = 2\alpha) = V$$

we can solve for the constants A and B to yield the following equation for the electric potential as a function of ϕ

$$\Gamma(\phi) = V\phi\,/\,2\alpha$$

The electric field **E** is related to the potential by the equation

$$\mathbf{E} = -\nabla\Gamma$$

which in spherical coordinates is

$$\mathbf{E} = -\,\delta\Gamma/\delta r\ \mathbf{i}_r - 1/r\ \delta\Gamma/\delta\theta\ \mathbf{i}_\theta - 1/(r\sin\theta)\ \delta\Gamma/\delta\phi\ \mathbf{i}_\phi$$

where $\mathbf{i}_r$, $\mathbf{i}_\theta$, and $\mathbf{i}_\phi$ are the unit vectors in the r, θ, and ϕ directions, respectively. Substituting the equation for the electric potential into the formula for electric field gives

$$\mathbf{E} = -V/(2\alpha r \sin\theta)\ \mathbf{i}_\theta$$

We then use the integral form of Gauss' law,

$$q = \varepsilon_0 \int_s \mathbf{E}\ d\mathbf{A}$$

where q is the charge enclosed within the surface, ε_0 is the permittivity of free space, and $\int_s$ denotes a surface integral. We can then enclose the upper plate with the surface integral and use the fact that the electric field and the area integral are oriented in the same direction to get the following expression for q

$$q = \varepsilon_0 \int_\theta \int_r (-V/2\alpha r \sin\theta)\ r\ dr\ d\theta\ ;\ \ R_1 \le r \le R_2\ ;\ \pi/2 - \alpha \le \theta \le \pi/2 + \alpha$$

Evaluating the integrals between the given limits yields the successive simplifications

$$q = -\varepsilon_0 V/2\alpha \int_\theta \int_r 1/\sin\theta\ dr\ d\theta\ ;\ \ R_1 \le r \le R_2\ ;\ \pi/2 - \alpha \le \theta \le \pi/2 + \alpha$$

$$q = -\varepsilon_0\, \ell V/2\alpha \int_\theta 1/\sin\theta\ d\theta\ ;\ \pi/2 - \alpha \le \theta \le \pi/2 + \alpha$$

$$q = -\varepsilon_0\, \ell V/2\alpha\ \ln[(1+\sin\alpha)/(1-\sin\alpha)]$$

The capacitance, C, is defined as

$$C = |q/V|$$

Substituting the above expression for q gives the capacitance of a square pyramid as approximated in the spherical coordinate system

$$C = \varepsilon_0 \ell/2\alpha \ln[(1+\sin\alpha)/(1-\sin\alpha)]$$

For small angles α, we can expand the exponential as a series

$$\ln[(1+\sin\alpha)/(1-\sin\alpha)] \approx 2\alpha + \alpha^3/3 + O(\alpha^5)$$

Substituting this expression into the equation for C and simplifying gives

$$C = \varepsilon_0 \ell[1 + \alpha^2/6 + O(\alpha^4)]$$

We can determine which higher order terms to neglect by examining the geometrical approximation made when converting the pyramidal geometry to the spherical coordinate system, namely the approximation of the top and bottom pyramid edges as arcs of constant radius rather than straight edges. The base length, b, of the pyramid is given by

$$b = \ell(1 - 2\sin\alpha)$$

whereas the length of the arc subtended by the radius R_2 and the angle 2α is

$$\text{arc} = \alpha \ell(1 - 2\sin\alpha)/\sin\alpha$$

The difference between the arc approximation and the true length is then

$$b - \text{arc} = \ell[1 - 2\sin\alpha - \alpha(1-2\sin\alpha)/\sin\alpha]$$

which can also be written as

$$b - \text{arc} = \ell[-\alpha^2/6 + O(\alpha^3)]$$

Because this difference is being neglected, it is appropriate to neglect terms of order $O(\alpha^2)$ and higher in the equation for the capacitance, giving

$$C = \varepsilon_0 \ell$$

as our final expression for the capacitance of a square pyramid. It is interesting that the geometrical factors largely cancel in this approximation due to the high degree of symmetry inherent in a square pyramid. Using this equation, the expected capacitance of the pyramid model is $C_{theory} \approx 0.5$ pF. Fitting the series RC circuit to the data given in Figure 10.1 for the impedance of the pyramid model gives an experimentally fit capacitance of $C_{exp} \approx 2.9$ pF, which is somewhat higher than calculated. Considering that second order terms were entirely neglected and that there may be some capacitance of the model or gasket, the agreement between theory and experiment is reasonably good.

10.4. Supplemental *in vitro* data

The results of the *in vitro* release experiments are described in chapter 5 along with plots of the best fit solution resistance and double layer capacitance. Appendix 10.4.1 briefly describes the results of two additional control experiments, the 'releases' of insoluble eicosane. Appendix 10.4.2 gives the raw impedance spectra used for the equivalent circuit fit results given in chapter 5. All 17 sets of impedance spectra are plotted, grouped in the same order as the resistance and capacitance plots in chapter 5: air releases, mannitol/eicosane releases into PBS, radiolabeled mannitol releases in stirred PBS, radiolabeled and unlabeled mannitol releases in the flow cell, and radiolabeled mannitol leak test monitoring in PBS.

10.4.1. Release of eicosane in PBS

Two negative control experiments were performed to demonstrate that the impedance does not change if the reservoir contents do not dissolve. Eicosane, a waxy compound, was loaded into two reservoirs of device R4B3 (the same device used to monitor dissolution of air into deaerated PBS). In each experiment, the reservoir was opened by removing the tape over the reservoir opening and the device was immersed in PBS. Impedance spectra were taken over a period of 71 hours. Even the slowest releases, the dissolution of air into PBS that had not been deaerated, showed significant changes in the impedance spectra within 24 hours. The slow releases of air into PBS were performed very early on and are not described in the thesis, although they can be found in laboratory notebook #2.

Figure 10.3 shows the impedance spectra taken over a 72 hour period of immersion in PBS for reservoirs filled with eicosane wax. The spectra change only very slightly with time. Equivalent circuit fitting shows some drop in best fit solution resistance between the beginning and end spectra. However, the four element circuit does not fit very well for mostly dry spectra and the uncertainty in the best fit solution resistance is high. During dissolution of air or mannitol, the impedance spectra change significantly in a matter of minutes, and the resistance drops by 1-2 orders of magnitude. As compared to spectra taken during dissolution of air or mannitol, the spectra taken during immersion of reservoirs filled with eicosane are essentially invariant.

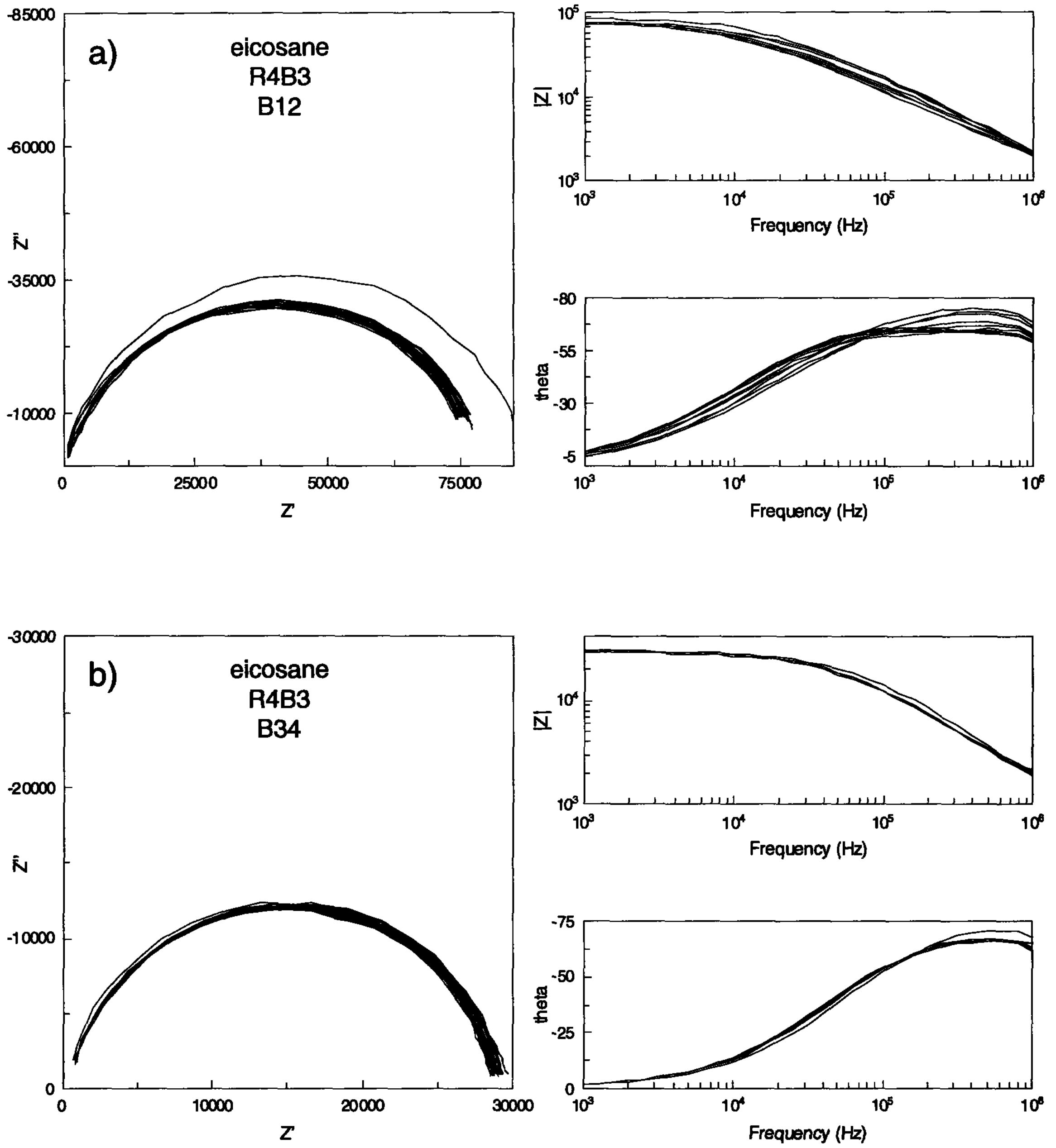

Figure 10.3. Impedance spectra recorded during 'release' of insoluble eicosane from MEMS devices submersed in PBS for 71 hours. **a)** device R4B3 reservoir B12, **b)** device R4B3 reservoir B34.

10.4.2. Impedance spectra from in vitro *release monitoring*

The sets of impedance spectra from the five types of *in vitro* releases are given in Figures 10.4 to 10.8: air, mannitol/eicosane, radiolabeled mannitol, mannitol in the flow cell, and leak test monitoring in PBS.

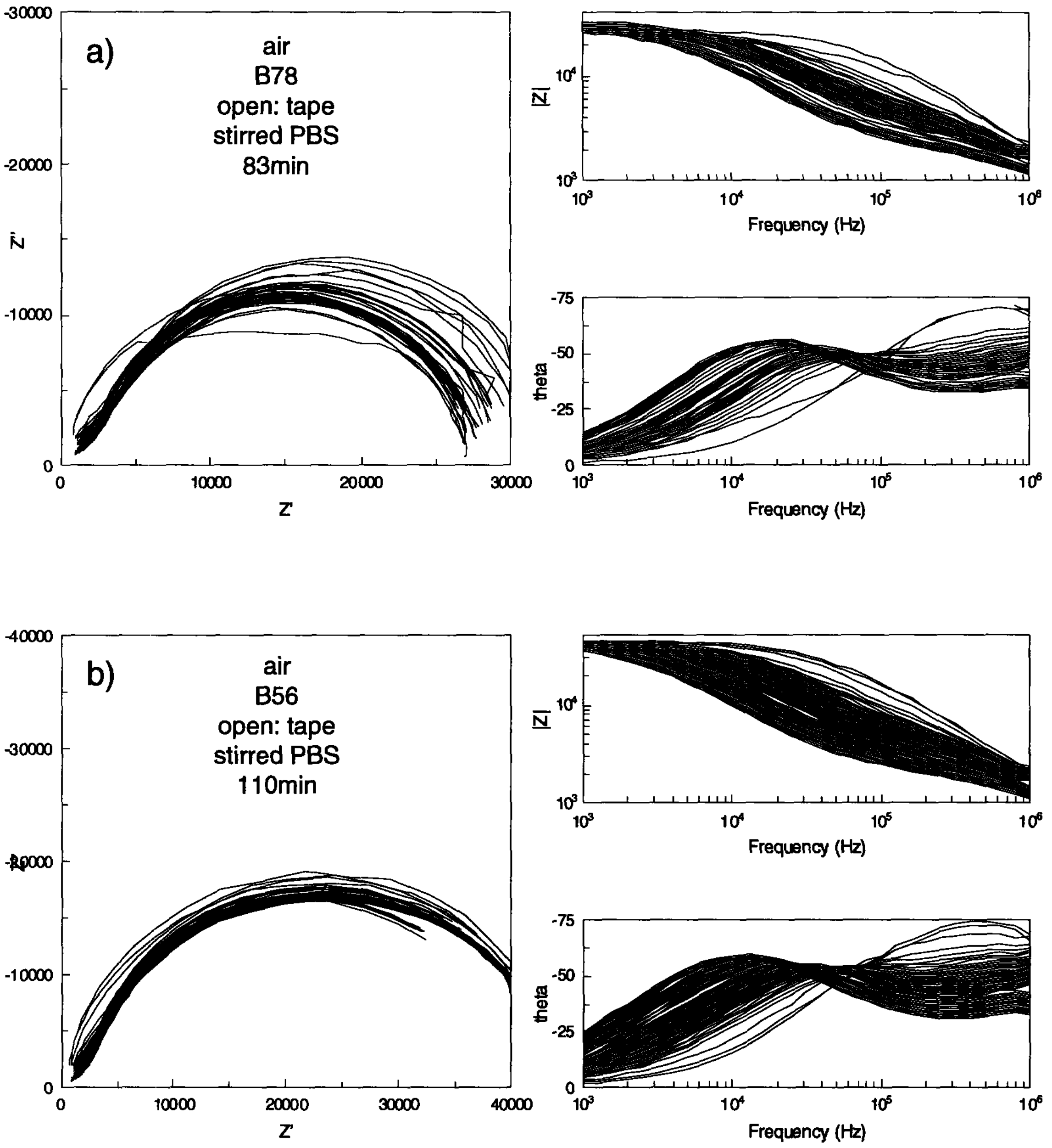

Figure 10.4a-b. Impedance spectra recorded during release of air from MEMS device R4B3 submersed in deaerated PBS. **a)** reservoir B78, **b)** reservoir B56.

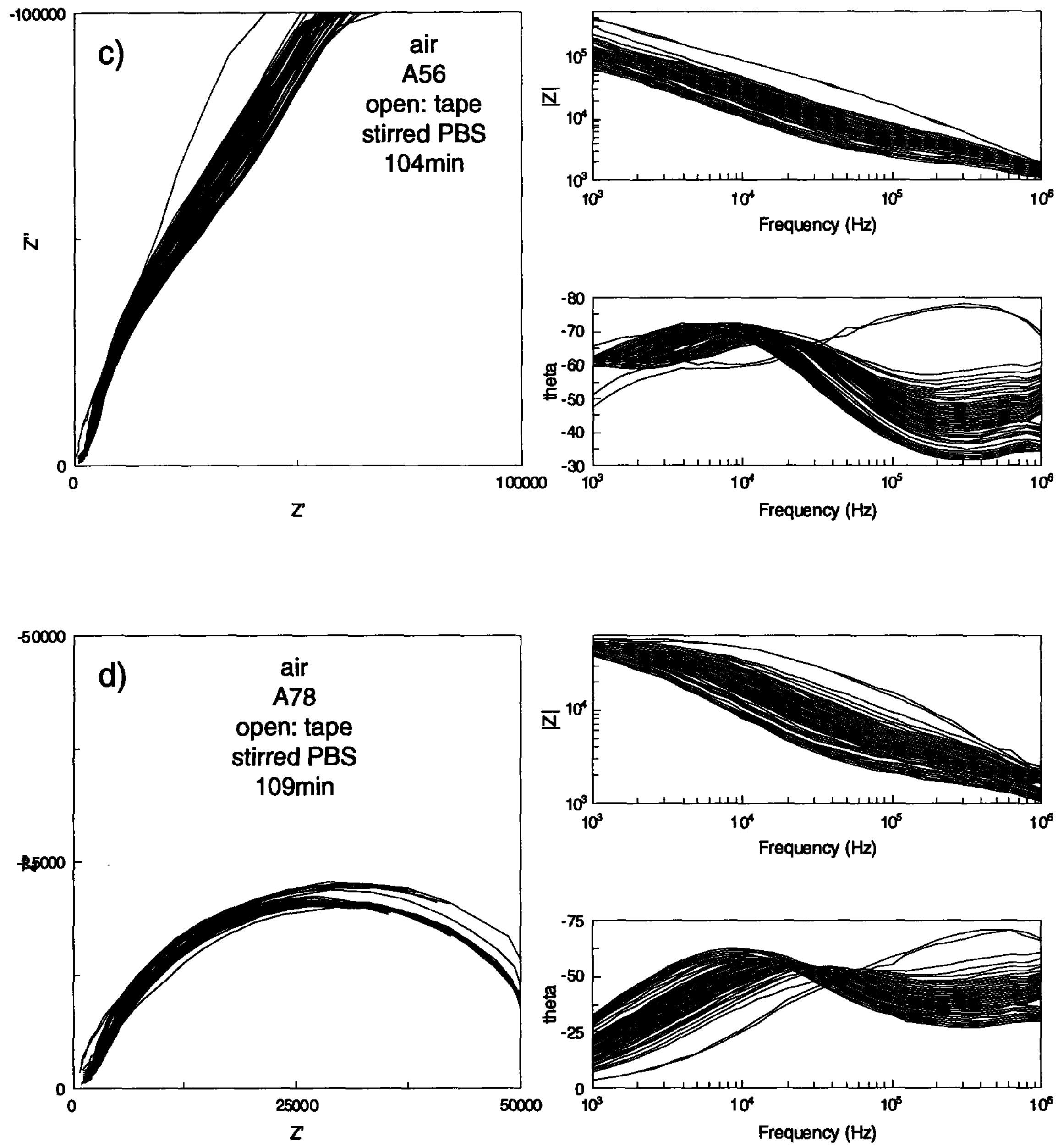

Figure 10.4c-d. Impedance spectra recorded during release of air from MEMS device R4B3 submersed in deaerated PBS. **c)** reservoir A56, **d)** reservoir A78.

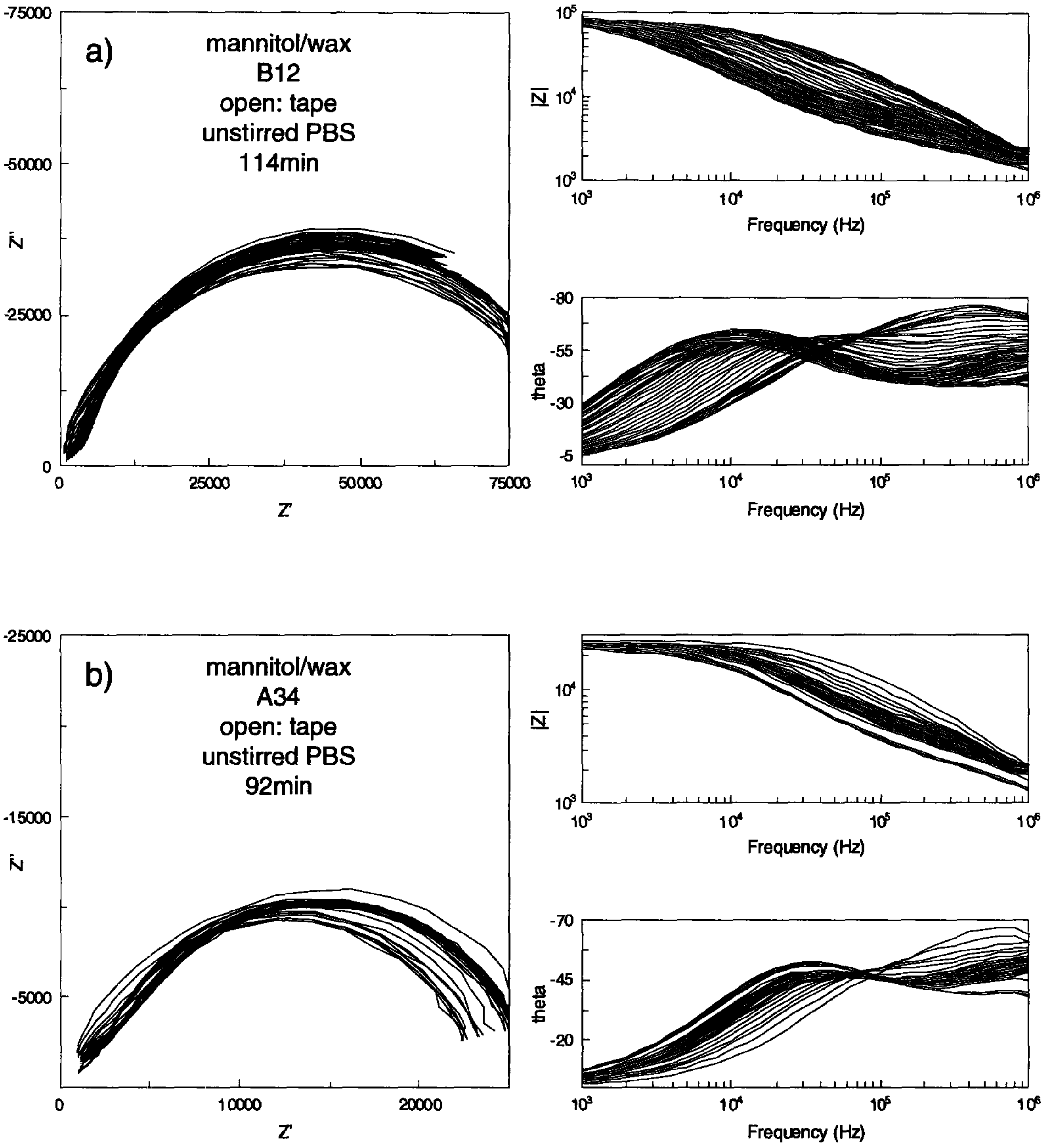

Figure 10.5. Impedance spectra recorded during release of mannitol backed by eicosane wax from MEMS device L4B4 submersed in unstirred PBS. **a)** reservoir B12, **b)** reservoir A34.

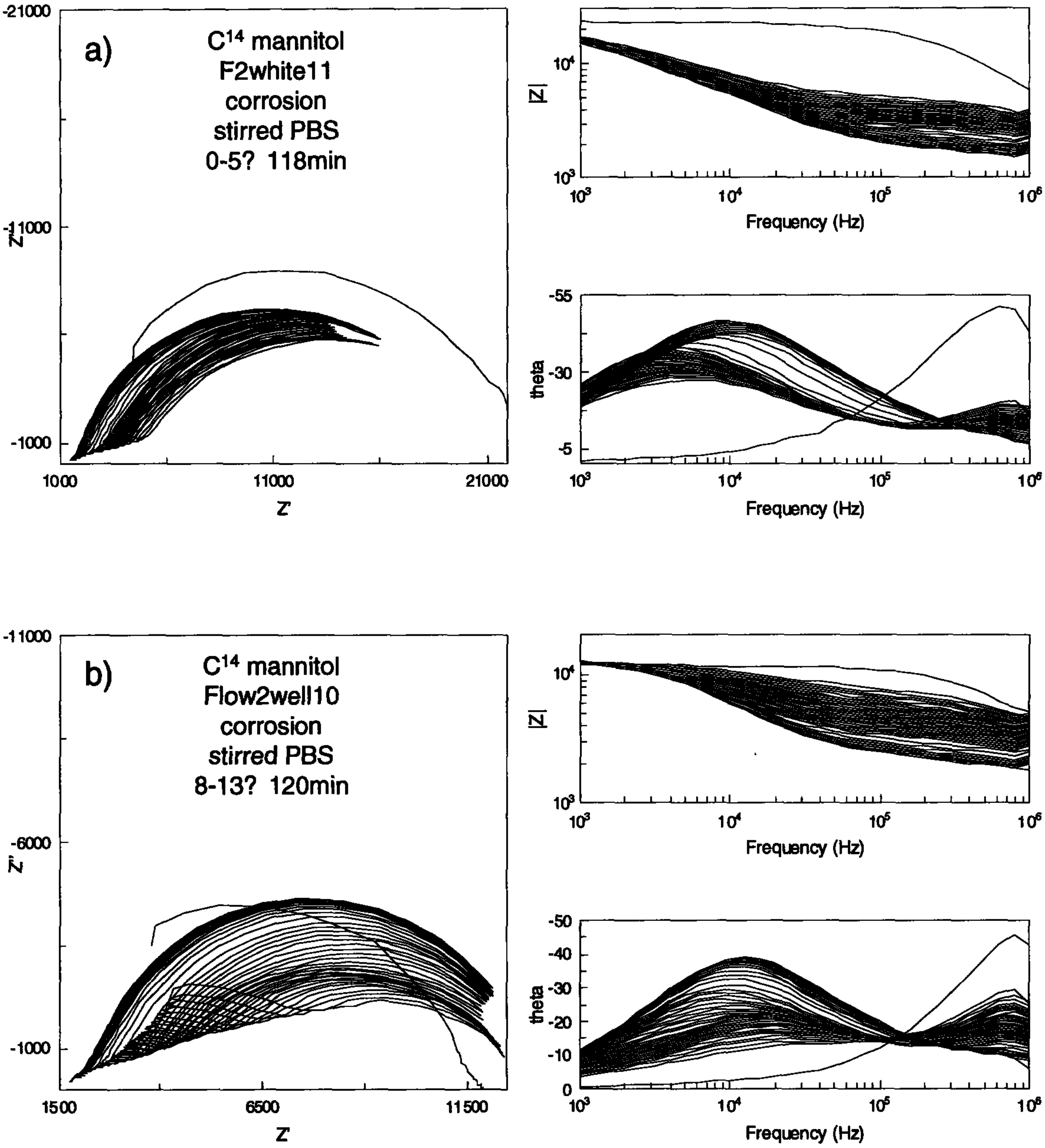

Figure 10.6a-b. Impedance spectra recorded during release of radiolabeled mannitol from MEMS devices submersed in stirred PBS. **a)** device F2 reservoir white11, **b)** device Flow2 reservoir 10.

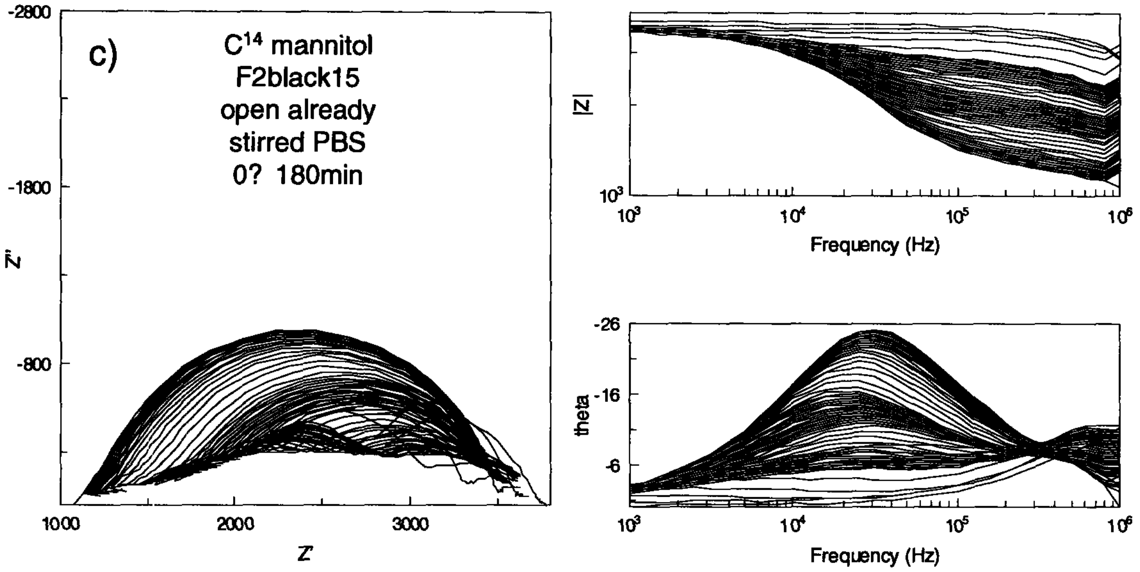

Figure 10.6c. Impedance spectra recorded during release of radiolabeled mannitol from MEMS devices submersed in stirred PBS. **c)** device F2 reservoir black15.

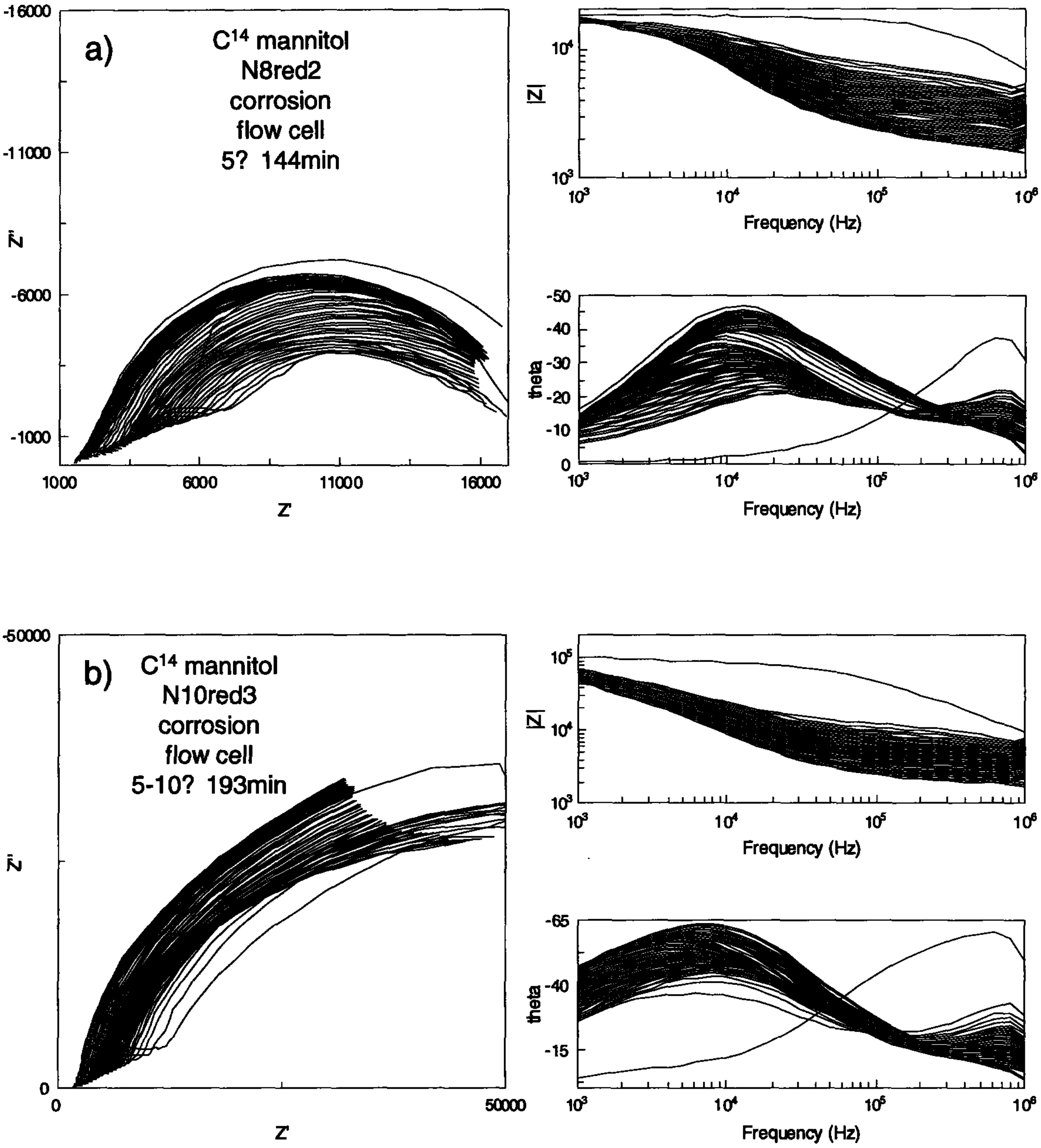

Figure 10.7a-b. Impedance spectra recorded during release of radiolabeled and unlabeled mannitol from MEMS devices into PBS in laminar flow cell. **a)** device N8 reservoir red2, **b)** device N10 reservoir red3.

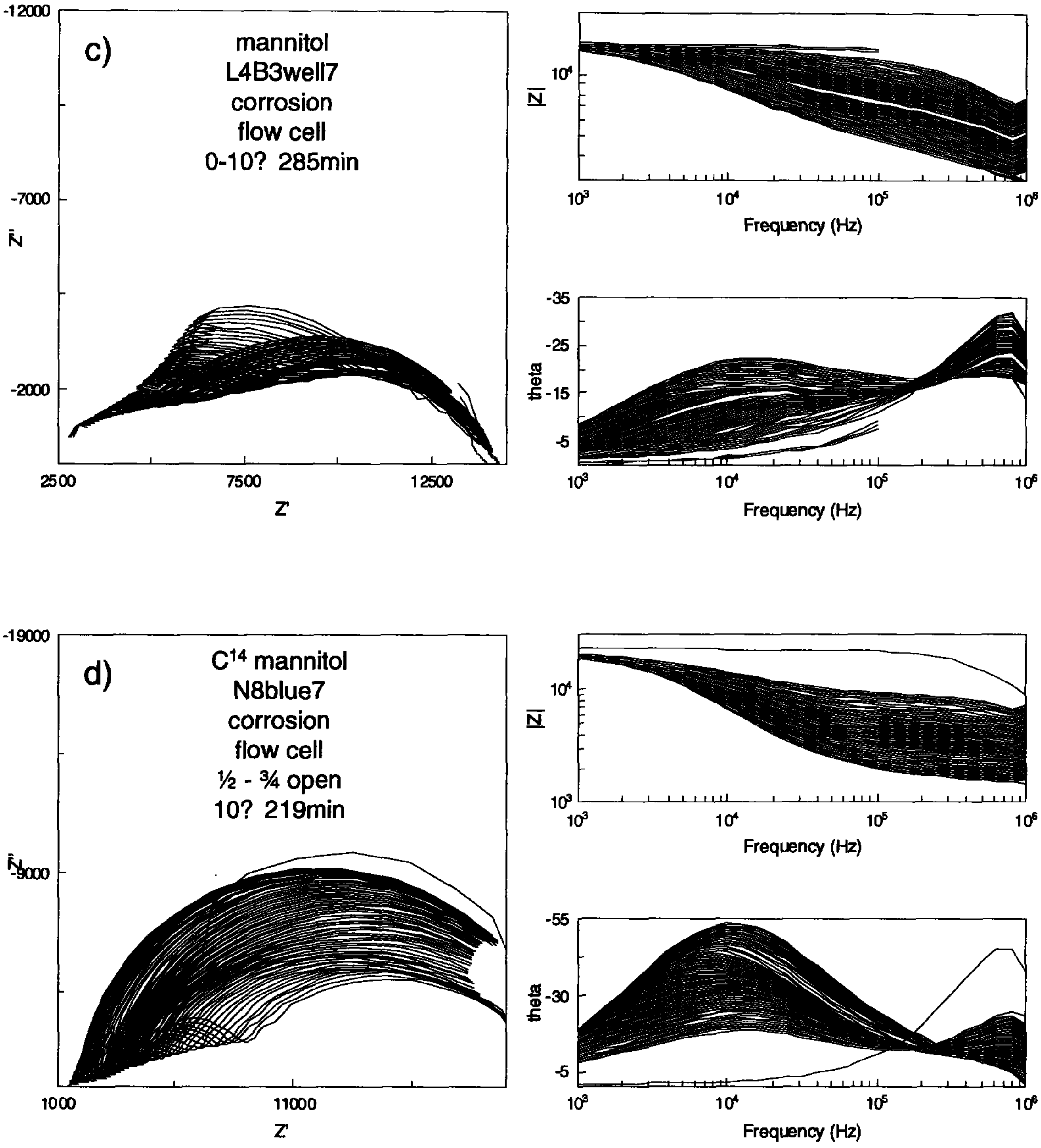

Figure 10.7c-d. Impedance spectra recorded during release of radiolabeled and unlabeled mannitol from MEMS devices into PBS in laminar flow cell. **c)** device L4B3 reservoir 7, **d)** device N8 reservoir blue7, which was ½ - ¾ covered by the flow cell gasket.

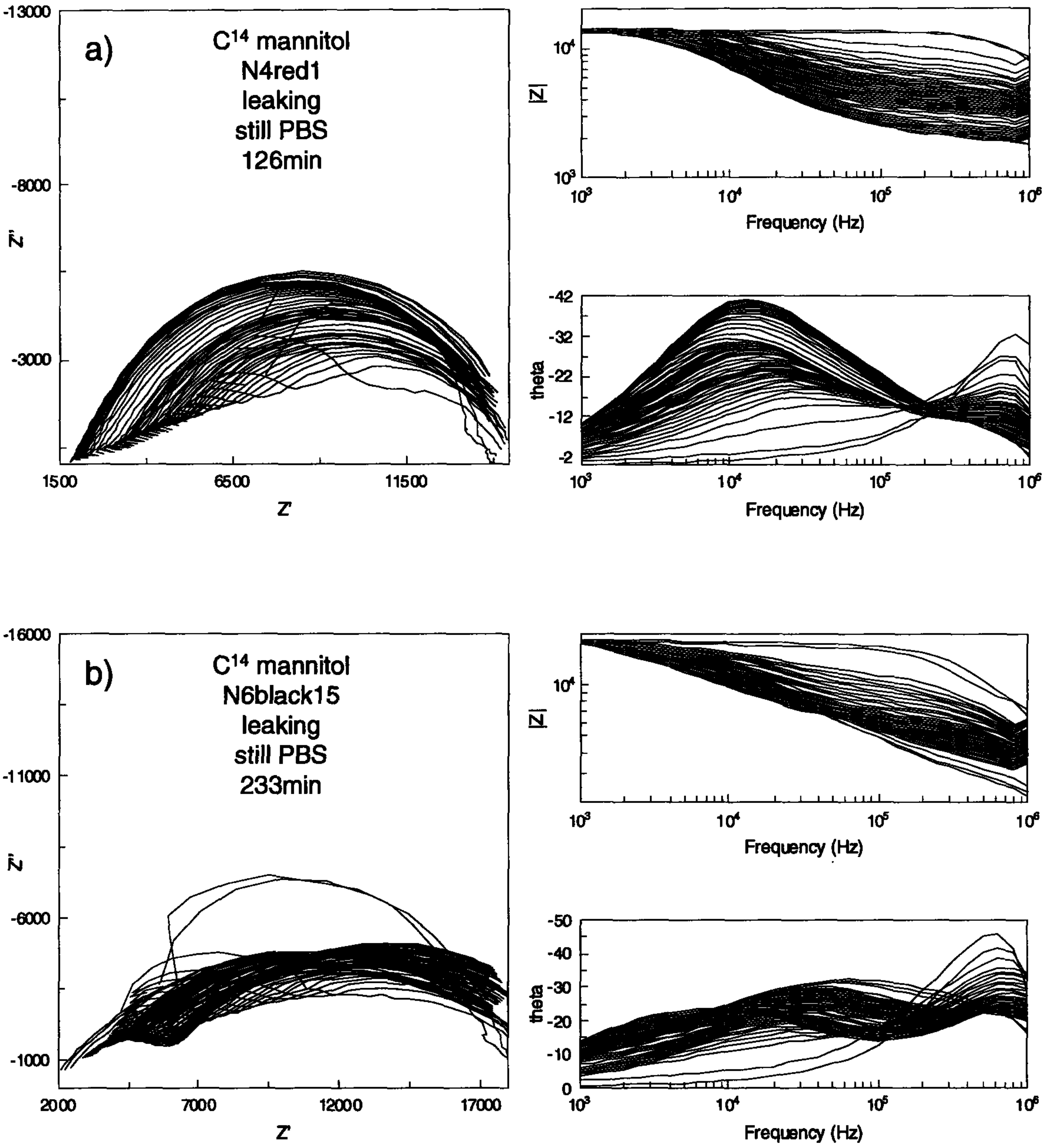

Figure 10.8a-b. Impedance spectra recorded during release of radiolabeled mannitol from MEMS devices into PBS during leak testing before implantation. **a)** device N4 reservoir red1, **b)** device N6 reservoir black15.

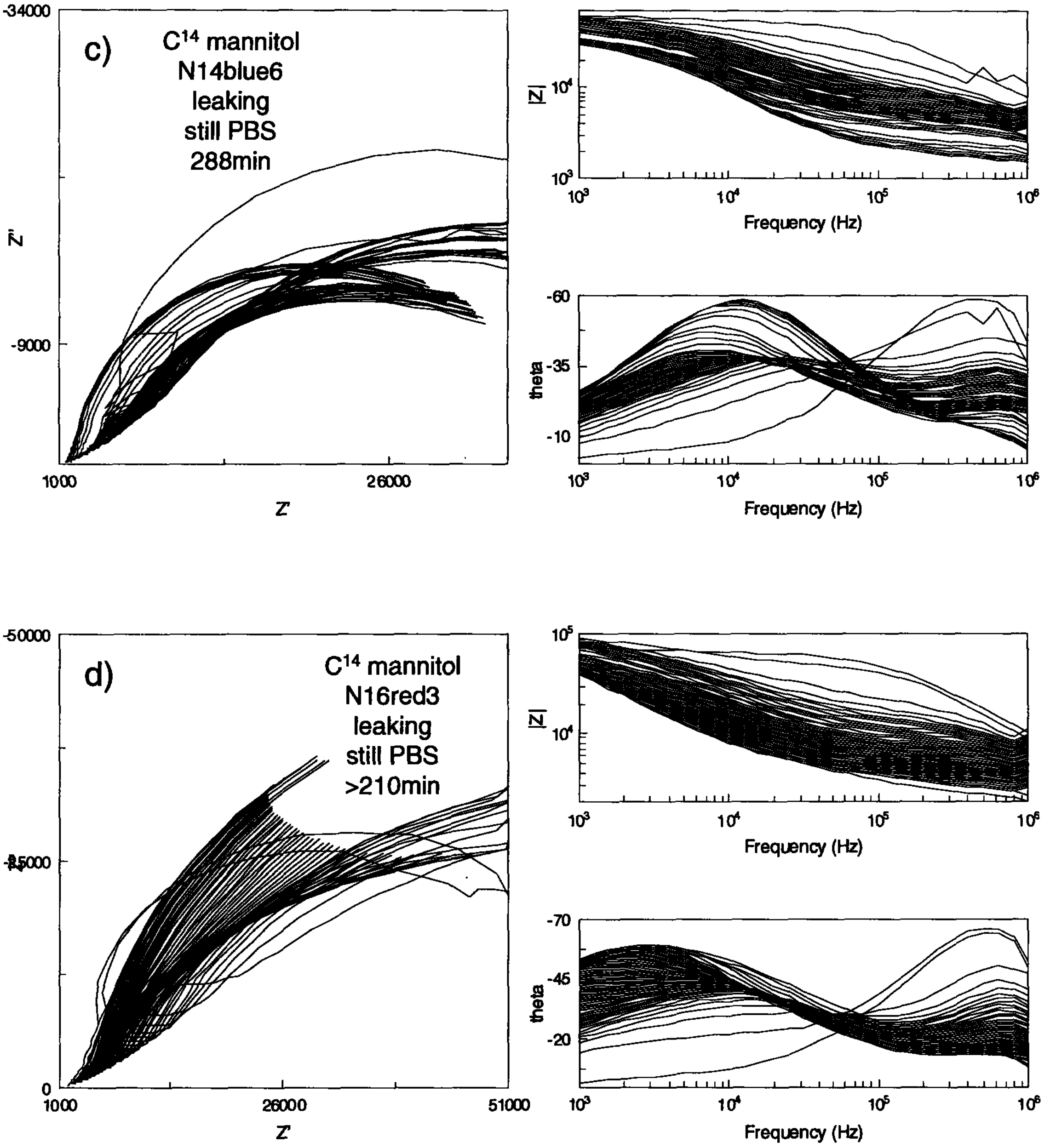

Figure 10.8c-d. Impedance spectra recorded during release of radiolabeled mannitol from MEMS devices into PBS during leak testing before implantation. **c)** device N14 reservoir blue6, **d)** device N16 reservoir red3.

10.5. Supplemental *in vivo* data

In addition to the data in chapter 6, the following data may be useful in evaluating the results of the *in vivo* studies. Included in this appendix are the standard curve prepared by Rebecca Shawgo for conversion of CPM to microcuries in rat urine, the cumulative radioactivity released during implantation for all six rats in the first *in vivo* study, and the sets of impedance spectra obtained during the seven *in vivo* releases.

10.5.1. Standard curve for CPM/μCi conversion

Figure 10.9 shows the standard curve prepared by Rebecca Shawgo for conversion of CPM (counts per minute) in rat urine to microcuries of mannitol loaded into the devices. It was made by dissolution of a piece of mannitol from the melt loading process in baseline rat urine and successive dilutions. The conversion factor may be too low, because the radioactivity released *in vivo* is consistently lower than expected. However, since the main goal of the radioactivity measurements was to verify that release had occurred, no further standard curves were prepared. The conversion factor obtained was 1.851 × 10^6 CPM/μCi, while the conversion factor for measurements in PBS or water is 2.2 × 10^6 DPM/μCi (with a corresponding factor of 1.13 DPM/CPM).

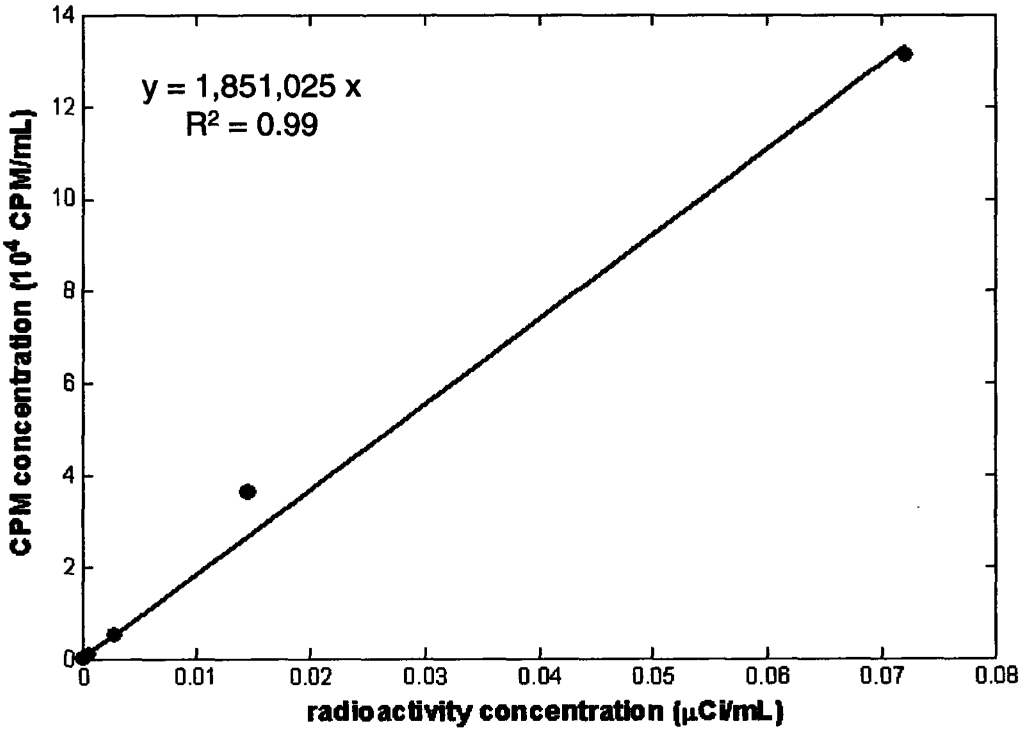

Figure 10.9. Standard calibration curve for conversion of CPM to microcuries of radioactivity in rat urine.

10.5.2. Cumulative radioactivity released from implants

The cumulative radioactivity released from all of the implants during the second *in vivo* study is reported in chapter 6 because all four devices showed at least one successful activation and monitoring. However, for the first *in vivo* study, only one of the six devices was successfully activated and monitored, and a graph of all six devices is cluttered by a number of leaks from broken membranes. Figure 10.10 shows the radioactivity detected in the urine for all six devices including the control device in the first study. The number of broken membranes was significantly reduced in the second study, making the data much easier to interpret than the data with several leaks shown in Figure 10.10.

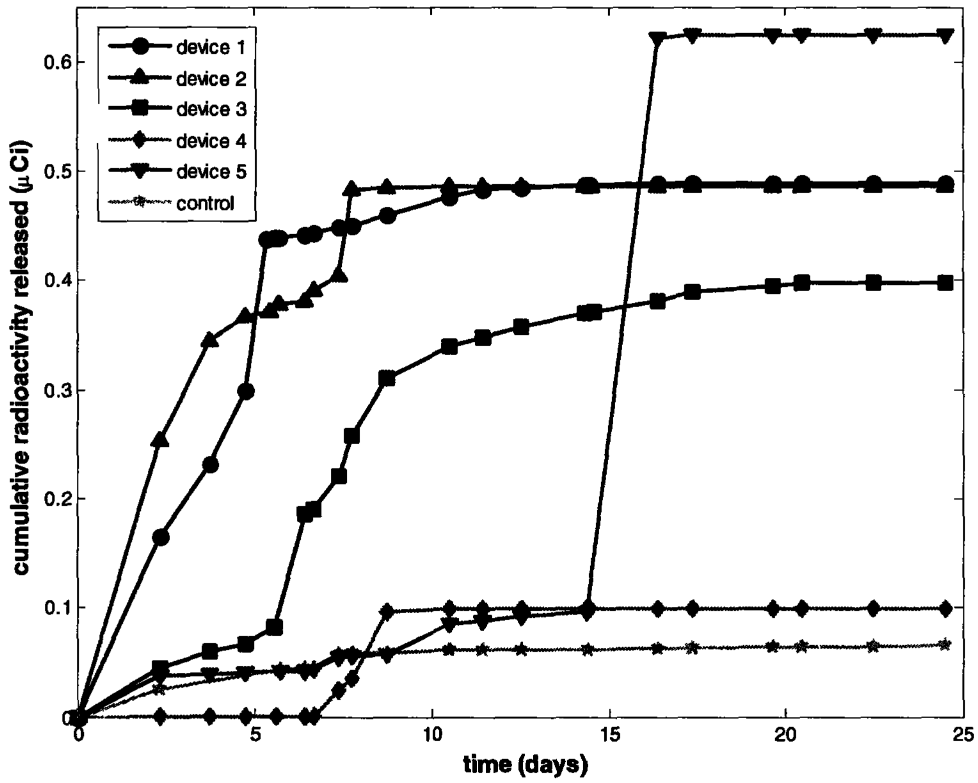

Figure 10.10. Cumulative radioactivity (C^{14} mannitol) released from implanted devices as measured by scintillation counting of urine samples during first *in vivo* study.

10.5.3. Impedance spectra during release monitoring

The raw sensor output takes the form of a series of impedance spectra. The spectra are fitted to the equivalent circuit to yield values of the silicon resistance, silicon capacitance, solution resistance, and double layer capacitance. The best-fit solution resistance and double layer capacitance are given in the figures in chapter 6. However, the original impedance data for the seven releases are given in Figure 10.11 for completeness.

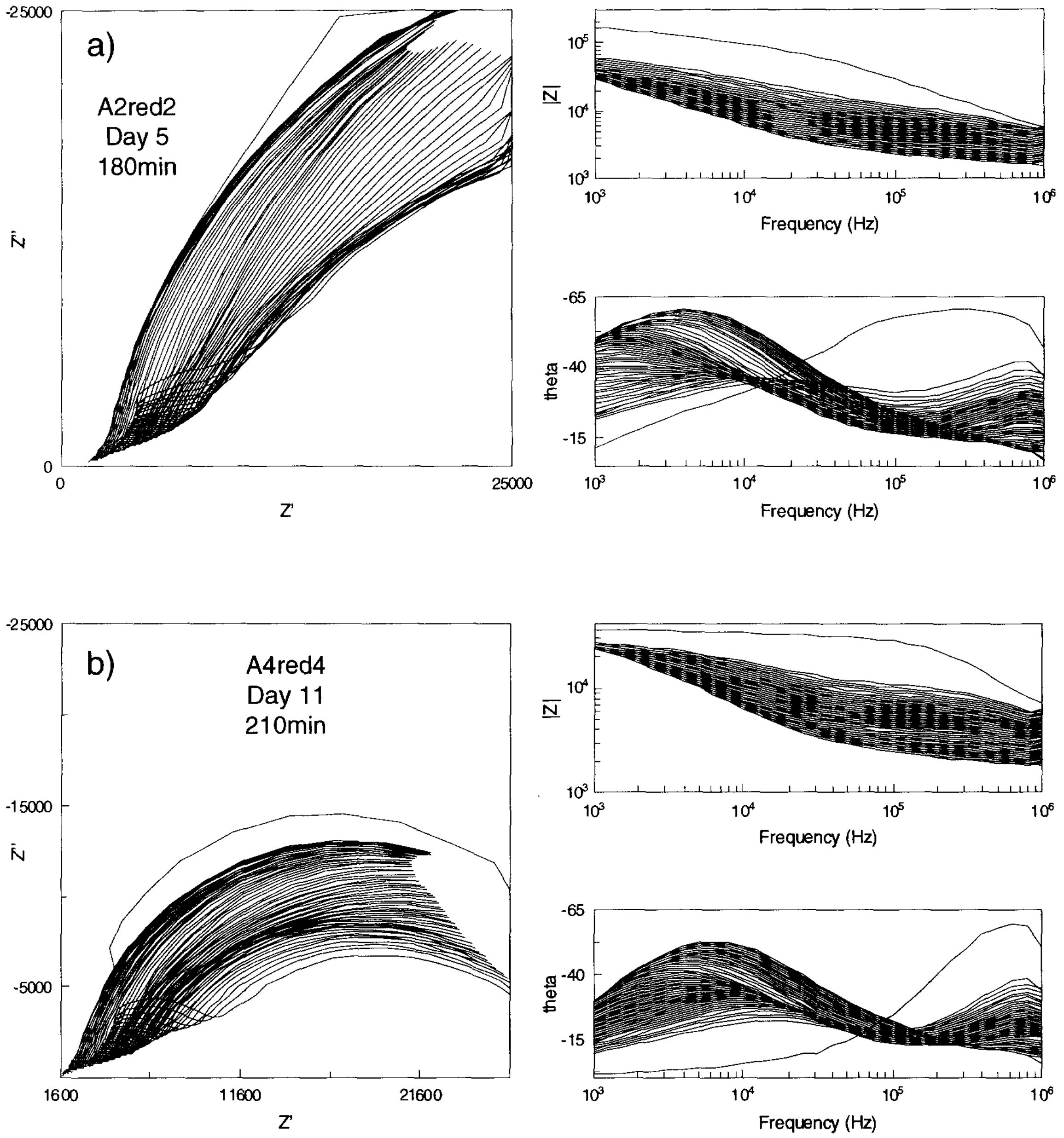

Figure 10.11a-b. Impedance spectra recorded during mannitol release from implanted MEMS devices. **a)** device A2 reservoir red2 release on day 5, **b)** device A4 reservoir red4 release on day 11.

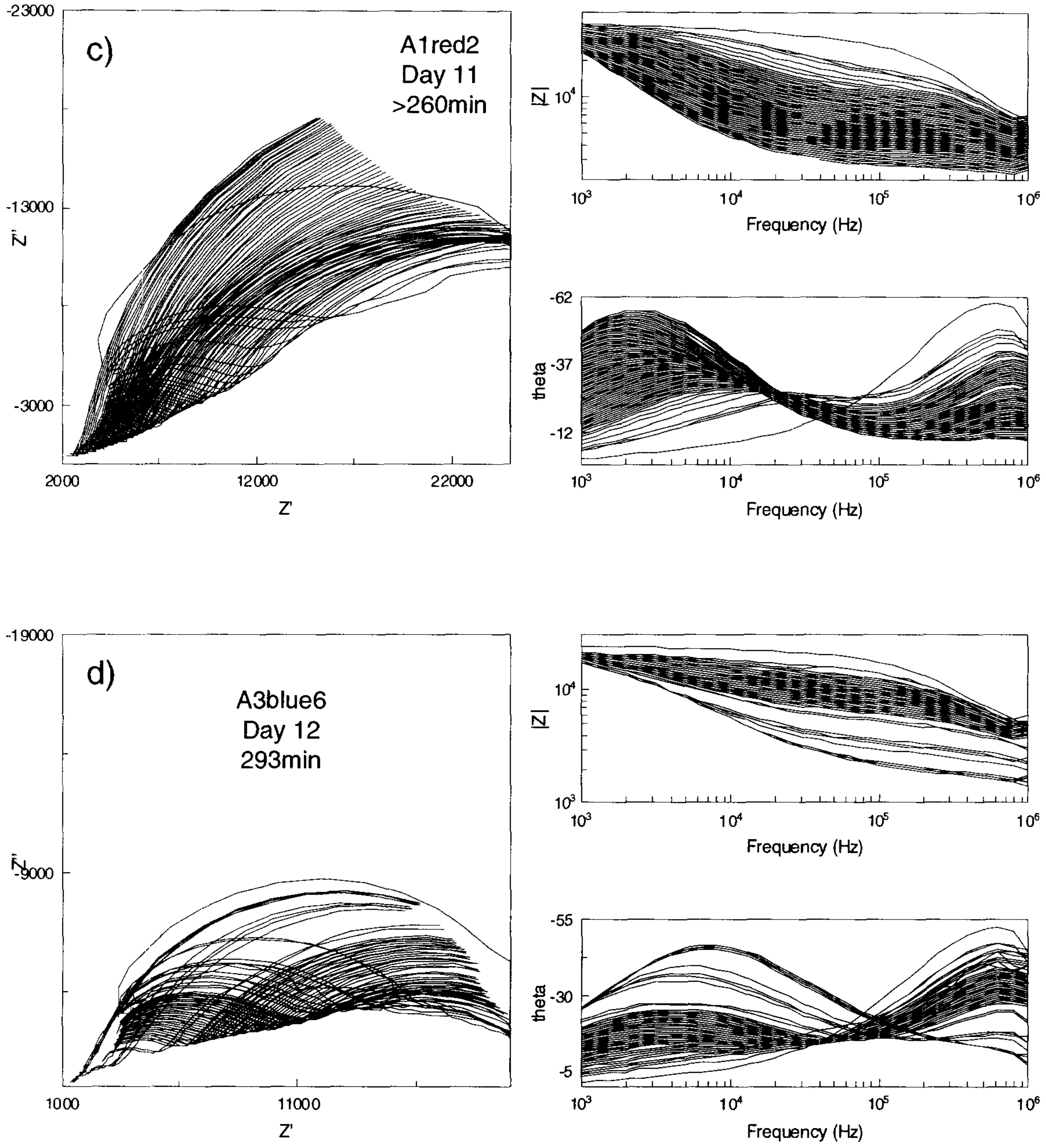

Figure 10.11c-d. Impedance spectra recorded during mannitol release from implanted MEMS devices. **c)** device A1 reservoir red2 release on day 11, **d)** device A3 reservoir blue6 release on day 12.

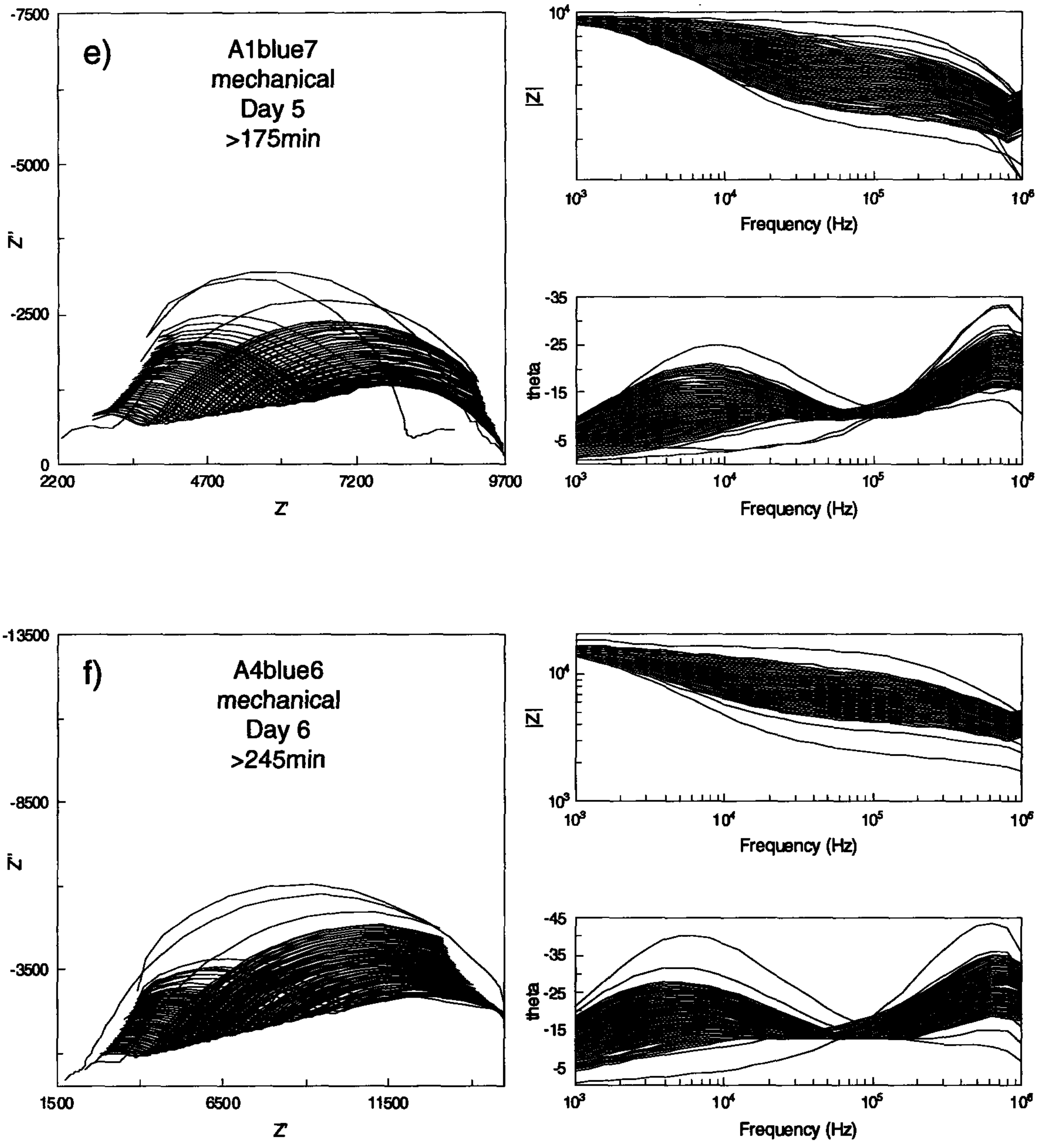

Figure 10.11e-f. Impedance spectra recorded during mannitol release from implanted MEMS devices. **e)** device A1 reservoir blue7 released mechanically on day 5, **f)** device A4 reservoir blue6 released mechanically on day 6.

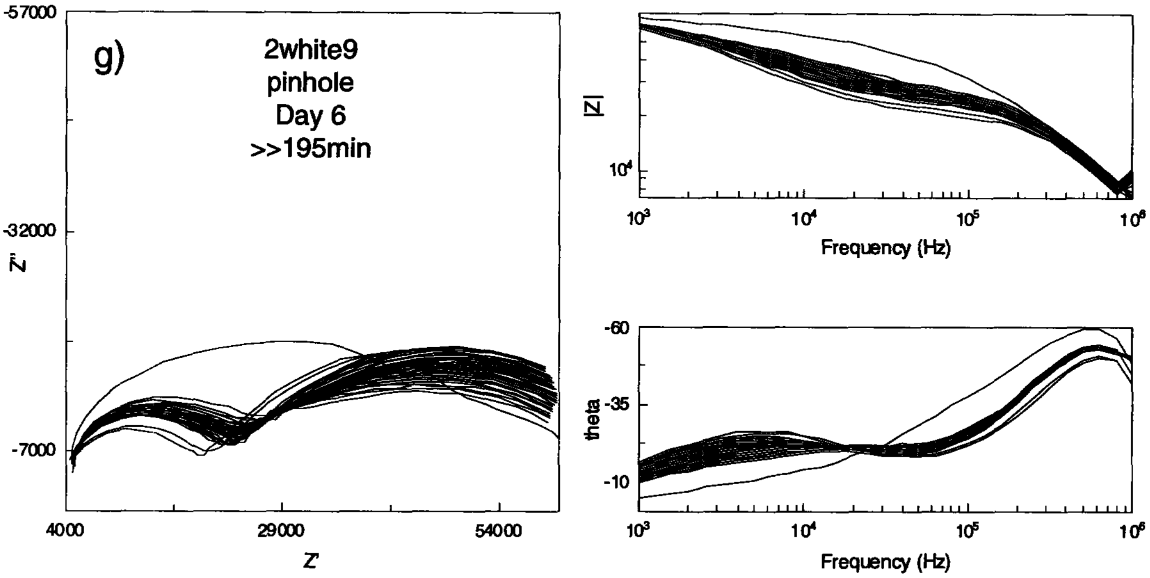

Figure 10.11g. Impedance spectra recorded during mannitol release from implanted MEMS devices. **g)** device 2 reservoir white9 release on day 6 during first *in vivo* study showing very slow release.

10.6. Machine shop schematics

Both the macromodel of a device reservoir and the laminar flow cell were constructed by the MIT machine shop. The specifications for each project are given below.

10.6.1. Reservoir macromodel schematic

The 100x scale model was built according to the schematic drawings in Figure 10.12.

Audrey Johnson
cameo@mit.edu
x3-6315

Drawings for construction of square pyramid model of well
Well should be watertight
Material should be transparent (plexiglass) and non-conducting (no metal)
Dimensions are for inside of pyramid -- wall thickness = ?
Tolerance: lengths should be +/- 0.5mm if possible
Top of pyramid is open, one side swings open on a hinge

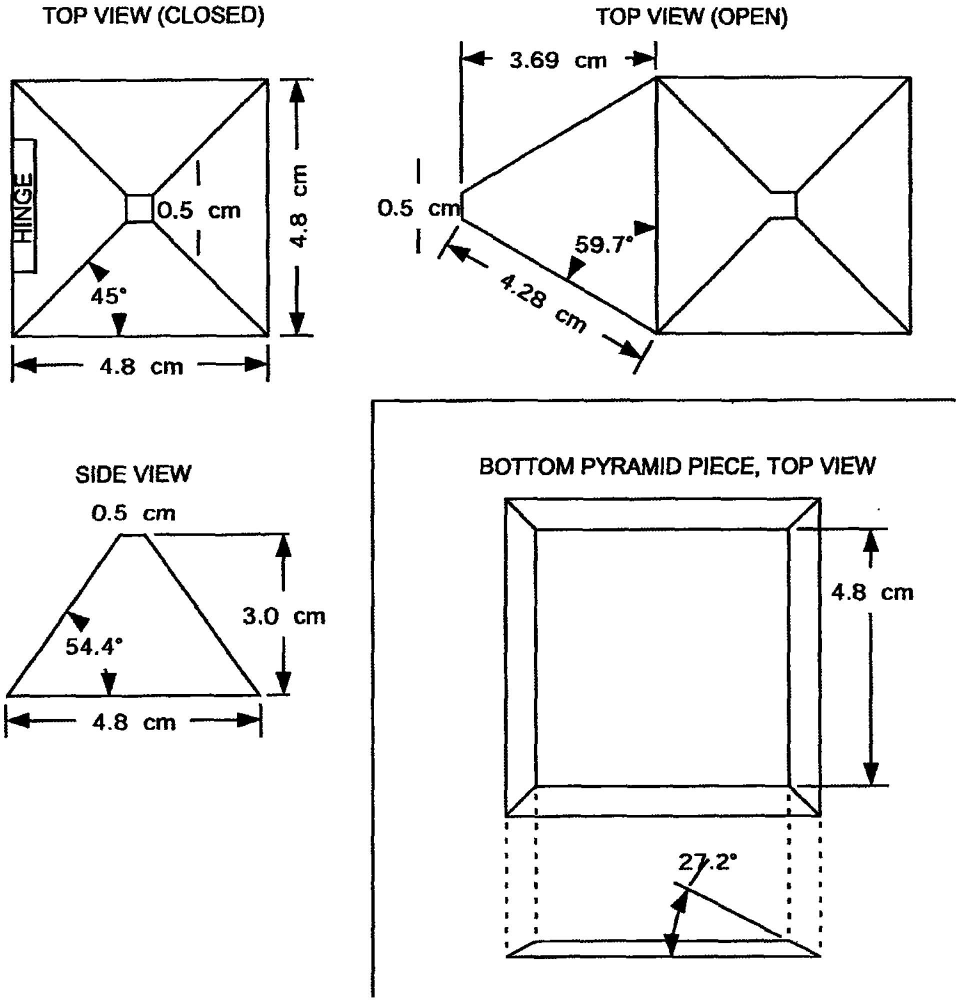

Figure 10.12a. First of two pages of macromodel schematic drawings.

Audrey Johnson
cameo@mit.edu
x3-6315

SIDE PIECES, LAID FLAT

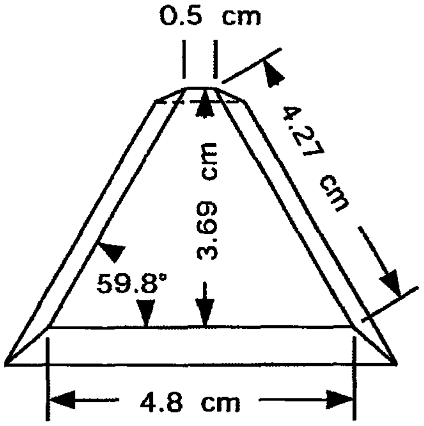

Inner dimensions are important, outer dimensions can vary depending on material thickness

Each edge is slanted to fit with other pieces of the pyramid, angles are given in lower drawings

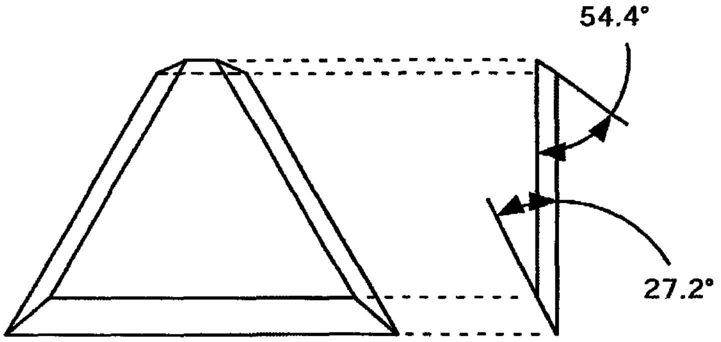

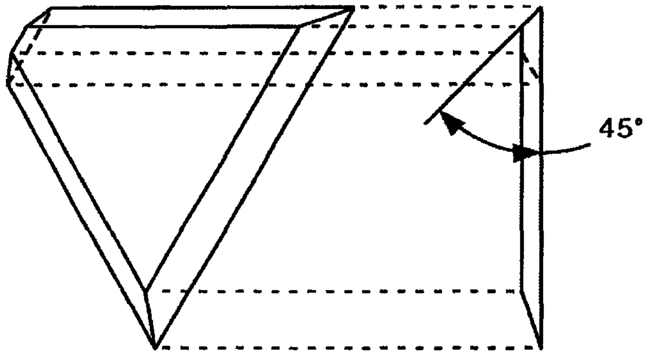

Figure 10.12b. Second and last page of macromodel schematic drawings.

10.6.3. Flow cell schematic

The flow cell is constructed out of three pieces: the main channel, a cover over the channel, and a backing plate that is placed behind the microchip to apply pressure. Figures 10.13 through 10.15 show the schematics for the construction of each flow cell component.

Audrey Johnson
cameo@mit.edu
x3-6315
Flow Cell Diagram, p1/3
Top and Side Views, no dimensions

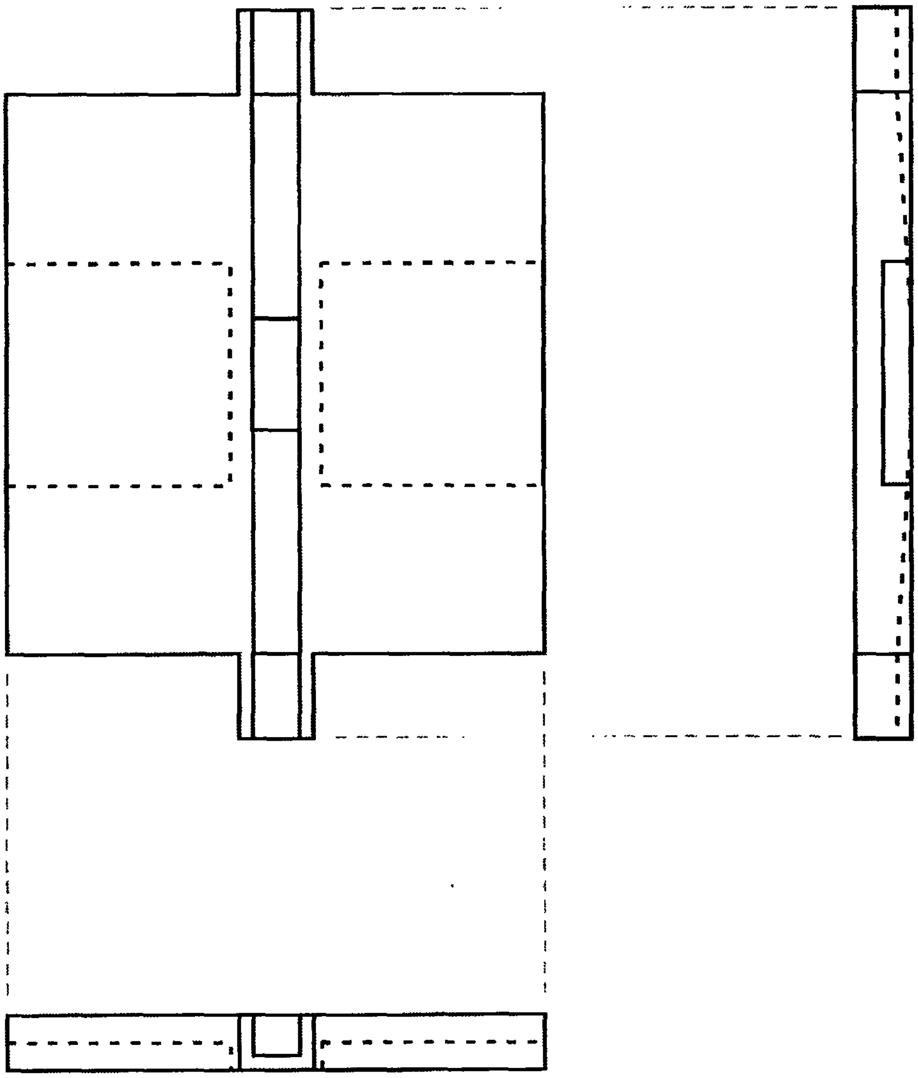

Figure 10.13a. First of three pages of flow cell schematic drawings.

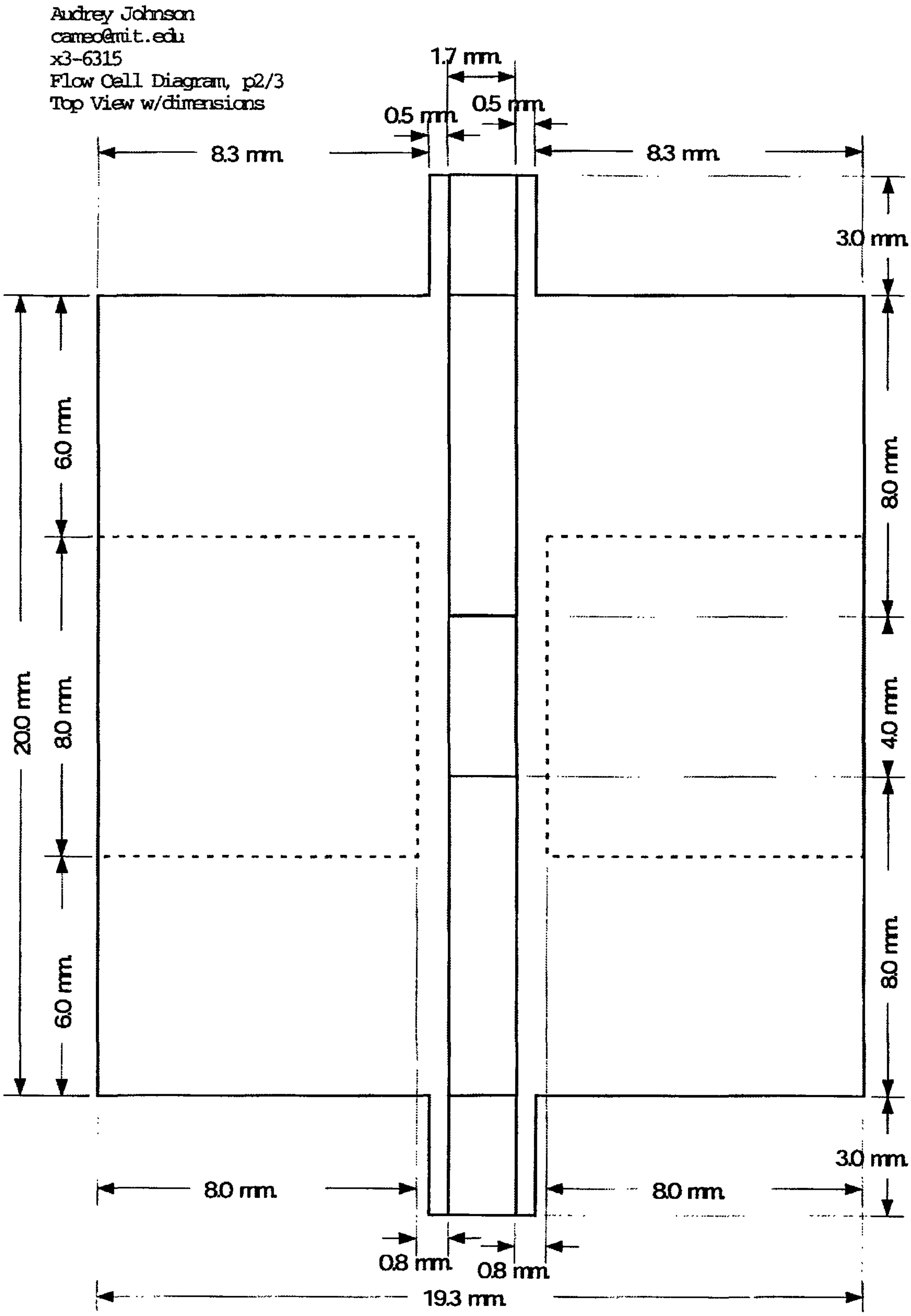

Figure 10.13b. Second of three pages of flow cell schematic drawings.

Audrey Johnson
cameo@mit.edu
x3-6315
Flow Cell Diagram, p3/3
Side Views w/dimensions

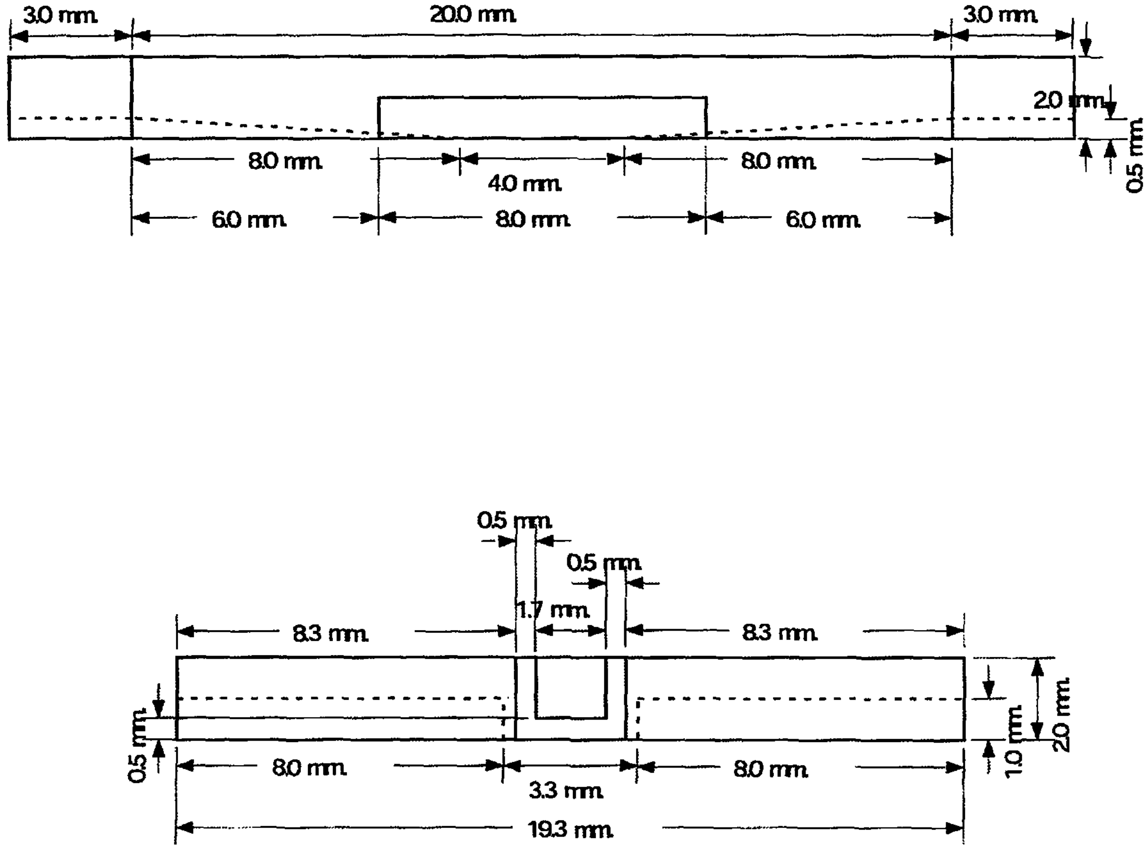

Figure 10.13c. Third and last page of flow cell schematic drawings.

Audrey Johnson
cameo@mit.edu
x3-6315
Flow Cell Cover Diagram, p1/2
Top and Side Views, no dimensions

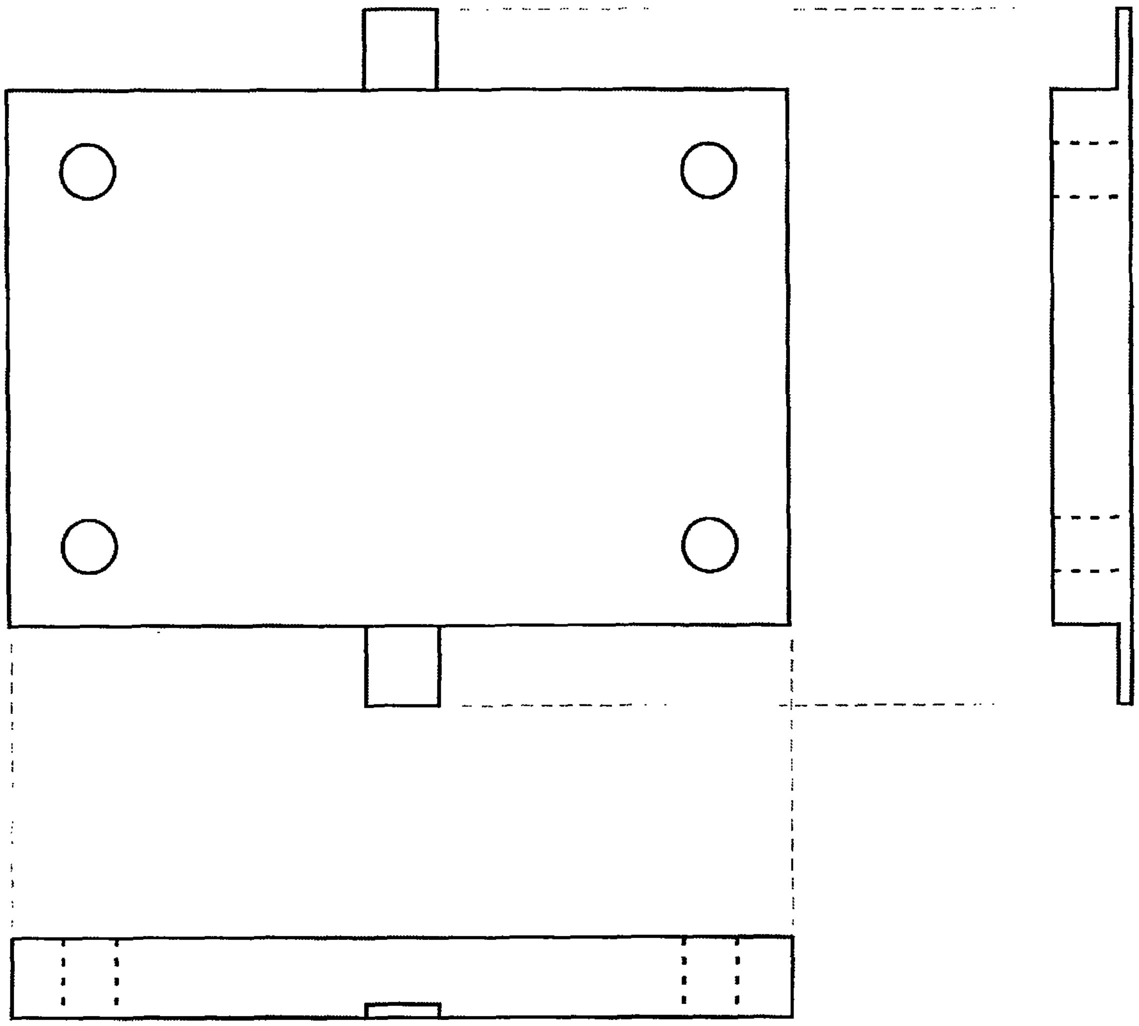

Figure 10.14a. First of two pages of flow cell cover schematic drawings.

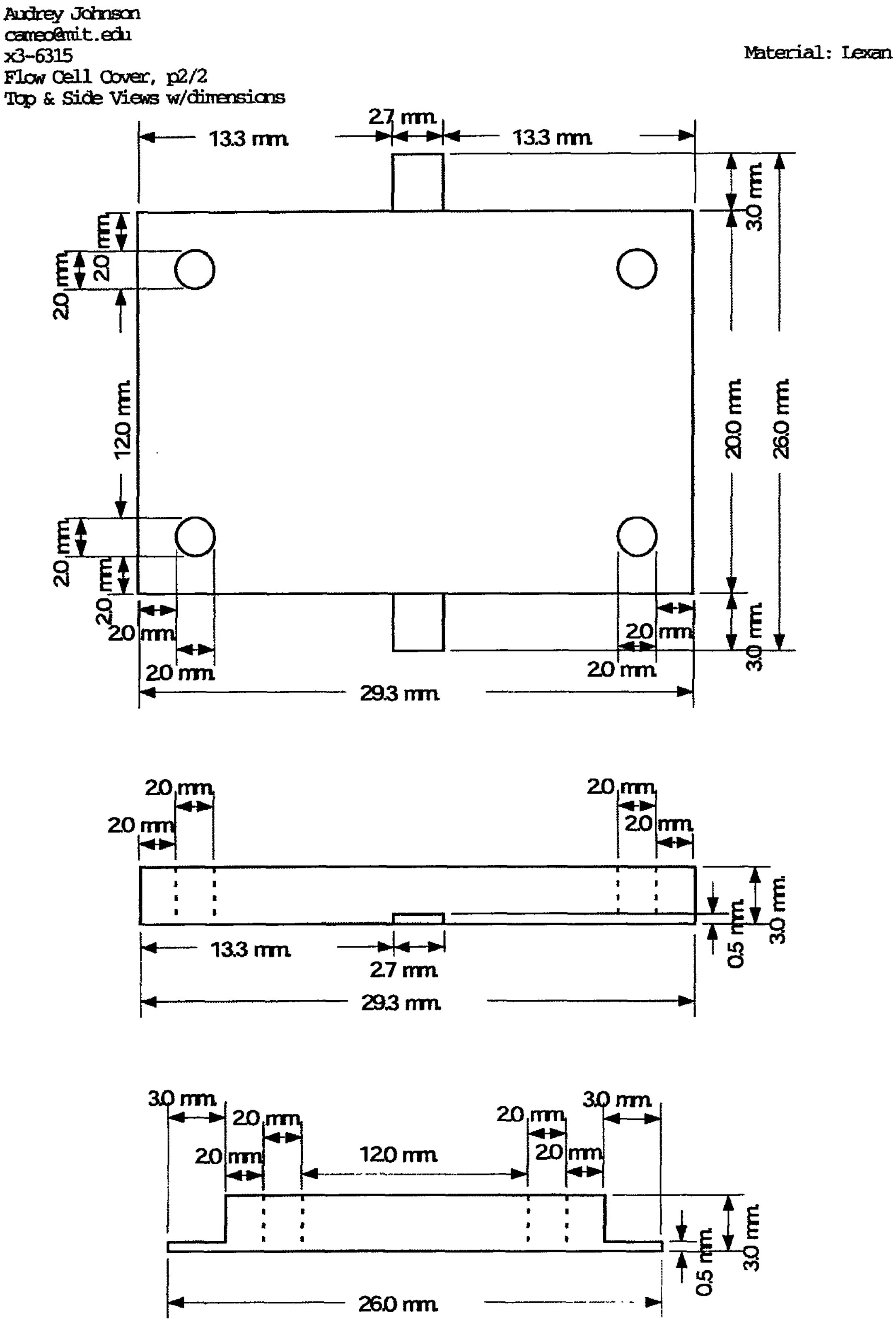

Figure 10.14b. Second and last page of flow cell cover schematic drawings.

Audrey Johnson
cameo@mit.edu
x3-6315
Flow Cell Bottom Diagram, p1/2
Top and Side Views, no dimensions

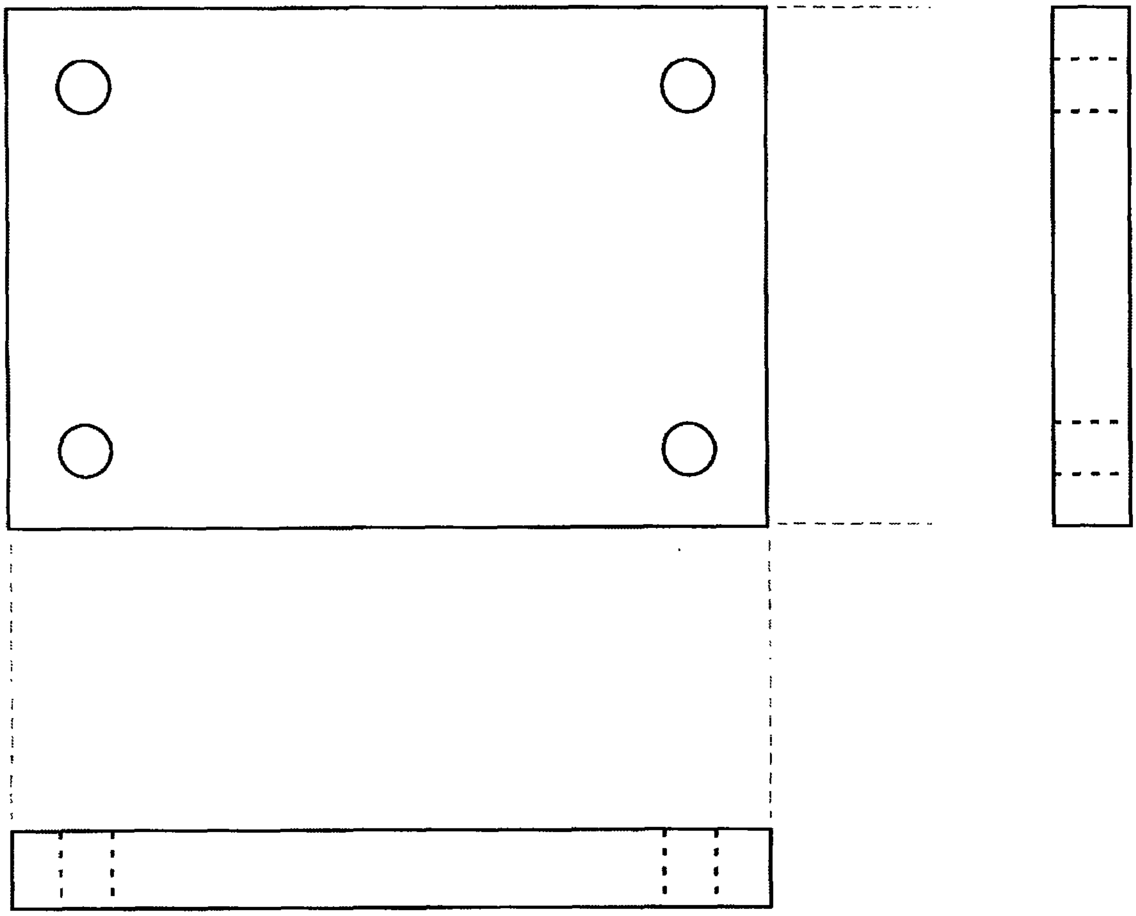

Figure 10.15a. First of two pages of flow cell back plate schematic drawings.

Audrey Johnson
cameo@mit.edu
x3-6315
Flow Cell Bottom, p2/2
Top & Side Views w/dimensions

Material: Stainless Steel

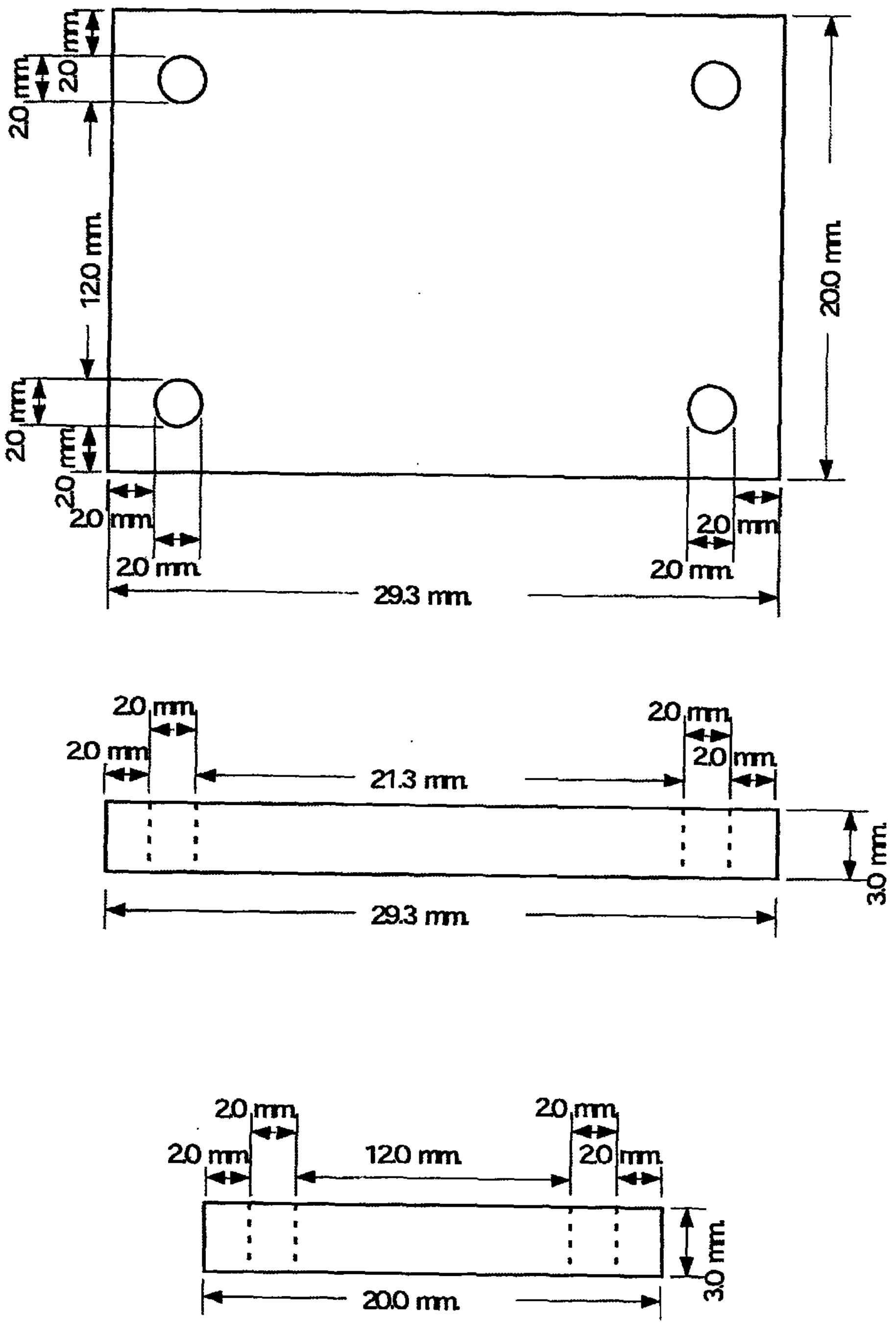

Figure 10.15b. Second and last page of flow cell back plate schematic drawings.

10.7. Numerical simulation MATLAB code

The MATLAB finite differences simulation of drug dissolution from a cylindrical reservoir into a dead space consists of five m-files: CylinderModel.m, calcA_Cylinder.m, calcb_Cylinder.m, calcb_Jac_Cylinder.m, and KJB_PDE_solver1_AJ.m. The file CylinderModel.m is the main program file that asks for input and calls the other programs. Three subprograms calculate the A matrix, the b vector, and the Jacobian matrix for the equation **Ax** = b. The solver program was written by Dr. Ken Beers for the 10.34 numerical methods course and is modified slightly to fit this simulation.

The first version of the program, developed for the course term project, used a fixed grid of points and a mass balance to move the boundary through them. The later version uses the stretch factor α to expand the grid points as the drug dissolves, as described in chapter 7. The stretch factor makes the simulation much more stable at early time points, because the grid points are automatically closer together at the beginning of the simulation when the concentration gradient is being established. Additional details of the scaling and discretization may be found in the final project report for course 10.34.

10.7.1. Main program file

```
% CylinderModelMannitol.m
% Audrey M. Johnson 8/16/2004
%
% This program solves the diffusion equation in two dimensions
% for the case of a cylindrical space with one face open to a
% large volume, with a moving boundary within the cylinder.
%
% This is an approximation of the dissolution of drug from a
% well on a drug delivery microchip, through a stagnant zone (fibrous
% capsule), into a well-mixed space (perfused tissue).
%
% The fluid velocity is assumed to be zero everywhere
% A volumetric generation rate is allowed but in
% most cases will be zero.
%
% For a picture of the system see notes.  The open face of the
% cylinder is located at zeta = 1, and the dissolution interface is zeta = 0
% The dissolution interface starts at a distance alpha_zero from the well
opening
% and moves back until alpha = WellDepth.  At that point the species is
% entirely dissolved and the simulation continues with a no flux condition
% at the back of the well.
%
% Note that when plotting concentration vs. the axial (zeta) coordinate,
% the points inside the well (zeta vector values from 0 to 1) should be entered
% into the following formula to get the 'true' distance in terms of a fixed
% zeta coordinate:
%    zeta_fixed = el + alpha*zeta
% The values of el and alpha vary with time while zeta does not.
% Values of the zeta vector from 1 to OutAxial should be entered into the
formula:
%    zeta_fixed = WellDepth - 1 + zeta
```

```
% The values of zeta_fixed obtained for these points (in the dead space outside
% the reservoir) will not vary with time.
%

% Restart option
restart = input('Is this a restart? (Y=1, N=0) : ');

if(restart==0)
% In this section we enter physical parameters
% Radius of well, depth of well, Axial edge, Radial edge, Solid conc'n,
% Volumetric generation rates inside and out

% Well geometry
% R = input('Input radius of well (microns) : ');
% H = input('Input depth of well (microns) : ');
% Rout = input('Input radius of dead space (microns) : ');
% delta = input('Input distance from chip wall to edge of dead space (microns)
: ');
% int_pos_zero = input('Input percentage of well filled with drug (1-99): ');
R = 25;
H = 300;
Rout = 150;
delta = 200; % to mimic FEMLAB
int_pos_zero = 90; % to mimic FEMLAB

WellDepth = H/R; % dimensionless depth
OutRad = Rout/R; % dimensionless radial edge
OutAxial = (H+delta)/R; % dimensionless edge position
el_zero = WellDepth*int_pos_zero/100; % dimensionless interface position
alpha_zero = WellDepth - el_zero; % stretching factor on zeta, initial value

% Other physical parameters
% PhiWell = input('Input volumetric generation rate in well : ');
% PhiOut = input('Input volumetric generation rate in dead space : ');
% ThetaS = input('Input ratio of solid conc''n to equilibrium conc''n : ');
PhiWell = 0;
PhiOut = 0;
ThetaL = 1;
ThetaS = 8.18; % Mannitol ThetaS = 1.489/0.182

% Now enter the simulation parameters
% Nzeta, Neta, Nzo, Nro, max iterations, time step size
% Nzeta = input('Enter number of points in axial direction in well : ');
% Neta = input('Enter number of points in radial direction in well : ');
% Nzo = input('Enter number of points in axial direction in dead space : ');
% Nro = input('Enter number of points in radial direction in dead space : ');
disp('Recommended to use time step less than 0.001 for first 100 steps or so');
dt = input('Enter time step size : ');

% For basic simulation
% Nzeta = 20;
% Neta = 10;
% Nzo = 20;
% Nro = 10;

% For 2x finer mesh
Nzeta = 40;
Neta = 20;
Nzo = 40;
Nro = 20;

Ntotal = Neta*Nzeta + Nro + Nzo*(Neta + Nro);
disp(['Total number of points in simulation : ' num2str(Ntotal)]);
```

```
% Define zeta and eta vectors
% zeta and eta are invariant with time, but zeta_fixed will change over
% time, and is related to zeta by zeta_fixed(i) = el + alpha*zeta(i)
% for i=1:Nzeta, and zeta_fixed(i) = zeta(i)-1+H/R for i=Nzeta+1:Nzeta+Nzo
% Alpha will be a function of time

zeta1 = linspace(0,1,Nzeta)';
zeta2a = linspace(1,1+delta/R,Nzo+1)';
zeta2b = linspace(0,0,Nzo)';
for i=1:Nzo
   zeta2b(i) = zeta2a(i+1);
end
zeta = [zeta1; zeta2b];

eta1 = linspace(0,1,Neta)';
eta2a = linspace(1,OutRad,Nro+1)';
eta2b = linspace(0,0,Nro)';
for i=1:Nro
   eta2b(i) = eta2a(i+1);
end
eta = [eta1; eta2b];

% Stack parameters to send them to other subroutines
N_param = Nzeta + Nzo + Neta + Nro + 7;
param = linspace(0,0,N_param);
k = 0;
param(k+1:k+Nzeta+Nzo) = zeta; k = k + Nzeta + Nzo;
param(k+1:k+Neta+Nro) = eta; k = k + Neta + Nro;
param(k+1) = PhiWell; k = k + 1;
param(k+1) = PhiOut; k = k + 1;
param(k+1) = ThetaL; k = k + 1;
param(k+1) = ThetaS; k = k + 1;
param(k+1) = WellDepth; k = k + 1;
param(k+1) = alpha_zero; k = k + 1;
param(k+1) = dt;

iparam = [Nzeta; Neta; Nzo; Nro];

% Now define an initial state vector

u_init = zeros(Ntotal,1);

for j=1:Neta
   i = 1;
   k = (i-1)*Neta + j;
   u_init(k) = ThetaL;
end

% Now define names of program that will calculate A, b, and b_Jac

calc_A = 'calcA_Cylinder3';
calc_b = 'calcb_Cylinder3';
calc_b_Jac = 'calcb_Jac_Cylinder3';

% Tell solver which points are differential equations (epsilon = 1)
% and which are algebraic (epsilon = 0)

epsilon = zeros(Ntotal,1);

% Differential equations are at all interior points (regions 1,2,8)
% Interior points in well and at opening (regions 1 and 8)
for i=2:Nzeta
```

```
   for j=2:Neta-1
      k = (i-1)*Neta + j;
      epsilon(k) = 1;
   end
end

% Interior points in dead space (region 2)
for i=Nzeta+1:Nzeta+Nzo-1
   for j=2:Neta+Nro-1
      k = Neta*Nzeta + Nro + (i-Nzeta-1)*(Neta+Nro) + j;
      epsilon(k) = 1;
   end
end

% Now define the remaining inputs for the solver (iopt, ropt)
% iopt(1) = 0, implicit Euler, = 2, trapezoid rule
% iopt(2) = non-zero, all variables constrained to be positive
% iopt(3) = 0, A matrix independent of u, non-zero, calculate new A for each
step
% iopt(4) = iprint, how often to write out results, = 0, write out end results
only
% iopt(5) = number of simulations steps performed between Jacobian calculation
% iopt(6) = total number of time steps performed
% ropt(1) = Time step size
% ropt(2) = Convergence tolerance, = 0, keep integrating until total number of
steps

iopt(4) = input('Enter number of time steps between reporting of results : ');
iopt(6) = input('Enter number of time steps : ');

iopt(1) = 2;
iopt(2) = 1;
iopt(3) = 1;
%iopt(4) = 10;
iopt(5) = 10;
%iopt(6) = 100;

ropt = linspace(0,0,2)';
ropt(1) = dt;
ropt(2) = 0;

else % if this is a restart
   dt = input('Enter time step size : ');
   param(N_param) = dt;
   last_step = size(u_traj_total,1);
   param(N_param-1) = a_traj_total(last_step);
   ropt(1) = dt;
   iopt(4) = input('Enter number of time steps between reporting of results :
');
   iopt(6) = input('Enter number of time steps : ');
   for i=1:Ntotal
      u_init(i) = u_traj_total(last_step,i);
   end
end

% The program calls subroutine 'KJB_PDE_solver1_AJ3.m' which integrates
% forward over time to get the system dynamics.

[t_traj,u_traj,alpha_traj,iflag] =
KJB_PDE_solver1_AJ3(u_init,epsilon,calc_A,calc_b,calc_b_Jac,iopt,ropt,param,ipa
ram);

% Combine trajectories into 'total' vectors that include initial state
```

```
if(restart==0)
   t_traj_total = [0;t_traj];
   u_traj_total = [u_init';u_traj];
   a_traj_total = [alpha_zero;alpha_traj];
else
   N_new_steps = length(t_traj);
   N_old_steps = length(t_traj_total);
   for i=1:N_new_steps
      t_traj(i) = t_traj(i) + t_traj_total(N_old_steps);
   end
   t_traj_total = [t_traj_total;t_traj];
   u_traj_total = [u_traj_total;u_traj];
   a_traj_total = [a_traj_total;alpha_traj];
end

% Plot interface position vs. time
last_step = size(u_traj_total,1);
el = zeros(last_step,1);
for i=1:last_step
   el(i) = WellDepth - a_traj_total(i);
end

figure;
plot(t_traj_total,el);
xlabel('Time');
ylabel('Interface position');
title('Interface position vs. time (dimensionless)');

% Plot centerline concentration profile vs. time

figure;
for itime=1:last_step
   center_conc = zeros(Nzeta+Nzo,1);
   for i=1:Nzeta
      j=1;
      k=(i-1)*Neta+j;
      center_conc(i) = u_traj_total(itime,k);
   end
   for i=Nzeta+1:Nzeta+Nzo
      j=1;
      k=Neta*Nzeta + Nro + (i-Nzeta-1)*(Neta+Nro) + j;
      center_conc(i) = u_traj_total(itime,k);
   end
   plot(zeta,center_conc);
   hold on;
end
hold off;
xlabel('Zeta (0 to 1 coordinates are compressed by alpha)');
ylabel('Concentration (dimensionless)');
title('Centerline concentration profiles vs. time');

% Plot concentration profile in dead space at final time
% Can modify the choosing of time_snap to give plots at various times

i_time_snap = last_step; % Choose final time step for plot
time_snap = t_traj_total(i_time_snap);

% Create zeta vector that excludes points inside well
for i=Nzeta:Nzeta+Nzo
   j=1;
   zout(i-Nzeta+1) = zeta(i) - 1;
end
```

```
% Extract concentration profile from u trajectory matrix into
% a matrix Theta in which Theta(row,col) = concentration at
% eta = eta(row) and zeta = WellDepth + zout(col)
for i=Nzeta:Nzeta+Nzo
   for j=1:Neta+Nro
      k=Neta*Nzeta + Nro + (i-Nzeta-1)*(Neta+Nro) + j;
      Theta(j,i-Nzeta+1) = u_traj_total(i_time_snap,k);
   end
end

[XX,YY] = meshgrid(zout,eta);
figure;
surf(XX,YY,Theta);
xlabel('Axial direction');
ylabel('Radial direction');
zlabel('Concentration');
phrase1 = ['Concentration profile in dead space at time = '
num2str(time_snap)];
title(phrase1);
```

10.7.2. Calculation of the A matrix

```
% calcA_Cylinder3.m
% Audrey M. Johnson 5/30/2001
%
% This subroutine calculates the A matrix associated with
% the simulation of diffusion from a cylindrical well into
% a large dead space (with a moving interface)
% The space is discretized so that the points representing
% the interior of the well are 'stretched' as the dissolution
% interface moves further toward the back of the well.
%

function [A,alpha,iflag] = calcA_Cylinder3(x_state,param,iparam);

% Unstack relevant parameters passed from main program in param vector
% Need: Nzeta, Neta, Nzo, Nro, PhiWell, PhiOut, ThetaL, ThetaS, alpha, dt
% and the vectors zeta and eta

Nzeta = iparam(1);
Neta = iparam(2);
Nzo = iparam(3);
Nro = iparam(4);

k = 0;
zeta = param(k+1:k+Nzeta+Nzo); k = k + Nzeta + Nzo;
eta = param(k+1:k+Neta+Nro); k = k + Neta + Nro;
PhiWell = param(k+1); k = k + 1;
PhiOut = param(k+1); k = k + 1;
ThetaL = param(k+1); k = k + 1;
ThetaS = param(k+1); k = k + 1;
WellDepth = param(k+1); k = k + 1;
alpha_old = param(k+1); k = k + 1;
dt = param(k+1);

% First, check to see if we're already at the back of the well
if(alpha_old>=WellDepth)
   solid_flag = 1;
else
   solid_flag = 0;
end

% Next, check to see if this is the first time we're calculating A
% The first time, x_state is still equal to the initial condition...
```

```
% Choose a point adjacent to the interface that should be zero only before
% any diffusion has taken place: i = 2, j = Neta - 1 --> k=2*Neta - 1;

test_point = x_state(2*Neta-1);
if(test_point==0)
   initial_calc = 1;
else
   initial_calc = 0;
end

% If this is not the first calculation and we are not at back of well, move
interface
ThetaQ = 0;
ThetaR = 0;
if(solid_flag==1)
   alpha = WellDepth;
   del = 0;
elseif(initial_calc==1)
   alpha = alpha_old;
   del = 0;
else
% First, extract average values of concentration next to interface
for j=2:Neta-1
   i = 2;
   k = (i-1)*Neta + j;
   ThetaQ = ThetaQ + x_state(k);
   ThetaR = ThetaR + x_state(k+Neta);
end
ThetaQ = ThetaQ/(Neta - 2);
ThetaR = ThetaR/(Neta - 2);

% Now, calculate the slope of the concentration curve near the interface
% Use a parabolic approximation of the form C = ax^2 + bx + c
% Then the slope at x = 0 is b
a_top = (ThetaL - ThetaQ)*(zeta(3) - zeta(2)) + zeta(2)*(ThetaR - ThetaQ);
a_bot = (zeta(2)*(zeta(3)^2-zeta(2)^2) - (zeta(3)-
zeta(2))*zeta(2)^2)*alpha_old^2;
a = a_top/a_bot;
Slope = (ThetaQ - ThetaL - a*zeta(2)*alpha_old^2)/(alpha_old*zeta(2));
del = -dt*Slope/(ThetaS-1);
alpha = alpha_old + del;

% Check to see if time step is too large (causes oscillations in alpha)
if(del<=0)
   disp(['Time step of ' num2str(dt) ' too large -- oscillations in
simulation!']);
end

% Check to make sure the interface hasn't been moved past the back of the well
if(alpha>=WellDepth)
   solid_flag = 1;
   alpha = WellDepth;
end

end % of if statement on whether the interface is moving

% Initialize A matrix to zero
Ntotal = Neta*Nzeta + Nro + Nzo*(Neta + Nro);
A = spalloc(Ntotal,Ntotal,5*Ntotal);

% Define interior points in well (region 1)
for i=2:Nzeta-1
   for j=2:Neta-1
```

```
      k = (i-1)*Neta + j;
      F = eta(j)*(eta(j+1)-eta(j-1))*(eta(j+1)-eta(j))*(eta(j)-eta(j-1));
      G = (zeta(i+1)-zeta(i-1))*(zeta(i+1)-zeta(i))*(zeta(i)-zeta(i-
1))*(alpha^2)/2;
      A(k,k+Neta) = (zeta(i)-zeta(i-1))/G;
      A(k,k+1) = (eta(j+1)+eta(j))*(eta(j)-eta(j-1))/F;
      A(k,k)=-((eta(j+1)+eta(j))*(eta(j)-eta(j-1))+(eta(j-1)+eta(j))*(eta(j+1)-
eta(j)))/F-(zeta(i+1)-zeta(i-1))/G;
      A(k,k-1) = (eta(j-1)+eta(j))*(eta(j+1)-eta(j))/F;
      A(k,k-Neta) = (zeta(i+1)-zeta(i))/G;
   end
end

% Define interior points in dead space (region 2)
for i=Nzeta+1:Nzeta+Nzo-1
   for j=2:Neta+Nro-1
      k = Neta*Nzeta + Nro + (i-Nzeta-1)*(Neta+Nro) + j;
      F = eta(j)*(eta(j+1)-eta(j-1))*(eta(j+1)-eta(j))*(eta(j)-eta(j-1));
      G = (zeta(i+1)-zeta(i-1))*(zeta(i+1)-zeta(i))*(zeta(i)-zeta(i-1))/2;
      A(k,k+Neta+Nro) = (zeta(i)-zeta(i-1))/G;
      A(k,k+1) = (eta(j+1)+eta(j))*(eta(j)-eta(j-1))/F;
      A(k,k)=-((eta(j+1)+eta(j))*(eta(j)-eta(j-1))+(eta(j-1)+eta(j))*(eta(j+1)-
eta(j)))/F-(zeta(i+1)-zeta(i-1))/G;
      A(k,k-1) = (eta(j-1)+eta(j))*(eta(j+1)-eta(j))/F;
      A(k,k-Neta-Nro) = (zeta(i+1)-zeta(i))/G;
   end
end

% Define centerline boundary points (region 3)
for i=1:Nzeta
   j = 1;
   k = (i-1)*Neta + j;
   Fa = eta(j+2)^2 - eta(j+1)^2 + 2*eta(j)*(eta(j+1) - eta(j+2));
   Ga = 2*eta(j)*eta(j+1) - eta(j)^2 - eta(j+1)^2;
   A(k,k) = 1;
   A(k,k+1) = Ga/Fa - 1;
   A(k,k+2) = -Ga/Fa;
end

for i=Nzeta+1:Nzeta+Nzo
   j = 1;
   k = Neta*Nzeta + Nro + (i-Nzeta-1)*(Neta+Nro) + j;
   Fa = eta(j+2)^2 - eta(j+1)^2 + 2*eta(j)*(eta(j+1) - eta(j+2));
   Ga = 2*eta(j)*eta(j+1) - eta(j)^2 - eta(j+1)^2;
   A(k,k) = 1;
   A(k,k+1) = Ga/Fa - 1;
   A(k,k+2) = -Ga/Fa;
end

% Define well wall boundary points (region 4)
for i=1:Nzeta
   j = Neta;
   k = (i-1)*Neta + j;
   A(k,k) = 1;
   Fa = eta(j-2)^2 - eta(j-1)^2 + 2*eta(j)*(eta(j-1) - eta(j-2));
   Ga = 2*eta(j)*eta(j-1) - eta(j)^2 - eta(j-1)^2;
   A(k,k-1) = Ga/Fa - 1;
   A(k,k-2) = -Ga/Fa;
end

% Define radial edge boundary points (region 5)
for i=Nzeta:Nzeta+Nzo
   j = Neta + Nro;
```

```
   k = Neta*Nzeta + Nro + (i-Nzeta-1)*(Neta+Nro) + j;
   A(k,k) = 1;
end

% Define chip wall boundary points (region 6)
for j=Neta+1:Neta+Nro-1
   i = Nzeta;
   k = Neta*Nzeta + Nro + (i-Nzeta-1)*(Neta+Nro) + j;
   Fa = zeta(i+2)^2 - zeta(i+1)^2 + 2*zeta(i)*(zeta(i+1)-zeta(i+2));
   Ga = 2*zeta(i)*zeta(i+1) - zeta(i)^2 - zeta(i+1)^2;
   A(k,k) = 1;
   A(k,k+Neta+Nro) = Ga/Fa - 1;
   A(k,k+2*Neta+2*Nro) = -Ga/Fa;
end

% Define axial edge boundary points (region 7)
for j=2:Neta+Nro-1
   i = Nzeta + Nzo;
   k = Neta*Nzeta + Nro + (i-Nzeta-1)*(Neta+Nro) + j;
   A(k,k) = 1;
end

% Define well opening points (region 8)
for j=2:Neta-1
   i = Nzeta;
   k = (i-1)*Neta + j;
   F = eta(j)*(eta(j+1)-eta(j-1))*(eta(j+1)-eta(j))*(eta(j)-eta(j-1));
   G = (alpha*(zeta(i)-zeta(i-1))+zeta(i+1)-zeta(i))*(zeta(i+1)-
zeta(i))*(zeta(i)-zeta(i-1))*alpha/2;
   A(k,k-Neta) = (zeta(i+1)-zeta(i))/G;
   A(k,k-1) = (eta(j-1)+eta(j))*(eta(j+1)-eta(j))/F;
   A(k,k) = -((eta(j+1)+eta(j))*(eta(j)-eta(j-1))+(eta(j-1)+eta(j))*(eta(j+1)-
eta(j)))/F;
   A(k,k) = A(k,k) - (alpha*(zeta(i)-zeta(i-1))+zeta(i+1)-zeta(i))/G;
   A(k,k+1) = (eta(j+1)+eta(j))*(eta(j)-eta(j-1))/F;
   A(k,k+Neta+Nro) = alpha*(zeta(i)-zeta(i-1))/G;
end

% Define dissolution interface or back of well (region 9)

if(solid_flag==1)
   % Define no flux at back of well (region 9b)
   for j=2:Neta-1
      i = 1;
      k = (i-1)*Neta + j;
      Fa = zeta(i+2)^2 - zeta(i+1)^2 + 2*zeta(i)*(zeta(i+1)-zeta(i+2));
      Ga = 2*zeta(i)*zeta(i+1) - zeta(i)^2 - zeta(i+1)^2;
      A(k,k) = 1;
      A(k,k+Neta) = Ga/Fa - 1;
      A(k,k+2*Neta) = -Ga/Fa;
   end
else
   % Define concentration at interface to be ThetaL (region 9a)
   for j=2:Neta-1
      i = 1;
      k = (i-1)*Neta + j;
      A(k,k) = 1;
   end
end

return;
```

10.7.3. Calculation of the b vector

```
% calcb_Cylinder3.m
% Audrey M. Johnson 5/30/2001
%
% This subroutine calculates the b vector associated with
% the simulation of diffusion from a cylindrical well into
% a large dead space (with a moving interface)

function [b,iflag] = calcb_Cylinder3(x_state,param,iparam);

% Unstack relevant parameters passed from main program in param vector
% Need: Nzeta, Neta, Nzo, Nro, PhiWell, PhiOut, and the vectors zeta, eta

Nzeta = iparam(1);
Neta = iparam(2);
Nzo = iparam(3);
Nro = iparam(4);

k = 0;
zeta = param(k+1:k+Nzeta+Nzo); k = k + Nzeta + Nzo;
eta = param(k+1:k+Neta+Nro); k = k + Neta + Nro;
PhiWell = param(k+1); k = k + 1;
PhiOut = param(k+1); k = k + 1;
ThetaL = param(k+1); k = k + 1;
ThetaS = param(k+1); k = k + 1;
WellDepth = param(k+1); k = k + 1;
alpha_old = param(k+1); k = k + 1;
dt = param(k+1);

% First, check to see if we're already at the back of the well
if(alpha_old>=WellDepth)
   solid_flag = 1;
else
   solid_flag = 0;
end

% Then, see if interface is reaching the back of well with this time step
ThetaQ = 0;
ThetaR = 0;
for j=2:Neta-1
   i = 2;
   k = (i-1)*Neta + j;
   ThetaQ = ThetaQ + x_state(k);
   ThetaR = ThetaR + x_state(k+Neta);
end
ThetaQ = ThetaQ/(Neta - 2);
ThetaR = ThetaR/(Neta - 2);

a_top = (ThetaL - ThetaQ)*(zeta(3) - zeta(2)) + zeta(2)*(ThetaR - ThetaQ);
a_bot = (zeta(2)*(zeta(3)^2-zeta(2)^2) - (zeta(3)-
zeta(2))*zeta(2)^2)*alpha_old^2;
a = a_top/a_bot;
Slope = (ThetaQ - ThetaL - a*zeta(2)*alpha_old^2)/(alpha_old*zeta(2));
del = -dt*Slope/(ThetaS-1);
alpha = alpha_old + del;

if(alpha>=WellDepth)
   solid_flag = 1;
   alpha = WellDepth;
end

% Initialize b vector to zero
```

```
Ntotal = Neta*Nzeta + Nro + Nzo*(Neta + Nro);
b = zeros(Ntotal,1);

% Define interior points in well (region 1)
for i=2:Nzeta-1
   for j=2:Neta-1
      k = (i-1)*Neta + j;
      b(k) = -PhiWell;
   end
end

% Define interior points in dead space (region 2)
for i=Nzeta+1:Nzeta+Nzo-1
   for j=2:Neta+Nro-1
      k = Neta*Nzeta + Nro + (i-Nzeta-1)*(Neta+Nro) + j;
      b(k) = -PhiOut;
   end
end

% Define well opening points (region 8)
for j=2:Neta-1
   i = Nzeta;
   k = (i-1)*Neta + j;
   b(k) = -PhiWell;
end

% Define dissolution interface (region 9a) or back of well (9b)
if(solid_flag==0)
   % Define concentration at interface to be ThetaL
   for j=2:Neta-1
      i = 1;
      k = (i-1)*Neta + j;
      b(k) = ThetaL;
   end
end

% For all other regions (boundaries, #3-7 and 9b), b(k) is zero
```

10.7.4. Calculation of the Jacobian matrix

```
% calcb_Jac_Cylinder3.m
% Audrey M. Johnson 5/30/2001
%
% This subroutine calculates the Jacobian matrix associated with
% the simulation of diffusion from a cylindrical well into
% a large dead space (with a moving interface)
% For this simulation, the Jacobian of the b matrix is zero
% (This subroutine exists only to fit the format of KJB_PDE_solver1_AJ3.m)

function [b_Jac,iflag] = calcb_Jac_Cylinder2(x_state,param,iparam);

% Unstack relevant parameters passed from main program in iparam
% Need: Nzeta, Neta, Nzo, Nro

Nzeta = iparam(1);
Neta = iparam(2);
Nzo = iparam(3);
Nro = iparam(4);

Ntotal = Neta*Nzeta + Nro + Nzo*(Neta + Nro);

b_Jac = spalloc(Ntotal,Ntotal,Ntotal);
```

10.7.5. Solver routine

```
% KJB_PDE_solver1_AJ3.m
% Modified slightly by Audrey M. Johnson, 5/30/2001
% (in order to report the interface position vs. time)
%
% This MATLAB m-file uses either implicit Euler time integration or
% the trapezoid rule to simulate a DAE system with the common structure
% of a discretized PDE.  Linearized forms of the updating equations
% are used.  The system is of the form :
%
%  epsilon_k * du_k/dt = \sum_j{ A_{kj} * u_j} - b_k(u_1,...,u_N)
%
% where for every equation corresponding to an interior point,
% epsilon_k is set equal to one to signify it is an ODE.  For
% every equation corresponding to a boundary condition, epsilon_k
% is set equal to zero.
%
% This subroutine is called with the following form.
%
% [t_traj,u_traj,alpha_traj,iflag] =
KJB_PDE_solver1_AJ3(u_init,epsilon,calc_A,calc_b,calc_b_Jac,iopt,ropt,param,ipa
ram)
%
% where the input arguments are :
%
% u_init = the initial state vector at the start of the simulation
% epsilon = a vector containing 1's for the ODE's and 0's for
%           the algebraic equations
% calc_A = name of subroutine that returns the A matrix given u
% calc_b = name of subroutine that returns the b vector given u
% calc_b_Jac = name of subroutine that returns the Jacobian of b
% Nsteps = number of time steps the integretor is to perform
% dt = the time step to be used during the simulation
% iopt : This is a column vector of five integer option values
%       iopt(1) if 0, use implicit Euler
%               if 2, use trapezoid rule
%       iopt(2) if non-zero, constrain all variables to
%               be positive
%       iopt(3) if 0, A matrix does not depend on u
%               if non-zero, calculate new A at each step
%       iopt(4) this variable, iprint, tells how often
%               to write out the results of the simulation.
%               If zero, only the final results are output.
%       iopt(5) This is how many simulation steps are to
%               be performed between calculations of the
%               Jacobian
%       iopt(6) This is the total number of simulation steps
%               to be performed
% ropt : This is a column vector of real parameters for the solver
%       ropt(1) this is the time step used for the solver
%       ropt(2) this is the convergence tolerance for
%               stopping at steady state.  If zero, then
%               the simulation is performed until the end
%               of the requested time period without stopping
%               at steady state
%               suggested value = 1e-10
%
% param = this is a vector of real parameters
% iparam = this is a vector of integer parameters
%
% The output arguments are :
%
```

```
% t_traj = column vector of the times at which the results are returned
% u_traj = matrix where the rows are the state vector at each time step
% alpha_traj = column vector of the interface position at each time step
% iflag = integer flag denoting completion or convergence
%
% Written by K.J. Beers. 4/20/2001

function [t_traj,u_traj,alpha_traj,iflag,error] =
KJB_PDE_solver1_AJ3(u_init,epsilon,calc_A,calc_b,calc_b_Jac,iopt,ropt,param,ipa
ram);

% We now unstack the iopt and ropt options.
i_method = iopt(1);
i_pos = iopt(2);
i_A_depend = iopt(3);
i_print = iopt(4);
i_Jac = iopt(5);
Nsteps = iopt(6);

dt = ropt(1);
tol_conv = ropt(2);

% Unstack iparam for updating alpha in loop later
Nzeta = iparam(1);
Neta = iparam(2);
Nzo = iparam(3);
Nro = iparam(4);
k_a = Nzeta + Nzo + Neta + Nro + 6;

iflag = 0;

% First, the state vector is set equal to the initial value.
u_state = u_init;
Nvar = length(u_init);

% Then, we make a list of the positions of all boundary points.
i_AE = find(epsilon - linspace(1,1,Nvar)');

% We now allocate memory for the output from printing.
count_print = 0;
if(i_print==0)
    next_print = Nsteps;
    num_print = 1;
else
    next_print = i_print;
    num_print = floor(Nsteps/i_print) + 2;
end
t_traj = linspace(0,0,num_print+1)';
u_traj = zeros(num_print+1,Nvar);
alpha_traj = linspace(0,0,num_print+1)';

time = 0;

if(i_Jac < 1)
    i_Jac = 1;
end
next_Jac = i_Jac;

if(i_method==0)
    theta = 1;  % implicit Euler
else
    theta = 0.5;  % trapezoid rule
end
```

```
% We calculate A and b_Jac if needed.
if(i_A_depend==0)
    A = feval(calc_A,u_state,param,iparam);
end
if(ne(i_Jac,1))
    b_Jac = feval(calc_b_Jac,u_state,param,iparam);
end

% We periodically print out when passing various measures of the
% error.
target_error_log10 = 10;

for istep = 1:Nsteps

    % If A has state dependence, we need to recalculate it.
    if(i_A_depend)
        [A,alpha] = feval(calc_A,u_state,param,iparam);
        % We must then make sure to update alpha in the param vector
        param(k_a) = alpha;
    end

    % Next, we calculate the b vector.
    b = feval(calc_b,u_state,param,iparam);

    % Then, we get the Jacobian of the b vector.
    if(istep >= next_Jac)
        b_Jac = feval(calc_b_Jac,u_state,param,iparam);
        next_Jac = next_Jac + i_Jac;
    end

    % For the Jacobian, we neglect the state dependence
    % of the A matrix.
    Jac = A - b_Jac;

    % Then, the time derivative.
    f = A*u_state - b;

    % We check now for convergence.
    error = sqrt(dot(f,f)/Nvar);
    error_log10 = log10(error);
    if(error_log10 <= target_error_log10)
        target_error_log10 = error_log10 - 1;
        disp([istep error_log10]);
    end
    if(error < tol_conv)
        iflag = 1;
        break;
    end

    % Then, we calculate the new state vector with a
    % linearized form of either implicit Euler or
    % the trapezoid rule.  The linear system to be
    % solved contains the standard updating equation
    % for the rows corresponding to the interior
    % point ODE's, and linearized equations for the
    % boundary point equations.  To lessen the
    % storage requirements, we store in the matrix
    % Jac the updating equation rather than create
    % a new matrix.

    Jac = speye(Nvar) - theta*dt*Jac;
    b_up = dt*f;
```

```
    for i=1:length(i_AE)
        k = i_AE(i);
        b_up(k) = b(k) - dot(A(k,:),u_state');
        Jac(k,:) = A(k,:);
    end

    delta_u = Jac\b_up;
    u_state = u_state + delta_u;
    time = time + dt;

    % As needed, the profiles are reported.
    if(istep >= next_print)
        disp(istep);
        count_print = count_print + 1;
        next_print = next_print + i_print;
        t_traj(count_print) = time;
        u_traj(count_print,:) = u_state';
        alpha_traj(count_print) = alpha;
     end

end

% Finally, we extract out the non-zero part of the
% trajectory matrix to report.
if(count_print > 1)
    t_traj = t_traj(1:count_print);
    u_traj = u_traj(1:count_print,:);
    alpha_traj = alpha_traj(1:count_print);
else
    t_traj = time;
    u_traj = u_state';
    alpha_traj = alpha;
end

return;
```